CHINESE NATIONAL COMMITTEE FOR COSPAR
CNCOSPAR

SPACE SCIENCE ACTIVITIES IN CHINA
National Report 2024—2026

Chief Editor: GUO Huadong

Deputy Chief Editor: WANG Chi, LI Lei

Editorial Staff: SUN Weiying, SONG Yana

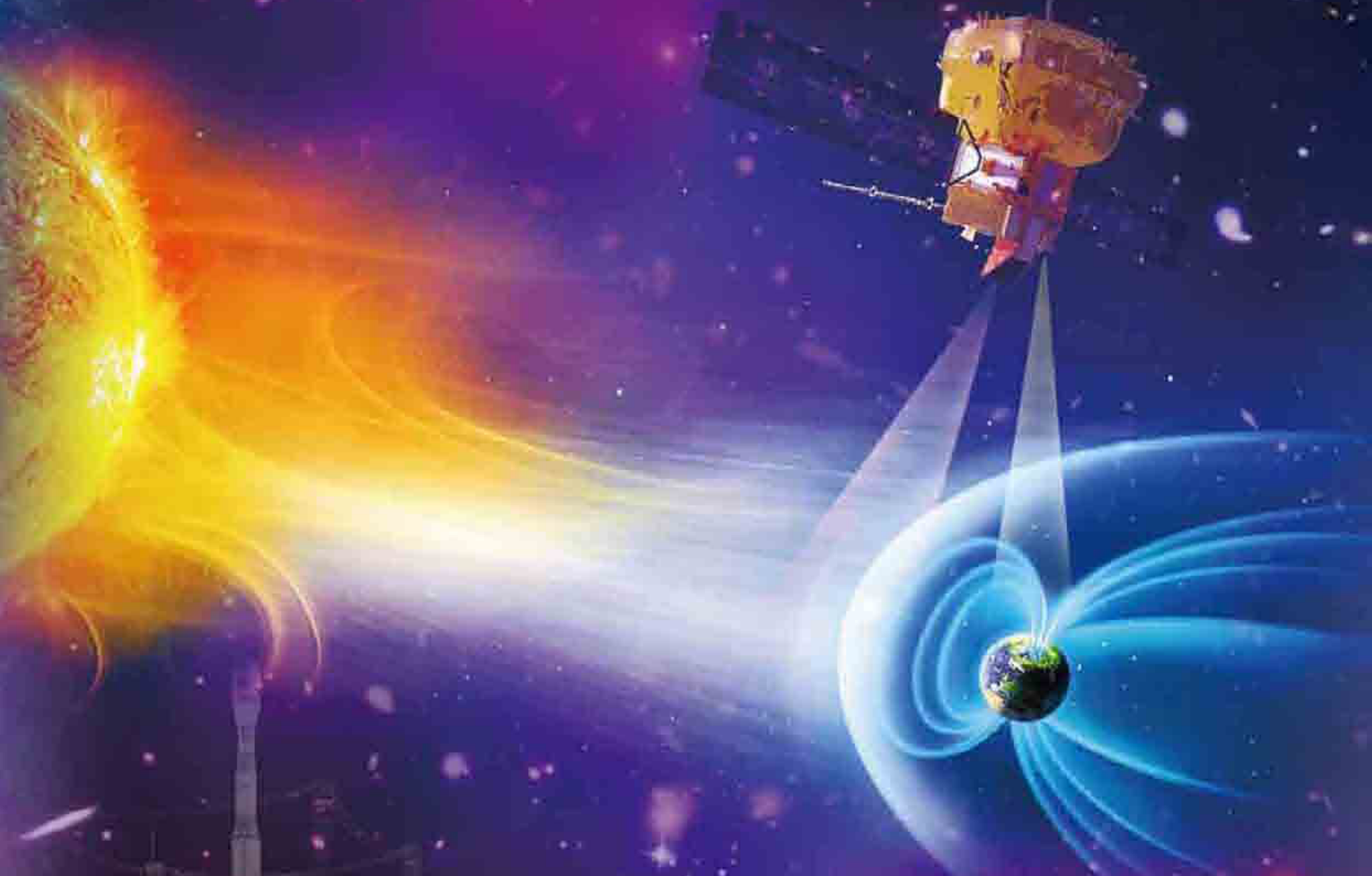

CNCOSPAR

August 2026

Preface

The period from 2024 to 2026 has witnessed remarkable progress in China’s space science, lunar and deep space exploration, manned spaceflight, and application satellite programs, delivering significant scientific outcomes and forging new pathways for international collaboration.

In 2024, the *National Mid- and Long-term Plan for Space Science in China (2024–2050),* the first of its kind at the national level, was jointly released by the Chinese Academy of Sciences, the China National Space Administration and the China Manned Space Agency, which will guide the country's planning of space science missions and space research from 2024 to 2050. It outlines the development goals of China's space science, including 17 priority areas under five key scientific themes, as well as a three-phase roadmap. The five key scientific themes include the extreme universe, space-time ripples, panoramic view of Sun-Earth, habitable planets, and biological and physical sciences in space.

The “Origins” Space Science Program directly addresses the first-phase objectives of the *National Mid- and Long-term Plan for Space Science in China (2024–2050)*. Focusing on fundamental questions concerning the “origins”, this program encompasses four flagship space science satellite missions: Discovering the Sky at the Longest wavelength (DSL), the Solar Polar Orbit Observatory (SPO), the Earth 2.0 (ET) mission, and the Enhanced X-ray Timing and Polarimetry (eXTP) mission. By 2025, all four missions have completed the Preliminary Design Phase and are currently in the Prototype Phase, with launches scheduled between 2028 and 2030.

For space science satellites, the Einstein Probe (EP) mission was successfully launched on 9 January 2024, with the objectives of carrying out a wide-field-view sky survey in the soft X-ray band, discovering high-energy transients and monitoring variable objects. The Space-based multi-band Variable Object Monitor (SVOM), a mission dedicated to studying Gamma-Ray Bursts (GRBs), was launched on 22 June 2024. The Solar wind Magnetosphere Ionosphere Link Explorer (SMILE), a flagship joint mission between the European Space Agency and the Chinese Academy of Sciences, was successfully launched on 19 May 2026 in Kourou, French Guiana. In this report, you will also find the progress of the various scientific missions in the Strategic Priority Program on Space Science initiated by the Chinese Academy of Sciences, including the Dark Matter Particle Explorer (DAMPE), the Hard X-ray Modulation Telescope (HXMT), the Gravitational wave high-energy Electromagnetic Counterpart All-sky Monitor (GECAM), the Advanced space-based Solar Observatory (ASO-S), *etc*. As a dedicated scientific satellite tailored to advance the implementation of the United Nations 2030 Agenda for Sustainable Development (2030 Agenda), the Sustainable Development Science Satellite 1 (SDGSAT-1) has entered its fifth year of in-orbit operation and its data has been used by more than 116 countries.

For manned spaceflight, the China Space Station (CSS) was assembled by the end of 2022, consisting of three modules with intravehicular science experiment racks and extravehicular exposed facilities. To date, it has been operating for over three years, and more than 170 science and utilization projects have been implemented. A series of original, cutting-edge and innovative progress and achievements have been achieved in space life sciences and biotechnology, space materials science, microgravity fluid and thermal physics, microgravity combustion science, microgravity fundamental physics, and space innovative technology demonstration.

For lunar and deep space exploration, China's lunar mission and Mars mission has entered a highly productive scientific stage, highlighted by the Chang'E-6 lunar sample return mission, the first-ever collection of samples from the far side of the Moon, and the continued scientific exploitation of Tianwen-1 Mars mission datasets, shedding light on terrestrial planet evolution, volatile histories, impact processes, and surface-environment interactions across the inner Solar System.

For ground-based observations, the second phase of the Chinese Meridian Project (CMP) passed its national acceptance review in March 2025, marking the completion of a comprehensive ground-based space environment monitoring network. Building upon the solid foundation of the Chinese Meridian Project, China, in partnership with global collaborators, has initiated the International Meridian Circle Program (IMCP), which aims to establish a globally distributed network of ground-based instruments—primarily along the 120°E and 60°W meridians, spanning multiple countries and continents, which will operate for at least a full solar cycle (11 years).

In the realm of application satellites, significant advances have been made across meteorological, oceanic, and land resources domains. For meteorological satellites, with the successful launch of FY-3H polar-orbiting satellite and FY-4C geostationary satellite, the FY constellation has improved the polar four-orbit networking and geostationary two-satellite coordinated configuration, realizing optimized GEO-LEO satellites collaborative observation. For ocean satellites, the successful launch of HY-4A has filled a gap in China's spaceborne ocean salinity observation capability and provided a foundational capacity for operational global ocean salinity monitoring and related scientific research. For land resources satellites, the China Seismo-Electromagnetic Satellite-02 (CSES-02) launched in June 2025, ZY-3 04 launched in December 2025, and High-Precision Greenhouse Gas Comprehensive Exploration Satellite (DQ-2) launched in April 2026 were successfully launched into orbits to enhance China's space-based infrastructure for geophysical field measurements, high-precision stereoscopic mapping, and greenhouse gas monitoring, respectively.

International cooperation remains an integral part of China's space science endeavors. All major space science missions include international collaborative elements, and partners from around the world are warmly welcomed to participate in Chinese scientific programs.

In this report, principal investigators of scientific missions and leading experts from various fields of space science in China present the major programs, highlight mission achievements, describe the status of upcoming missions, and outline future planning. We hope that readers will gain a comprehensive picture of the recent progress in space research in China, and we cordially invite the international community to make use of the publicly available data from Chinese space science missions.

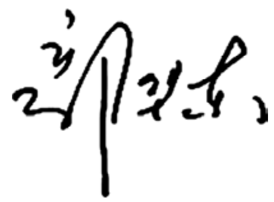

Prof. GUO Huadong
President of Chinese National Committee for COSPAR

Contents

0254-6124/2026/46(4)-0001-30 *Chin. J. Space Sci.* 空间科学学报

GU Yidong, WANG Qiang, LÜ Congmin, LI Xuzhi, ZHONG Hongen, LIU Guoning, ZHANG Wei, ZHANG Jiuxing, BA Jin. Progress in Space Science and Utilization on the China Space Station in 2024–2026. *Chinese Journal of Space Science*, 2026, **46**(4): 1–30. CSTR:32142.14.cjss.2026–yg05. DOI:10.11728/cjss2026.04.2026–yg05

Progress in Space Science and Utilization on the China Space Station in 2024–2026

GU Yidong WANG Qiang LÜ Congmin LI Xuzhi ZHONG Hongen
LIU Guoning ZHANG Wei ZHANG Jiuxing BA Jin

(*Key Laboratory of Space Utilization, Technology and Engineering Center for Space Utilization, Chinese Academy of Sciences, Beijing* 100094)

Abstract The China Space Station was assembled by the end of 2022, comprising three modules equipped with intravehicular science experiment racks and extravehicular exposed facilities. Operating for over three years, the station has implemented more than 170 science and utilization projects. A series of original, cutting-edge achievements has been attained in space life sciences and biotechnology, space materials science, microgravity fluid and thermal physics, microgravity combustion science, microgravity fundamental physics, and space innovative technology demonstration. This paper introduces the general progress of in-orbit science and utilization, along with typical scientific discoveries—such as the mammal on-orbit feeding experiment, growth of InSe semiconductor crystals, fabrication of high-performance field-effect transistors on ground, and observation of a metastable Body-Centered Cubic (BCC) phase in the crystallization of charged colloids. Planned science and utilization projects will be executed progressively and systematically. Furthermore, applications and transformations of these findings will be further promoted.

Key words China Space Station (CSS), Microgravity, Space science, Space utilization, On-orbit experiment

Classified index P35, V47

1 Introduction to the China Space Station

The China Space Station (CSS)[1–4] represents a comprehensive low-Earth space research platform in China. It was assembled by the end of 2022, which was in the “T” shape with three modules: the Core Module named “Tianhe”, and the Experimental Module I named “Wentian”, and the Experimental Module II named “Mengtian”. The CSS has exhibited a consistent operational stability over a period of three years, successfully accomplishing seven manned launch missions (SZ-16, 17, 18, 19, 20, 21, 23), five cargo resupply missions (TZ-6, 7, 8, 9, 10), and eight spacecraft return missions (SZ-15, 16, 17, 18, 19, 20, 21, 22), including the first emergency launch (SZ-22). Seven astronaut crew groups have participated in long-term stays in orbit, engaging in more than ten times extravehicular activities.

A suite of advanced scientific experimental racks have been deployed within the three experimental modules[4–6], including Life and Ecology experiment Rack (LER), BioTechnology experiment Rack (BTR), High-Temperature Materials experiment Rack (HTMR), Containerless Materials Processing Rack (CMPR), Fluids Physics experiment Rack (FPR), Two-Phase System experiment Rack (TPSR), Combustion Science experi-

Received May 20, 2026

ment Rack (CSR), High Microgravity Level Rack (HMLR), Cold Atom Physics experiment Rack (CAPR), High-Precision Time-Frequency System (HPTFS), Variable Gravity experiment Rack (VGR), Glovebox and Cold Storage Rack (GCSR), on-orbit Maintenance and Manipulation Workbench (MMW), and three extravehicular exposed experimental platform, including Exposed Radiation Biology Facility (ERBF), Exposed Materal Fcility (EMF), Exposed Component Facility (ECF). These facilities aboard the CSS have effectively supported cutting-edge scientific exploration, national needs, and technological progress. In addition, the China Space station Survey Telescope (CSST)[7] is currently under construction and it is a 2-meter caliber telescope with high-performance design. The telescope will fly and operate in conjunction with the CSS and is expected to facilitate groundbreaking researches of fundamental cosmology, such as the nature of dark energy and dark matter, galaxies and active galactic nuclei, the Milky Way and neighboring galaxies. The High Energy cosmic-Radiation Detection (HERD) facility[8] is currently under construction to support significant researches including the search for dark matter, the origin of cosmic ray, and the evolution of extreme celestial, *etc*. The expansion module is being planned to support the installation and operation of the HERD. Therefore, the basic configuration of the CSS will be upgraded from "T" to "X". Moreover, it is worth mentioning that the space science experimental racks and extravehicular experimental facilities in various areas will further expand the science and utilization scale[9].

2 Space Science and Utilization of the CSS

Four primary research areas have been delineated: space life science and human research (including space life sciences and biotechnology, space human research), microgravity physics (including space materials science, microgravity fluid and thermal physics, microgravity combustion science, and microgravity fundamental physics), space astronomy and earth science(including space astronomy and astrophysics, space earth science, space physics and space environment), and space innovative technology and application (including space innovative technology demonstration and aerospace technology experiment).

Regular solicitation, selection, and space science and utilization projects implementations have been effectively conducted and a project research and management framework has been established. The public project solicitation and selection were conducted in 2019, 2023 and 2024, respectively. In addition, three annual summaries and evaluations (in 2023, 2024, 2025) were carried out, laying the foundation for the general progress, achievement evaluation, and project completion. The China Manned Space Agency (CMSA) has released two public "Progress Report on Scientific Research and Application of the China Space Station" (2024 and 2025)[6,10] to the society. These reports detailed a total of 67 cases of science and utilization research progress, as well as 11 cases of scientific popularization. The first academic conference concerning space science and utilization of the CSS was successfully held in Xi'an in 2024. These activities have attracted experts and scholars to actively participate in the CSS science and utilization projects.

As of 20 June 2026, the CSS had successfully deployed and implemented more than 170 science and utilization projects in orbit, achieving large number of science and utilization achievements and engineering technology breakthroughs[6,10,11]. The following section will present these achievements in detail. In the aforementioned areas of life, materials, fluid, combustion, fundamental physics, and innovative technology demonstration, a substantial body of scientific data, amounting to over 450 TB, has been obtained, and more than 500 papers have been published based on ground matching experiments, on-orbit experimental samples, and scientific data. The space materials science and technology special issue has been published in "*SCIENCE CHINA Technological Sciences*", and the scientific data simulation special issue of the CSST has been published in "*Research in Astronomy and Astrophysics*". These achievements and breakthroughs have had a significant impact on the development of space science and utilization in China. A preliminary investigation has been made regarding applications and transformations.

3 Space Life Science and Biotechnology

The area of space life science and biotechnology focuses primarily on fundamental biology, space life ecology, space biotechnology and its applications, as well as the origin of life and interdisciplinary research in space. A multi-level research system has been established that spans from the molecular and cellular levels to tissues, organs and individual organisms. The system elucidates the mechanisms and response patterns through which the space environment impacts life at various levels. Thirty-nine projects (statistics as of 20 June 2026) have been successfully implemented in orbit, achieving significant advancements in cell biology, botany, zoology, protein crystallization, the origin of life and radiation biology aboard the CSS. The progress and achievements have sparked new ideas and strategies, also yielding novel concepts and methodologies for the prevention and treatment of associated pathologies, the design and formulation of related pharmaceuticals, the cultivation of space plants, and the building of experimental platforms, among other applications.

3.1 The First Mouse Experiment aboard the CSS

The primary technology verification had been conducted for mouse feeding based aboard the CSS, thereby overcoming the efficient and precise biological control technology for mammals in small enclosed spaces[10,12]. The first small mammal feeding device for the CSS was independently developed, and a comprehensive process experimental system for small mammals was established in China. Four SPF grade C57 BL/6 JNifdc experimental mice that had been screened and trained were sent to the CSS, where they completed a 14-day space-enclosed mice feeding experiment in orbit (Figure 1). During the on-orbit period, the intelligent observation system was utilized to record the real-time movement trajectory, feeding frequency, and sleep patterns of mice. It was found that mice adapted to the microgravity environment of the CSS, exhibiting normal behavioral rhythms and stable states. After completing the on-orbit experiment, the mice were successfully returned with the Shenzhou 20 crew. On the ground, the mice successfully were pregnant and gave birth to offspring. This preliminary finding indicated the safety of short-term spaceflight on the constructed mammalian reproductive system, and some behavioral differences were observed.

This experiment is the first to implement on-orbit feeding and scientific experiments aboard the CSS, expanding the categories and contents of space life science experiments in China. It provides important first-hand data for the study of microgravity effects and behavioral research of various organs in space mice, the exploration opportunity of the research paradigm of small sample sharing and multidimensional big data analysis of space mammals, and the preliminary research on key indicators of mouse behavior, physiology, and biochemistry. In the future, the research team will further explore the response of mouse multi-organ systems to the

Fig. 1 In-orbit experiment photo of mice. (a) Daytime working lighting, (b) night infrared lighting

space environment, as well as changes in behavior, growth and development, reproductive behavior, and aging processes throughout the entire life cycle, and explore relevant mechanisms to deeply reveal the biological effects of microgravity, radiation, and other factors. The experiment lays an important foundation for the development and construction of the space mammal experimental platform to support systematic research on mammalian space science for the future.

3.2 A *Drosophila* Study: Biological Effects of Two Space Factors, Microgravity and Hypomagnetic Field

During evolution, terrestrial organisms have adapted to Earth's physical environment, particularly to Earth's Gravity (EG) and the Geomagnetic Field (GMF). In outer space, however, both parameters are drastically reduced, typically to less than 1‰ of their terrestrial levels. Even on nearby planetary bodies such as the Moon and Mars, the gravitational acceleration is only about 1/6 and 1/3 of that on Earth, respectively. Moreover, compared to the GMF, which ranges from 25 to 65 μT, the magnetic fields on the Moon (<300 nT[13,14]) and Mars (approximately 300 nT to 5 μT[15]) are substantially weaker, representing a hypomagnetic field (HMF) environment. Consequently, during deep-space exploration missions, Earth-originated organisms, including humans, will inevitably be exposed to these extreme physical conditions.

To investigate the biological effects of these two environmental factors, we developed a *Drosophila* experimental module equipped with both GMF and HMF units aboard the CSS, operating under microgravity (MG) conditions. An identical module was employed as a ground-based control (Figure 2a, b). For both situations, temperature and humidity were maintained at 25 ± 1℃ and 50 ± 5%RH, respectively. During the 40-day experimental period, the magnetic field intensity (MFint) was monitored in all four units. The MFint in the on-orbit GMF unit was $(4.99 \pm 0.15) \times 10^4$ nT, which was comparable to that in the ground-based GMF unit in Beijing, $(4.81 \pm 0.00) \times 10^4$ nT. In contrast, the MFint in the HMF units was significantly lower, measuring $(1.31 \pm 0.01) \times 10^2$ nT in the ground unit and $(1.12 \pm 0.02) \times 10^2$ nT in the on-orbit unit. Accordingly, the experiment was

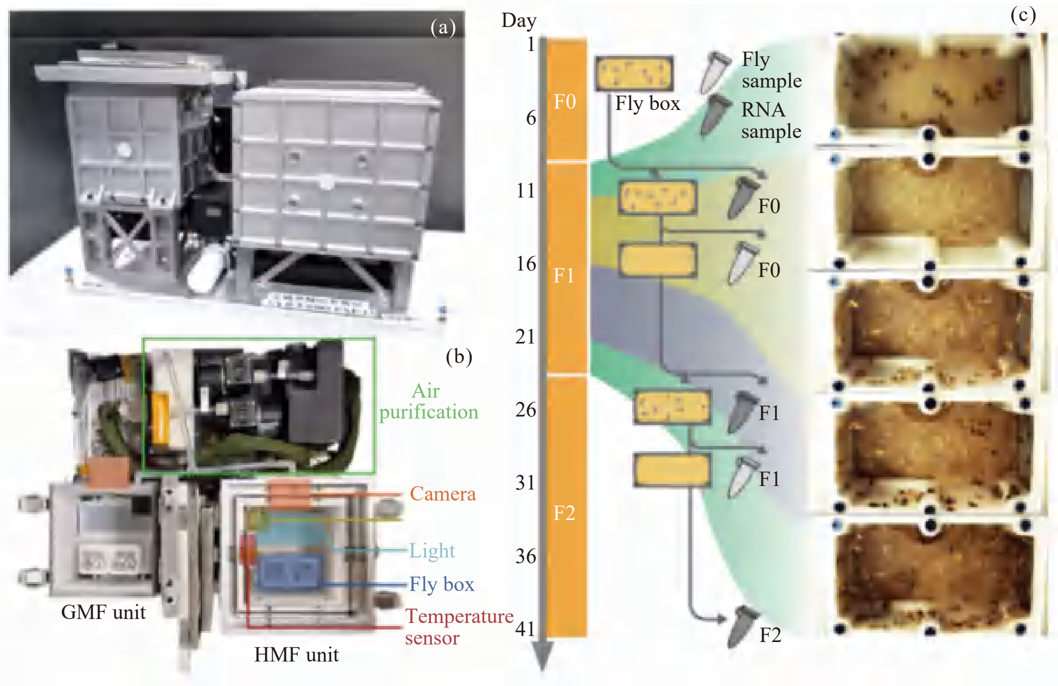

Fig. 2 *Drosophila* experimental module and procedures for multi-generational cultivation under combined microgravity and hypomagnetic conditions. (a) External appearance of the custom-designed module used aboard the CSS. (b) Internal configuration of the module, showing the GMF and HMF units. (c) Schematic timeline of the three-generation cultivation, concurrent on-orbit and ground-based sampling, and video acquisition

conducted in four parallel groups, EG+GMF, EG+HMF, MG+GMF, and MG+HMF.

Utilizing these two modules, we successfully conducted three consecutive generations of *Drosophila* cultivation both aboard the CSS and on the ground. As illustrated in Figure 1(c), the entire developmental process and adult behaviors were continuously monitored *via* video recording. Concurrently, fly samples from each generation were collected on the same schedule in orbit and on Earth. Through integrated analysis of the video data and transcriptomic profiles from the collected samples, this study enables a systematic investigation into the biological effects of gravity, magnetic fields, and their interaction across developmental, behavioral, and gene expression levels. To our knowledge, this represents the first biological investigation under two space environments, MG and HMF. The findings are anticipated to illuminate the potential challenges that Earth organisms may encounter during deep space exploration, and to guide the formulation of adaptive strategies for future interplanetary missions.

The SpaceAnimal Dataset[16] was constructed to support behavior analysis in complex spaceflight scenarios, covering three representative model organisms, including *Drosophila, Caenorhabditis elegans*, and zebrafish. Based on this dataset, a structure-aware pose estimation algorithm and a dual-stream fusion-based multi-object tracking framework were further developed, enabling high-precision pose estimation and trajectory tracking for space animal behavior analysis[16–18].

3.3 Seed-to-Seed Growth of Rice under Microgravity

The responses of plants to space environmental factors can affect adaptation and genetic stability of important agronomic traits of crop. However, the mechanisms priming crop plant response to space environment for the completion of the seed-to-seed have not been elucidated. We have finished the experiments of *Arabidopsis thaliana* from seed-to-seed on board the Chinese space lab TG-2 and the CSS, which found potential regulatory modules to integrate microgravity signals into flowering pathways in plants grown in space (Figure 3)[19–21]. The completion of the CSS provides us with a new permanent space experimental platform for long-term plant research in space. The rice had completed life cycle from seed-to-seed under microgravity aboard the CSS (Figure 4)[22]. As we know, this is the first space experiment achieving the complete rice life cycle from seed to seed in space.

Some of these space rice seeds have been used to subsequent experiments to successfully produce a fourth generation after returning to the Earth. Analyses of the mature space seeds and samples collected by astronauts in orbit indicate that rice has an excellent space adaptation ability, but some negative characteristics have also been found, such as altered phenotypes[19–21,23], small seeds, decreased seed setting rate and altered starch particle morphology. The rice phenotypic changes under

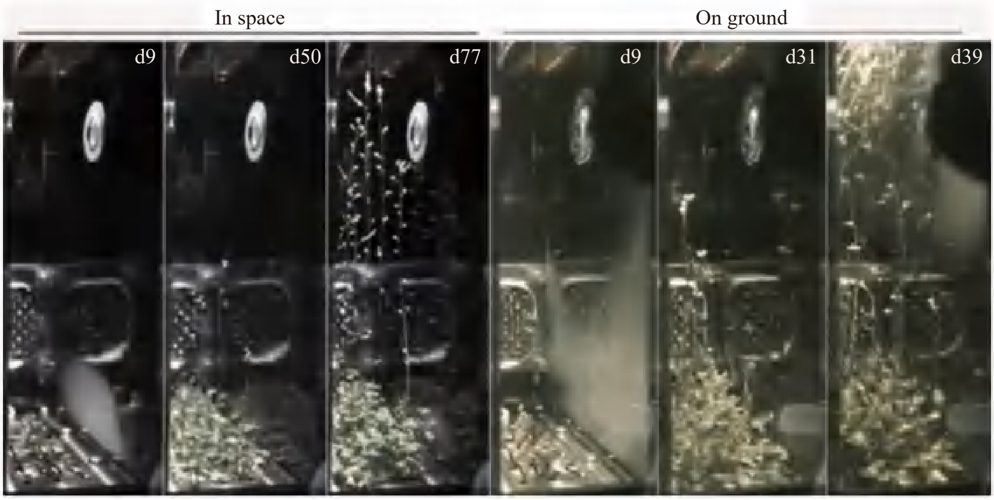

Fig. 3 Time-course series of digital images showing the growth and development of Arabidopsis plants grown in space and on ground

Fig. 4 (a) Time-course series of digital images showing the growth and development of rice plants grown in space, (b) diagram showing transition time of developmental stages of rice in space, (c) enlarged spike images of rice plants grown in space

microgravity conditions were observed, including abnormal increases in leaf angles, high-position tillering, unclosed glume, and unique stomatal structures in leaves, along with transcriptomic data.

Subsequent plants were grown from space developed parental seeds in field on Earth with higher germination rate, demonstrating the viability and reproductive capacity of rice seeds developed in the CSS, indicating the possibility of cultivating the important food crop rice throughout its entire life cycle under the spaceflight environment. However, we are now going beyond plant survival in space, but to develop a biological life support system with higher resource-use efficiency, which needs higher-yield plants. Thus, we suggest that a systematic analysis of genetic stability within consecutive multi-generation for rice plant should be performed to understand the mechanism of plant adaptation to long-term spaceflight conditions. In addition, key genes with significant application value should be identified for developing new germplasm resources with high yield, which is required for establishing reliable and efficient BLSS.

3.4 Microgravity Induces Lipid Droplet Accumulation in Hepatocytes

Although spaceflight is well documented to disrupt hepatic lipid homeostasis, the molecular mechanisms underlying gravitational sensing and mechanotransduction in hepatocytes remain incompletely elucidated. To bridge this gap, a team from the Institute of Mechanics, CAS (Chinese Academy of Sciences) has conducted an integrated *in vitro* study aboard the CSS, examining hepatic Huh-7 cell line cultured under both static and shear-flow conditions during real microgravity exposure[24]. Their findings demonstrate that microgravity induces pathological intracellular lipid droplet accumulation in Huh-7 cells under static culture, whereas physiologically relevant shear flow significantly attenuates this phenotype. Transcriptomic and proteomic analyses identify sterol regulatory element-binding proteins (SREBPs) as central mediators: microgravity activates SREBPs, thereby upregulating *de novo* lipogenesis and cholesterol biosynthesis. Mechanistically, microgravity-triggered disassembly of F-actin cytoskeleton is shown to be sufficient for SREBP activation. Conversely, shear flow preserves F-actin architecture and suppresses SREBP nuclear translocation. Collectively, these results identify SREBPs as gravity-sensitive regulators of lipid accumulation in hepatocytes, highlighting potential therapeutic targets for maintaining liver health in space travelers during long-duration missions (see Figure 5).

3.5 Effects of Microgravity on Skeletal Muscle Cell Autophagy and miRNA Regulation

During spaceflight, adaptive atrophy of skeletal muscle poses a serious threat to astronaut health and mission performance. A team from the Shanghai Institute of Nutrition and Health, CAS, focuses on the biological basis of the effects of space microgravity on skeletal muscle. They utilized a biotechnology experimental cabinet to successfully achieve on-orbit culture and differentiation of mouse skeletal muscle cells. A skeletal muscle cell-based autophagy fluorescence reporter system was employed, in combination with space-ground comparative analysis and high-throughput sequencing, to obtain the gene expression profile of skeletal muscle cells in space. The study identified that dysregulated molecule during spaceflight can influence skeletal muscle autophagy during exercise by modulating lactate levels[25] (Figure 6). Furthermore, based on miRNA sequencing data from recovered cells and their culture media, the patterns of alterations in miRNA expression and secretion in skeletal muscle cells under space culture conditions were revealed. Subsequently, the regulatory mechanism by which dysregulated miRNAs (in terms of expression and secretion) in space culture mediate skeletal muscle stem cell dysfunction and systemic metabolic abnormalities was elucidated[26,27]. In addition, this study uncovered the regulatory mechanism of aberrantly expressed chromatin regulator in the space environment on skeletal muscle stem cells and skeletal muscle regeneration[28]. These findings provide new strategies for the prevention and treatment of muscle atrophy-related diseases.

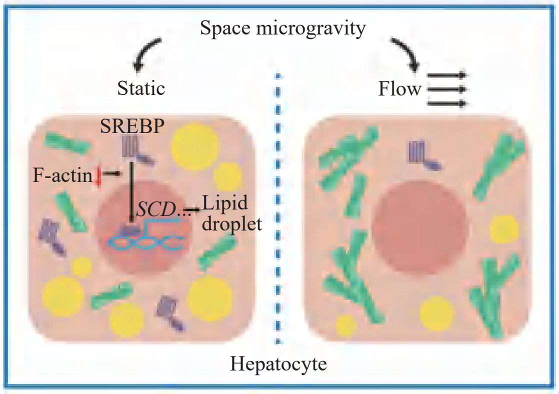

Fig. 5 Shear flow alleviates spaceflight-induced hepatic lipid dysregulation[10]

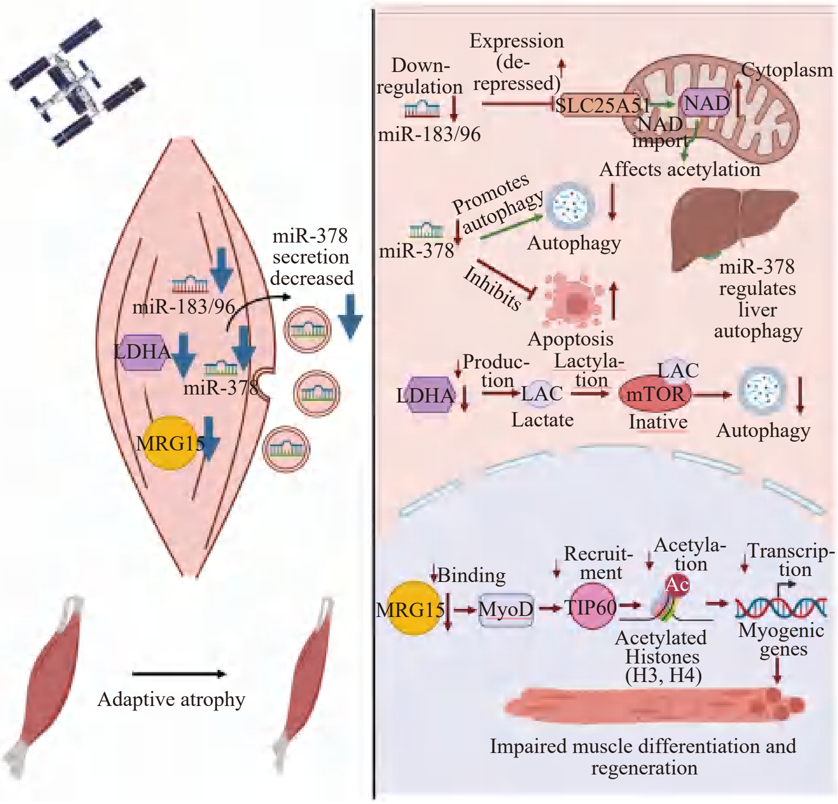

Fig. 6 Summary model diagram of the mechanism of action of dysregulated molecules in skeletal muscle cells during space flight

3.6 Protein Crystallization Experiment from Space Microgravity Conditions

The changes in the interaction between water and protein molecules caused by microgravity environment in the solution can improve crystal performance and enhance resolution. With the construction of the CSS, special conditions were provided for the biotechnology development, such as protein assembly. In addition, the experimental facilities were designed and arranged for the assembly and application of the protein drug molecules, and for the preparation of single crystals of medicinal proteins/nucleic acids and their small molecule complexes in this platform.

Various proteins had been screening under high-throughput crystallization conditions for 180 days in the microgravity environment. The results show that four types of protein single crystals were obtained, which were absent under normal gravity conditions. In addition, 11 types of protein crystals have better resolution.

We also performed protein crystallization screening on the T6 topoisomerase II ATPase domain. High-quality protein crystal samples were obtained (Figure 7a), and a local view of the active center was different from cryo-EM (Figure 7b), clearly indicating the binding sites of ATP (Figure 7c), and the good electron cloud density clearly demonstrated the differences between the two catalytic centers. One subunit is a binding site for Mg^{2+}, while the other subunit is completely different. A new magnesium binding mode in ATPase type II topoisomerase of T-even bacteriophage had been revealed [10,29]. These results are important for understanding its catalytic mechanism and dynamic process, and provide important structural parameters and new ideas for future related drug design.

3.7 Abiotic Synthesis of Peptides, Nucleotides

Exploring the origin of life in space and searching for extraterrestrial life are of great significance for the development of space resources and the expansion of human habitats. From the Murchison meteorite to the asteroids Ryugu and Bennu, the relevant findings have demonstrated that amino acids, nucleobases, ribose, and other life-related organic molecules are extensively distributed in the universe. By utilizing the extravehicular exposure platform for radiation biology of the CSS, a research team from Xiamen University investigated the

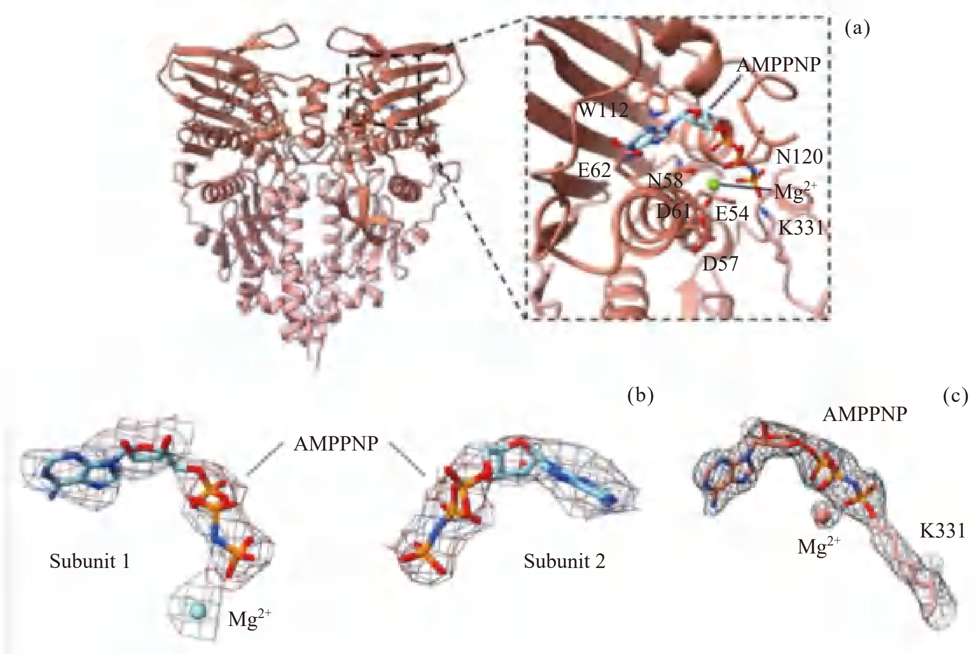

Fig. 7 Protein samples returned from on-orbit test [10,29]. (a) Overall structure of the T6 Topo II ATPase domain crystal and a local view of the active center. (b) The local density of magnesium ions and AMPPNP in the two active centers of the cryo-EM. (c) The local density of magnesium ions and AMPPNP in the active center of the crystal structure

feasibility of solid-phase condensation reactions of these "prebiotic organic molecules" driven by the coupling effect of ionizing radiation and forsterite. The cumulative effect of long-term, low-dose ionizing radiation under the coupling effect with forsterite was found to not only drive the formation of various dipeptides and the phosphorylation of nucleosides but also facilitate the formation of aminoacyl-adenylate analogues. Forsterite plays important auxiliary roles in this photochemical reaction process by providing an alkaline environment, electrostatic adsorption, interface catalysis centered on magnesium ions, and radiation resistance. The experiments were performed outside the Mengtian Module of the CSS. Both the sample container and the integrated experimental unit were fabricated from polyimide, which can effectively shield against UV radiation and expose the reaction systems to space ionizing radiation[30].

In addition, an investigation was conducted to focus on the influence of microgravity on the origin of life by utilizing a ternary chemical model that includes phosphorus activation, peptide formation, and phosphorylation of nucleosides in the Wentian Module of the CSS. The entire experimental system is placed in an SPU drawer (Figure 8). It is equipped with a centrifuge for online sample mixing (Figure 8a) and four fan-shaped microfluidic chip experiment units (Figure 8b–d). The reaction process is monitored through miniature electrochemical sensors (Figure 8e).

3.8 Research on Technologies for Mining Space Radiation Biological Markers from High-Dimensional Data on Small Samples

Space radiation is one of the most significant health risks in manned space missions. Molecular markers of space radiation and techniques for assessing radiation doses are considered key bottlenecks affecting the accuracy of radiation monitoring, damage assessment, and health risk warning. In response to the environmental factors present in space biology data and the multi-omics characteristics of different dimensions such as "small samples, high dimensions", the research team led by Professor Sun Yeqing from the Institute of Environmental Systems Biology at Dalian Maritime University has developed a series of technologies integrating feature selection, cross-species comparison, and single-sample network analysis to explore the mechanisms of space radiation damage and sensitive molecular markers. By deeply coupling genetic algorithms with multiple machine learning models, the study identified key genes responsive to space radiation and established a method applicable for radiation dose assessment. Multi-omics data from different model organisms of different batches (with different exposure doses) were analyzed and verified.

The results of the verification show that the conservation molecular response mechanisms of invertebrates and humans to the space environment have been revealed[32]. The discovery of the cumulative effect of space radiation leads to a stronger molecular stress re-

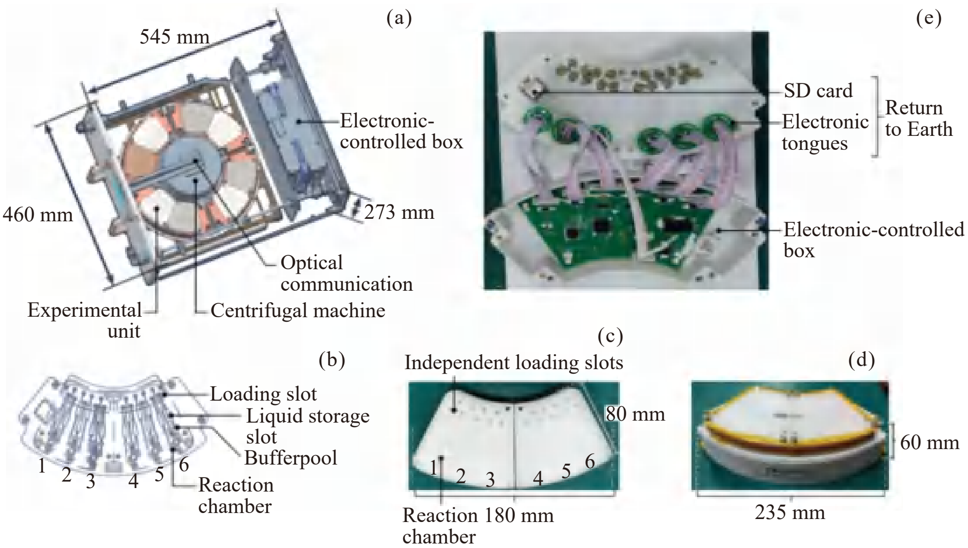

Fig. 8 Schematic view of origin of life space experiment[31]

sponse and adaptive regulatory characteristics. The key molecules sensitive to space radiation and their functional characteristics have been identified[33], the types of sensitivity and disease risks in different tissues and organs have been obtained, and a dose prediction model based on space radiation sensitivity genes has been constructed to conduct a systematic analysis and prediction of health risks induced by the space environment[34] (Figure 9).

4 Space Materials Science

The area of space materials science focuses primarily on the mechanisms and processes involved in the preparation of materials under microgravity, novel materials and fabrication technology for important applications, ser-

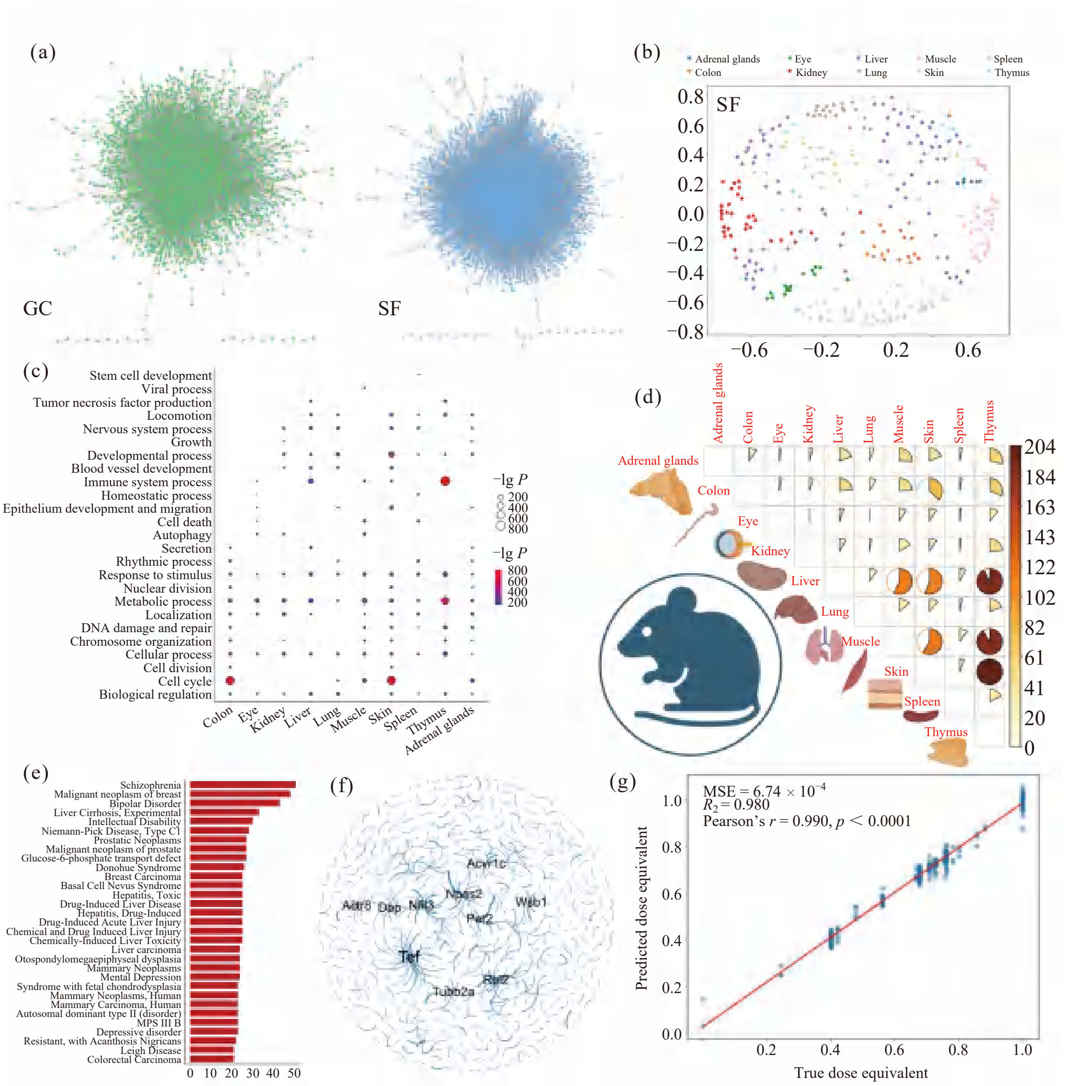

Fig. 9 Analysis of the molecular interaction patterns among different tissues of mice in a single-sample network algorithm in a space environment, as well as the assessment and risk prediction analysis of spatial radiation doses[34].
(a) Schematic diagram of single-sample networks for mice in the ground control group and space flight group.
(b) Principal component analysis results of the transcriptomes of different tissues of mice in the space environment.
(c) Enrichment results of differentially expressed genes in different tissues of mice in the space environment.
(d) Overlapping situation of differentially expressed genes in different tissues of mice in the space environment.
(e) Disease risk prediction analysis in the space environment. (f) Mining of key response genes in mice in the space environment. (g) Prediction results of spatial radiation doses based on key response genes of mice in the space environment

vice behavior of space application materials, *etc*. Seventy four projects (statistics as of 20 June 2026) have been successfully implemented in orbit. A series of significant studies and experiments were conducted in space environments, encompassing the structures, properties and physicochemical processes of various materials, the solidification mechanism of space high-temperature alloys, the macroscopic performance control mechanisms, and the operational behavior in space. Significant discoveries and breakthroughs have been made in the solidification of refractory alloys and performance regulation, semiconductor crystal growth and fabrication, microstructures and thermophysical properties measurements, lubricant materials service behavior in space, *etc*. The progress and achievements have enriched and developed the fundamental theory of research in related materials science, with some preliminary applications being attempted.

4.1 Growth Characteristics of Refractory Alloys

In containerless solidification experiments aboard the CSS, (Nb) dendrites in hypoeutectic and eutectic Nb-Si alloys preferentially form at the junctions of eutectic cells. At low undercoolings, they exhibit two-dimensional symmetric growth, at high undercoolings, three-dimensional oriented growth dominates, and dendrite tips deviate from the classical parabolic shape into dome-like, finger-like, and needle-like non-parabolic morphologies[35]. Independent Nb_3Si dendrites (decoupled growth) are observed in hypoeutectic and eutectic alloys. In the hypereutectic Nb-Si-Zr alloy, the primary phase changes from equilibrium Nb_5Si_3 to metastable Nb_3Si at large undercoolings, forming columnar or flaky dendrites[36]. In the hypoeutectic Nb-Si alloy, low undercooling produces a mixture of lamellar and rod-like eutectic; high undercooling induces a sequential transition from worm-like to lamellar and faceted eutectic[35] (Figure 10). In the eutectic Nb-Si alloy, low undercooling yields radial lamellar eutectic; at high undercooling, worm-like eutectic appears near nucleation sites and rod-like/short-lamellar eutectic at cell boundaries. In the hypereutectic Nb-Si-Zr alloy, irregular faceted, irregular lamellar-like, and regular lamellar eutectics are observed[36]. Under microgravity, the eutectic and dendritic zones exhibit spatially ordered separation, whereas buoyancy-driven convection on the ground disrupts this order.

This work systematically reveals the multi-mode transition of eutectic structures in refractory alloys under space microgravity, establishing a synergistic control mechanism of temperature gradient and absolute temperature on eutectic morphology.

A distinctive ripple-like microstructure composed of anomalous eutectic was observed in the $Zr_{57}V_{43}$ alloy solidified under microgravity. Driven by the combined effects of internal microflow and compositional fluctuations, the (Zr) and V_2Zr phases are arranged alternately like water ripples along the direction of heat flow, ultimately forming a distinctive ripple-like microstructure. The ripple-like structure also contributes to improved mechanical properties. The anomalous eutectic and finer

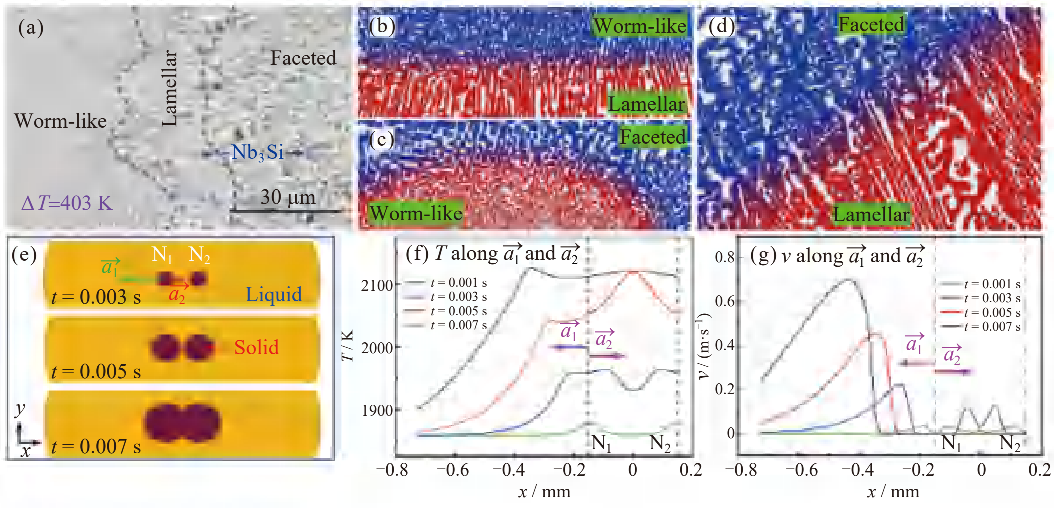

Fig. 10 Various eutectic growth modes solidified at large undercoolings under microgravity and the numerical simulation[35]

lamellar eutectic lead to increases of 11.7% and 13.2%, respectively, in the micro-indentation hardness of the $Zr_{57}V_{43}$ alloy compared with that of the alloy solidified on the ground at a similar undercooling[37].

4.2 Ultra-High Temperature Materials Science Experiment

The CMPR had operated stably for over five years[38]. The breakthroughs had been made and multiple independently controllable key technologies had been mastered, including long-term stable electrostatic levitation under microgravity, multi-beam laser composite heating, single/dual-wavelength coupled ultra-high-temperature infrared thermometry, and high-precision thermal property measurement. The full experimental process had been standardized for the containerless materials science experiments in space (Figure 11), a high-fidelity containerless scientific matching experimental platform and digital twin model had been established, and the novel experimental mode of “space-ground collaboration + digital experimentation” had been implemented[39]. We have successfully achieved laser heating and thermal property measurement of materials at 3100℃ under microgravity, obtaining space-based solidification characteristics and critical thermal property data of ultra-high-temperature melts.

The CMPR has become a crucial space laboratory for studying the behavior of refractory metal melts. Space-based ultra-high-temperature materials science experimental techniques can support the researches on the solidification mechanisms of refractory metals and on deep undercooling and non-equilibrium solidification, the design of new high-temperature materials, and the database of thermophysical property. These techniques can enable the acquisition of intrinsic thermophysical property data of melts that cannot be obtained on ground, laying a solid experimental foundation for the design and development of ultra-high-temperature materials in China.

4.3 InSe Semiconductor Crystal Growth

Microgravity in space provides a unique environment for the growth of high-quality semiconductor crystals, especially for layered materials that are highly sensitive to convection, sedimentation, and compositional segregation during solidification. Researchers from Shanghai Dianji University and Shandong University achieved the microgravity growth of InSe aboard the CSS and subsequently fabricated high-performance Field-Effect Transistors (FETs)[40]. Spherical Aberration Corrected Scanning Transmission Electron Microscope (AC-STEM) demonstrates that the as-grown space InSe exhibits expanded atomic microstructure and lattice constants compared with the InSe grown on the ground. The as-grown space InSe possesses a γ phase similar to the ground-grown InSe, but with significantly reduced intrinsic defects. The natural space environment eliminates the sedimentation/flotation and convection driven by the effect of gravity and facilitates high-quality single crystal growth. In addition, the larger defect formation energy induced by lattice expansion contributes to the improvement of crystal quality, thus boosting the electrical and photoelectrical performance of the FETs (Figure 12).

Meanwhile, a collaborative report from Shanghai Dianji University and East China Normal University shows that the unique microgravity environment can effectively annihilate the naturally existing stacking faults in flexible InSe, thereby directly activating its intrinsic

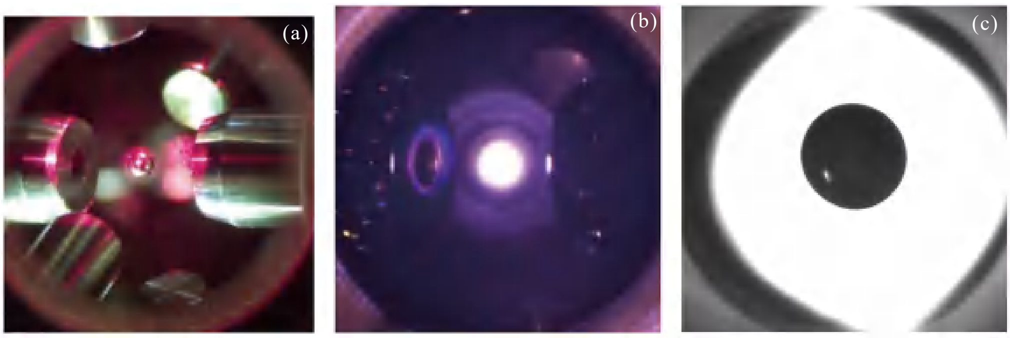

Fig. 11 Sample experimental process. (a) Stable suspension in space, (b) Heating and melting of samples, (c) Measurement of melt density

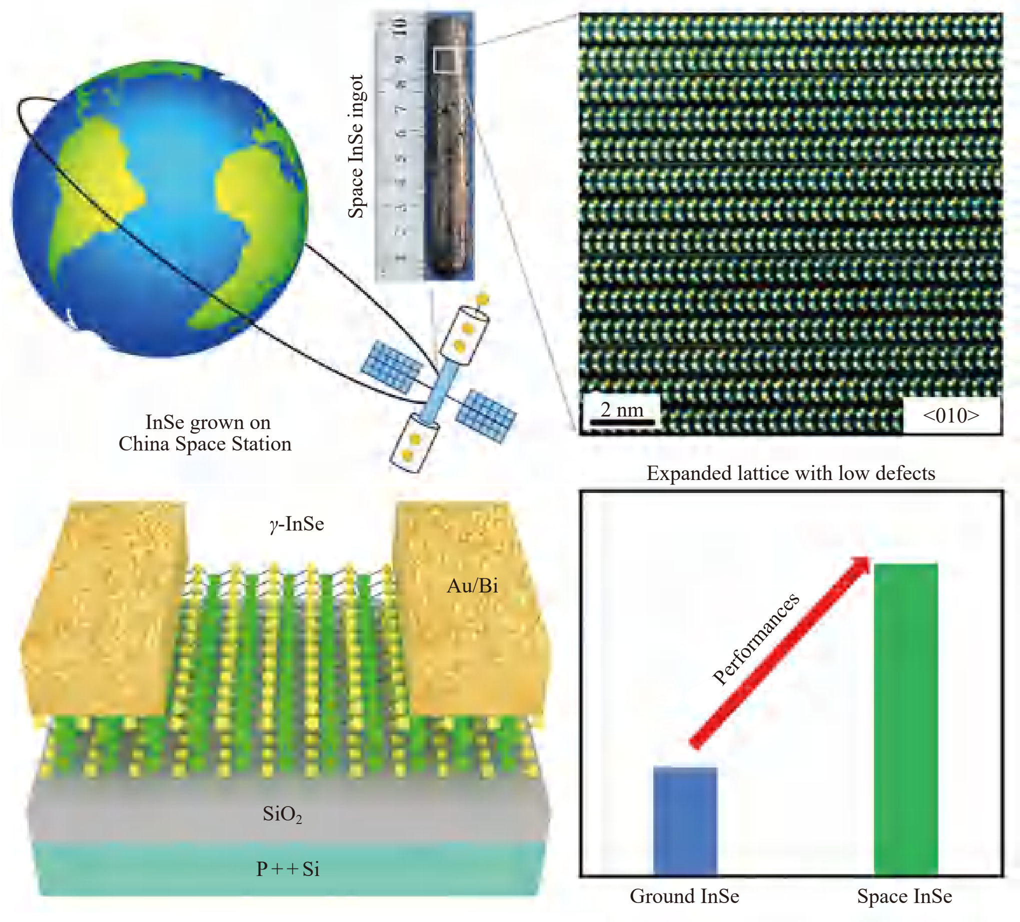

Fig. 12 Microstructure of space grown InSe crystal and high performance field-effect transistors[40]

sliding ferroelectricity with excellent retention stability[41]. The corresponding ferroelectric semiconductor field-effect transistors present obviously large nonvolatile memory window, high on/off ratio, and excellent mobility (Figure 13). More importantly, they also show superior amplified spontaneous emission with exceptionally low excitation thresholds of photons, indicating strong potential for near infrared nonlinear light sources. These findings not only present an unconventional strategy for achieving high-quality van der Waals layered single crystals such as InSe, but also highlight their potential for next-generation emitter-integrated computing architectures combining memory and sensor functions.

4.4 Microstructures and Magnetic Properties of FeCoB Alloy Fabricated

FeCoB alloys were successfully fabricated by heating and melting in a containerless materials processing rack aboard the CSS. As shown in the SEM image of Figure 14(a), the phase boundaries of the sample fabricated in outer space are flat and straight, with corners tending to form right angles. In contrast, the phase boundaries of the sample fabricated on the ground are more rounded with the precipitate phase (FeCo) taking on elliptical or flow-like elongated morphologies (Figure 14b). Phase-field simulations revealed that the microgravity environment promotes higher coherent strain energy, favoring the formation of planar coherent interfaces (Figure 14c). Conversely, the reduced coherent strain energy on the ground leads to the formation of incoherent interfaces (Figure 14d).

In addition, the samples solidified under microgravity show an observable improvement in overall magnetic performance, exhibiting higher saturation magnetization along with lower coercivity. This improvement is attributed to the larger volume fraction of the FeCo precipitate phase in the outer space samples. Furthermore, coherent interfaces enable more efficient magnetoelastic

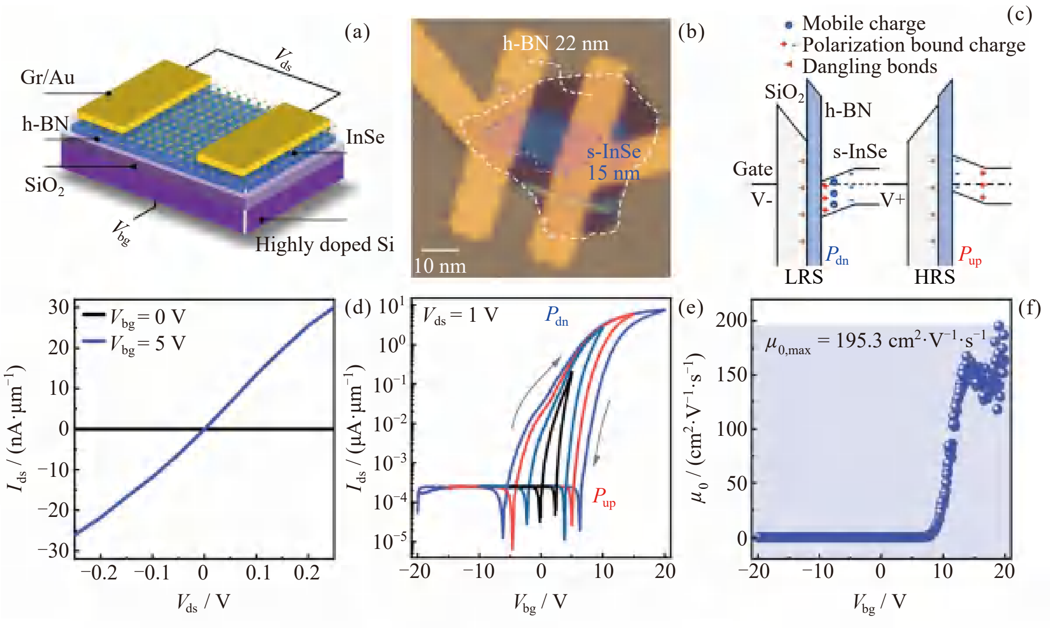

Fig. 13 Electrical performance of back-gated ferroelectric semiconductor field effect transistors[41]

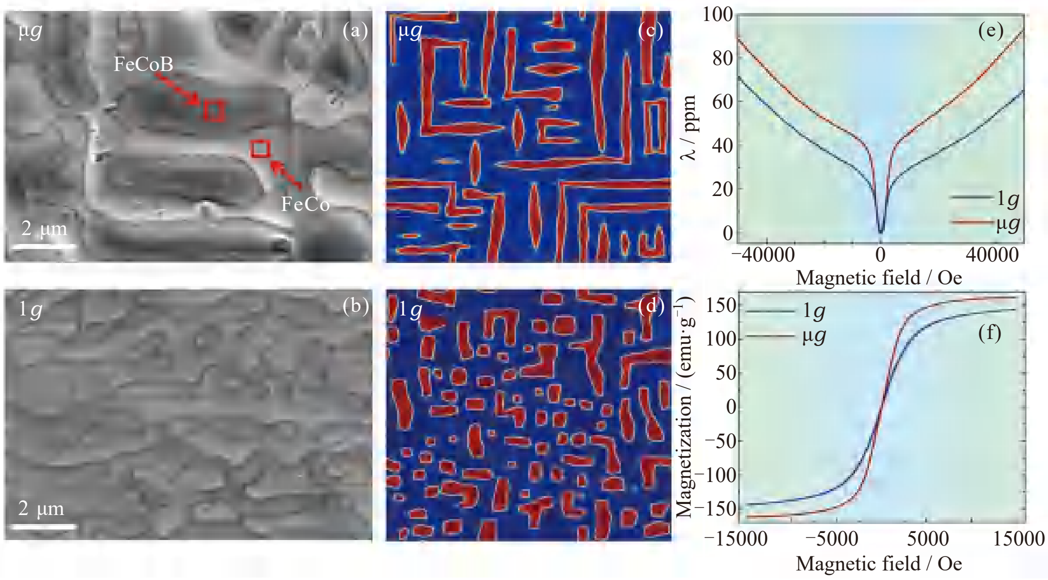

Fig. 14 Microstructures and magnetic properties of FeCoB alloys solidified in outer space and on the ground[10]

coupling, resulting in superior magnetostrictive properties and higher magnetic response sensitivity, which provides a new approach for designing high-performance magnetostrictive materials.

4.5 Thermophysical Measurements of Metallic Glass-Forming Liquid

The thermophysical properties of Metallic Glass-Forming Liquids (MGFLs) are crucial for understanding glass formation and optimizing metallic glass processing. However, high-temperature metallic melts are highly reactive and easily interact with container walls, which limits the applicability of conventional contact-based measurements. In ground-based containerless experiments, terrestrial gravity makes it difficult for the sample to maintain a perfectly spherical shape, thereby significantly reducing the accuracy of thermophysical property measurements.

The microgravity environment in the Electrostatic

Levitation (ESL) facility aboard the CSS provides an unprecedented opportunity for high-accuracy measurements of the thermophysical properties of high-temperature metallic melts. The research team from Shanghai University sought to measure the viscosity and surface tension of a Cu–Zr–Al MGFL aboard the CSS at temperatures inaccessible to conventional ground-based methods[42]. Figure 15(a)–(d) shows the morphological evolution of a levitated sample during melting, isothermal equilibration, free cooling, and complete solidification, while the corresponding temperature profile recorded by a pyrometer is presented in Figure 15(e). Drop oscillation experiments were conducted after thermal equilibrium was reached. Figure 15(f) presents real-time images of the oscillating droplets together with the extracted oscillation amplitudes. The oscillation decay signals recorded by a photoelectric sensor are shown in Figure 15(g). The damping constant and resonance frequency were determined by fitting the decay signals and performing a fast Fourier transform, from which the viscosity and surface tension were derived (Figure 15h). Compared with contact-based Couette rheology, the viscosity data obtained aboard the CSS not only significantly extend the experimentally accessible upper temperature limit, but also eliminate anomalous viscosity signals arising from chemical reactions, demonstrating the supe-

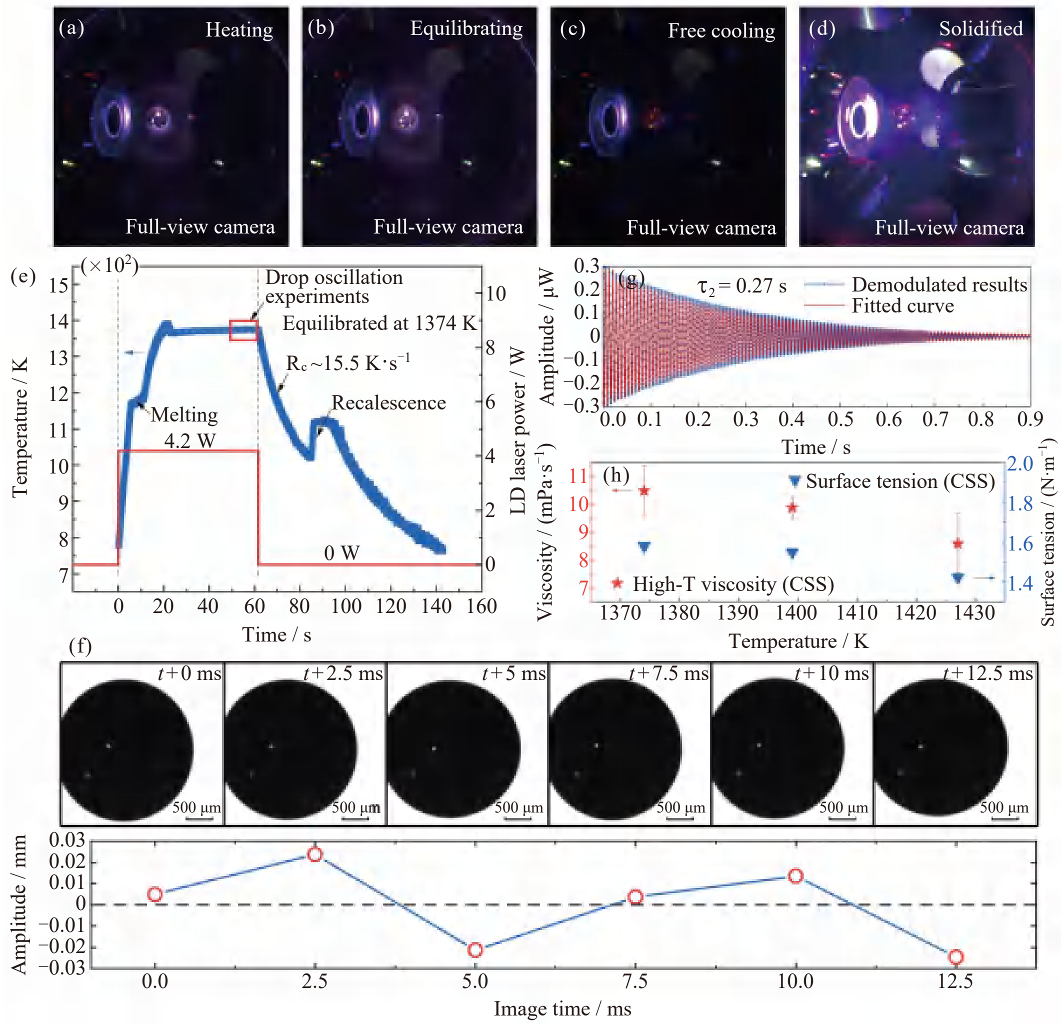

Fig. 15 On-orbit ESL experiments. (a)–(d) Full-view camera images showing the suspended sample during heating, isothermal equilibration, free cooling, and after solidification. (e) Temperature-time profile and applied laser power. (f) Images of an oscillating droplet and the corresponding oscillation amplitude. (g) Oscillation decay curve and fitted curve. (h) Temperature dependences of viscosity and surface tension[42]

riority of the on-orbit containerless method for thermophysical measurements of high-temperature MGFLs.

4.6 Microgravity-Induced Suppression of Phase Segregation and Defects in Directionally Solidified $FeSe_{0.5}Te_{0.5}$ Superconductors

The mechanism by which microgravity influences the segregation of the second phase in monotectic alloys remains highly complex and urgently needs elucidation. This issue not only represents a frontier topic in solidification theory but also serves as a theoretical cornerstone for the terrestrial application of monotectic alloys. The research group at the Institute of Electrical Engineering, CAS, systematically investigated the solidification behavior of the $FeSe_{0.5}Te_{0.5}$ monotectic alloy and conducted the first microgravity experiment on iron-based superconductors aboard the CSS[43]. This study revealed the microstructure evolution and control mechanisms during space directional solidification (Figure 16a–c).

Under microgravity conditions, the absence of natural convection effectively eliminates the macro-segregation of the Se-rich phase in the liquid-liquid separation system. Concurrently, microgravity significantly weakens the crucible wall effect, suppressing the formation of stray grains induced by heterogeneous nucleation (Figure 16d, e). This promotes crystal growth along the thermal gradient direction, enabling the successful fabrication of large-sized, directionally solidified rods (3 cm in length) that are unattainable under terrestrial conditions. The texture degree, characterized by the *F*-factor, increases from 0.42 to 0.78 (Figure 16f), ultimately yielding the iron-based superconducting rod samples exhibiting strong melt texture and high compositional homogeneity. Even under rapid solidification conditions, the superconducting phase maintains an exceptionally low density of crystalline defects. This behavior is attributed to the diffusion-controlled growth regime dominant under microgravity. Microgravity markedly suppresses the formation of crystal defects during rapid directional solidification, leading to a significant reduction in interstitial iron atom density under this diffusion-dominant growth mechanism. The superconducting volume fraction of the space-processed sample exceeds twice that of its ground-based counterpart, while the superconducting transition temperature (T_c) increases from 13.2 K to 14.2 K (Figure 16g).

Space directional solidification demonstrates significant advantages in preparing monotectic FeSe-based superconductors with strong texture, high homogeneity,

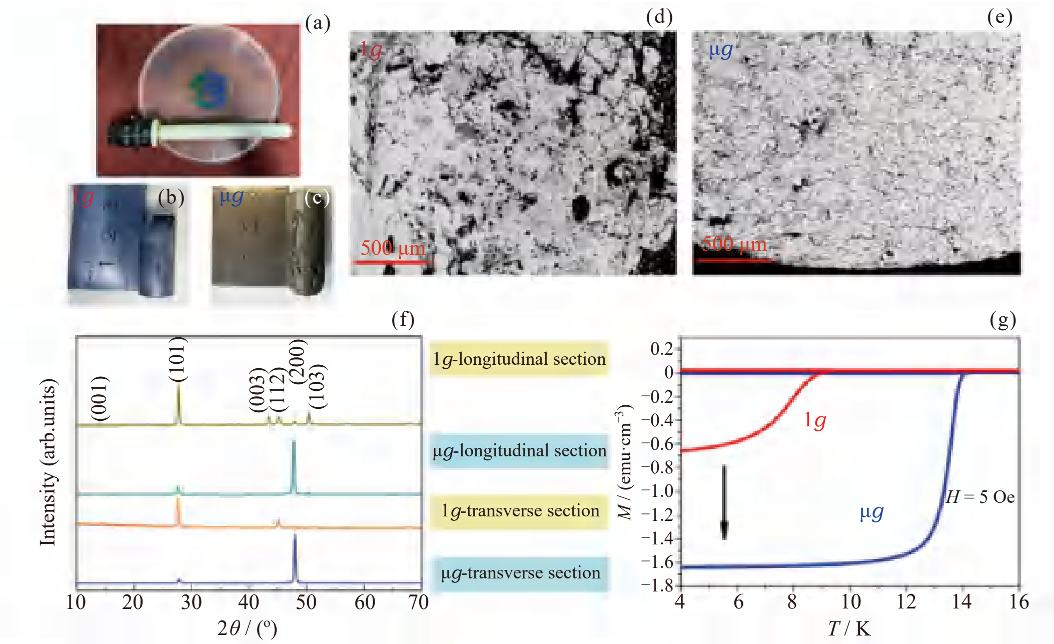

Fig. 16 Comparison of directionally solidified FeSeTe samples[10]. (a) Returned sample ampoule; (b) 1 *g* (ground) and (c) μ*g* (microgravity) sample rods; Backscattered Electron (BSE) images of the (d) 1 *g* and (e) μ*g* samples, respectively; (f) XRD patterns; (g) superconducting transition

and superior superconducting properties. These findings open a new technological pathway to overcome the bottleneck in texture fabrication of iron-based superconducting materials. The developed preparation method is applicable to the manufacturing of high-stability superconducting magnetic bearings and maglev transportation systems.

4.7 Performance of Self-constraining PFPE Gel Lubricants

Developing highly reliable lubricating materials is critical to ensuring the stable operation of spacecraft mechanical systems and extending their service life. Perfluoropolyether (PFPE) lubricants, which are the most widely used and possess excellent chemical stability, are prone to issues such as creep and migration due to their low surface tension, posing risks of lubrication failure and equipment contamination. To address this challenge, researchers at the Lanzhou Institute of Chemical Physics, CAS, have developed a self-constraint supramolecular gel lubricant by constructing a supramolecular network to confine the PFPE oil. During the first six-month extravehicular exposure experiment, the performance evolution of the gel lubricant under real space conditions (involving the synergistic effects of multiple factors) was evaluated[44]. Returned samples exhibited slight surface oxidation and discoloration due to atomic oxygen erosion, yet their internal structure remained intact (Figure 17a). Notably, compared to the original sample, the thermal stability of the exposed gel was slightly improved (the initial decomposition temperature rose from ~290 ℃ to ~310 ℃, and the maximum decomposition rate decreased from 29% min^{-1} to 11% min^{-1}), exhibiting no significant change in thixotropic properties and retaining excellent tribological performance (coefficient of friction ~0.03) (Figure 17). Investigation of the lubrication mechanism confirmed the formation of a protective tribofilm on the friction surface, composed of an adsorption layer and products of tribochemical reactions. These results indicate that this supramolecular gel lubricant possesses synergistic lubrication-sealing functions and excellent resistance to space environment-induced coupled damage, offering a promising material solution for long-life, high-reliability aerospace applications.

4.8 Space Lubrication Experiment

Lubricating materials are essential for the normal operation of moving components in space. To address the drawbacks of current solid lubricants used in space applications (such as high friction resistance, high energy consumption, short service life) as well as the tendency of liquid lubricants to migrate and evaporate easily, a novel composite superlubrication strategy combining solid and liquid lubricants has been proposed. This approach aims to overcome the limitations of single-type lubricants. Furthermore, an extravehicular tribology experiment has been carried out using an extravehicular

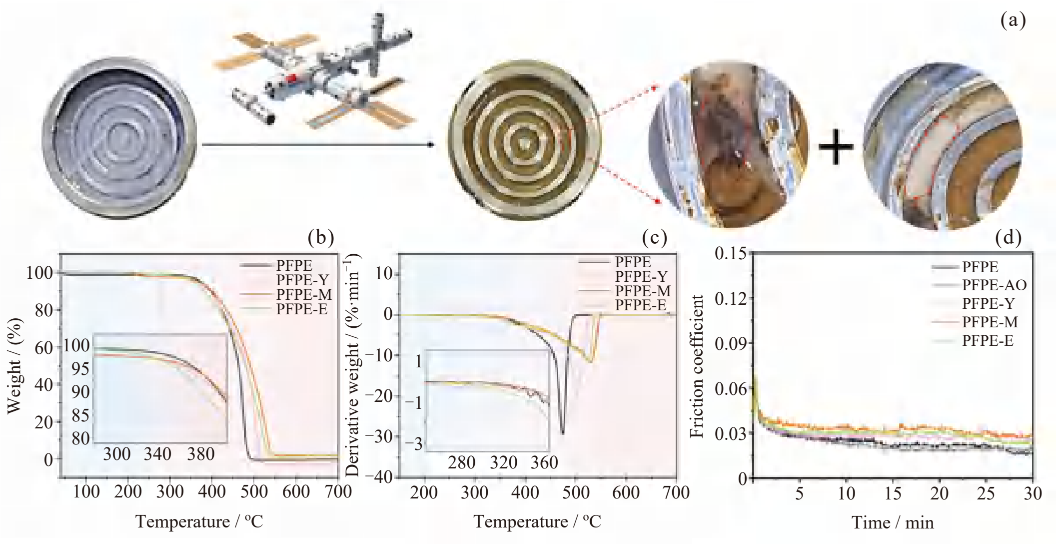

Fig. 17 Comparison of supramolecular gel before and after space exposure: (a) photographs, (b) thermogravimetric analysis curves, (c) derivative thermogravimetric curves, (d) coefficient of friction[44]

material exposure device equipped with a “solid-liquid composite lubrication tribology test box” (Figure 18a).

In recent experiments, four types of greases with ultra-low outgassing rates were designed to carry out ball-on-disk contact sliding tribological experiments on solid-liquid composite lubricating materials, and an extravehicular life verification of 3×10^5 revolutions was completed. Among them, some tribological properties can achieve short-term superlubrication (coefficient of friction < 0.01) or near-zero wear. Compared with the individual lubrication method, the samples based on solid-liquid composite lubrication have the lowest wear rate. In addition, novel mechanisms for achieving space superlubrication were innovatively proposed, including the shear-thinning effect and interfacial molecular absorption[45] (Figure 18b). Furthermore, the static exposure experiments of the lubricating grease revealed the mechanism of its property evolution under alternating high and low temperatures. The research results indicate that the lubrication strategy based on solid-liquid composite can effectively reduce friction and wear, with the potential to achieve “near-zero” friction and wear in space and to improve the level of space lubrication by orders of magnitude, providing new strategies for space motion equipment to achieve lower energy consumption, higher reliability, and longer operational life.

5 Microgravity Fluid and Thermal Physics

The area of microgravity fluid and thermal physics focuses primarily on a range of topics including microgravity fluid dynamics, multiphase flow and phase change heat transfer, complex fluid and soft matter, and associated applications. A body of research has been conducted on unique fluid and statistical physics phenomena under microgravity conditions. In addition, new laws of inertial particle motion in turbulent flow fields have been discovered. Furthermore, gravity mechanisms and fundamental problems have been investigated, which are difficult to delve into on the ground. Twenty-six projects (statistics as of 20 June 2026, excluding international cooperation projects) have been successfully implemented in orbit. These projects have yielded a series of significant breakthroughs in the fields of colloids crystallization, condensation heat transfer, annular flow, granular motion, among others. The progress and achievements have offered novel methodologies, technologies and systems for enhancing fluid, heat transfer and thermal management in space.

5.1 Crystallization of Charged Colloids

It is fundamentally important to study colloidal crystallization and its underlying mechanisms, as colloids are often regarded as “big atoms” to mimic the liquid-solid phase transition and the formed colloidal crystals are valuable materials that can be applied in various fields, such as micro- and nano-optical devices, biosensors, photonic devices, energy storage, and computer engineering. However, the effects of gravity, including sedimentation, convection and size fraction, *etc.* may significantly affect the colloids on earth, so as to make some intrinsic aspects of colloidal crystallization altered or even masked.

With respect to the mechanism of colloidal crystal-

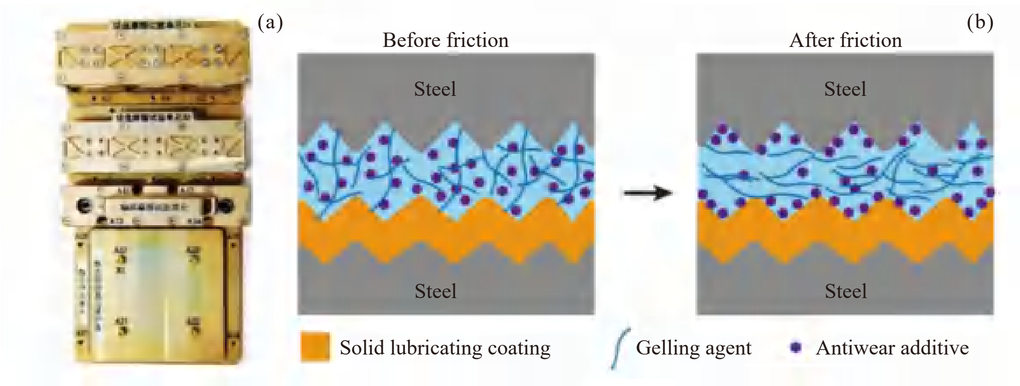

Fig. 18 Solid-liquid composite lubrication. (a) solid-liquid composite lubrication tribology test box[10], (b) solid-liquid composite lubrication mechanism

lization, both experiments and numerical simulations have shown that the crystal nucleation is not a one-step process as described in the framework of Classic Nucleation Theory (CNT), but rather a two or even multi-step process. For the charged colloids, whose effective interactions based on DLVO (Derjaguin, Landau, Verwey, and Overbeek) theory can be tuned relatively freely, we have recently investigated its crystallization using the reflection spectrometer in the CSS (see Figure 19). The colloidal sample, which exhibits a thermodynamically stable Face-Centered Cubic (FCC) phase in normal gravity, manifests a long-lived metastable Body-Centered Cubic (BCC) phase under microgravity (see Figure 20). The simulation of molecular dynamics is in agreement with the observations of space experiment, as it also shows the formation of metastable BCC crystals. Furthermore, the free-energy calculations suggest that BCC-FCC transition cannot be fully realized within the temporal confines of the space experiment. Those findings not only demonstrate Ostwald's step rule and Alexander-McTague argument specifically for charged colloidal systems where the metastable BCC crystals are formed, but also provide further evidence that gravity effects may play a substantial role in promoting the BCC-FCC transition.

5.2 Film Condensation Heat Transfer on Single Pin-Fin Structure Surface

To elucidate the effects of microgravity on film condensation behavior on a single pin-fin surface, the Southeast University research team previously conducted experiments and multi-scale numerical simulations on ground and in the falling tower[47–49]. To obtain the complete evolution process of the liquid film from formation to spreading on a single pin-fin surface under long-term microgravity, the team conducted film condensation experiments using HFE-7100 as the working fluid on the single pin-fin surface aboard the CSS (Figure 21a). As shown in Figure 21b, under microgravity conditions, the condensate film does not spread uniformly; instead, it accumulates at the base of the pin-fin and gradually extends outward, leading to a significant reduction in heat transfer performance. Compared with the terrestrial gravitational environment, gravitational drainage is considerably weakened under microgravity, resulting in a prolonged residence time of the liquid film at the pin-fin base and the formation of a thicker local liquid film layer. This phenomenon increases the thermal resistance at the condensation interface and substantially degrades the overall heat transfer performance. Figure 21(c)(d) illustrate the characteristics of the velocity field and surface temperature distribution during the evolution of the condensation interface. It is evident that a temperature non-uniformity exists along the height direction of the pin-fin, which enhances the surface tension gradient and thus induces strong thermocapillary convection (Marangoni effect). Thermocapillary convection promotes micro-convection within the liquid film and intensifies interfacial fluctuations, thereby improving, to some extent, the condensation heat transfer performance under microgravity. This result indicates that, although the absence of gravitational drainage deteriorates heat transfer in the microgravity environment, the thermocapillary effect driven by temperature non-uniformity may serve as a beneficial compensatory mechanism. This study enriches the stability theory of microgravity condensation liquid films and provides support for the design of two-phase thermal management systems in future space exploration.

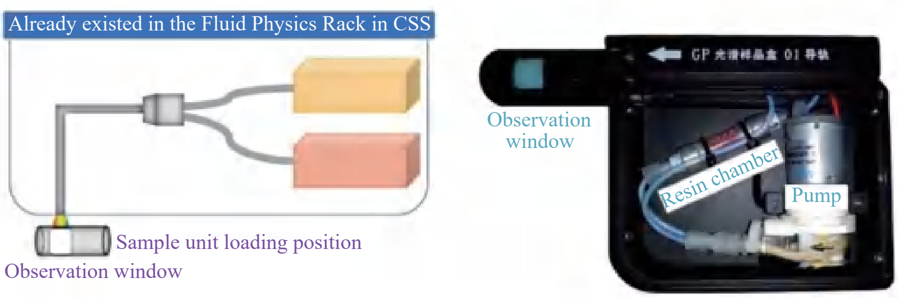

Fig. 19 Reflection spectrometer and sample unit. (a) Reflection spectrometer in the Fluid Physics Rack. (b) Photograph of the sample unit[46]

5.3 Oscillation and Transition Characteristics of Microgravity Annular Flow

Thermocapillary convection, driven by the variation of the free surface tension of fluids with temperature gradients, is a typical nonlinear flow. It plays an irreplaceably critical role in applications such as microgravity material crystal growth, spacecraft thermal management, chip cooling, and microfluidic device design. Among these applications, the study of thermocapillary convection under microgravity annular flow scenarios is particularly significant. The stability and oscillatory characteristics of its flow modes directly affect the morphology of crystal growth interfaces, heat and mass transfer efficiency, and the operational performance of microdevices, thus becoming a research focus in the interdisciplinary field of fluid mechanics and engineering thermophysics.

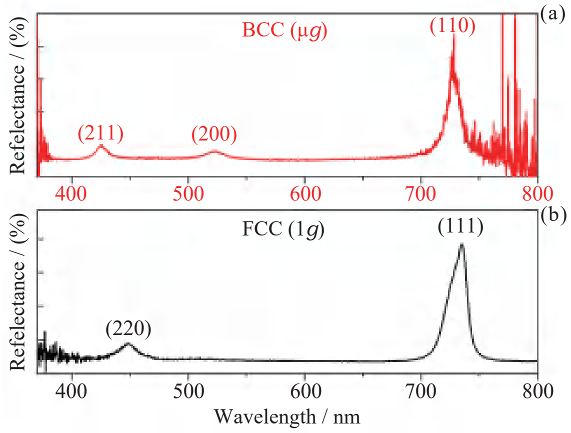

Fig. 20 Reflection spectra of colloidal crystals formed in space (a) and on the ground (b). The crystal structures are metastable BCC and stable FCC, respectively[46]

An annular flow system with three fully controllable parameters—fixed central cylinder, rotating central cylinder, and lifted central cylinder—has been established in the microgravity environment[50]. We discovered the critical jump phenomenon of hydrothermal waves affected by the volume ratio effect, verified the universality of this effect, and revealed the intrinsic nature of the instability steps of high-frequency and low-frequency waves. Additionally, we obtained the multimodal evolution and competitive propagation laws of hydrothermal waves in the supercritical regime, including Standing Waves (SW), Traveling Waves (TW), linear waves, and chaotic waves (Figure 22), which exhibit strong nonlinear effects[51]. Forced convection (Taylor-

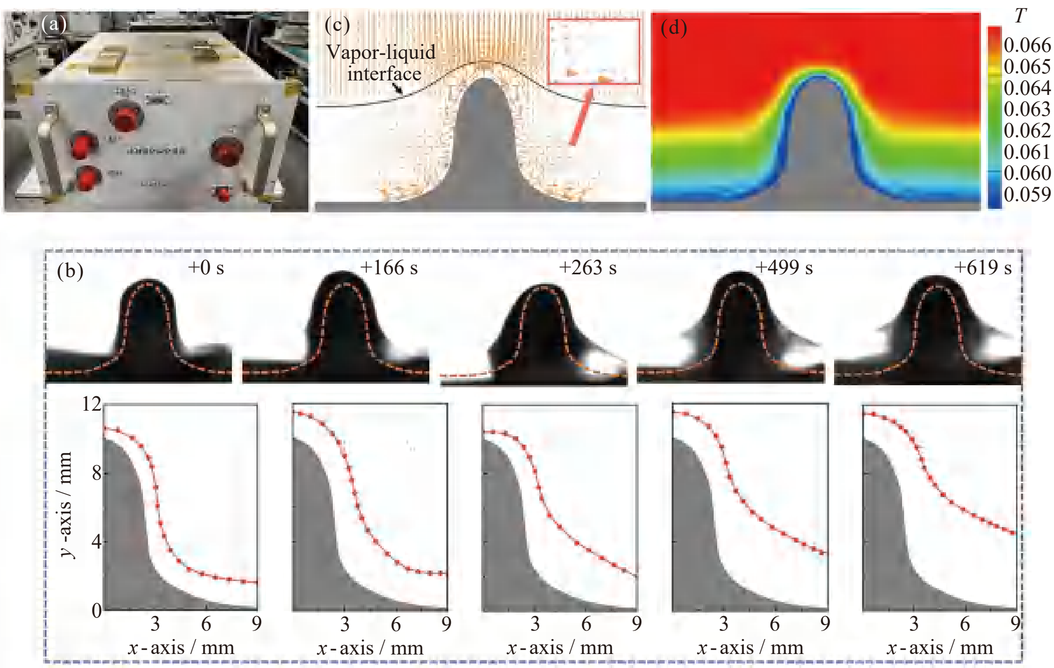

Fig. 21 Evolution behavior and heat transfer of the space condensation liquid film on a single pin-fin surface[10]. (a) experimental setup for film condensation under microgravity, (b) evolution of the condensation interface on the single pin-fin surface under microgravity, (c) velocity field distribution, (d) temperature distribution

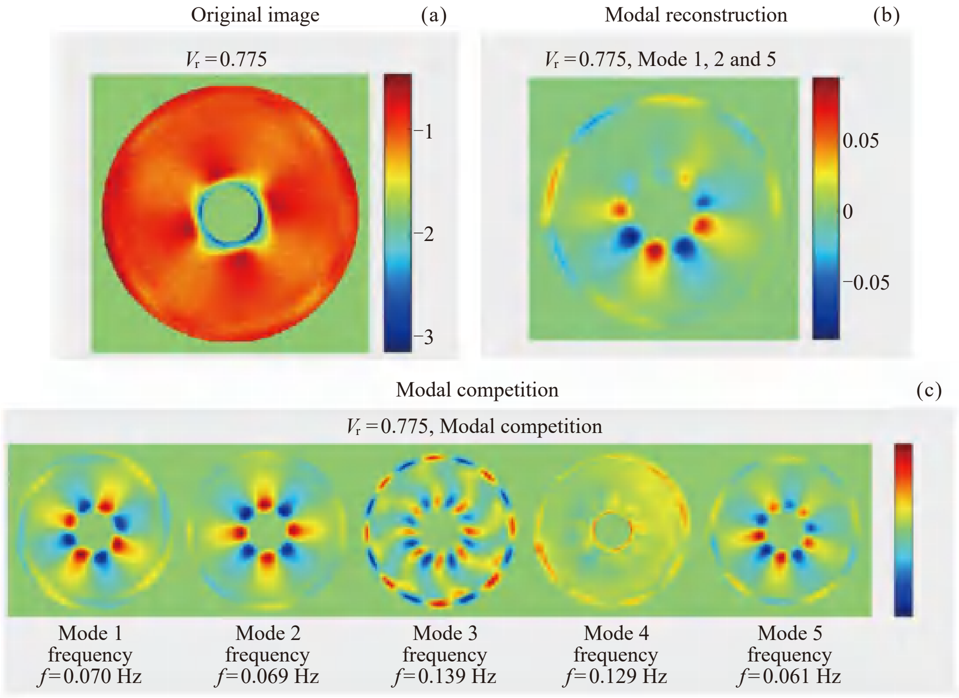

Fig. 22 Modal competition of thermal fluid waves under microgravity annular flow[6]

Couette flow) was introduced to regulate thermal convection, ultimately achieving the control of the quasi-equilibrium state of the flow.

These findings deepen the understanding of thermal convection turbulence dominated by surface forces in space environments, provide guidance for the selection of key parameters for high-quality crystal growth, and offer theoretical support for industrial crystal growth practices.

5.4 Influence of the Friction Coefficient on the Motion of Dry Granular Materials in Variable Gravity Environments

The systematic investigation of the influence of friction is provided on the motion of dry granular materials across gravity fields ranging from 0.01 g to 1 g[52–54]. By eliminating inter-particle cohesion and electrostatic forces, the study examines this behavior from two complementary perspectives: the dynamic and static angles of repose (Figure 23a), and the segregation dynamics of particles with differing sizes (Figure 23b). In Compartment A, observations of quasi-static and free-collapse pile angles revealed that the static angle of repose is independent of gravity level, whereas the dynamic angle of repose decreases markedly below lunar gravity (≈0.165 g). In Compartment B, experiments tracking the upward migration of a single large particle in a vibrating granular bed showed that higher vibration accelerations are required to initiate movement under reduced gravity — an effect that becomes pronounced only below lunar gravity[54] (Figure 24). Collectively, these findings demonstrate that the static friction coefficient remains essentially unchanged with gravity, while the rolling friction coefficient is a function of gravitational acceleration. Consequently, particle resistance to sliding stays stable across Earth, lunar, and asteroid environments, yet weaker gravity markedly facilitates rolling, flow, and reorganization. This enhanced granular fluidity in microgravity environments significantly increases the susceptibility of asteroid surface materials to deformation, loosening, rotational instability, and local collapse.

6 Microgravity Combustion Science

The area of microgravity combustion science focuses primarily on the investigations of the near-limit flammability and their underlying physics, critical combustion mechanisms, and applied research, material ignition characteristics and protective measures under microgravity, *etc*. Thirteen projects (statistics as of 20 June 2026) have been successfully implemented in orbit, and a se-

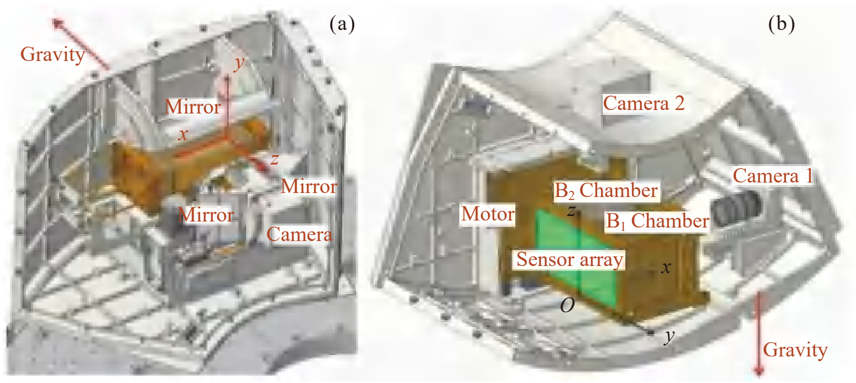

Fig. 23 Setup diagram of the CSS granular fluidization Experiments for Chamber A (a) and Chamber B (b)

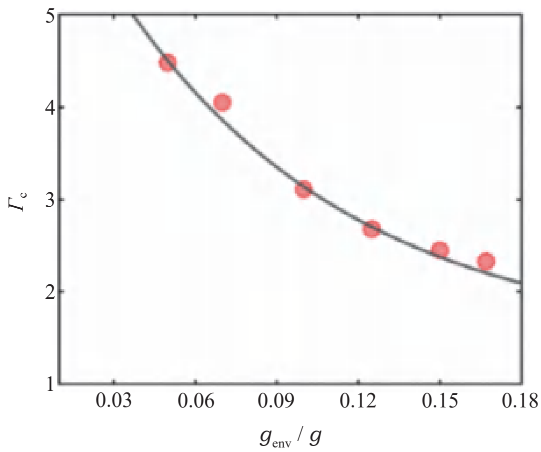

Fig. 24 Critical vibration acceleration required for large particles to move upwards decreases as gravity increases

ries of discoveries and breakthroughs have been achieved in basic combustion processes and mechanisms. These include multi-jet diffusion flames, soot production, and near-limit partially premixed flames, among others. The progress and achievements have yielded novel findings and insights relevant to the technological development, including low-carbon combustion, advanced power, and efficient clean energy, *etc*.

6.1 Research on Multi-jet Diffusion Flames

Leveraging the Gaseous Combustion Experiment Insert (GCEI) aboard the CSS, this study developed a multi-jet combustion assembly tailored for orbital environments. By integrating high-resolution imaging with advanced optical diagnostics, we achieved the precise observations of flame morphology, temperature distributions, and radiative intensities of methane multi-jet flames under microgravity. The results reveal that the suppression of buoyancy-induced convection leads to a highly symmetric and stable flame structure, where inter-jet interactions are primarily governed by momentum flux and molecular diffusion, resulting in a distinct reaction zone distribution[55].

Critically, a significant enhancement in flame radiation under microgravity was observed. The coupling between fuel jets and soot evolution was found to be dual-faceted: intensified high-temperature zones at elevated flow rates accelerate soot inception, whereas enhanced mixing in the diffusion-dominated regions promotes oxidation, thereby suppressing soot emissions[56]. Numerical simulations—incorporating reduced chemical kinetics, radiative heat transfer, and semi-empirical soot models—demonstrate that multi-jet coupling fundamentally alters precursor distributions and reaction pathways, which dictates the spatial characteristics of pollutants. Furthermore, the study characterizes the influence of fuel blending on flame merging behavior under microgravity as shown in Figure 25, providing a foundational theoretical framework for spacecraft fire safety and combustion control.

6.2 Soot Production in Non-buoyant Laminar Diffusion Flames

Soot represents one of the fundamental topics in combustion and fire research. Experiments with non-buoyant laminar diffusion flames are crucial for both elucidating the soot processes and providing more tractable model systems that are relevant to turbulent flames. A series of microgravity experiments has been performed to investigate soot properties of laminar diffusion flames aboard the CSS. Axisymmetric jet flames in coflowing oxidizer stream were tested, and hundreds of diffusion flames were recorded at various conditions. The experimental conditions included pure methane, nitrogen- or

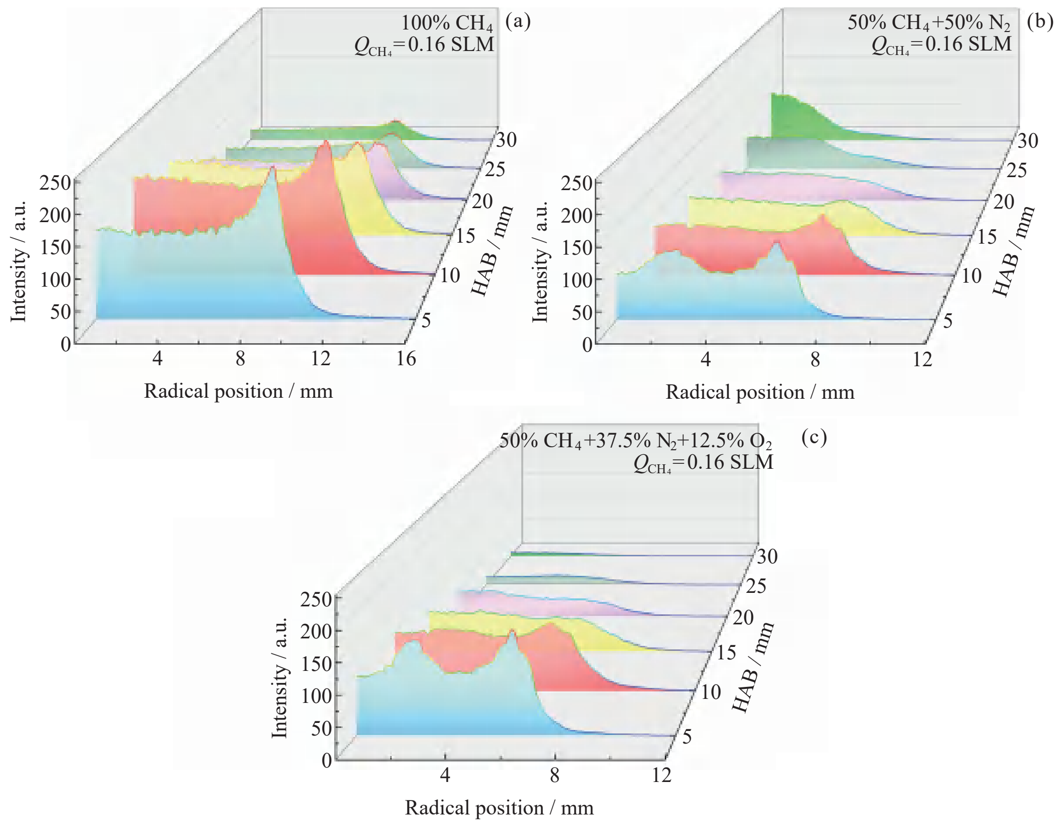

Fig. 25 CH* radical intensity with radial position at different heights of the flames

argon-diluted fuel, air coflow, and nitrogen- or argon-diluted coflow.

According to extracted data, the volume fraction of the inert dilution gas and the flame temperature are recommended to characterize the dilution and thermal effects on soot production, respectively. With a diluted coflow, comparing to the undiluted case, the region where soot formation is more prevailed over soot oxidation decreases in height, while the oxidation-dominated region expands simultaneously. The observed trend continues as the dilution gas increases, resulting in the decrease of the overall soot concentration and the maximum soot load in the diffusion flame[57] (Figure 26). Hydrodynamic effects on the soot processes are revealed under the research context, and a correlation model for smoke point is proposed to explicitly consider the apparent effects of jet outlet diameter and coflow magnitude[58].

6.3 Liftoff Stabilization and Extinction Behaviors of Near-limit Partially Premixed Flame

As the first series of combustion experiments aboard the CSS, transient extinction and stabilization of partially premixed methane-air flames were conducted using a co-flow jet burner (Figure 27a) within the Gas Combustion Experiment Insert (GCEI) [59]. The investigations systematically varied jet velocity, equivalence ratio, and dilution (N_2, Ar) to independently examine the effect of Damkohler and Markstein numbers on the flame stabilization and extinction. Contribution of radiation to the extinction behaviors was analyzed using MultiDiffFOAM simulations[60]. Flames with identical conditions under 1*g* and μ *g* (Figure 27b) suggest significant differences and hence highlight the necessity of experiments under microgravity.

Aerodynamic strain and flame curvature effects were separately studied for macroscopic flame liftoff. It was found that liftoff height correlates with the inverse mixing Damköhler number (Da_m^{-1}) (Figure 27c), which effectively links macroscopic flow timescales to microscopic stretch dynamics. Markstein numbers for curvature (Ma_C) and flow strain (Ma_S) were calculated along the flame. Results revealed that curvature-induced stretch dominates over strain ($|Ma_C| > |Ma_S|$) on the flame globally, and presence of gravity suppresses cur-

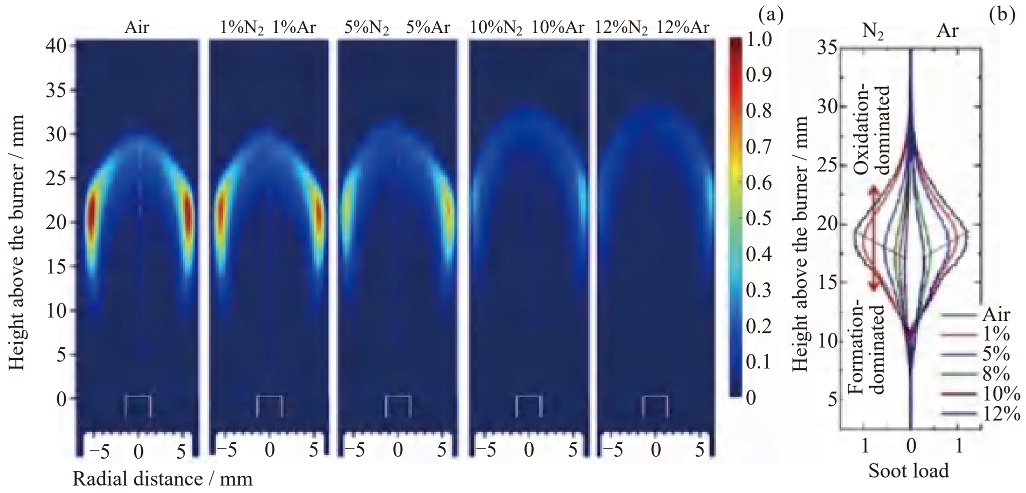

Fig. 26 Soot concentration distributions (a) and evolution of soot load (b) under microgravity laminar diffusion flames at various coflowing oxidizer conditions

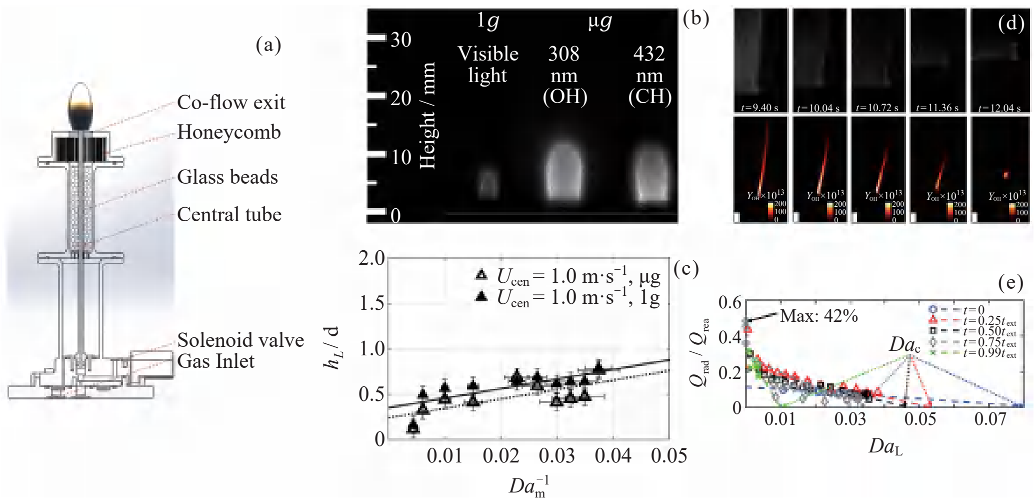

Fig. 27 Liftoff stabilization and extinction behaviors of near-limit partially premixed flame under microgravity[6,10]. (a) Burner configuration, (b) Lift-off flame in 1 *g* and μ *g*, (c) Flame liftoff height h_L over burner size *d*, *i.e.* h_L/d *vs*. inverse of mixing Damköhler number Da_m^{-1}, (d) Extinction of partially premixed flame under microgravity (upper: experiment; lower: simulation), (e) Analysis from simulation for Q_{rad}/Q_{rea} (radiative heat loss over total reaction heat release) *vs*. Damköhler number Da_L

vature while enhancing strain while Ar amplifies curvature sensitivity. By quantitatively separating the competing effects of radiation, strain, and curvature in a buoyancy-free environment, this research provides a physically interpretable framework and critical data for refining combustion models.

Under some near-limit conditions (Figure 27d), the Non-Premixed Flame (NPF) branch of a partially premixed flame exhibits a ring-like structure with partially premixed hooks prior to global extinction[61]. In such a newly observed behavior, radiative heat loss occupied up to 40% of local heat release at the NPF edges (Figure 27e). These flame edges retract in a premixed manner, shifting the local extinction mechanism from strain-controlled to radiation-controlled, which ultimately triggers the extinction of the entire NPF region.

7 Microgravity Fundamental Physics

The area of microgravity fundamental physics focuses primarily on space cold atom physics, high-precision time-frequency and related fundamental physics, microgravity plasma physics, *etc*. Five projects (statistics as of 20 June 2026) have been successfully implemented in orbit. A series of significant breakthroughs have been achieved in the fields of cold atom physics, interferometer, and others in space. Current breakthroughs lay a foundation for ongoing research, with studies continuing to ultra-low temperature quantum states, ultra-cold optical lattice quantum simulations, high-precision atomic clocks and time-frequency transmission technology. The progress and achievements made in these fields will be applied to fundamental physics theory testing and navigation timing.

7.1 Space Cold Atom Interferometer for Inertial Sensing

Cold Atom Interferometers (CAIs) can measure absolute acceleration and rotation with high precision. Benefiting from long interrogation time under microgravity, the inertial measurement precision of CAIs is significantly enhanced, making space CAIs an important candidate for high-precision inertial sensors in space. We developed a highly integrated optical architecture for the CSS Atom Interferometer (CSSAI). The scheme uses only two seed lasers, one tapered amplifier, and one acousto-optic modulator to generate all required frequencies for cooling, state preparation, Raman transitions, and detection. A fused silica optical bench with double-sided bonding minimizes thermal deformation, while silicone vibration isolators protect the bench during launch. The assembled optics measures 250 mm×240 mm×104 mm and weighs 5.2 kg, the most compact space CAI optics to date (Figure 28a). Launched to the CSS in 2022, the system has operated reliably for over two years without manual tuning. Output laser power fluctuations remain below 2.5% over months, and frequency stability stays better than 1 MHz[62].

For inertial measurement, the CSSAI performed on-orbit characterization under the station's high-dynamic rotation (about 15 times Earth's rate). A closed-loop two-axis piezoelectric mirror cancels the angular motion, enabling point-source interferometry. With 75 ms interrogation time, the gyroscope achieves a rotation resolution of 50 μrad·s^{-1} per shot and 17 μrad·s^{-1} after averaging 32 shots. The measured orbital rotation rate is (−1142±29) μrad·s^{-1}, agreeing with the CSS platform's classical gyroscope (−1137.0±2.3) μrad·s^{-1}. The same interferometer simultaneously measures linear acceleration with a single-shot resolution of 1.0 μm·s^{-2}, demonstrating a standalone quantum inertial measurement unit[63] (Figure 28b).

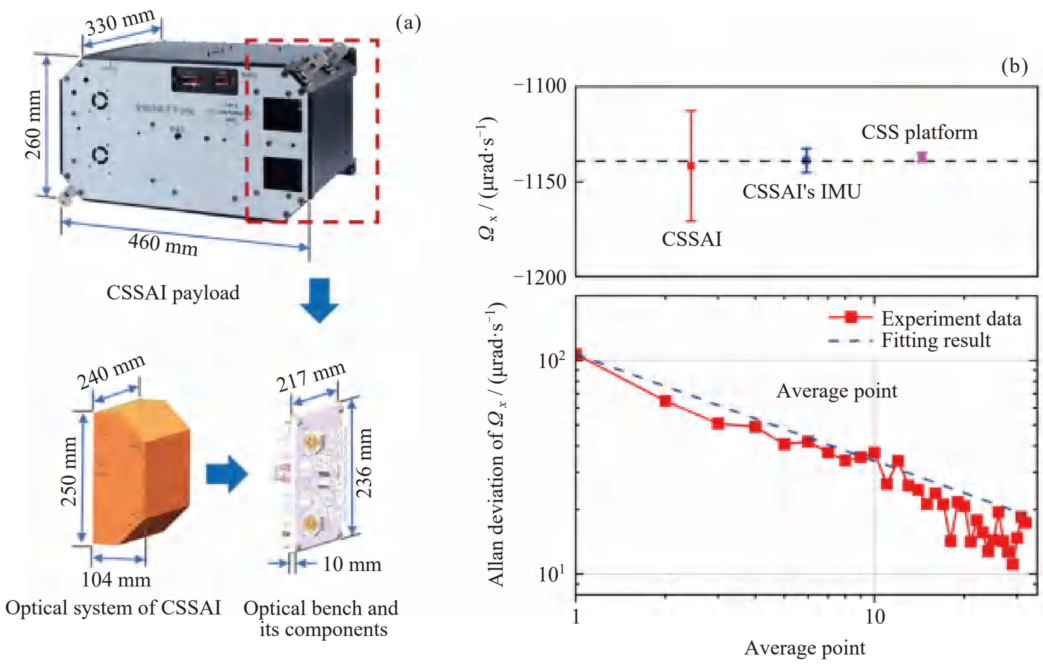

Fig. 28 The CSSAI and rotation measurement. (a) The CSSAI and its optical system[6], (b) Rotation measurement in space

7.2 Realization of Laser Cooling Alkaline-Earth Atom under Microgravity

Relying on the strontium optical clock payload aboard the CSS, laser cooling of alkaline-earth atoms was achieved in a space microgravity environment[64]. This successfully expands the capability boundary of cold-atom physics experiments under the extreme conditions of microgravity, representing a landmark advancement in the space-based cold-atom physics experimental technologies in China. Alkaline-earth elements such as strontium possess a dual-valence-electron structure with singlet and triplet states, making their laser cooling more complex in optical configuration and control logic than alkali-metal systems and imposing higher technical demands. The project team developed a highly integrated miniaturized space strontium optical clock physics system, overcoming challenges in the miniaturization and vibration resistance of sophisticated opto-mechatronic systems. The system integrates more than ten high-stability lasers and achieved on-orbit frequency locking for each laser beam[65]. Having successfully endured the rigors of rocket launch and the on-orbit environment, the system has operated stably over extended periods, realizing the laser cooling of both strontium isotopes, ^{87}Sr and ^{88}Sr, under microgravity conditions (Figure 29). Cameras inside the optical clock system clearly captured images of laser-cooled strontium cold-atom clouds in a magneto-optical trap, verifying the effective implementation of laser cooling.

The accomplishment of on-orbit laser cooling (first-stage cooling) of alkaline-earth strontium atoms lays a solid technical foundation for the operation of high-performance space optical clocks. This breakthrough not only expands the frontier of microgravity cold-atom physics, but also strongly advances China's establishment of an independent, world-leading, space-ground integrated high-precision time-frequency system. It provides crucial support and assurance for major future needs, including next-generation satellite navigation, deep-space exploration, tests of general relativity, and even future gravitational-wave detection.

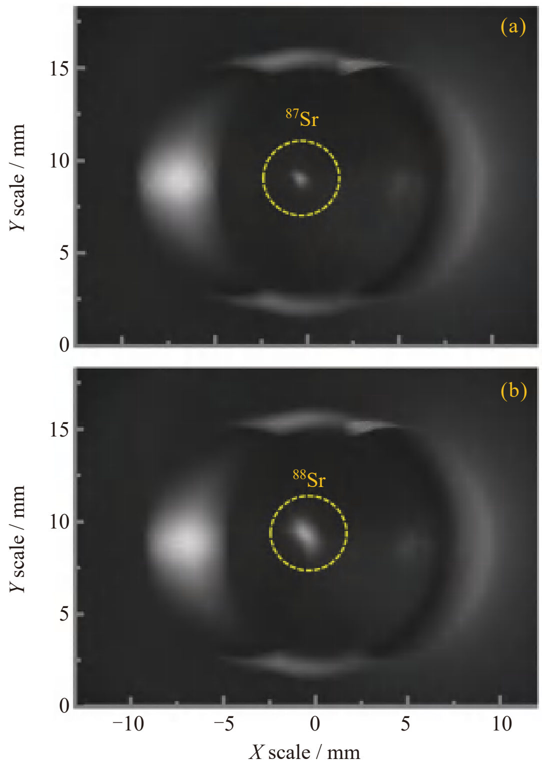

Fig. 29 Magneto optical trap (MOT) atoms photography shot by the CCD camera[64]. (a) ^{87}Sr MOT atoms, (b) ^{88}Sr MOT atoms

8 Space Innovative Technology Demonstration

The area of space innovative technology demonstration focuses primarily on the space effect mechanism of components and assemblies, space information and precision measurement, *etc*. Fifteen projects (statistics as of 20 June 2026) have been successfully implemented in orbit. Valuable mechanisms of space effects have been acquired, and a series of key technology breakthroughs have been accomplished on high-performance, complex, and new electronic components and sensors. Some of these technologies have been promoted and transitioned into the aerospace technology and other fields. The field is dedicated to the demonstration and transformation of high-precision space detection and measurement technologies.

Example of progress: verification of key performance parameters for fiber optic sensors. The anti-radiation fiber grating temperature sensor is fabricated by femtosecond laser engraving method[66]. The measurement range of the sensor is –65–135℃, and the temperature measurement accuracy is 0.1℃. In addition, according to the performance characteristics of the irradiation sensitive optical fiber, the high sensitive optical fiber is selected to make the optical fiber irradiation sensor[67] (Figure 30). The experiment verifies the reliability of the design of the new optical fiber sensor, and tests the performance and life of the optical fiber sensing system under the coupling environment of complex factors such as space irradiation, single particle and atomic oxygen under the long-term on-orbit working state[68]. The results provide technical support for the application of optical fiber sensing technology in orbit.

9 International Cooperations

We have gradually promoted the establishment of a broad and multi-level international cooperation network, including major foreign space agencies such as ESA, DLR, CNES, SUPARCO, EGSA, SSA, SSO, ASI, *etc*., as well as important international space organizations, including UNOOSA, UNESCO, IAF, COSPAR, MVA. We have also engaged in comprehensive and systematic international cooperation with universities and research institutions.

In recent years, by comprehensively utilizing flight resources such as Shenzhou spacecraft, Tiangong laboratory, the CSS, the International Space Station, some scientific satellites, parabolic aircraft and sounding rockets, China has carried out joint research and development of scientific experiment payloads with foreign partners and supported Chinese and foreign scientific teams in conducting scientific research and academic exchanges. A large number of valuable scientific research achievements have been made. Nearly 40 joint experiments have been successfully carried out, and more than 20 international cooperation projects are being cultivated, demonstrated and implemented. A demonstration effect has been initially achieved. International mega science program is also in plan.

Fig. 30 Experiment unit and fiber optic irradiation sensors[10]

10 Summary

The science and utilization mission has been executed in an efficient manner, and the advanced experiments conducted aboard the CSS have revealed a series of novel scientific phenomena and laws under space conditions in diverse areas, including life sciences, materials science, fluid physics, combustion, and cold atom physics, *etc*. A series of research models have been developed, and a range of key technology breakthroughs have been achieved, including space animal cultivation, the preparation of important crystal materials, fluid and thermal management, space cold atom interferometer, and on-orbit combustion experimental technologies. In addition, applications and transformations have been initially attempted. Two annual progress reports (in 2024 and 2025) had been released, which cover a substantial array of achievements across multiple areas. Therefore, the progress greatly advance the development of space science, utilization, and technology in China.

In the future, science and utilization projects will be dynamically solicited and selected on a continuous implementation basis. Meanwhile a series of management policies will be gradually established for the projects. According to the plan, nearly a thousand projects will be implemented. These projects will focus on the frontiers of science and technology, serve national strategic needs, and call on more high-level experts and teams to actively participate in the CSS science and utilization research.

Acknowledgements We would like to express sincere gratitude to the CMSA for its organization and leadership, and sincerely thank all the project teams for their guidance and help, including: Wang Hongmei, Li Tianda, Li Yan, Zhen Huiqiong, Long Mian, Li Ning, Ying Hao, Li Yuying, Zhang Chunlin, Zhao Yufen, Liu Yan, Sun Yeqing, Wei Bingbo, Wang Haipeng, Liu Xuechao, Yu Jianding, Jin Min, Yang Sen, Wang Yu, Wang Gang, Ma Yanwei, Tang Minghui, Zhou Feng, Cai Meirong, Wang Daoai, Chen Xi, Chang Hong, Xu

Shenghua, Chen Zhenqian, Xu Bo, Duan Li, Kang Qi, Hou Meiying, Tian Zhenyu, Wang Shuangfeng, Zhang Yang, Liu Youcheng, Zhu Lianqing, Gao Fuyu, Li Shengyang, Liu Kang, as well as other related colleagues in general establishment of space science and utilization, including Zhao Liping, Gong Yongsheng, He Yufeng, Ma Ping, Han Pei, Zhang Yingyi, Liu Yan, Wang Chong, Feng Xuan, Jiao Jian, Han Yuexia, *etc*.

References

[1] ZHOU J P. Chinese Space Station Project Overall Vision[J]. *Manned Spaceflight*, 2013, **19**(2): 1-10 (in Chinese)

[2] WANG X, WANG W. Key technical characteristics of the Tiangong Space Station[J]. *SCIENTIA SINICA Technologica*, 2021, **51**: 1287-1298. (in Chinese)

[3] GU Y D. The China Space Station: a new opportunity for space science[J]. *National Science Review*, 2022, **9**: nwab219

[4] GU Y D, GAO M, ZHAO G H. Space Research Plan of China's Space Station[J]. *Chinese Journal of Space Science*, 2016, **36**(05): 595-599

[5] GU Y D, GAO M, ZHAO G H. Science research and utilization planning of China's Space Station in operation period 2022—2032[J]. *Chinese Journal of Space Science*, 2020, **40**(5): 609-614

[6] China Manned Space Agency. Report on Scientific Research and Application Progress of the China Space Station (2024) [EB/OL]. 2024-12-30 [2026-04-30]. https://www.cmse.gov.cn/xwzx/202412/W020241231661310955564.pdf

[7] YAN Gong, MIAO Haitao, ZHAN Hu, *et al*. Introduction to the Chinese Space Station Survey Telescope (CSST) [J]. SCIENCE CHINA Physics, Mechanics & Astronomy, 2026, **69**(3): 239501. DOI: 10.1007/s11433-025-2809-0

[8] ZHANG S N, DONG Y W, GAO X H, *et al*. The high energy cosmic-radiation detection (HERD) facility in space[J]. *Manned Spaceflight*, 2015, **21**(1): 69-74

[9] China Manned Space Agency, Press conference held for the Shenzhou-17 manned space mission [OL]. CMSA. 2023-10-25[2026-05-12]. https://www.cmse.gov.cn/xwzx/202310/t20231025_54498.html (in Chinese)

[10] China Manned Space Agency. Report on Scientific Research and Application Progress of the China Space Station (2025) [R]. Beijing, 2026. (in Chinese). 2026-01-08 [2026-04-30]. https://www.cmse.gov.cn/xwzx/202601/W020260108444152803150.pdf [EB/OL]

[11] GU Y D, GAO M, ZHAO G H, *et al*. Recent progress in space science and applications on Chinese Space Station in 2022-2024[J]. *Chinese Journal of Space Science*, 2024, **44**(4): 607-621

[12] YUAN R, SUN H Y, ZHANG Q, *et al*. Gas Purification Technology Suitable for Space Mice Cultured in Sealed Box[J]. *Processes*, 2025, **13**(10): 3277

[13] CAIN J C, FERGUSON B B, MOZZONI D. An n = 90 internal potential function of the Martian crustal magnetic field[J]. *Journal of Geophysical Research Planets*, 2003, **108**: 1-19

[14] SINČÁK M, SEDLAKOVA-KADUKOVA J. Hypomagnetic fields and their multilevel effects on living organisms[J]. *Processes*, 2023, **11**(1): 282

[15] BERGUIG M S, HAMOUDI M, LEMOUËL J L. et al. Validate global mapping of internal lunar magnetic field[J]. *Arabian Journal of Geosciences*, 2011, **6**: 1063-1072

[16] LI S Y, LIU K, WANG H, *et al*. Pose estimation and tracking dataset for multi-animal behavior analysis on the China Space Station[J]. *Scientific Data*, 2025, **12**(1): 766

[17] ZHOU Z, LI S Y, LV Y X, *et al*. A deep learning framework for multi-object tracking in space animal behavior studies[J]. *Animals*, 2025, **15**(16): 2448

[18] LIU K, LI S Y, LV Y X, *et al*. Structure-aware multi-animal pose estimation for space model organism behavior analysis[J]. *Animals*, 2025, **15**(21): 3139

[19] XIE J Y, ZHU J C, WANG L H, *et al*. Potential regulatory modules to integrate microgravity signals into flowering pathways in Arabidopsis thaliana grown in space[J]. ResearchGate, DOI: 10.21203/rs. 3. rs-5775481/v1. npj Microgravity, 2025, **11**: 87. DOI:10.1038/s41526-025-00539-z

[20] XIE J Y, WANG L H, ZHENG H Q. Molecular basis to integrate microgravity signals into the photoperiodic flowering pathway in Arabidopsis thaliana under spaceflight condition. International Journal of Molecular Sciences, 2022, **21**(1): 63. DOI:10.3390/ijms23010063

[21] WANG L H, XIE J Y, MOU C H, *et al*. Transcriptomic analysis of the interaction between FLOWERING LOCUS T induction and photoperiodic signaling in response to space flight[J]. *Frontiers in Cell and Developmental Biology*, 2022, **9**: 813246

[22] JIA C X, ZHENG W B, LIU F W, *et al*. Biological culture module for plant research from seed-to-seed on the Chinese Space Station[J]. *Life Science in Space Research*, 2024, **42**: 47-52

[23] WU Y Y, XIE J Y, WANG L H, *et al*. Circumnutations and growth of inflorescence stems of Arabidopsis thaliana in response to microgravity under different photoperiod conditions[J]. *Life* (*Basel*), 2020, **10**(3): 26

[24] LI N, ZHANG X Y, LUO H, *et al*. Shear flow alleviates spaceflight-induced hepatic lipid dysregulation via suppression of SREBP mechanotransduction [J]. Science Bulletin, 2026. Doi: 10.1016/j.scib.2026.01.072

[25] LI Y, XUE L M, WANG F J, *et al*. , Lactylation of mTOR enhances autophagy in skeletal muscle during exercise[J]. Cell Chemical Biology, 2025. **32**(11): 1367-1380 e5. DOI: 10.1016/j.chembiol.2025.10.007

[26] NIU Z M, YAN Y, LIU W, *et al*. Aberrant miR-378 expression promotes hepatic lipid accumulation via hijacking the bile acid-regulated autophagy[L]. Life Metabolism, 2026. **5**(1): loaf038

[27] MA M, MA R S, LI Z Y, *et al*. NAD+ subcellular partitioning mediated by miR-183 and miR-96 regulates muscle stem cell differentiation[J]. Journal Molecular Cell Biology, 2026, mjag015

[28] LI Z Y, MA M, MA R S, *et al*. , MRG15 decline in aged/injured MuSCs hinders regeneration via differentiation defects[J]. *Cell*

Regeneration, 2026, **15**(1): 8

[29] XIN Y H, XIAN R Q, YANG Y G, *et al*. Structural and functional insights into the T-even type bacteriophage topoisomerase II[J]. *Nature Communications*, 2024, **15**: 8719-8733

[30] DING R W, QIU S W, GUO X F, *et al*. Space ionizing radiation triggers the formation of peptides and organophosphates on olivine surfaces. Nature Communications, 2026, **17**: 3210. DOI:10.1038/s41467-026-69575-x

[31] LIU Y, YING J X, DING K, *et al*. Origin of life experiments onboard Tiangong[J]. *Nature astronomy*, 2024, **8**: 1343

[32] LI Z J, ZHAO L, ZHANG G, *et al*. Optimized combination methods for exploring novel space environment-responsive genes and their roles: Insights from space-flown C. elegans and their implications for astronauts[J]. *International Journal of Radiation Biology*, 2025, **101**: 891-911

[33] ZHANG G, ZHAO L, LI Z J, *et al*. Integrated spaceflight transcriptomic analyses and simulated space experiments reveal key molecular features and functional changes driven by space stressors in space-flown C. elegans[J]. *Life Sciences in Space Research*, 2025, **44**: 10-22

[34] ZHANG Y, ZHAO L, SUN Y Q. Using single-sample networks to identify the contrasting patterns of gene interactions and reveal the radiation dose-dependent effects in multiple tissues of spaceflight mice[J]. *npj Microgravity*, 2024, **10**: 45

[35] LIAO H, WANG H P, LIU D N *et al*. Dynamic localization effect of dendritic and eutectic growth patterns stimulated by space fluid flow[J]. *Advanced Materials*, 2025, **37**(47): e08092

[36] WANG H P, LIAO H, WANG Y B, *et al*. Solidification mechanism and microstructure evolution of refractory Nb-Si and Nb-Si-Zr alloys aboard China Space Station[J]. *SCIENTIA SINICA Technologica*, 2025, **55**: 1989-2005

[37] WANG H P, LI H Z, ZHENG C H *et al*. Eutectic growth kinetics and microscopic mechanical property of refractory Zr57V43 alloy under space and ground conditions[J]. *Acta Materialia*, 2025, **295**: 11

[38] YU J D, ZHANG W, YANG S, *et al*. Recent advances and future prospects of space materials science[J]. *Review of Materials Research*, 2025, **1**(2): 100065

[39] ZHANG P, ZHANG Y, WANG Z L. *et al*. 1D and 3D co-simulation and self-adaptive position control of electrostatic levitation in China's Space Station [J]. npj Microgravity. 2022, **8**: 29. DOI:10.1038/s41526-022-00215-6

[40] WANG Z H, JIN M, SONG K P, *et al*. Expanded InSe crystal structure with reduced intrinsic defects for high-performance field-effect transistors[J]. *Advanced Materials*, 2025, **38**(4): e06506

[41] JIN R, SUI F R, YU Y L, *et al*. Microgravity-activated high-performance van der Waals InSe ferroelectric semiconductor[J]. *Nature Communications*, 2026, **17**: 3851

[42] JIANG H R, GAO Y F, CAO L, *et al*. Viscosity of a metallic glass-forming liquid by high-rate calorimetry and containerless electrostatic levitation in microgravity[J]. *Journal of Materials Science & Technology*, 2026, **273**: 212-222

[43] ZHANG Z G, TANG M H, DONG C H, *et al*. Phase selection and structural evolution in the solidified FeSe0.5Te0.5 superconductor via gradient temperature quenching[J]. *Acta Materialia*, 2026, **309**: 122071

[44] BAI Y Y, LYU H Y, WANG K, *et al*. The space environment effects and performance evolution of perfluoropolyether-based supramolecular gel lubricants (inChinese). SCIENTIA SINICA Technologica, 2025, **55**(12): 2014-2030

[45] WANG L C, ZHANG L Q, ZHENG R H, *et al*. Macroscale Superlubrication Achieved with Shear-Thinning Semisolid Lubricants[J]. Advanced Materials, 2024, 2412257. DOI:10.1002/adma.202412257

[46] ZHOU H W, ZOU S Y, OUYANG W Z, *et al*. Long-lived metastable bcc phase in the crystallization of charged colloids under microgravity[J]. *Journal of Colloid and Interface Science*, 2025, **695**: 137841

[47] ZHANG L G, XU B, SHI J, *et al*. Experimental study on condensation heat transfer of FC-72 in a narrow rectangular channel with ellipse-shape pin fins: Ground and microgravity experiments[J]. *International Journal of Heat and Mass Transfer*, 2019, **141**: 1272-1287

[48] XU B, CHEN Z Q. Condensation on Composite V-Shaped Surface with Different Gravity in Nanoscale[J]. *Microgravity Science and Technology*, 2019, **31**(5): 603-613

[49] GUO S, LIU M Q, XU B, *et al*. Vapor condensation and droplet directional migration on the surface of asymmetric triangular micropillar array structures using a hybrid thermal lattice Boltzmann method[J]. *International Communications in Heat and Mass Transfer*, 2025, **169**: 109557

[50] WANG J, WU D, ZHAO Y F, *et al*. Spatiotemporal correlation and chaotic dynamics analysis of annular flow with small volume ratio under microgravity[J]. *Physics of Fluids*, 2026, **38**: 014114.

[51] WU D, TANG W Z, WANG J, *et al*. On Chinese space station: pioneering space experiments unraveling the hydrodynamic instability of annular thermocapillary convection[J]. *Scientific Reports*, 2025, **15**: 24807

[52] HOU M Y, CHENG X H, YANG S, *et al*. Gravity-Dependent Rate Sensitivity in Granular Intrusion: Microgravity Experiments and Simulations[J]. *npj Microgravity*, 2026, **12**: 19

[53] YANG S, CHENG X H, HOU M Y, *et al*. Assessment of the Equivalent Low-Gravity of the granular collapse equipment in the VGR of the Chinese Space Station[J]. *Microgravity Science and Technology*, 2025, **37**: 59

[54] CHENG K, HOU M Y, SUN W, *et al*. Unraveling the role of gravity in shaping intruder dynamics within vibrated granular media[J]. *Communications Physics*, 2024, **7**: 425

[55] WANG W J, JIN K R, ZHENG Z H, *et al*. Research progress on soot formation from C1-C4 hydrocarbon fuel Combustion under microgravity[J]. *Journal of Tsinghua University* (*Science and Technology*), 2025, **65**(09): 1763-1773 (in Chinese)

[56] WANG W J, JIN K R, SHI H Q, *et al*. Variable Gravity Combustion: New Frontiers in Flame Studies [J]. npj Space Exploration. 2025, 1: 14. DOI:10.1038/s44453-025-00016-7

[57] ZHU F, LI D, WANG S F, *et al*. Shape and sooting characteristics of methane laminar-jet diffusion flames in microgravity[J]. *Chinese Journal of Space Science*, 2026, **46**(1): 121-130.

[58] LIU K, ZHU F, WANG S F, *et al*. Influence of hydrodynamics on soot process in laminar jet diffusion flame[J]. *Microgravity Science and Technology*, 2025, **37**: 42

[59] LIU Y S, LI X X, WEN Y Z. *et al*. Gas jet flame science experiments aboard the China Space Station[J] Journal of Tsinghua University (Science and Technology), 2025, **65**(9): 1609-1620 (in Chinese)

[60] CHEN T, YU S, LIU Y C. Effects of pressure on propagation characteristics of methane-air edge flames within two-dimensional mixing layers: A numerical study[J]. *Fuel*, 2021, **301**: 120857

[61] WEN Y Z, LI L F, LI X X, *et al*. Extinction of microgravity partially premixed flame aboard the Chinese Space Station. Proceedings of the Combustion Institute, 2024, **40**: 105574. DOI: 10.1016/j.proci.2024.105574

[62] ZHANG D F, LI J T, WANG W Z, *et al*. Compact and robust design of the optical system for cold atom interferometer in space[J]. *Optics Express*, 2025, **33**(17): 35419-35436

[63] LI J T, CHEN X, ZHANG D F, *et al*. Realization of a cold atom gyroscope in space[J]. *National Science Review*, 2025, **12**: nwaf012

[64] ZHAO G D, XIA J, LIU Y, *et al*. Laser Cooling Alkaline-earth Atoms for Optical Clock in Chinese Space Station[J]. *Chinese Physics Letters*, 2025, **42**(6): 063701

[65] XIA J, WANG W H, ZHAO G Z, *et al*. Optical system for a strontium optical lattice clock aboard the Chinese Space Station[J]. *Review of Scientific Instrument*, 2025, **96**(9): 093201.

[66] SHAO C Y, YU C L, HU L L. Radiation-Resistant Active Fibers for Space Applications[J]. *Chinese Journal of Lasers*, 2020, **47**(5): 0500014

[67] ZHENG Y, SUN S H, WANG X F, *et al*. Influence of γ-radiation on the output properties of narrow linewidth fiber laser and photo bleaching effect[J]. *High Power Laser and Particle Beams*, 2024, **36**(12): 8-14

[68] GONG Y L, ZHANG J G, LI W B. Application of Optical Fiber Sensing in Health Monitoring of Aerospace Composite Structure[J]. *Spacecraft Engineering*, 2022, **31**(5): 60-66

Author Biography

GU Yidong An expert in space science and utilization technology and an academician of the Chinese Academy of Sciences (CAS). He currently serves as the Chief Scientist for Space Science of the China Manned Space Engineering Program (CMS). He graduated from the Department of Engineering Physics, Tsinghua University in 1970. His previous posts include Deputy Director of the Cosmic Ray Research Laboratory at the Institute of High Energy Physics (CAS), Director of the National Space Science Center (CAS) and Academy of Opto-Electronics (CAS), Chief Designer and General Commander of the Space Utilization System in CMS, and President of the Chinese Society for Space Research. He led the development of an integrated space–ground utilization technology system for CMS, organized groundbreaking scientific and utilization missions aboard the Shenzhou series spaceship and the Tiangong space laboratory. He also led the planning and demonstration of space science and utilization missions for the China Space Station

0254-6124/2026/46(4)-0031-08 *Chin. J. Space Sci.* 空间科学学报

LIU Yang, HUANG Liying, ZHOU Xiang, ZOU Yongliao. Latest Scientific Results of China's Lunar and Deep Space Exploration (2024–2026). *Chinese Journal of Space Science*, 2026, **46**(4): 31−38. CSTR:32142.14.cjss.2026−yg15. DOI:10.11728/cjss2026.04.2026−yg15

Latest Scientific Results of China's Lunar and Deep Space Exploration (2024–2026)*

LIU Yang HUANG Liying ZHOU Xiang ZOU Yongliao

(*State Key Laboratory of Space Weather*, *National Space Science Center*, *Chinese Academy of Sciences*, *Beijing* 100190)

Abstract China's deep-space exploration program has entered a highly productive scientific stage, highlighted by the Chang'E-6 lunar farside sample return mission and continuous scientific exploitation of Tianwen-1 orbital and Zhurong rover datasets. This review summarizes the major scientific advances achieved between 2024 and 2026 in lunar and Martian explorations. The first returned samples from the lunar farside have provided unprecedented constraints on the formation of the South Pole-Aitken basin, early lunar crustal evolution, farside volcanism, mantle heterogeneity, volatile evolution, and space weathering processes. These studies reveal a complex evolutionary history involving long-lived magmatism, impact-driven crustal reworking, hemispheric differences in mantle composition, and distinctive regolith evolution. Meanwhile, recent Tianwen-1 investigations have significantly advanced our understanding of Martian surface composition, subsurface structure, geomorphological evolution, and the near-Mars space environment, providing new evidence for aqueous alteration, shallow ice-bearing materials, possible ancient shoreline deposits, and solar-wind-driven plasma processes. These achievements demonstrate the increasing scientific impact of China's planetary exploration program and provide important new perspectives on terrestrial planet evolution, volatile histories, impact processes, and surface-environment interactions across the inner Solar System.

Key words Lunar and deep space exploration of China, Chang'E-6 mission, Tianwen-1 mission

Classified index P184

1 Introduction

Over the past two decades, China has established a comprehensive deep-space exploration program that has significantly advanced planetary science. Through the successive Chang'E lunar exploration missions and the Tianwen planetary exploration program, China has achieved a series of major technological and scientific breakthroughs, including lunar orbiting, landing, roving, sample return, and independent exploration of Mars. These missions have not only provided unique datasets and returned samples, but have also enabled fundamental advances in understanding the origin and evolution of the Moon, Mars, and other bodies in the Solar System.

The period from 2024 to 2026 marks a particularly important stage in China's deep-space exploration. The successful return of 1935.3 g of lunar samples by the Chang'E-6 (CE-6) mission represents the first sample return from the lunar farside, opening an entirely new window into the South Pole-Aitken (SPA) basin and enabling direct investigation of the lunar farside, one of the least understood regions of the Moon[1]. At the same time, continued analyses of data acquired by the Tianwen-1 orbiter and the Zhurong rover have substantially improved our understanding of Martian surface processes, subsurface structure, aqueous history, and the near-

* Supported by Strategic Research Projects of National Natural Science Foundation of China (42542007)
Received May 20, 2026

Mars space environment. Together, these achievements have produced a large number of high-impact scientific results that reshape current views of planetary evolution.

This review summarizes the major scientific advances arising from China's lunar and deep-space exploration between 2024 and 2026, with particular emphasis on the CE-6 sample return mission and recent discoveries based on Tianwen-1 observations. For the Moon, we highlight new constraints on the formation of the SPA basin, early lunar evolution, farside volcanism, mantle evolution, volatile inventories, and space weathering processes. For Mars, we review recent progress in surface geology, subsurface structure, orbital remote sensing, and the Martian plasma environment. These results collectively demonstrate the growing scientific impact of China's planetary exploration program and provide important constraints on the evolution of terrestrial planets and other airless bodies in the Solar System.

2 Chang'E-6 Mission

The CE-6 mission represents the first successful sample return from the lunar farside, landing at the Apollo basin within the South Pole-Aitken (SPA) impact structure (41.625°S, 153.978°W) and returning 1935.3 g of lunar samples. As the oldest and deepest recognized impact basin on the Moon, SPA provides a unique geological window into the lunar interior and the early impact history of the inner Solar System. The CE-6 landing site is located on a complex basaltic plain within SPA, characterized by volcanic constructs, tectonic features, and impact structures, recording prolonged magmatic and impact reworking[2]. Consequently, CE-6 samples preserve a mixed record of farside volcanism, SPA-related ejecta, and subsequent impact modification, offering an unprecedented opportunity to investigate lunar farside evolution.

2.1 Early Lunar Evolution and SPA Formation

CE-6 samples are dominated by basaltic fragments, impact melts, and minor highland lithologies[1], recording intense impact mixing and long-term crustal reworking. Ancient anorthositic clasts and highland-derived fragments provide constraints on the primary lunar crust and magma ocean differentiation. Impact processes emerge as the dominant agents shaping the farside crust. Widespread impact-melt rocks, breccias, and shock metamorphic minerals record high-temperature and high-pressure conditions and subsequent recrystallization, reflecting sustained modification of the SPA region over time. These observations provide critical constraints on early lunar crustal cycling and impact flux evolution.

Importantly, ancient norite clasts dated at ～4.25 Ga suggest excavation from deep SPA crust or melt-sheet-derived materials, providing a temporal constraint on early SPA evolution. Recent studies further identified a new suite of impact-derived noritic rocks (SPANs), which yield Pb-Pb ages of ～4.25 Ga and ～3.87 Ga. The older population is interpreted as crystallization products of SPA impact melt sheets, indicating that SPA likely formed at ～4.25 Ga[3]. This provides a key anchor for lunar early bombardment chronology and suggests broadly similar early impact fluxes between the nearside and farside. In addition, CE-6 anorthositic clasts indicate that the farside primary crust is compositionally and temporally comparable to the nearside. A ～4.41 Ga KREEP-related thermal overprint further supports a Moon-wide magma ocean crystallization sequence and argues against asymmetric primary crystallization models[4].

2.2 Farside Volcanism and Lunar Interior Evolution

CE-6 basaltic fragments provide the first direct chronological constraints on farside volcanism. The main basaltic unit yields an age of ～2.807 ± 0.003 Ga, demonstrating that farside volcanic activity persisted into the middle-late lunar history[5,6]. This significantly extends the duration of lunar volcanism compared with nearside Apollo and CE-5 samples (～2.0 Ga)[7,8]. A subordinate population of high-Al basalts with ages of ～4.2 Ga further indicates that farside magmatism was episodic and long-lived, spanning at least ～1.4 billion years[6]. The persistence of volcanism into the late stages of lunar evolution raises fundamental questions regarding the heat sources capable of sustaining prolonged magmatic activity. Recent petrological and geochemical studies of CE-6 basalts identified two compositionally distinct volcanic suites, including ～2.9 Ga very-low-Ti basalts and ～2.8 Ga low-Ti basalts derived from mantle sources at different depths[9]. Modeling suggests that these source regions correspond to pyroxenitic lithologies formed during lunar magma ocean crystallization, including shallow Ilmenite-Bearing Cumulates (IBC). Because both CE-5 and CE-6 basalts originated from water-poor and KREEP-poor mantle sources, conventional models invoking mantle hydration or radiogenic enrichment are insufficient to explain these young volcanic episodes. Instead, thermal transfer from magmas ponded within the thickening lithosphere has been proposed as a mechanism capable of remobilizing shallow IBC-rich mantle reservoirs and sustaining late-stage volcanism. These observations suggest that ~3.0 Ga may represent a transition in lunar thermal evolution, after which shallow lithospheric heating became increasingly important for magma generation[9]. Collectively, these results imply a prolonged thermal evolution of the lunar interior, with farside mantle sources evolving from early enriched to later depleted compositions.

Paleomagnetic and oxygen fugacity studies further refine this picture. CE-6 basalts record paleointensities of ~5–21 μT at ~2.8 Ga, suggesting that the lunar dynamo weakened after ~3.1 Ga but may have experienced a later rebound rather than a monotonic decay[10]. Oxygen fugacity measurements indicate a more reduced farside mantle (Iron-Wüstite (IW) buffer, with ΔIW ≈–1.93) compared to the nearside (≈ –0.8), providing the first direct evidence for redox heterogeneity between lunar hemispheres[11]. This hemispherical contrast may reflect either asymmetric magma ocean crystallization or localized modification by SPA-forming impacts.

2.3 Volatiles and Mantle Heterogeneity of the Farside

Volatile studies of CE-6 samples provide the first direct constraints on farside mantle water content. Melt inclusions and apatite analyses indicate extremely low water abundances, with mantle source estimates of ~1–1.5 $\mu g \cdot g^{-1}$[12], significantly lower than nearside estimates (~7.5 $\mu g \cdot g^{-1}$) derived from Apollo and CE-5 basalts[13]. These results suggest a potential hemispherical dichotomy in lunar mantle hydration, with a "drier farside mantle" relative to the nearside. However, broader sample coverage is still required to confirm this global pattern. In addition, CE-6 impact glass beads demonstrate that solar-wind-derived hydrogen is efficiently implanted and stored in basaltic glasses but poorly retained in anorthositic glasses[14]. This compositional dependence indicates that regolith components play distinct roles in the lunar surface water cycle[14]. Recent isotopic studies further suggest that this volatile depletion may be linked to the formation of the SPA basin itself. High-precision Fe and K isotope measurements of CE-6 basalts reveal unusually heavy K isotopic compositions that cannot be explained solely by magmatic differentiation processes. Instead, modeling indicates that volatile loss associated with the SPA-forming impact could account for the observed signatures, implying that the giant impact may have modified the volatile budget of the underlying mantle and contributed to the long-term suppression of volcanism on the lunar farside[15].

2.4 Regolith Evolution and Space Weathering

CE-6 regolith provides the first in situ record of farside space weathering. The samples contain nanophase iron, impact melt products, and glassy materials formed by micrometeorite bombardment and solar wind irradiation, indicating coupled control by space weathering processes. Compared with nearside samples, CE-6 regolith shows differences in maturation degree, nanophase iron distribution, and amorphous rim development, reflecting variations in impact flux and geomagnetic shielding effects. Together with CE-5 and Apollo samples, these results suggest hemispherical asymmetry in space weathering intensity driven by both solar wind exposure and impactor population differences. Additional discoveries, including CaS minerals[16], Fe-Cu-S system mobility[17], Fe-oxide formation (including hematite)[18], and metallic copper and iron assemblages[17], reveal that impact-induced transient high-temperature and partially oxidizing environments can locally modify redox conditions on an otherwise reducing Moon.

Finally, nanoscale noble metal phases (*e.g.*, Ruthenium)[19] and carbon nanostructures (including single-walled carbon nanotubes)[20] highlight the Moon as a natural laboratory for extreme physicochemical processes, with implications for both regolith evolution and in situ resource utilization.

3 Tianwen-1 Mission

Tianwen-1 is China's first independently conducted Mars exploration mission. It was launched in July

2020 and was inserted into Martian orbit in February 2021. The Zhurong rover, carried by the Tianwen-1 spacecraft, landed in southern Utopia Planitia in May 2021 at 109.925°E and 25.066°N. During its surface operations, the rover worked for 347 Martian sols and travelled 1921 m, collecting images, spectra, radar profiles, meteorological measurements, and surface compositional data. From 2024 to 2026, studies based on data from the Tianwen-1 orbiter and the Zhurong rover continued to advance, covering Martian surface composition, weathering processes, subsurface structures, orbital remote-sensing observations, and the near-Mars space environment. These studies provide important constraints on the history of Martian aqueous activity, surface modification processes, and space-environment responses.

3.1 Martian Surface Composition and Properties

Recent work on the Zhurong landing site has substantially refined interpretations of hydrous materials in southern Utopia Planitia. Rather than treating the hydration signatures as isolated mineral absorptions, studies combining Multispectral Camera (MSCam) and Short-Wave Infrared (SWIR) observations emphasize their close relationship with dusty surfaces. The 1.9 μm feature, observed at both the Zhurong and Perseverance landing sites, is interpreted as a hydration signal that may be common in Martian dust. In contrast, the 2.2 μm band appears to be more locally characteristic of the Zhurong region and is consistent with hydrated silica in terms of spectral position and shape. These observations suggest that the hydrous components at the landing site may reflect a combination of aeolian deposits from nearby cones and local aqueous alteration products[21].

Rock-surface observations further indicate that aqueous weathering affected some materials at the landing site. Some rocks bear dark patches that are regarded as dust-free surfaces; these patches exhibit near-infrared spectra with a concave-up blue slope. These spectral properties are interpreted as evidence for silica-enriched leached rinds on basaltic glass, implying that acidic fluids may once have modified rock surfaces at the landing site[22]. Textural features on rock surfaces related to salt activity may have experienced dust deposition, surface adsorption, salt deliquescence, and modification by transient brine activity. Climate simulations indicate that, from late spring to summer, near-surface temperature and relative humidity from nighttime to predawn may intermittently approach the deliquescence thresholds of some hygroscopic salts, resulting in cycles of brine formation and salt crystallization. This provides new observational evidence for short-lived brine activity in the modern near-surface environment of Mars[23]. In addition, unmixing studies based on laboratory binary mixtures and SWIR spectra further quantified the abundance of hydrated minerals on the surface of the landing site, indicating short-term fluid-rock interactions involving ice and snow melt under cold climatic conditions and a low to moderate degree of water-limited alteration[24,25].

Elemental measurements provide an additional perspective on these alteration processes. Studies based on Laser-Induced Breakdown Spectroscopy (LIBS) data indicate that sulfur is mainly associated with gypsum and other sulfates, whereas hydrogen may be hosted by hydrous mineral assemblages such as gypsum, hydrated silica, and ferrihydrite. These phases are consistent with acidic weathering processes at the landing site[26]. Trace-element studies further show that Li, Sr, and Rb are mainly linked to igneous components in rocks and soils. The inferred secondary mineral assemblage is dominated by minor sulfates, whereas clay minerals appear to be absent or rare. This supports a scenario in which surface igneous materials were derived from relatively late Amazonian lava flows and subsequently experienced limited acidic alteration[27].

Beyond composition, Zhurong data have also been used to characterize surface structure and photometric behavior. Navigation and Terrain Camera (NaTeCam) images, together with inertial measurement unit data, enabled the construction of spatially continuous 3 D models and Digital Elevation Models (DEMs). These products allow degraded small-scale structures, directional degradation, and textured features in depressions to be recognized[28]. Based on multi-phase-angle images acquired by the NaTeCam, together with the Discrete Ordinates Radiative Transfer (DISORT) model and the Hapke radiative transfer model, the photometric and microphysical properties of the soils were retrieved. The retrieved parameters indicate that soils at the landing site are dominated by backscattering, have relatively high particle porosity and/or heterogeneous grain-size distributions, and show low macroscopic roughness. The observation of phase reddening, with a maximum near a phase angle of about 60°. These results provide important ground-truth information for quantitative spectral interpretation of the Zhurong landing site and surrounding regions[29].

3.2 Subsurface Structure and Physical Properties

The Zhurong Rover Penetrating Radar (RoPeR) has provided key constraints on the subsurface structure and aqueous history of southern Utopia Planitia. RoPeR observations reveal northward-dipping reflectors at depths of 10–35 m along an approximately 1.3 km northward traverse. Their dip angles, geometry, thickness, and low-permittivity characteristics are comparable to terrestrial coastal deposits. This interpretation supports the presence of ancient prograding shoreline deposits and provides subsurface sedimentological evidence relevant to the ancient ocean hypothesis for the Martian northern lowlands[30].

RoPeR analyses also highlight the heterogeneity of shallow to intermediate-depth materials. Frequency-domain studies identify an approximately 7 m thick low-loss layer whose dielectric properties are compatible with water ice. This layer may indicate ice-bearing material at depths of 15–57 m, and simulations suggest that dirty ice mixed with stones provides the closest match to the observations[31]. For the uppermost approximately 4 m, attenuation analyses yield a loss tangent of about 0.0079, with lateral variations possibly related to changes in duricrust abundance[32]. High-frequency quad-polarization radar observations further reveal complex subsurface structures, including three shallow subsurface layers, buried craters, and other features. These features are likely to have formed in aqueous environments during the middle to late Amazonian period, implying that water-related processes in Utopia Planitia may have persisted into relatively recent geological times[33].

3.3 Mars Orbital Observations

The Tianwen-1 orbiter has advanced studies of Martian geomorphology and mineralogical mapping. Orbital observations from Tianwen-1 have provided new constraints on the origin of pitted cones in the Zhurong landing region. HiRIC topographic and imaging data suggest that these cone-like landforms may be related to mud volcanism rather than representing a single simple volcanic or periglacial process. Their middle-to-late Amazonian ages, kilometer-scale inferred source depths, and preferred structural orientations indicate that subsurface material mobilization was likely controlled by regional tectonic and volcanic processes, including trough-related fracturing, basin subsidence, and activity associated with the Elysium volcanic province[34]. Related flow features, including tongue-shaped lobes on cone flanks, apron-like deposits within pits or at cone bases, and adjacent rough units, provide additional evidence that these landforms may be connected to volcanic or volatile-driven processes[35]. At a broader scale, orbital remote-sensing mapping identified geomorphological features in southern Utopia Planitia that are consistent with a nearshore zone, indicating the presence of different types of marine environments. Combined with Zhurong in situ observations, these results suggest that the region may have experienced flooding from the Late Noachian to the Early Hesperian, followed by volatile loss during the Amazonian epoch[36].

Tianwen-1 Mars Mineralogical Spectrometer (MMS) data have been used to map ferric oxides across Mars after systematic spectral processing. The results show that ferric oxides are widely distributed, with nanophase ferric oxides dominating bright terrains. The study also identified crystalline hematite in Meridiani Planum and Aram Chaos, including a newly reported red crystalline hematite deposit in southeastern Aram Chaos. These observations provide orbital mineralogical evidence for past aqueous and oxidative processes on Mars[37].

In aeolian geomorphology, AiTARs-Net was developed to automatically detect Transverse Aeolian Ridges (TARs) with arbitrary orientations, improving the efficiency of TARs mapping over large areas[38]. Complementary orbital statistical analyses indicate that landform type, elevation, and slope all influence the distribution and dimensions of TARs around the Zhurong landing area[39].

3.4 Near-Mars Space Environment and Interplanetary Space

The Tianwen-1 orbiter has provided valuable multi-spacecraft observations for understanding the response of the Martian plasma environment to solar-wind variations. Joint measurements with MAVEN show that even relatively weak solar-wind disturbances can produce large-scale motions of the Martian bow shock, highlighting the importance of upstream plasma conditions, especially the magnetosonic Mach number, in controlling the location and variability of this boundary[40]. During ICME events, simultaneous observations by Tianwen-1 and MAVEN further demonstrate that the Martian bow shock responds differently to solar-wind dynamic pressure and interplanetary magnetic-field strength: enhanced dynamic pressure compresses the boundary planetward, whereas stronger magnetic fields can favor outward displacement[41]. In addition, joint observations and hybrid simulations indicate that Mars can still sustain an induced magnetosphere under radial IMF conditions, suggesting that magnetic-field draping and induced fields remain important even when the IMF is nearly aligned with the solar-wind flow[42].

Beyond Mars itself, the Tianwen-1 orbiter has also extended its scientific role beyond Mars-focused observations. The HiRIC CMOS camera was used to observe the interstellar object 3 I/ATLAS from Mars orbit, demonstrating the potential of a Mars orbiter for small-body and interplanetary-object studies. Because the observations were obtained from a geometry different from Earth-based views, they provided useful constraints on the evolution of the object's coma and tail and helped interpret its dust activity[43].

4 Summary

Recent advances from the CE-6 and Tianwen-1 missions demonstrate the growing importance of China's deep-space exploration program in addressing key questions in planetary science. For the Moon, CE-6 samples provide the first direct laboratory constraints from the lunar farside, refining our understanding of early lunar evolution and SPA formation, the duration and mechanisms of farside volcanism, the volatile and redox heterogeneity of the lunar mantle, and the evolution of farside regolith under space weathering. These findings show that the lunar farside preserves a distinctive record of impact, thermal, volatile, and surface modification processes, rather than simply representing an extension of the nearside. For Mars, Tianwen-1 and Zhurong results have linked surface composition, subsurface radar sounding, orbital remote sensing, and plasma-environment observations into a more integrated view of the Zhurong landing region and the near-Mars environment. Evidence for hydrated minerals, limited acidic alteration, transient brine activity, possible coastal deposits, subsurface ice-bearing materials, and solar-wind-controlled plasma responses indicates that Mars has experienced both long-term aqueous modification and ongoing surface-atmosphere-space interactions. Overall, these studies highlight the value of combining sample analysis, in situ measurements, orbital observations, and multi-spacecraft monitoring to reconstruct planetary evolution. They also provide a strong scientific foundation for future Chinese missions to the lunar south pole, near-Earth asteroids, main-belt comets, and the outer Solar System.

References

[1] LI C L, HU H, YANG M F, *et al*. Nature of the lunar far-side samples returned by the Chang'E-6 mission[J]. *National Science Review*, 2024, **11**(11): nwae328

[2] QIAN Y Q, HEAD J, MICHALSKI J, *et al*. Long-lasting farside volcanism in the Apollo basin: Chang'E-6 landing site[J]. *Earth and Planetary Science Letters*, 2024, **637**: 118737

[3] SU B, CHEN Y, WANG Z L, *et al*. South pole-Aitken massive impact 4.25 billion years ago revealed by Chang'E-6 samples[J]. *National Science Review*, 2025, **12**(6): nwaf103

[4] WANG Z L, CHEN H J, CHEN Y, *et al*. Chang'E-6 farside anorthosites indicate hemispherically comparable magma ocean solidification[J/OL]. *Nature Communications*, (2026-05-15). https://doi.org/10.1038/s41467-026-73258-y

[5] CHE X C, LONG T, NEMCHIN A, *et al*. Isotopic and compositional constraints on the source of basalt collected from the lunar farside[J]. *Science*, 2025, **387**(6740): 1306-1310

[6] ZHANG Q W L, YANG M H, LI Q L, *et al*. Lunar farside volcanism 2.8 billion years ago from Chang'E-6 basalts[J]. *Nature*, 2025, **643**(8071): 356-360

[7] CHE X C, NEMCHIN A, LIU D Y, *et al*. Age and composition of young basalts on the Moon, measured from samples returned by Chang'E-5[J]. *Science*, 2021, **374**(6569): 887-890

[8] LI Q L, ZHOU Q, LIU Y, *et al*. Two-billion-year-old volcanism on the Moon from Chang'E-5 basalts[J]. *Nature*, 2021, **600**(7887): 54-58

[9] WANG C Y, QIAN Y Q, WANG J T, *et al*. The source and thermal driver of young (<3.0 Ga) lunar volcanism[J]. *Science Advances*, 2025, **11**(34): eadv9085

[10] CAI S H, QI K X, YANG S H, *et al*. A reinforced lunar dynamo recorded by Chang'E-6 farside basalt[J]. *Nature*, 2025,

643(8071): 361-365

[11] ZHANG H J, YANG W, ZHANG D, *et al*. A more reduced mantle beneath the lunar South Pole-Aitken basin[J]. *Nature Communications*, 2025, **16**(1): 6985

[12] HE H C, LI L X, HU S, *et al*. Water abundance in the lunar farside mantle[J]. *Nature*, 2025, **643**(8071): 366-370

[13] HU S, HE H C, JI J L, *et al*. A dry lunar mantle reservoir for young mare basalts of Chang'E-5[J]. *Nature*, 2021, **600**(7887): 49-53

[14] HE H C, HU S, GAO L, *et al*. Lunar dichotomy in surface water storage of impact glass beads[J]. *Nature Communications*, 2025, **16**(1): 4971

[15] TIAN H C, ZHANG C, LI W J, *et al*. Isotopic evidence for volatile loss driven by South Pole-Aitken basin-forming impact[J]. *Proceedings of the National Academy of Sciences of the United States of America*, 2026, **123**(3): e2515408123

[16] LI C, LI Y, PANG R H, *et al*. Impact-induced ultra-high melting point oldhamite discovered in Chang'E-6 lunar soil[J]. *Nature Communications*, 2025, **16**(1): 2155

[17] GUO Z, SONG D S, SONG W L, *et al*. Impact-induced high-temperature formation of metallic copper and bornite in Chang'E-6 lunar soils[J]. *NPJ Space Exploration*, 2026, **2**(1): 13

[18] LIU R R, ZHANG X P, ZHAO S Z, *et al*. Million-year solar wind irradiation recorded in Chang'E-5 and Chang'E-6 samples[J]. *Nature Communications*, 2025, **16**(1): 9197

[19] LI L X, QIU M F, HU S, *et al*. Delivery of carbonaceous materials to the Moon[J]. *Icarus*, 2026, **444**: 116802

[20] ZHANG W, WANG Z Z, LIU F X, *et al*. Discovery of naturally occurring single-walled carbon nanotubes and graphitic carbon on the far side of the Moon[J]. *Nano Letters*, 2026, **26**(2): 917-925

[21] ZHANG Q, VINCENDON M, POULET F, *et al*. Hydrous components of dusty surfaces inferred from Zhurong in situ observations[J]. *Geophysical Research Letters*, 2025, **52**(18): e2025GL115266

[22] ZHANG Q, CARTER J, VINCENDON M, *et al*. In situ observation of weathering rinds at the Zhurong landing site, Mars[J]. *Journal of Geophysical Research: Planets*, 2025, **130**(9): e2025JE009196

[23] WU X, ZHOU X, ZHAO J N, *et al*. Zhurong rover reveals salt weathering-driven surface modification by transient brine activity on Mars[J/OL]. *Science Bulletin*, (2026-03-13). https://doi.org/10.1016/j.scib.2026.03.028

[24] JU E M, LIU C Q, CHEN J, *et al*. Detection of allophane by the Zhurong rover indicates water-limited alteration at Utopia Planitia, Mars[J]. *Earth and Planetary Science Letters*, 2024, **639**: 118769

[25] ZHOU X, WU X, ZOU Y L, *et al*. Quantitative mineral analysis of zhurong landing area based on in-situ SWIR spectral unmixing[C]//EGU General Assembly 2025. Vienna: EGU, 2025: EGU25-10183

[26] ZHANG Y Z, REN X, CHEN Z P, *et al*. Volatile elements characterized by MarSCoDe in materials at Zhurong landing site[J]. *The Astronomical Journal*, 2024, **168**(4): 150

[27] LUO Y X, LIU J J, CHEN Z P, *et al*. Alkali trace elements observed by MarSCoDe LIBS at Zhurong landing site on mars: quantitative analysis and its geological implications[J]. *Journal of Geophysical Research: Planets*, 2024, **129**(7): e2024JE008366

[28] LIU R R, XU Y, YANG Q Q. High-resolution and spatial-continuous 3-D model reconstruction of martian surface by integrating multisensor data of Zhurong Rover[J]. *IEEE Transactions on Geoscience and Remote Sensing*, 2024, **62**: 4601216

[29] ZHOU X, YANG Y Z, WU X, *et al*. Spectrophotometric properties of Martian soil at the landing area of the Tianwen-1 Zhurong rover[J]. *Astronomy & Astrophysics*, 2026, **708**: A134

[30] LI J H, LIU H, MENG X, *et al*. Ancient ocean coastal deposits imaged on Mars[J]. *Proceedings of the National Academy of Sciences of the United States of America*, 2025, **122**(9): e2422213122

[31] MENG X D, ZHANG L, XU Y, *et al*. Evidence of shallow subsurface ice at Tianwen-1 landing site[J]. *Earth and Planetary Science Letters*, 2026, **678**: 119832

[32] SUN J B, FENG Y J, CAO Y Z, *et al*. Exploring the dielectric loss of Martian regolith in the frequency domain using Zhurong radar data[J]. *Icarus*, 2025, **425**: 116315

[33] LIU Y K, YAN T F, QIN X G, *et al*. Multipolarized radar reveals shallow subsurface structure and middle-late Amazonian aqueous activity in Utopia Planitia, Mars[J]. *National Science Review*, 2025, **12**(12): nwaf505

[34] ZHANG J J, REN X, CHEN Y, *et al*. Potential formational scenarios of the mud volcanoes in the Zhurong landing area in Utopia Planitia, observed by Tianwen-1[J]. *Earth and Planetary Science Letters*, 2024, **647**: 119024

[35] ZHANG C L, CONWAY S J, LIU Y. Flow features potentially related to pitted cones in southern Utopia Planitia, Mars[C]//EGU General Assembly 2025. Vienna: EGU, 2025: EGU25-8518.

[36] WU B, DONG J, WANG Y R, *et al*. A probable ancient nearshore zone in southern Utopia on Mars unveiled from observations at the Zhurong landing area[J]. *Scientific Reports*, 2024, **14**(1): 24389

[37] REN P Y, LIU C Q, WANG Y Z, *et al*. Global maps of ferric oxides on the Martian surface based on processed Tianwen‑1 Mars Mineralogical Spectrometer (MMS) data[J]. *Journal of Geophysical Research: Planets*, 2026, **131**(3): e2025JE009532

[38] CAO Z, KANG Z Z, HU T, *et al*. AiTARs-Net: a novel network for detecting arbitrary-oriented transverse aeolian ridges from Tianwen-1 HiRIC images[J]. *ISPRS Journal of Photogrammetry and Remote Sensing*, 2024, **211**: 135-155

[39] REN Xiaolan, CAO Zhen, KANG Zhizhong, *et al*. Study on distribution and morphology of transverse aeolian ridges in the landing area of Zhurong rover[J]. *Journal of Deep Space Explor-*

ation, 2024, **11**(6): 594-604 (任晓兰, 曹震, 康志忠, 等. 火星“祝融号”着陆区横向风成脊的分布及形态研究 [J]. 深空探测学报 (中英文), 2024, **11**(6): 594-604)

[40] CHENG L, WANG Y M, MA Y J, *et al*. Bow shock oscillations of Mars under weakly disturbed solar wind conditions[J]. *Nature communications*, 2025, **16**(1): 9649

[41] WANG M, ZHANG J Q, LU J Y, *et al*. Simultaneous two-point study of the Martian bow shock affected by an interplanetary coronal mass ejection: Tianwen-1 and MAVEN observations[J]. *Geophysical Research Letters*, 2025, **52**(4): e2024GL112219

[42] LIN R T, HUANG S Y, ZHOU J Y, *et al*. Mars’ induced magnetosphere can form under radial interplanetary magnetic field[J]. *The Innovation*, 2026, **7**(6): 101312

[43] REN X, YAN W, ZHAO R N, *et al*. Interstellar object 3I/ATLAS observed from Mars by China’s Tianwen-1 spacecraft[J]. *The Astrophysical Journal Letters*, 2026, **1003**(1): L10

Author Biography

LIU Yang is a Professor at the National Space Science Center in of the Chinese Academy of Sciences (CAS). Professor Liu’s research interest is focused on understanding the formation and evolution of planetary surfaces by integrating remote sensing observations, quantitatively theoretical modeling, and laboratory spectroscopy. He has published more than 100 papers in high rank journals including Nature Astronomy and Science Advances.

E-mail: yangliu@nssc.ac.cn

0254-6124/2026/46(4)-0039-08 *Chin. J. Space Sci.* 空间科学学报

CHANG Jin. Recent Progresses of the DAMPE Mission. *Chinese Journal of Space Science*, 2026, **46**(4): 39–46. CSTR:32142.14.cjss.2026–yg14. DOI:10.11728/cjss2026.04.2026–yg14

Recent Progresses of the DAMPE Mission*

CHANG Jin

(*Key Laboratory of Dark Matter and Space Astronomy*, *Purple Mountain Observatory*, *Chinese Academy of Sciences*, *Nanjing* 210033)

(*School of Astronomy and Space Science*, *University of Science and Technology of China*, *Hefei* 230026)

Abstract The Dark Matter Particle Explorer (DAMPE) is a space high-energy particle and γ-ray detector whose major scientific goals are the indirect detection of dark matter particles, the origin of cosmic rays and high-energy γ-ray astronomy. Since its successful launch in December, 2015, the DAMPE has been operated smoothly in orbit for more than 10 years. The precise measurement of the secondary boron spectrum reveals a spectral hardening with a very high significance. The spectra of five primary cosmic-ray nuclei, *i.e.* protons, helium, carbon, oxygen, and iron, are measured to unprecedented high energies, revealing the universal charge-dependent spectral softening for the first time. The energy spectrum of nickel is firstly measured to above TeV/n. The Fermi bubbles and GCE are detected in the γ-ray flux map at very high significances. The DAMPE measurements are expected to significantly advance our understanding of the fundamental problems in astroparticle physics.

Key words DAMPE, Dark matter, Cosmic rays, γ-ray

Classified index P35

1 Introduction

It is now well established from precision cosmological observations that the Universe is composed of approximately 4.9% baryonic matter, 26.8% Dark Matter (DM), and 68.3% dark energy[1]. Uncovering the physical nature of dark matter remains one of the most fundamental questions in modern physics. Since the discovery of the existence of DM, many types of new candidate models have been proposed by the theoretical physicists. Among them, Weakly Interacting Massive Particles (WIMPs) represent one hypothesized class of particles beyond the Standard Model of particle physics, strongly motivated by the relic abundance of dark matter and the bottom-up evolution of the large-scale structures of the Universe[2,3]. Extensive experimental efforts have been devoted to searching for WIMPs, including direct detection of WIMP-nucleon scattering with underground detectors, indirect detection of annihilation or decay products in cosmic radiation, and searches for WIMP pair production at high-energy particle colliders[4]. Despite several decades of dedicated investigation, no conclusive evidence has yet been obtained. Particularly, the direct detection experiments push the WIMP-nucleon scattering strength to a very low level[5], which has already severely constrained a series of WIMP models.

It is noteworthy that some unexpected anomalies have been revealed in recent Cosmic Ray (CR) and γ-ray observations, such as the cosmic-ray positron flux excess discovered by PAMELA[6], Fermi-LAT[7], and AMS-02[8], and the associated total Cosmic Ray Electron plus positron (CRE) flux excess detected by

* Supported by the National Natural Science Foundation of China (12588101) and the Strategic Priority Program on Space Science of CAS (E02212A02S)

Received May 15, 2026

ATIC[9], Fermi-LAT[10], AMS-02[11], DAMPE[12] and CALET[13]. Those observed positrons and CRE flux excesses can be explained either by astrophysical sources such as pulsars or by DM annihilation or decay[14–18]. However, current observational data are limited by detection precision and energy range, making it impossible to identify the physical origin. Higher precision measurements in a wider energy band are thus crucial to draw a definitive conclusion. Other anomalies in high-energy observations, include the γ-ray excess in the Galactic center[19], and potential excess of CR antiprotons[20,21], are also related to the indirect detection of DM.

The Dark Matter Particle Explorer (DAMPE) mission is designed to search for potential annihilation or decay signatures of DM in high-energy CREs and γ-rays, benefiting from unprecedentedly high energy resolution and strong background rejection power[22–24]. Beyond this primary goal, DAMPE serves as a general-purpose high-energy particle detector for observations of CR nuclei and γ-rays, making it particularly valuable for studying high-energy astrophysical phenomena and CR physics[23]. Since launched into a 500 km Sun synchronous orbit on 17 December 2015, the DAMPE satellite has kept an excellent performance and operated stably in space for more than 10 years. The daily event rate of DAMPE is about 5 million, and it has recorded in total over 18 billion CR events as of May 2026, most of which are CR nuclei.

2 Detector and On-orbit Performance

The DAMPE instrument consists of four sub-detectors[23], which are, the Plastic Scintillator strip Detector (PSD[25]), the Silicon-Tungsten tracKer-converter (STK[26]), the $Bi_4Ge_3O_{12}$ (BGO) imaging calorimeter[27], and the NeUtron Detector (NUD[28]), as shown in Figure 1. The PSD, composed of 82 organic plastic scintillators arranged in double layers, is to measure the electric charge of incident particles from protons (Z=1) up to heavy nuclei (Z>30) *via* the ionization effect. It also provides charged-particle background rejection for the γ-ray observation. The STK, composed of 12 silicon strip layers, is to measure the trajectories of incident particles with a very high angular resolution. It can also measure

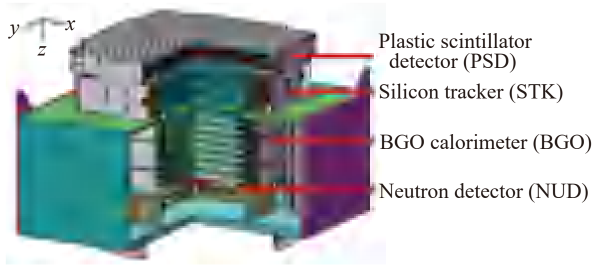

Fig. 1 Schematic plot of the DAMPE detector [23]

the charge of light nuclei (Z<8). The BGO calorimeter, composed of about 32 radiation lengths of BGO scintillation crystals arranged hodoscopically in 14 layers, is to precisely measure the energy deposition and distinguish between electromagnetic and hadronic particles by imaging the 3D profile of the shower development. The NUD at the bottom is to provide additional electron/hadron discrimination by measuring the secondary neutrons mainly produced in hadronic showers rather than in electromagnetic ones.

Dedicated calibration of each unit of the detector has been done using the on-orbit data [29], which enables precise measurements of the physical quantities of each event. The charge resolution of the PSD is about 0.20e (e represents the electron charge) for Z=8 (Oxygen) and 0.30e for Z=26 (Iron) [30]. Such a good charge resolution is the basis of precise spectral measurements of each species. The angular resolution of the STK is well calibrated using the bright γ-ray sources, which is better than 0.2° for energies higher than 10 GeV [31].

The considerable thickness of BGO calorimeter, *i.e.* 32 radiation lengths, ensures that the electromagnetic showers can be well contained without significant energy leakage from the bottom, even at energies up to the TeV scale. The comparisons of beam test data and MC simulations verify that the energy resolution for CREs of DAMPE is better than 1.2% for energies above 100 GeV [32].

3 Scientific Results

Figure 2 shows the separate CR electron and positron spectra and the positron fraction in the energy range from 10 to 20 GeV measured with the geomagnetic field on DAMPE[33]. As the DAMPE detector does not carry an onboard magnet, the geomagnetic field is used to dis-

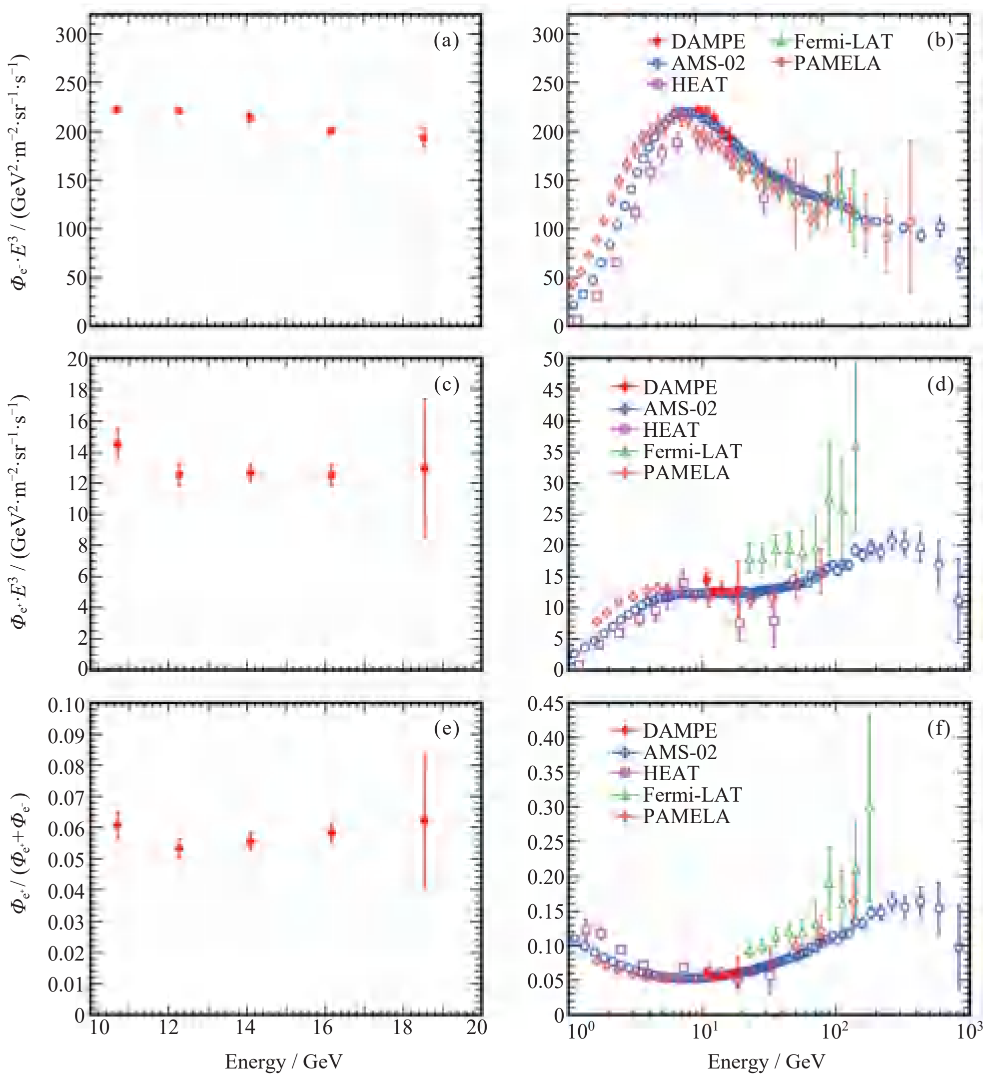

Fig. 2 CR electron spectrum (a), positron spectrum (c) and positron ratios (e) measured by DAMPE. Previous measurements from other experiments are presented for comparisons in (b)(d)(f)

tinguish CR electrons and positrons based on their opposite deflections. The effective energy range of this method is currently limited at high energy by the zenith-pointing orientation of DAMPE. The DAMPE results in the energy range from 10 to 20 GeV are consistent with previous measurements by AMS-02 and PAMELA. In addition, by employing a similar geomagnetic separation technique as that used by the Fermi collaboration, this analysis helps fill the gap in the lower energy region that is not covered by Fermi-LAT.

Figure 3 shows the direct measurement of the secondary CR boron spectrum from 10 GeV/n to 8 TeV/n with 8 years of data collected by DAMPE, with high statistics and well controlled systematic uncertainties[34]. Boron nuclei in cosmic rays are believed to be mainly produced by the fragmentation of heavier nuclei, such as carbon and oxygen, *via* collisions with the interstellar matter. Therefore, the precise measurement of the boron spectrum is an essential probe to study CR propagation. The measured spectrum shows a hardening at 182±24 GeV/n with a spectral index of –3.02±0.01 before the break and an index change of 0.31±0.05 after the break. A simple power law model is disfavored at a confidence level of 8σ.

For the first time, a spectral hardening is directly observed for the secondary CR nuclei. The spectral index change of 0.31±0.05 suggests that secondary boron hardens about twice as much as primaries such as pro-

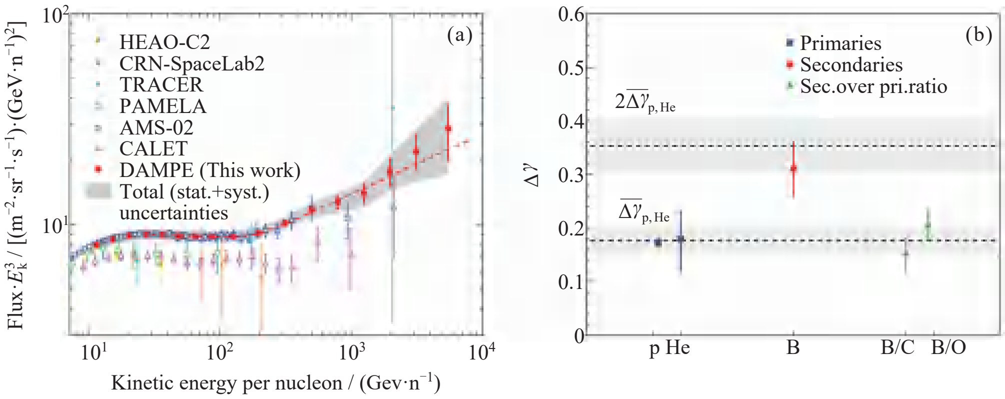

Fig. 3 CR boron spectrum as a function of kinetic energy per nucleon measured by DAMPE[34] (red filled dots), compared with measurements from other experiments (a), and the spectral index change values of the hardening in the spectra of proton, helium, B/C, B/O, and boron measured with DAMPE[34] (b)

ton and helium as previously measured by DAMPE [35,36], as shown in Figure 3(b). The result is also consistent with the hardenings in boron-to-carbon and boron-to-oxygen flux ratios[37], for case that carbon and oxygen show similar hardenings with protons and helium. Such an observational fact supports a propagation related mechanism to interpret the spectral hardenings of cosmic rays observed at hundreds of GeV/n. With the data accumulation of DAMPE, improved measurement of the boron spectrum with higher statistics and lower systematics is expected to extend to above 10 TeV/n in the future.

Figure 4 show the spectra of CR proton, helium, carbon, oxygen and iron measured with 9 years of on-orbit data collected by DAMPE [38]. For the first time, distinct spectral softenings are directly detected in the spectra of carbon, oxygen and iron. The significance of the softening is 3.2σ, 4.1σ and 2.4σ with the break rigidity of 16.1±5.6 TV, 15.4±4.8 TV and 13.8±6.0 TV for carbon, oxygen and iron, respectively. The updated proton and helium spectra yield softening rigidity at 14.6±1.3 TV and 15.3±2.3 TV, respectively. It has been established that the softenings occur at the same rigidity of about 15 TVs for all the five species, and the nuclei-mass-dependent softening is rejected at a confidence level of >99.999% (4.4σ), as shown in Figure 5. The universal softening feature in the spectra of primary CRs from protons (Z=1) to iron nuclei (Z=26) and the charge dependence of the softening energy indicate a common origin of the break due to acceleration.

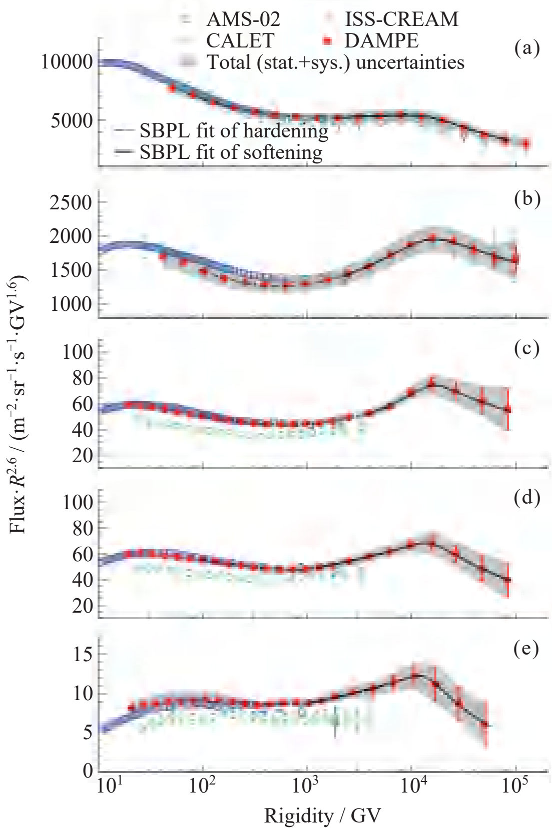

Fig. 4 Spectra of protons (a), helium (b), carbon (c), oxygen (d) and iron (e) measured by DAMPE (red filled dots) [38], compared with measurements from other experiments

Combined with large-scale anisotropy measurements, the results indicate a nearby CR accelerator, with the universal spectral softening marking its charge-dependent energy upper limit. The DAMPE observation provides the first direct experimental verification for the charge-dependent acceleration model first proposed in the 1960 s[39], offering a key clue toward solving the longstanding mystery of CR origin.

Figure 6 shows the CR nickel spectrum from 10 GeV/n to 2 TeV/n measured with 9 years of on-orbit data collected by DAMPE[40]. Nickel is the most abundant heavy element beyond iron in CRs. With DAMPE's excellent charge resolution and broad energy range, the accurate measurement of CR nickel spectrum is directly extending to TeV/n for the first time. The nickel spectrum is consistent with a single power law with spectral index −2.60±0.03 from 40 GeV/n to 1 TeV/n. In addition, the energy dependence of the nickel to iron flux ratio (Ni/Fe) is well described by a constant fit, which is structurally consistent with previous CALET measurements[41] in the same energy range. The constant Ni/Fe abundance ratio in CRs further indicates the similar origin, acceleration and propagation mechanism for both elements. The accumulating experimental data of DAMPE would facilitate more precision measurements of nickel extending to higher energy in the future.

Figure 7 shows the detection of Fermi bubbles by DAMPE and the measurement of spectral energy distribution (SED)[42]. With the 102 months of data collected by DAMPE, the Fermi bubbles are detected at a significance of ~26σ from the observed γ-ray flux map above 2 GeV. The SED values measured by DAMPE are consistent with the results from Fermi-LAT[43]. By the comparison of the fitting with Power-Law (PL) and Power-Law Cutoff (PLEC) models, a cutoff at ~200 GeV is detected with a significance of 3σ. The SED values of the northern and southern lobes are also measured separately and they are in excellent agreement, supporting the identical physical origin of the two lobes.

Figure 8 show the spectral measurement of the

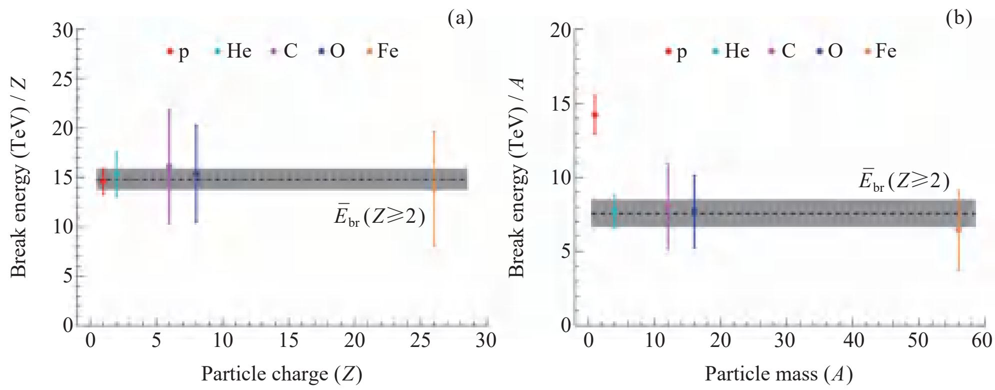

Fig. 5 Break energies for different species divided by particle charge Z (a) and particle mass A (b) [38]

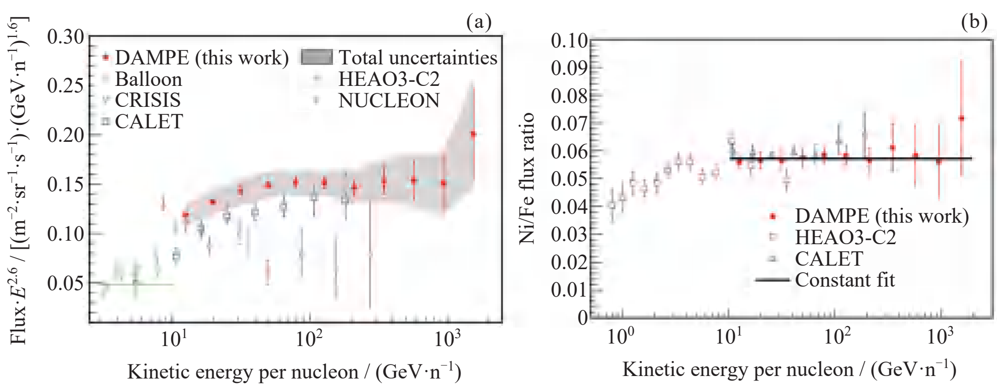

Fig. 6 CR nickel energy spectrum as a function of kinetic energy per nucleon measured by DAMPE[40] (red filled dots), compared with measurements from other experiments (a), and the nickel to iron flux ratios measured by DAMPE (red filled dots) fit with a constant function (black line)[40] (b)

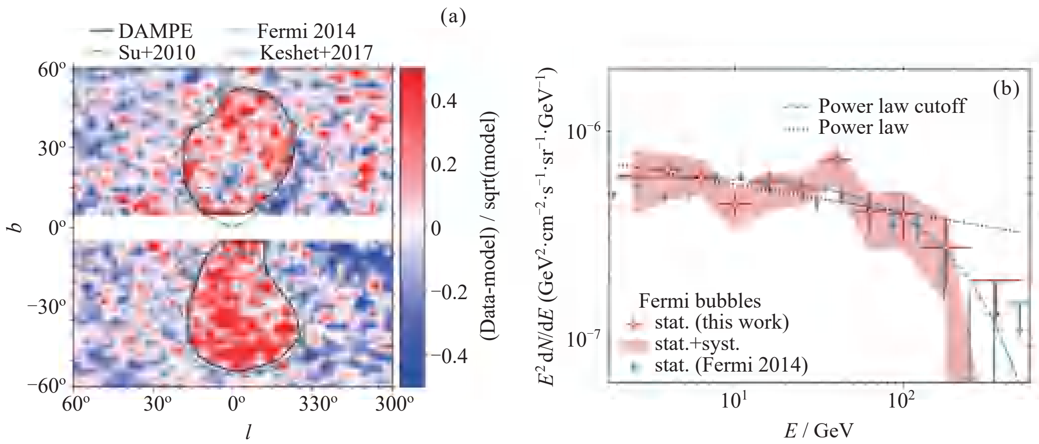

Fig. 7 Significance of the residual maps for the model without Fermi bubbles[42] (a) and the SED of the Fermi bubbles measured by DAMPE[42] (red points) compared the results from Fermi-LAT[43] (b)

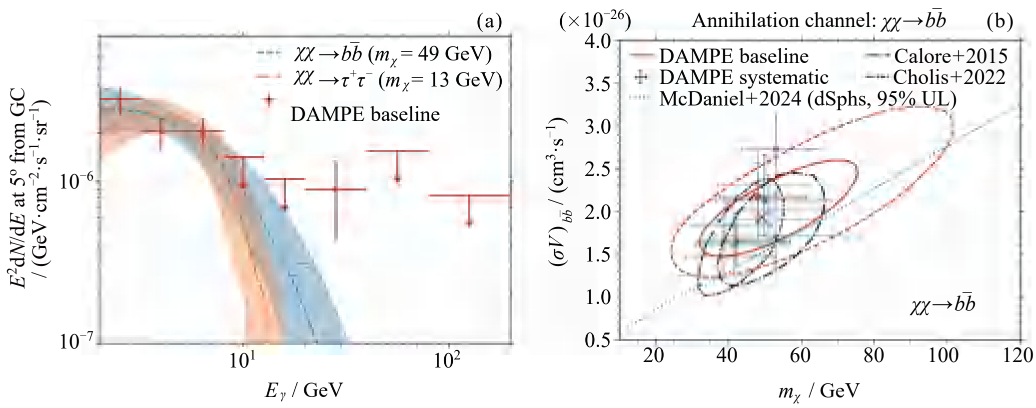

Fig. 8 Spectral measurement of the GCE by DAMPE (a) and the prefered DM parameter space for the annihilation channel $\chi\chi\to b\bar{b}$ (b)[42]

Galactic center excess (GCE) by DAMPE and the preferred DM parameter space for the annihilation channel $\chi\chi \to b\bar{b}$ [42]. With the 102 months of data collected by DAMPE, the GCE is detected with a TS value of 80.1, which corresponds to a significance of 7.5σ with 8° of freedom. The If the excess is explained with the DM annihilation into $b\bar{b}$, DM particles with mass $m_\chi = 49^{+16}_{-12}$ GeV and cross section $\langle\sigma\nu\rangle = \left(1.9^{+0.4}_{-0.3}\right) \times 10^{-26}$ $\mathrm{cm}^3 \cdot \mathrm{s}^{-1}$ is required. The DM parameter space is consistent with the Fermi-LAT[44].

4 Summary

DAMPE has been operating smoothly in orbit for more than eight years. Based on the accumulated high-quality data recorded by DAMPE, multiple latest scientific results have been obtained, regarding CR physics and γ-ray astronomy. The precise measurement of the secondary boron spectrum reveals a spectral hardening with a very high significance, which provides important implications in understanding the CR propagation. The latest measurements of the spectra of five primary cosmic-ray nuclei, *i.e.* protons, helium, carbon, oxygen, and iron, provide the first direct experimental verification for the charge-dependent acceleration model. The energy spectrum of nickel is firstly measured to above TeV/n and a constant Ni/Fe ratio is observed. The Fermi bubbles and GCE are detected at very high significances, providing the first independent detection of these two intriguing diffuse γ-ray sources besides Fermi-LAT. In the near future, more scientific progresses from DAMPE are expected to shed new light on our understandings about

DM, CR origin and the high-energy Universe.

Acknowledgements The DAMPE mission was funded by the strategic priority science and technology projects in space science of the Chinese Academy of Sciences.

References

[1] ADE P A R, AGHANIM N, ARNAUD M, *et al*. Planck 2015 results. XIII. Cosmological parameters[J]. *Astronomy & Astrophysics*, 2016, **594**: A13

[2] JUNGMAN G, KAMIONKOWSKI M, GRIEST K. Supersymmetric dark matter[J]. *Physics Reptorts*, 1996, **267**(5/6): 195-373

[3] BERTONE G, HOOPER D, SILK J. Particle dark matter: evidence, candidates and constraints[J]. *Physics Reptorts*, 2005, **405**(5/6): 279-390

[4] BI X J, YIN P F, YUAN Q. Status of dark matter detection[J]. *Frontiers of Physics*, 2013, **8**(6): 794-827

[5] ZHAO L, LIU J L. Experimental search for dark matter in China[J]. *Frontiers of Physics*, 2020, **15**(4): 44301

[6] ADRIANI O, BARBARINO G C, BAZILEVSKAYA G A, *et al*. An anomalous positron abundance in cosmic rays with energies 1.5-100 GeV[J]. *Nature*, 2009, **458**(7238): 607-609

[7] ACKERMANN M, AJELLO M, ALLAFORT A, *et al*. Measurement of separate cosmic-ray electron and positron spectra with the Fermi large area telescope[J]. *Physical Review Letters*, 2012, **108**(1): 011103

[8] AGUILAR M, ALBERTI G, ALPAT B, *et al*. First result from the alpha magnetic spectrometer on the international space station: Precision measurement of the positron fraction in primary cosmic rays of 0.5-350 GeV[J]. *Physical Review Letters*, 2013, **110**(14): 141102

[9] CHANG J, ADAMS J H, AHN H S, *et al*. An excess of cosmic ray electrons at energies of 300-800 GeV[J]. *Nature*, 2008, **456**(7220): 362-365

[10] ABDO A A, ACKERMANN M, AJELLO M, *et al*. Measurement of the cosmic ray $e^{+}+e^{-}$ spectrum from 20 GeV to 1 TeV with the Fermi large area telescope[J]. *Physical Review Letters*, 2009, **102**(18): 181101

[11] AGUILAR M, AISA D, ALPAT B, *et al*. (AMS collaboration). Precision measurement of the $(e^{+}+e^{-})$ flux in primary cosmic rays from 0.5 GeV to 1 TeV with the alpha magnetic spectrometer on the international space station[J]. *Physical Review Letters*, 2014, **113**(22): 221102

[12] AMBROSI G, AN Q, ASFANDIYAROV R, *et al*. Direct detection of a break in the teraelectronvolt cosmic-ray spectrum of electrons and positrons[J]. *Nature*, 2017, **552**(7683): 63-66

[13] ADRIANI O, AKAIKE Y, ASANO K, *et al*. Direct measurement of the spectral structure of cosmic-ray electrons + positrons in the TeV region with CALET on the international space station[J]. *Physical Review Letters*, 2023, **131**(19): 191001

[14] SHEN C S. Pulsars and very high-energy cosmic-ray electrons[J]. *The Astrophysical Journal*, 1970, **162**: L181

[15] HOOPER D, BLASI P, SERPICO P D. Pulsars as the sources of high energy cosmic ray positrons[J]. *Journal of Cosmology and Astroparticle Physics*, 2009, **2009**(1): 025

[16] YÜKSEL H, KISTLER M D, STANEV T. TeV gamma rays from Geminga and the origin of the GeV positron excess[J]. *Physical Review Letters*, 2009, **103**(5): 051101

[17] CIRELLI M, KADASTIK M, RAIDAL M, *et al*. Model-independent implications of the $e^{\pm}$, $\bar{p}$ cosmic ray spectra on properties of dark matter[J]. *Nuclear Physics B*, 2009, **813**(1/2): 1-21

[18] YIN P F, YUAN Q, LIU J, *et al*. PAMELA data and leptonically decaying dark matter[J]. *Physical Review D*, 2009, **79**(2): 023512

[19] HOOPER D, GOODENOUGH L. Dark matter annihilation in the Galactic Center as seen by the Fermi Gamma Ray Space Telescope[J]. *Physics Letters B*, 2011, **697**(5): 412-428

[20] CUI M Y, YUAN Q, TSAI Y L S, *et al*. Possible dark matter annihilation signal in the AMS-02 antiproton data[J]. *Physical Review Letters*, 2017, **118**(19): 191101

[21] CUOCO A, KRÄMER M, KORSMEIER M. Novel dark matter constraints from antiprotons in light of AMS-02[J]. *Physical Review Letters*, 2017, **118**(19): 191102

[22] CHANG J. Dark matter particle explorer: The first Chinese cosmic ray and hard γ-ray detector in space[J]. *Chinese Journal of Space Science*, 2014, **34**(5): 550-557

[23] CHANG J, AMBROSI G, AN Q, *et al*. The dark matter particle explorer mission[J]. *Astroparticle Physics*, 2017, **95**: 6-24

[24] YU Y H, SUN Z Y, SU H, *et al*. The plastic scintillator detector for DAMPE[J]. *Astroparticle Physics*, 2017, **94**: 1-10

[25] AZZARELLO P, AMBROSI G, ASFANDIYAROV R, *et al*. The DAMPE silicon-tungsten tracker[J]. *Nuclear Instruments and Methods in Physics Research Section A*: *Accelerators, Spectrometers, Detectors and Associated Equipment*, 2016, **831**: 378-384

[26] ZHANG Z Y, ZHANG Y L, DONG J N, *et al*. Design of a high dynamic range photomultiplier base board for the BGO ECAL of DAMPE[J]. *Nuclear Instruments and Methods in Physics Research Section A*: *Accelerators, Spectrometers, Detectors and Associated Equipment*, 2015, **780**: 21-26

[27] HE M, MA T, CHANG J, *et al*. GEANT4 simulation of neutron detector for DAMPE[J]. *Chinese Astronomy and Astrophysics*, 2016, **40**(4): 474-482

[28] AMBROSI G, AN Q, ASFANDIYAROV R, *et al*. The on-orbit calibration of dark matter particle explorer[J]. *Astroparticle Physics*, 2019, **106**: 18-34

[29] DONG T K, ZHANG Y P, MA P X, *et al*. Charge measurement of cosmic ray nuclei with the plastic scintillator detector of DAMPE[J]. *Astroparticle Physics*, 2019, **105**: 31-36

[30] DUAN K K, SHEN Z Q, XU Z L, *et al*. PSF calibration of DAMPE for gamma-ray observations[J]. *Astroparticle Physics*, 2025, **165**: 103058

[31] YUE C, ZANG J J, DONG T K, *et al*. A parameterized energy correction method for electromagnetic showers in BGO-ECAL of DAMPE[J]. *Nuclear Instruments and Methods in Physics Research Section A*: *Accelerators, Spectrometers, Detectors and

Associated Equipment, 2017, **856**: 11-16

[32] ALEMANNO F, AN Q, AZZARELLO P, *et al*. Measurement of separate electron and positron spectra from 10 to 20 GeV with the geomagnetic field on DAMPE[J]. *Chinese Physics C*, 2025, **49**(11): 115001

[33] ALEMANNO F, ALTOMARE C, AN Q, *et al*. Observation of a spectral hardening in cosmic ray boron spectrum with the DAMPE space mission[J]. *Physical Review Letters*, 2025, **134**(19): 191001

[34] AN Q, ASFANDIYAROV R, AZZARELLO P, *et al*. Measurement of the cosmic ray proton spectrum from 40 GeV to 100 TeV with the DAMPE satellite[J]. *Science Advances*, 2019, **5**(9): eaax3793

[35] ALEMANNO F, AN Q, AZZARELLO P, *et al*. Measurement of the cosmic ray helium energy spectrum from 70 GeV to 80 TeV with the DAMPE space mission[J]. *Physical Review Letters*, 2021, **126**(20): 201102

[36] ALTOMARE C, AN Q, AZZARELLO P, *et al*. Detection of spectral hardenings in cosmic-ray boron-to-carbon and boron-to-oxygen flux ratios with DAMPE[J]. *Science Bulletin*, 2022, **67**(21): 2162-2166

[37] ALEMANNO F, AN Q, AZZARELLO P, *et al*. Charge-dependent spectral softenings of primary cosmic rays below the knee[J]. *Nature*, 2026, **653**(8113): 52-55

[38] PETERS B. Primary cosmic radiation and extensive air showers[J]. *Il Nuovo Cimento (1955-1965)*, 1961, **122**(4): 800-819

[39] ALEMANNO F, AN Q, AZZARELLO, *et al*. Measurement of the cosmic ray nickel energy spectrum from 10 GeV/n to 2 TeV/n with the DAMPE space mission[OL]. arXiv preprint arXiv: 2512. 11425 , 2026

[40] ADRIANI O, AKAIKE Y, ASANO K, *et al*. Precision spectral measurements of chromium and titanium from 10 to 250 GeV/*n* and sub-iron to iron ratio with the calorimetric electron telescope on the international space station[J]. *Physical Review Letters*, 2025, **135**(2): 021002

[41] ALEMANNO F, AN Q, AZZARELLO P, *et al*. Observations of the Fermi bubbles and the galactic center excess with the dark matter particle explorer[J]. *The Astrophysical Journal Supplement Series*, 2026, **284**(1): 22

[42] ACKERMANN M, ALBERT A, ATWOOD W B, *et al*. The spectrum and morphology of the *Fermi* bubbles[J]. *The Astrophysical Journal*, 2014, **793**(1): 64-97

[43] CALORE F, CHOLIS I, WENIGER C. Background model systematics for the Fermi GeV excess[J]. *Journal of Cosmology and Astroparticle Physics*, 2015, **2015**(3): 038

[44] CHOLIS I, ZHONG Y M, MCDERMOTT S D, *et al*. Return of the templates: Revisiting the Galactic Center excess with multimessenger observations[J]. *Physical Review D*, 2022, **105**(10): 103023

Author Biography

CHANG Jin Male, born in 1966, chair scientist of the DArk Matter Particle Explorer (DAMPE, also called as "WuKong") project. He has long been engaged in the space detections and researches of high energy cosmic rays and gamma-rays.
E-mail: chang@pmo.ac.cn

0254-6124/2026/46(4)-0047-11 *Chin. J. Space Sci.* 空间科学学报

ZHANG Shu, ZHANG Shuangnan. Insight-HXMT Research Progress in 2024–2026. *Chinese Journal of Space Science*, 2026, **46**(4): 47–57. CSTR:32142.14.cjss.2026–yg09. DOI:10.11728/cjss2026.04.2026–yg09

Insight-HXMT Research Progress in 2024–2026*

ZHANG Shu ZHANG Shuangnan

(*State Key Laboratory of Particle Astrophysics*, *Institute of High Energy Physics*, *Chinese Academy of Sciences*, *Beijing* 100049)

Abstract Since the launch in 2017 June, Insight-HXMT has been in service smoothly in orbit and its scientific productivity has been particularly high since 2024. Among a total number of 425 papers published so far based on Insight-HXMT data, roughly 150 were published from April 2024 to June 2026, accounting for 35% of the total. These studies cover a variety of scientific subjects, including the basic properties of black holes and neutron stars, the outbursts of accreting black hole and neutron star X-ray binaries, thermal nuclear burst probes, quasi-periodical oscillations, cyclotron resonant scattering features, fast radio bursts and gamma-ray bursts, etc. This paper reviews the overall progress with a focus on some potential breakthroughs.

Key words Insight-HXMT, Black hole, Neutron star, Outburst

Classified index P17

1 Introduction

The Hard X-ray Modulation Telescope (HXMT) is China's first X-ray astronomy satellite and was launched in June 2017, dubbed as Insight-HXMT in honor of the Chinese scientist Prof. He Zehui. There are three slat-collimated instruments onboard Insight-HXMT. For the details of the three telescopes and the mission, please refer to Ref. [1–4].

So far, Insight-HXMT has been operating well, and its scientific outputs have accumulated to more than 400 papers. Discoveries derived during 2017–2024 provided clues for our understandings the neutron star merging by joining the global campaign of observing the historical event of the first event GW 170817[5], the properties of accretion matter (jet, corona and accretion disk) and Quasi Periodic Oscillations (QPO) with a series of discoveries from MAXI J1820+070 and improving a technique of the so-called Hilbert-Huang Transform (HHT)[5–8], the mechanism of Galactic Ultra Luminous Source (ULX) and properties of the magnetic poles by detecting the highest energy of the Cyclotron Resonant Scattering Feature (CRSF) at 146 keV from Swift J0243.6+6124 and four regimes (hence three critical luminosities) in evolution of the CRSF centroid energy against the accretion rate revealed in 1 A0535+262[9–11], and decoding the mysteries of a Fast Radio Burst (FRB) by identifying the first X-ray counterpart of FRBs[12]. See details for the previous progress reports in Ref. [13,14] and the references therein. In this paper, we review the state-of-art results of Insight-HXMT, which are either highly supplementary to those key issues as shown above or new breakthroughs and applications with Insight-HXMT.

2 Black Hole X-ray Binaries

2.1 Swift J1727.8-1613

Swift J1727.8-1613 is a newly discovered black hole X-ray binary system which underwent a huge outburst in

* Supported partially by the National Key R&D Program of China (2021YFA0718500), the National Natural Science Foundation (12333007, 12027803) and International Partnership Program of Chinese Academy of Sciences (113111KYSB20190020

Received May 20, 2026

2023 and was subsequently listed as one of a few samples observed by Insight-HXMT with high cadence. So far, there are 24 papers since 2024 with the data from the observations mainly based on Insight-HXMT. As a comparison, MAXI J1820+070 as Insight-HXMT's previous leading source in the number of publications both in normal and top-tier journals, so far 27 papers have been published with Insight-HXMT data since its huge outburst in 2018. This demonstrates that, Insight-HXMT has increasing impact in the high energy astrophysical society once there is new bright source for which Insight-HXMT will make high cadence observations with the best quality and quantity due to its advantages with wide energy coverage, high time resolution and the largest detection area at hard X-rays. Accordingly, Swift J1727.8-1613 with Insight-HXMT observations turns out to be another good laboratory to our further understanding ofthe basic physical process of accreting black hole X-ray system.

2.1.1 A Variety of Temporal and Spectral Features

In 2023, Swift J1727.8-1613 underwent an outburst with a typical evolution track in the Hardness-Intensity Diagram (HID). An investigation of the energy dependence of RMS of the Low-Frequency Quasiperiodic Oscillation (LFQPO) (*e.g.* type-C QPO) shows a transition at the frequency around 3 Hz: while RMS increases continuously below 3 Hz, it drops at LE band but remains stable at ME and HE bands[15]. Positive correlation between QPO frequency and RMS was seen as well in GRS 1915+105 at frequency below 2 Hz[16], and the low-energy RMS drop at higher frequency is common in BHXRB outbursts. One interpretation could be that, during the initial phase of the outburst, the truncated inner disk moves toward the BH and the Lense-Thirring (L-T) precession strengthens with increasing precessing angle. The low energy QPO RMS may drop with more disk contribution, along with outburst evolving to the soft intermediate state. For probing the possible origin of QPO, an interesting trial of performing the bicoherence analysis indicates that the type-C QPO is coupled with noise rather than generated independently[17].

The RMS spectrum of the type-C QPO evolves with outburst in a manner significantly different from other BHXRBs: the RMS spectrum has an obvious excess at energies above 40 keV and evolves gradually to a flatter one typical to the usual RMS spectral shape at high energies[18] (see Figure 1). Together with the spectral analysis reported by Peng *et al*.[19] that a strong power component shows up apart from the corona component; this peculiar RMS spectrum suggests again that the additional hard component comes from jet emission.

Xu *et al*.[20] found a rare anticorrelation between the unscattered disk emission and the QPO frequency at the early outburst phase when the QPO frequency is below 3 Hz, which may indicate the coupling between the inner hot flow and the inner disk. They proposed a possible scenario that the truncated inner disk can penetrate the corona, thus leading to a larger covering fraction of the corona and hence the decreasing unscattered disk emission (see Figure 2).

Ma *et al*.[21] tested the L-T procession origin of QPO by fitting the broadband energy spectrum with SSSED model, and found that the estimated truncated inner disk radius decreases from 45 R_g to 9 R_g. However, with this evolution of radius, the QPO frequency is systematically higher than the L-T prediction by a factor of a few, if assuming that the QPO originates from the L-T precession of the hot inner flow.

Diagnostics with cross and biphase spectrum, Bollemeijer *et al*.[22] investigated the QPO waveforms for both the fundamental and harmonic. They found that the phase lag between the fundamental and second harmonic QPO is highly energy dependent: the waveform changes to almost opposite at energies above 15–20 keV. Also, the time lag of the harmonic QPO extends to a broader frequency range and may be related to

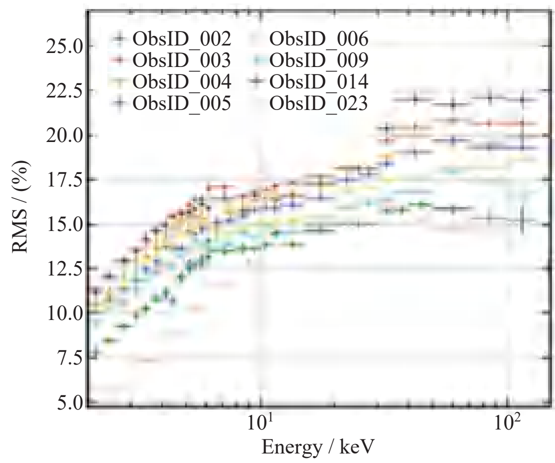

Fig. 1 Evolution of QPO RMS spectrum observed by Insight-HXMT during outburst of Swift J1727.8-1613 [18]

the broad band noise variabilities.

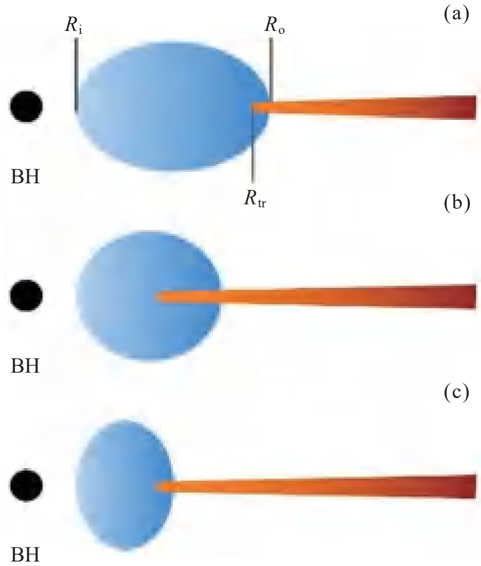

Fig. 2 Disk-corona connection introduced to explain the observed QPO frequency evolution[20]

2.1.2 Geometry of the Accretion Flow Revealed by HHT Technique

The most powerful diagnostics of the inner accretion flow were performed with HHT analysis[23]. The QPO phase-resolved spectra reveal that both thermal and non-thermal components of the spectrum exhibit strong variations along with the QPO phases. The spectral parameters of the disk temperature, spectral indices and reflection fraction modulate with QPO phases with significances above 5 sigma (see Figure 3). Notably, the variation of the disk temperature precedes the variations of the disk flux and normalization by 0.4–0.5 QPO cycles. Two nonthermal components have different QPO modulations: while the spectral index follows the QPO waveform which resembles that found in MAXI J1820+070[8] for one component, it shows the opposite modulation with respect to the QPO waveform for the other component. This clearly demonstrates the co-existence for precession of both hot corona and jet.

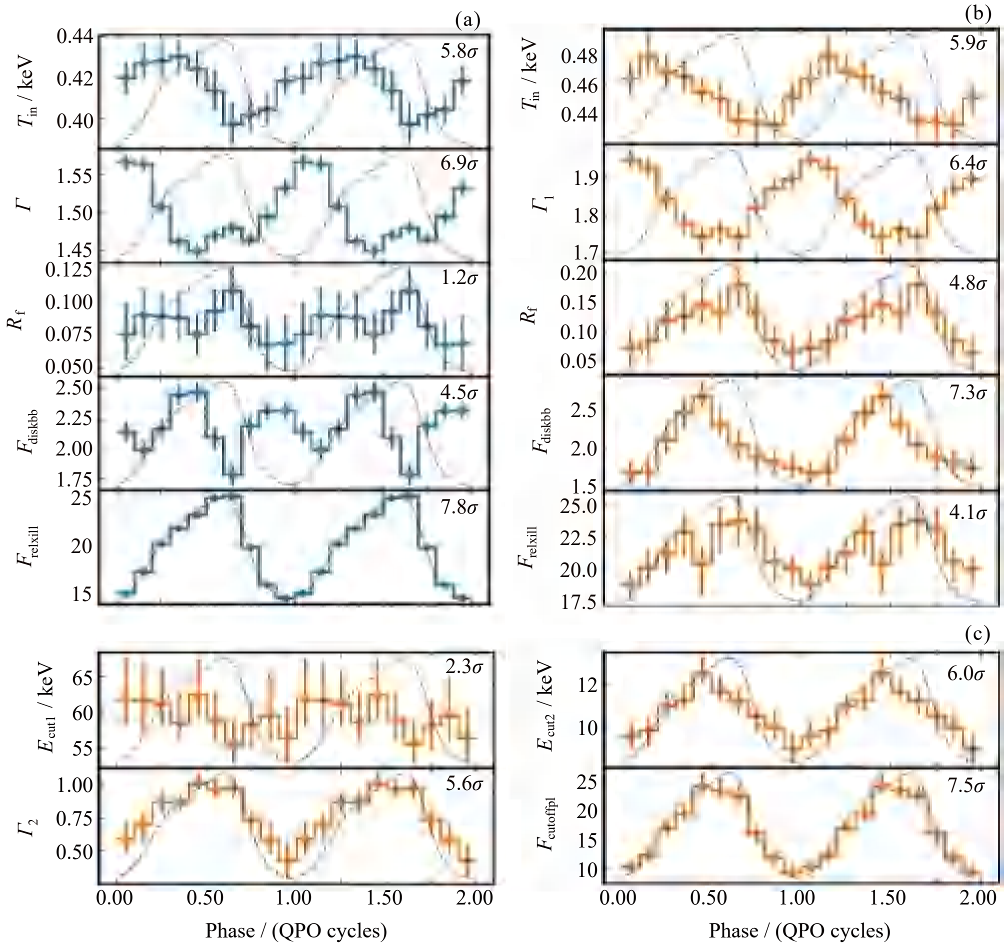

Fig. 3 Spectral parameters modulation with QPO phases derived with HHT [23]

2.1.3 New World Record of the Highest Energy of QPO

With a novel HHT-based QPO searching technique[24], significant QPO signals (above 5 sigma) at energies above 250 keV are detected by either NaI or CsI of HE[25]. At energies around 300 keV, QPO was detected with a significance level of 3 sigma. The previous QPO's highest energy was also from Insight-HXMT observations, but instead from MAXI J1820+070[6], which reached only above 200 keV.

2.1.4 A Scenario Tailored for a Series of Rare Flares

Swift J1727.8-1613 underwent a series of flares when the source started to enter the soft state. The properties of these flares were investigated in details by Cao *et al.*[26], where they found that the source stepped into very high state during the first flare, characterized by fast enhanced disk emission, a steep power law component, and weak reflection. These features can be understood in a scenario where during the flares, the jet is accelerated and hot inner flow contributed weak reflection (see Figure 4).

2.2 Other Sources

The excellent Insight-HXMT data on MAXI J1820+070 collected during the initial Insight-HXT phase keep bringing us more exciting discoveries and Insight-HXMT observations on some peculiar BHXRB outbursts shed light on understanding the evolution between different spectral states.

2.2.1 New Landscape for Shaping the Broadband Noise

Yang *et al.*[27] carried out the covariance spectrum of MAXI J1820+070 and investigated the nature of the inner accretion flow. There, they found that for both the long- and short-timescales the coherence at hard X-ray decreases with respect to the soft X-rays, while the electron temperature associated with the long-time variability is generally larger than that with the short-time variability. Accordingly, they introduced a two-Comptonization framework to make a possible interpretation. Interestingly, the broadband noise studied by Gao *et al.*[28] based on the same outburst revealed that, during the outburst evolution, the characteristic frequency of the low/high-frequency broad band noise decreases/increases against the increasing photon energy (see Figure 5). Both results require the corona to have an inhomogeneous temperature distribution and probably the inner hot corona responds less efficiently to the disk variability due the block of the outer cooler corona located in between.

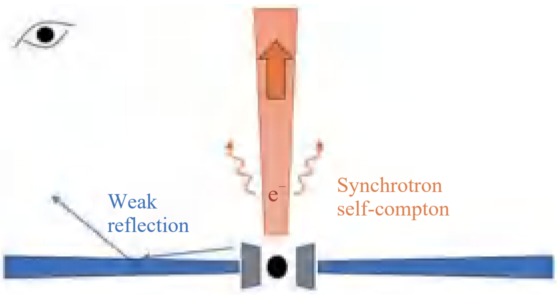

Fig. 4 A jet-disk-corona scenario introduced to match the flare properties observed in Swift J1727.8-1613 [26]

2.2.2 Unified Disk-corona Configuration Across Huge BH Mass Range

Constrained by the limited detection area of the previous hard X-ray telescopes and the extremely short time scale of the time lags caused by coronal X-rays reflecting off the disk, previous measurements of reverberation lags for stellar-mass BHs are limited to energies below 10 keV. A breakthrough was made by You *et al.*[29] by detecting for the first time the Compton hump reverberation, peaking at about 30 keV, from the X-ray binary MAXI J1820+050 as observed by Insight-HXMT. The accompanying detection of an iron line feature at about 6.4 keV confirms the X-ray reverberation scenario and provides strong evidence that accretion flows in AGNs and X-ray binaries are governed by a ubiquitous process.

2.2.3 Condition for Disk Transition to Slim One

Peng *et al.*[30] made a spectral analysis of the outbursts of 4 U 1630-472 observed by Insight-HXMT in 2022 and 2023. They found that the disk temperature - flux relation is roughly consistent with that of a standard disk by taking the hardening factor into account. With the p-free model, although the standard disk cannot be excluded, the evolution of decreasing p with disk temperature is visible. These findings may suggest that the previously reported apparently standard regime may not be fully relevant to a slim disk but instead implies an evolution toward a slim disk. The formation of a slim disk may be influenced, apart from the accretion rate, as well by the disk/corona properties (*e.g.*, nonthermal fraction) in the

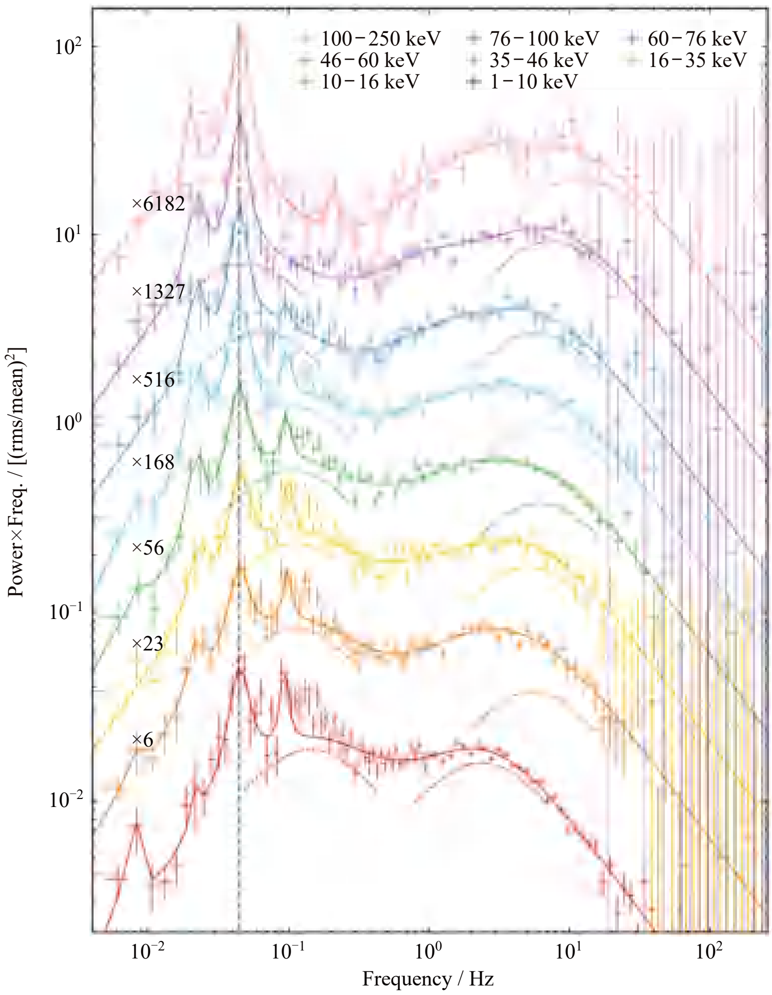

Fig. 5 Simultaneous PDS in different energy bands obtained from the Insight-HXMT observation carried out during 27 March 2018 [27]

HSS. A slim disk may be less likely to form with the presence of the dominant nonthermal emission in the HSS. The existence of a hot corona may help to ionize the outer part of the disk in the vertical direction and hence hinder the formation of a slim disk by reducing the optical depth (see Figure 6).

3 Neutron Star X-ray Binaries

Insight-HXMT archival data of the high-cadence observations of two bright sources, Swift J0243.6+6124 and 1 A 0535+262, have enabled more than 20 publications, and additional interesting results derived in the last two years are introduced in what follows.

3.1 Rapid Quasi-periodic Reconfiguration of the Accretion Column

CRSF is a probe of the emission site of the accretion column of the accretion neutron star system and long-term CRSF-luminosity correlations reflect changes in column geometry driven by variations in the mass accretion rate. So far, it remains a puzzle for CRSF properties on a short time scale of such as a few seconds. Kong *et al.*[31] found that, during a giant outburst of the X-ray pulsar 1 A 0535+262, X-ray QPO is accompanied by synchronized oscillations of the cyclotron line energy, with amplitudes exceeding those expected from simple accretion-rate fluctuations. The anti-correlation between cyclotron energy and apparent flux provides direct spectral-timing evidence for rapid changes in the line-forming region, which is interpreted as a geometric reconfiguration of the accretion column. The CRSF modulation therefore reflects an intrinsic, dynamical reconfiguration of the accretion column geometry on timescales of tens

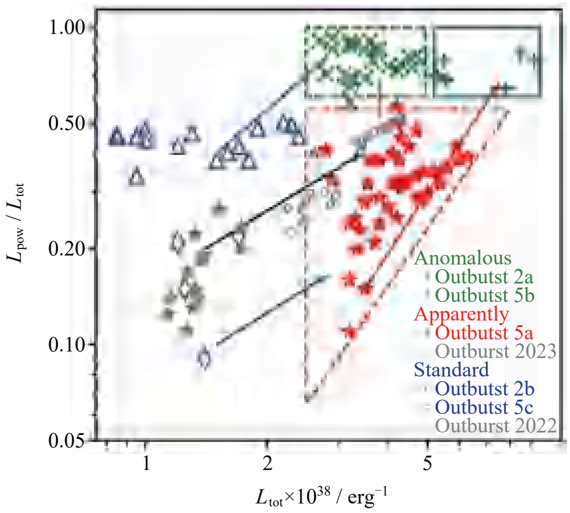

Fig. 6 Evolution of the luminosity ratio of the nonthermal to the total luminosity against the total luminosity for different outbursts from 4 U 1630-472[30]

of seconds, linking the emergence of high-energy QPOs to the formation of a radiation-supported column with rapid geometric restructuring.

3.2 Hunting the Highest Energy of Pulsation from PULX

Pulsating Ultraluminous X-ray (PULX) sources are generally thought to have its apparent high luminosity relevant to relativistic or geometric beaming effect. The discovery of > 130 keV pulsation from PULX RX J0209.6-7427[32] reveals that the emission should be in fan mode but not pencil beaming. The breakthrough of measuring the highest energy of 146 keV CRSF from the Galactic PULX Swift J0243.6+6124[10] provides the first evidence that the high luminosity is accompanied with the real super-Eddington accretion. Here, with a novel pulse-profile-correlation technique, the highest energy of pulsation observed by Insight-HXMT in the outburst of Swift J0243.6+6124 is found to have positive correlation with accretion rate, with the highest one reaching around 200 keV, which is the new world record in accretion pulsar systems and serves as additional evidence that PULXs have non-beaming emission[33].

3.3 Diagnostic of the Radiation Regime of PULX at Low Luminosity

The discovery of the 146 keV CRSF and no propeller effect during outburst tail suggests that the PULX Swift J0243.6+6124 holds a NS with multiple-B structure. However, consolidation of this scenario needs more detailed exploration of the source properties at low-luminosity periods. Chen *et al.*[34] performed a detailed spectral analysis of Swift J0243.6+6124 in its sub-Eddington regime, with observations from Insight-HXMT and NICER during a series of outbursts, and found a new transition at $L_t \sim 4.5 \times 10^{37}$ erg·s^{-1}, which is the fifth transition luminosity identified so far, accompanied by significant turnover of the blackbody normalization. They proposed a scenario by introducing a multipolar magnetic field configuration, where weak (~2.8×10^{12} G) and strong (~1.6×10^{13} G) magnetic poles govern the emission at different accretion rates. Such a magnetic field configuration is equivalent to a relatively weak pure dipole magnetic field of ~6.6×10^{12} G on the scale of the magnetospheric radius, and allows the local magnetic field of the neutron star to exceed 10^{13} G (see Figure 7).

3.4 Diagnostic of the Accretion with Type-I Burst Probe

Type-I bursts are the thermal nuclear burning on the surface of a neutron star, and the interactions of the soft X-ray shower with the surrounding environment leave the footprint of either the enhancement of the disk emission due to the Poynting–Robertson (PR) dragging or the shortage of the hard X-ray emission due to the corona cooling. Accordingly, the frontier researches are led by different international groups. For example, the latter is led by the Insight-HXMT team due to Insight-HXMT's large detection area at hard X-rays. Previous researches show large difference for the hard X-ray shortage induced by type-I bursts: almost 100% hard X-ray shortage observable for the atoll source[35], while only roughly shortage visible for the millisecond accretion pulsar[36]. This implies that the non-cooling part comes from the accretion site of the magnetic pole where the hard X-ray pulsation originates, while for atoll sources, the hard X-rays are mainly contributed by the corona and hence are short of the emission from the sites around magnetic poles. The type-I burst influence upon the polar cap of the millisecond pulsar MAXI J18160195 is investigated by Ji *et al.*[37]. Apart from the burst-induced hard X-ray shortage, the properties of the pulsation within bursts shows no difference compared to those observed in the non-burst period. This provides evidence supporting that only the surrounding corona can be

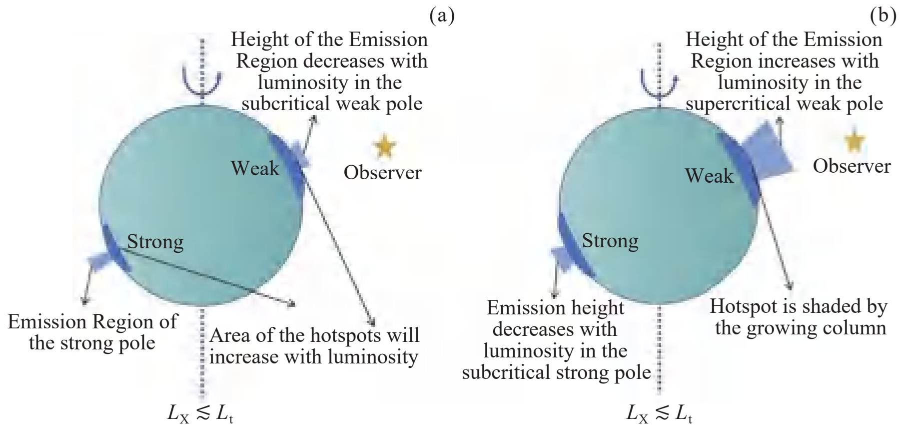

Fig. 7 Sketch of the two zones defined by the discovery of an additional critical luminosity during the sub-Eddington regime of Swift J0243.6+6124[34]

cooled off, and emissions from the polar cap are less influenced. Pulsations were also studied by Li *et al*.[38] for the accretion millisecond pulsar SRGAJ144459.2-604207, where a significant time lag with respect to the non-burst period shows up mainly at low energies. Such a time lag may be induced by the PR effect: during a type-I burst the highly enhanced accretion rate alters the local geometry of the site around the polar cap.

4 Extremely Violent Events

4.1 Gamma-ray Bursts

4.1.1 GRB Catalogues

GRB study is one of the Insight-HXMT core sciences. Owning to its largest detection area at hundreds keV to a few MeV and good time resolution, Insight-HXMT contributes to the GRB community, together with the joint observations of other GRB detectors in service, by precise measurement of the BAND function and improvement of the spectral break locations. Accordingly, so far two Insight-HXMT catalogues are released, namely the first Insight-HXMT GRB catalogue (also the first GRB catalogue in China), which hosts the GRB samples observed in the first 4 years[39], and the refined locations for the Short GRB (SGRB)[40]. For the former, noting that Insight-HXMT can detect more than 80 GRBs per year, the statistics of BAND function parameters will be largely improved for years to come. For the latter, by taking a localization method of so-called LI-CCF[41], the localization accuracies of 72 SGRBs are improved by 59% (3 sigma level), compared to that with Fermi/GBM alone. A series of research will benefit from this refined location catalogue, for example, the search for the GW counterpart, GRB association with neutrinos and so on.

4.1.2 Peculiar GRB Samples

Insight-HXMT also detected peculiar GRBs which are helpful for understanding the underlying GRB mechanism. The latest news from Insight-HXMT observations on the BOAT (brightest of all time) GRB221009 A is that, after the deadtime and saturation corrections, ME and LE lightcurves of the secondary particles induced by the interaction of the primary GRB photons with detectors are consistent with those from GECAM which are free of saturation problem. With the ME lightcurve, the minimum variability timescale of the main burst episode is measured as 0.1 s for the first time for GRB 221009 A[42]. As a long-duration GRB associated with strong precursor and Kilonova (KN), GRB211211 A provides chance to investigate the pre-merger status. Although the precursor is rather rare for SGRBs, the detection of a non-thermal spectrum (cutoff power law) and a QPO (3 sigma level, so far the highest one among precursors) (see Figure 8) make this GRB extremely unique[43]. The authors proposed that either the premerger magnetosphere interaction or magnetar crust oscillation could be at work for possible explanations of this peculiar precursor. GRB240825 A is another peculiar GRB with three spectral components (see Figure 9), which is rather rare for GRB, measured jointly with a series of GRB telescopes[44]. The bulk Lorentz factor estimated from the spectral components other than the band function favors jet penetration scenario, and the multi-

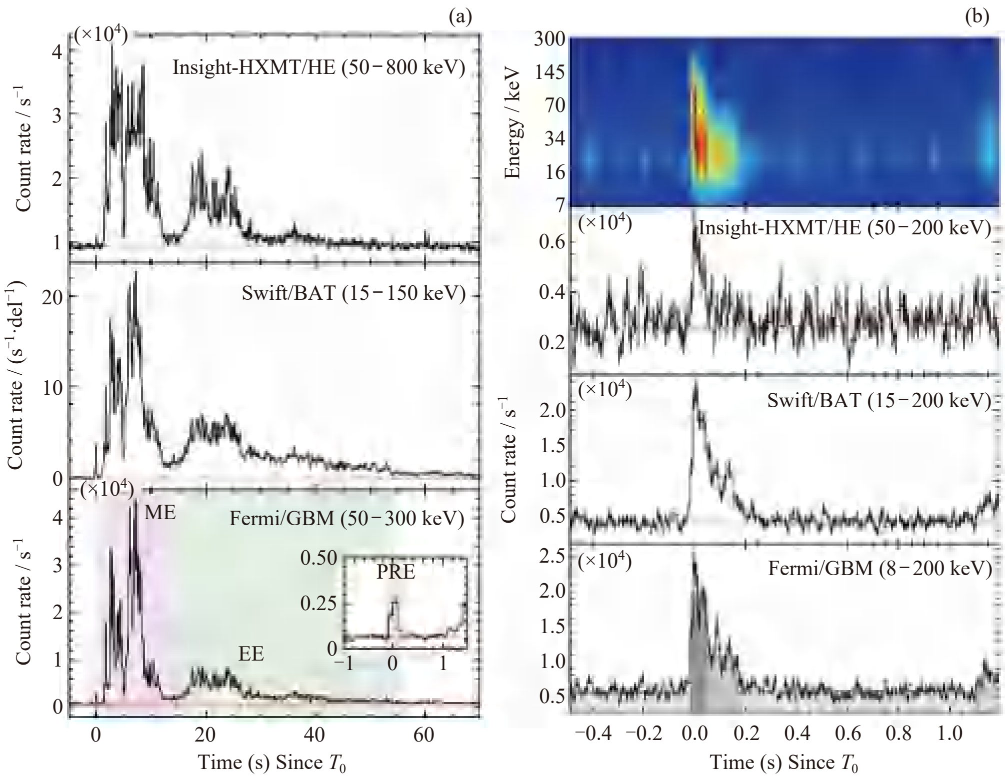

Fig. 8 Precursor and main burst of GRB211211 A recorded by different telescopes[43]

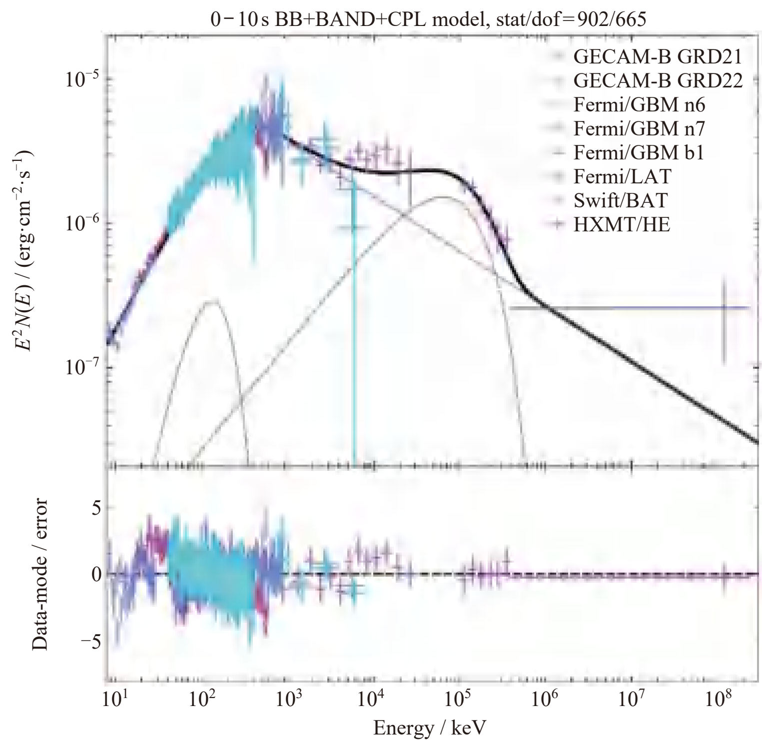

Fig. 9 Energy spectrum of GRB240825 A with three components[44]

segment broken power-law feature observed in the lightcurves suggests the presences of an early afterglow and a possible two-jet structure: a narrow early one followed by a latter broader one.

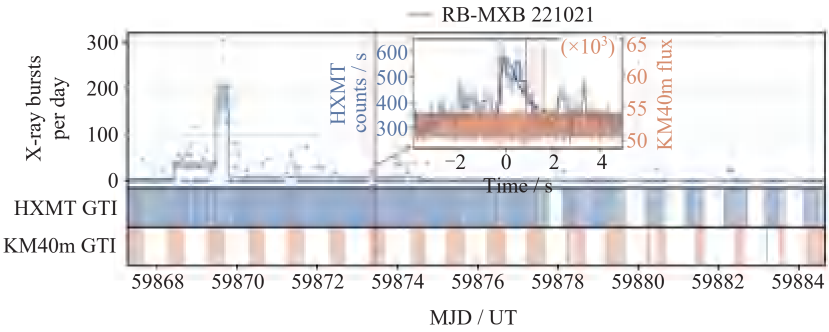

Fig. 10 Association of X-ray burst with radio bursts observed by Insight-HXMT at X-rays and KM40 m at radio band [45]

4.2 Fast Radio Bursts

Following the first FRB identification with a magnetar SGR 1935+2154[5], Insight-HXMT detected another X-ray burst, namely MXB 221021, associated with a radio burst measured by KM40 m radio telescope[45] on 21 October 2022. As shown in Figure 10, the X-ray burst is accompanied by three radio bursts with fluence ranging between 13–37 Jy·ms. Different from MXB/FRB200428, in this X-ray/radio association, the radio lags X-ray by roughly 1 second and the radio-to-X-ray fluence ratio is orders of magnitude lower. They noticed that such a radio burst is not likely the giant pulse of radio pulsar; otherwise the association with the X-ray burst would require a power far beyond the rotational energy budget. This association event may bridge the phenomenological gap between the normal radio emission and the FRB-like radio burst.

5 Insight-HXMT Applications

Insight-HXMT can also be used to observe the Terrestrial Gamma-ray Flash (TGF) and measure the density of the Earth's atmosphere, which is highly relevant to the living environment of human being. By comparing the large sample of TGF collected with Insight-HXMT and the lightning events recorded by the World Wide Lightning Location Network (WWLLN), close connection between TGF and the most intense lightning is confirmed[46]. By taking the earth osculation data collected by Insight-HXMT observations of Crab, the atmospheric densities at altitudes spanning from 55 to 130 km are precisely measured, which indicates that the NRLMSIS (Navy Research Laboratory Mass Spectrometer Incoherent Scatter Radar Exosphere) model overestimates atmospheric density at altitudes 90–95 km and 100–120 km by 15%–20%[47].

6 Summary and Outlook

Insight-HXMT still keeps bringing us interesting and exciting results with more observations, new ideas and novel techniques developed for exploring the data archive. In near future, the joint eXTP and Insight-HXMT will build the most powerful constellation in probing the fundamental physical laws under different extremes. The Insight-HXMT mission is currently still operating quite well and will be available to the world-wide community for years to come. Please visit hxmt.org for further information about Insight-HXMT and downloading data.

References

[1] LIU C Z, ZHANG Y F, LI, X F, *et al*. The High Energy X-ray telescope (HE) onboard the *Insight*-HXMT astronomy satellite[J]. *Science China Physics, Mechanics & Astronomy*, 2020, **63**(4): 249503

[2] CAO X L, JIANG W C, MENG B, *et al*. The Medium Energy X-ray telescope (ME) onboard the *Insight*-HXMT astronomy satellite[J]. *Science China Physics, Mechanics & Astronomy*, 2020, **63**(4): 249504

[3] CHEN Y, CUI W W, LI W, *et al*. The Low Energy X-ray telescope (LE) onboard the *Insight*-HXMT astronomy satellite[J]. *Science China Physics, Mechanics & Astronomy*, 2020, **63**(4): 249505

[4] ZHANG S N, LI T P, LU F J, *et al*. Overview to the Hard X-ray Modulation Telescope (*Insight*-HXMT) satellite[J]. *Science China Physics, Mechanics & Astronomy*, 2020, **63**(4): 249502

[5] LI T P, XIONG S L, ZHANG S N, *et al*. *Insight*-HXMT observations of the first binary neutron star merger GW170817[J]. *Science China Physics*, *Mechanics & Astronomy*, 2018, **61**(3): 031011. DOI: 10.1007/s11433-017-9107-5

[6] MA X, TAO L, ZHANG S N, *et al*. Discovery of oscillations

above 200 keV in a black hole X-ray binary with Insight-HXMT[J]. *Nature Astronomy*, 2021, **5**(1): 94-102

[7] YOU B, TUO Y L, LI C Z, *et al*. Insight-HXMT observations of jet-like corona in a black hole X-ray binary MAXI J1820+070[J]. *Nature Communications*, 2021, **12**(1): 1025

[8] SHUI Q C, ZHANG S, ZHANG S N, *et al*. A phase-resolved view of the low-frequency quasiperiodic oscillations from the black hole binary MAXI J1820+070[J]. *The Astrophysical Journal*, 2023, **957**(2): 84-98

[9] DOROSHENKO V, ZHANG S N, SANTANGELO A, *et al*. Hot disc of the *Swift* J0243.6+6124 revealed by Insight-HXMT[J]. *Monthly Notices of the Royal Astronomical Society*, 2020, **491**(2): 1857-1867.

[10] KONG L D, ZHANG S, ZHANG S N, *et al*. Insight-HXMT discovery of the highest-energy CRSF from the first galactic ultraluminous X-Ray pulsar swift J0243.6+6124[J]. *The Astrophysical Journal Letters*, 2022, **933**(1): 3-10.

[11] SHUI Q C, ZHANG S, WANG P J, *et al*. Cyclotron line evolution revealed with pulse-to-pulse analysis in the 2020 outburst of 1A 0535+262[J]. *Monthly Notices of the Royal Astronomical Society*, 2024, **528**(4): 7320-7332

[12] LI C K, LIN L, XIONG S L, *et al*. HXMT identification of a non-thermal X-ray burst from SGR J1935+2154 and with FRB 200428[J]. *Nature Astronomy*, 2021, **5**(4): 378-384

[13] ZHANG S, ZHANG S N, LU F J, *et al*. The insight-HXMT mission and its recent progresses[C]//Proceedings of SPIE 10699 Space Telescopes and Instrumentation 2018: Ultraviolet to Gamma Ray. Austin: SPIE, 2018: 106991U. DOI: 10.1117/12.2311835

[14] ZHANG S, ZHANG S N. Insight-HXMT research progress since 2023[J]. *Chinese Journal of Space Science*, 2024, **44**(4): 643-667

[15] ZHU H F, WANG W. Energy dependence of the low-frequency quasiperiodic oscillations in swift J1727.8-1613[J]. *The Astrophysical Journal*, 2024, **968**(2): 106-115

[16] YAN S P, DING G Q, WANG N, *et al*. A statistical study on the low-frequency quasi-periodic oscillation amplitude spectrum and amplitude in GRS 1915+105[J]. *Monthly Notices of the Royal Astronomical Society*, 2013, **434**(1): 59-68

[17] ZHU H F, WANG W, ZHU Z Y. The bicoherence analysis of type-C quasiperiodic oscillations in swift J1727.8−1613[J]. *The Astrophysical Journal*, 2024, **974**(2): 303-314

[18] YANG Z X, ZHANG L, ZHANG S N, *et al*. A timing view of the additional high-energy spectral component discovered in the black hole candidate swift J1727.8-1613[J]. *The Astrophysical Journal Letters*, 2024, **970**(2): 33-40

[19] PENG J Q, ZHANG S, SHUI Q C, *et al*. NICER, NuSTAR, and Insight-HXMT views to the newly discovered black hole X-ray binary swift J1727.8-1613[J]. *The Astrophysical Journal Letters*, 2024, **960**(2): 17-26

[20] XU S E, YOU B, LONG Y, *et al*. Temporal evolution of quasiperiodic oscillations in an accreting black hole swift J1727.8-1613: coevolution of the disk–corona during the state transition[J]. *The Astrophysical Journal*, 2025, **993**(1): 40-52

[21] MA R C, DONE C, KUBOTA A. Testing the Lense–Thirring precession origin of the QPO in *Swift* J1727.8−1613[J]. *Monthly Notices of the Royal Astronomical Society*, 2025, **543**(2): 1748-1760

[22] BOLLEMEIJER N, UTTLEY P, YOU B. A broad-band spectral-timing study of QPOs in the bright black hole X-ray binary *Swift* J1727.8−1613[J]. *Monthly Notices of the Royal Astronomical Society*, 2025, **540**(2): 1394-1411

[23] SHUI Q C, ZHANG S, PENG J Q, *et al*. Phase-resolved spectroscopy of low-frequency quasiperiodic oscillations from the newly discovered black hole X-ray binary swift J1727.8-1613[J]. *The Astrophysical Journal*, 2024, **973**(1): 59-70

[24] SHUI Q C, ZHANG S, ZHANG S N, *et al*. Recovery of high-energy low-frequency quasiperiodic oscillations from black hole X-ray binary MAXI J1535-571 with a Hilbert-Huang transform method[J]. *The Astrophysical Journal Letters*, 2024, **965**(1): 7-22

[25] MA X, SHUI Q C, GE M Y, *et al*. Search for the highest-energy quasiperiodic oscillation in the black hole X-ray binary candidate swift J1727.8−1613[J]. *The Astrophysical Journal*, 2026, **1002**(2): 180-186

[26] CAO J Y, LIAO J Y, ZHANG S N, *et al*. Spectral analysis of the X-ray flares in the 2023 outburst of the new black binary transient swift J1727.8-1613 observed with Insight-HXMT[J]. *The Astrophysical Journal*, 2025, **983**(1): 23-38

[27] YANG S K, YOU B, BOLLEMEIJER N, *et al*. Covariance spectrum of MAXI J1820+070: on the nature of the Comptonizing flow[J]. *The Astrophysical Journal*, 2026, **1000**(1): 20-29

[28] GAO C X, YU W F, YAN Z. On the broadening of the characteristic frequency range toward higher photon energies in the X-ray variability of the black hole transient MAXI J1820+070[J]. *The Astrophysical Journal*, 2025, **986**(2): 226-235

[29] YOU B, YU W, INGRAM A, *et al*. Reverberation lags viewed in hard X-rays from an accreting stellar-mass black hole[J]. *Nature Communications*, 2026, **17**(1): 2860-2870

[30] PENG J Q, ZHANG S, SHUI Q C, *et al*. The peculiar disk evolution of 4U 1630-472 observed by Insight-HXMT during its 2022 and 2023 outbursts[J]. *The Astrophysical Journal*, 2024, **975**(1): 4-15

[31] KONG L D, DAI X H, *et al*. Rapid quasi-periodic reconfiguration of the accretion column in 1A 0535+262[J]. *Nature Communications*, 2026 (in press)

[32] HOU X, GE M Y, JI L, *et al*. Fan-beamed X-ray emission from 1 to above 130 keV from the ultraluminous X-ray pulsar RX J0209.6-7427 in the Small Magellanic Cloud[J]. *The Astrophysical Journal*, 2022, **938**(2): 149-163

[33] ZHAO Q X, HOU X, GE M Y, *et al*. Searching for the highest energy of pulsation and critical luminosity of Swift J0243.6+6124 observed by Insight-HXMT[J]. *Research in Astronomy and Astrophysics*, 2024, **24**(5): 055006-055015

[34] CHEN B Y, ZHANG S, SHUI Q C, *et al*. Discovery of a new spectral transition in Swift J0243.6+6124 in the sub-Eddington

regime[J]. *The Astrophysical Journal*, 2026, **998**(1): 184-198

[35] PENG J Q, ZHANG S, CHEN Y P, *et al*. New insight into the hard X-ray emission influenced by the type I bursts observed by Insight-HXMT during the outburst of 4U 1636-536[J]. *Astronomy & Astrophysics*, 2024, **685**: 71-81

[36] CHEN Y P, ZHANG S, JI L, *et al*. The prolific thermonuclear X-ray bursts from the outburst of the newly discovered millisecond pulsar MAXI J1816-195 observed by Insight-HXMT and NICER[J]. *The Astrophysical Journal Letters*, 2022, **936**(2): 21-31

[37] JI L, GE M Y, CHEN Y P, *et al*. The influence of thermonuclear bursts on polar caps of the accreting X-ray millisecond pulsar MAXI J1816-195[J]. *The Astrophysical Journal Letters*, 2024, **966**(1): 3-7

[38] LI Z S, KUIPER L, PAN Y Y, *et al*. Timing and spectral studies of SRGA J144459.2−604207 with NICER, Einstein Probe, IXPE, NuSTAR, Insight-HXMT, and INTEGRAL during its 2024 outburst[J]. *The Astrophysical Journal*, 2025, **990**(1): 15-27

[39] SONG X Y, XIONG S L, ZHANG S N, *et al*. The first Insight-HXMT gamma-ray burst catalog: the first four years[J]. *The Astrophysical Journal Supplement Series*, 2022, **259**(2): 46-61

[40] XIAO S, ZHANG Y T, WANG Y, *et al*. The first Insight-HXMT localization catalog of short-duration gamma-ray bursts: the first six years[J]. *The Astrophysical Journal Supplement Series*, 2025, **278**(2): 60-72

[41] LI T P, QU J L, FENG H, *et al*. Timescale analysis of spectral lags[J]. *Chinese Journal of Astronomy and Astrophysics*, 2004, **4**(6): 583-598

[42] ZHANG W L, XUE W C, LI C K, *et al*. Insight-HXMT observations of the extremely bright GRB 221009A[J]. *The Astrophysical Journal*, 2025, **986**(2): 170-178

[43] XIAO S, ZHANG Y Q, ZHU Z P, *et al*. The peculiar precursor of a gamma-ray burst from a binary merger involving a magnetar[J]. *The Astrophysical Journal*, 2024, **970**(1): 6-17

[44] WANG C W, TAN W J, XIONG S L, *et al*. Evolution of the three spectral components in the prompt emission of GRB 240825A[J]. *The Astrophysical Journal Letters*, 2025, **985**(2): 30-47

[45] XUE W C, TAN W J, HUANG Y X, *et al*. Joint observation of SGR J1935+2154 with Insight-HXMT and KM40m during the active episode of 2022 October[J]. *The Astrophysical Journal Letters*, 2026, **998**(2): 44-55

[46] YI Q B, GUO H X, XIONG S L, *et al*. Unveil the TGF-lightning relation with a large sample of TGFs detected by *Insight*-HXMT[J]. *Science China Physics, Mechanics & Astronomy*, 2025, **68**(8): 281011-281017

[47] ZHANG H H, XUE W C, LI X B, *et al*. Measurement of neutral atmosphere density during the years of increasing solar activity using Insight-HXMT data with the earth occultation technique[J]. *The Astrophysical Journal*, 2025, **988**(2): 233-242

Author Biography

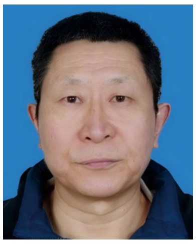

ZHANG Shu Male, born on 1 September 1969 in Hebei Province, professor and PhD supervisor in Institute of High Energy Physics, CAS. Research fields: high energy observations and emission mechanism of X-ray binary systems.
E-mail: szhang@ihep.ac.cn

0254-6124/2026/46(4)-0058-05 *Chin. J. Space Sci.* 空间科学学报

XIONG Shaolin. Overview of Gravitational-wave High-energy Electromagnetic Counterpart All-sky Monitor Observations from 2024 to 2026. *Chinese Journal of Space Science*, 2026, **46**(4): 58–62. CSTR:32142.14.cjss.2026–yg19. DOI:10.11728/cjss2026.04.2026–yg19

Overview of Gravitational-wave High-energy Electromagnetic Counterpart All-sky Monitor Observations from 2024 to 2026*

XIONG Shaolin

(*State Key Laboratory of Particle Astrophysics*, *Institute of High Energy Physics*, *Chinese Academy of Sciences*, *Beijing* 100049)

Abstract During the past two years, the Gravitational-wave high-energy Electromagnetic Counterpart All-sky Monitor (GECAM) has developed into a multi-instrument constellation, including GECAM-A/B, GECAM-C, and GECAM-D, for monitoring high-energy transients over a broad energy range from about 10 keV to 5 MeV. GECAM observations have produced important results on gamma-ray bursts, compact binary mergers, magnetar X-ray bursts, high-energy counterparts of fast X-ray transients, and terrestrial high-energy events. This review summarizes highlight of GECAM results published from 2024 to 2026, emphasizing observations of GRB 221009A, GRB 230307A, and the prolific Galactic magnetar SGR J1935+2154. These observations demonstrate the important role of GECAM as a high-time-resolution, all-sky gamma-ray monitor in time-domain multi-messenger astronomy and space science.

Key words GECAM, Gamma-ray bursts, Magnetars, Fast radio bursts, High-energy transients

Classified index V474

1 Introduction

Gamma-ray transients are sudden enhancements of high-energy emission that may originate from astrophysical or near-Earth sources. They include cosmological Gamma-Ray Bursts (GRBs), GRBs associated with Gravitational Waves (GWs), Soft Gamma-ray Repeaters (SGRs), bursts associated with Fast Radio Bursts (FRBs), Solar Flares (SFLs), Terrestrial Gamma-ray Flashes (TGFs), Terrestrial Electron Beams (TEBs), particle precipitation events, and related phenomena. The joint detection of GW170817 and GRB 170817 A established compact-object mergers as a central topic of multi-messenger astronomy[1,2]. GECAM was primarily designed to provide all-sky, wide-band, high-time-resolution monitoring for these critical events and other gamma-ray transients.

GECAM-A and GECAM-B were launched on 10 December 2020 (Beijing Time). GECAM-C, carried by the SATech-01 satellite, was launched on 27 July 2022, and deorbited in February 2025, and GECAM-D, carried by the DRO-A spacecraft, was launched on 13 March 2024. The GECAM series now provides multi-platform monitoring with gamma-ray detectors and charged-particle detectors, covering roughly 10 keV to 5 MeV for various high-energy transients.

The main science targets of GECAM remain on high-energy counterparts of GWs and FRBs, GRBs, and SGRs. In addition, GECAM has become useful for studies of solar flares, TGFs/TEBs, particle precipitation,

* Funded by the National Natural Science Foundation of China (12273042)
Received June 30, 2026

and high-energy cosmic rays in low Earth orbit.

2 GRBs

GRBs are among the most luminous explosive phenomena in the universe. The underlying physics and mechanisms of GRBs remain uncertain. Bright GRBs provide an important opportunity to probe these questions. GECAM is particularly valuable for these studies because its detectors can record very bright events with high time resolution and reduced saturation effects.

2.1 GRB 221009 A

GRB 221009 A, the brightest gamma-ray burst of all time, remains one of the most important bursts. GECAM-C recorded the prompt emission without the severe saturation that affected several other instruments, allowing precise measurements of the prompt burst, early afterglow, flare component, and high-energy spectral evolution[3–7]. Additional results based on GECAM observations of this burst have been reported during the past two years.

A major result reported in 2024 was the identification of time-evolving spectral-line features in GRB 221009 A (see Figure 1). The line centroid was reported to reach up to 37 MeV and to decrease approximately as a power law with time, while the line energy flux also decayed as a power law [6]. Subsequent theoretical work discussed the production mechanism of the high-energy emission line, including an interpretation based on electron-positron pair annihilation followed by down-Comptonization in an evolving GRB outflow[7]. These studies suggest that line features could become a direct diagnostic of the bulk Lorentz factor and radiation region in GRB jets.

GECAM observations also help connect flare activity with prompt emission in extremely bright GRBs. A recent analysis reported the brightest GRB flare observed in GRB 221009 A and argued that the flare occupies the parameter space between classical X-ray flares and prompt-emission pulses, helping to bridge the gap between late internal activity and the prompt phase[8].

2.2 GRB 230307 A

GRB 230307 A is the second-brightest GRB and the brightest merger-origin GRB reported so far. Although its duration is long, its prompt properties measured by GECAM, host-galaxy environment, and kilonova association indicate a compact-object-merger origin[9,10]. This event therefore strengthens the view that the physical classification of GRBs cannot rely only on the duration of prompt emission.

Broadband GECAM and LEIA observations revealed a transition from gamma-ray emission to an extended X-ray component, interpreted as evidence for a long-lived central engine. An achromatic temporal break in the GECAM-detected hard X-ray light curve during the prompt phase was interpreted as a jet edge effect, providing a new way to constrain jet geometry directly during prompt emission[9].

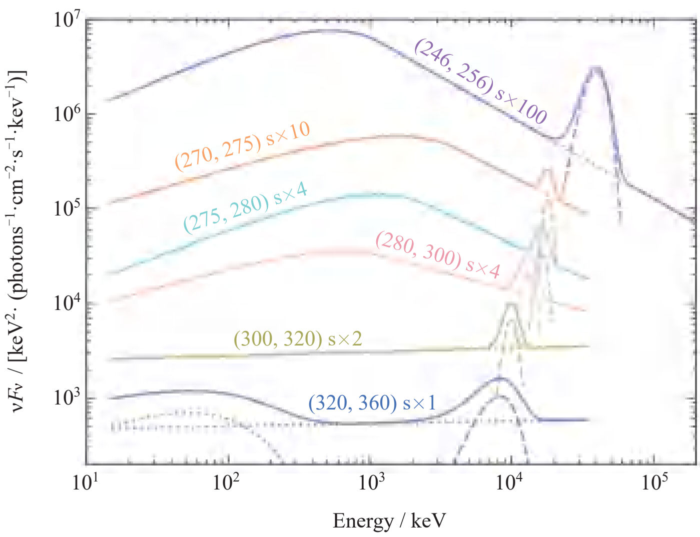

Fig. 1 MeV emission lines found in GRB 221009 A by jointly analyzing the GECAM-C and Fermi/GBM data[6]

Modeling of the rapidly variable components in the saturation-free light curve of GRB 230307 A measured by GECAM supports a minijet-emission interpretation in a large emission region within a magnetically dominated jet[10]. Further work on GRB 230307 A and related long merger-origin bursts identified distinctive prompt-emission properties, including exponential evolution of pulse intensities, waiting times, pulse widths, and spectral peak energy[11]. Remarkably, a brief 909 Hz gamma-ray periodic signal has been revealed in the GECAM accurate light curve of GRB 230307 A, providing strong evidence for a millisecond-magnetar central engine in this burst [12].

2.3 Other GRBs

The operation of Einstein Probe (EP) has increased the need for high-energy monitoring of fast X-ray transients (FXTs). A systematic search for gamma-ray counterparts of EP fast X-ray transients using GECAM together with Insight-HXMT and Fermi/GBM found that about 22% of FXTs have gamma-ray counterparts [13]. Another systematic search of Fermi/GBM subthreshold triggers in GECAM data extended the short-GRB population, improving the statistical context for weak compact-merger candidates [14]. GECAM also detected early emission from the very important ultralong GRB 250702 B/EP250702 a. A targeted ETJASMIN search over a 30-day window using GECAM, Insight-HXMT, and Fermi/GBM data revealed multi-episode main emission lasting several hours, making it one of the longest GRBs ever detected[15].

3 SGRs and FRB-associated Bursts

SGRs are recurrent X-ray and soft gamma-ray bursts from magnetars, a class of neutron stars with extremely strong magnetic fields. SGR J1935+2154 is the most important GECAM magnetar target because it produced FRB 200428 and later radio-burst-associated X-ray bursts. GECAM observations from the 2021 and 2022 active episodes have enabled catalogue-level studies of burst timing, spectra, and morphology [16–19]. Together with Fermi/GBM and Insight-HXMT data, the GECAM sample supports studies of burst waiting times, duration, spectral hardness, and correlations among temporal and spectral parameters.

Several studies used this sample to examine magnetar-burst phenomenology. Spectral lag and minimum variation timescale studies indicate millisecond-scale structures and energy-dependent timing behavior, pointing to compact emission regions in the magnetosphere[17,18]. Power density spectrum and self-organized criticality analyses further suggest that some timing properties are scale invariant across the burst population[19,20].

Remarkably, GECAM detected rare Magnetar X-ray Bursts (MXBs) associated with radio bursts from SGR J1935+2154, including MXB 221014 and the peculiar MXB 221120[21,22]. These observations strengthen the empirical connection between magnetar X-ray bursts and FRB-like radio emission, while showing that radio association is not a simple function of X-ray fluence alone.

GECAM observations have also revealed more detailed light-curve morphology in magnetar bursts. Recent studies of GECAM observations of SGR J1935+2154 revealed a peculiar burst pattern called ERCOD [23] and eclipse features in X-ray bursts that can be used to probe trapped fireballs and magnetospheric geometry[24].

Overall, the magnetar results from 2024 to 2026 indicate that GECAM is useful both for event discovery and for population studies. The same data set supports burst catalogues, FRB-association searches, timing analyses, and physical modeling of magnetar fireballs.

4 High-energy Transients around the Earth

GECAM's configuration of both gamma-ray detectors and charged-particle detectors provides a way to study near-Earth particle phenomena as well as gamma-ray transients. Building on earlier TGF and TEB observations[25], recent work reported peculiar oscillating particle-precipitation events discovered by GECAM[26]. These events indicate that GECAM data can probe the coupling between magnetospheric particles and the near-Earth environment.

A related methodological advance is the pitch-angle measurement method based on detector-count distributions of GECAM[27]. By using the relative count rates of multiple detectors, the method aims to infer the incident direction and pitch-angle information of charged particles. This expands the scientific use of GECAM from transient detection to quantitative studies of particle anisotropy and precipitation geometry.

Finally, a systematic study of simultaneous events detected by GECAM suggests a novel way to monitor and characterize high-energy cosmic rays in low Earth orbit [28].

5 Summary

From 2024 to 2026, GECAM research has moved from mission demonstration to systematic exploitation of the transient universe. For GRBs, GECAM provided key unsaturated observations of the brightest events, including GRB 221009 A and GRB 230307 A, and contributed to studies of jet structure, spectral-line features, prompt emission and flare connections, and merger-origin long GRBs. For magnetars, GECAM observations of SGR J1935+2154 enabled burst catalogues, timing analyses, FRB-association burst studies, and constraints on magnetar and fireball geometry. Additionally, GECAM has contributed to a broader transient science program, including particle-precipitation and cosmic-ray events in low Earth orbit. These results confirm GECAM's role as an important Chinese high-energy transient monitor in the era of time-domain multi-messenger astronomy and space science.

References

[1] ABBOTT B P, ABBOTT R, ABBOTT T D, *et al*. Gravitational waves and gamma-rays from a binary neutron star merger: GW170817 and GRB 170817A[J]. *The Astrophysical Journal Letters*, 2017, **848**(2): L13

[2] GOLDSTEIN A, VERES P, BURNS E, *et al*. An ordinary short gamma-ray burst with extraordinary implications: *Fermi*-GBM Detection of GRB 170817A[J]. *The Astrophysical Journal Letters*, 2017, **848**(2): L14

[3] LIU J C, ZHANG Y Q, XIONG S L, *et al*. GRB 221009A: HEBS detection[J/OL]. *GRB Coordinates Network*, (2022-10-14). https://ui.adsabs.harvard.edu/abs/2022GCN.32751....1L/abstract

[4] AN Z H, ANTIER S, BI X Z, *et al*. Insight-HXMT and GECAM-C observations of the brightest-of-all-time GRB 221009A[OL]. arXiv preprint arXiv: 2303.01203, 2023

[5] ZHENG C, ZHANG Y Q, XIONG S L, *et al*. Observation of GRB 221009A early afterglow in X-ray/gamma-ray energy bands[J]. *The Astrophysical Journal Letters*, 2024, **962**(1): L2

[6] ZHANG Y Q, XIONG S L, MAO J R, *et al*. Observation of spectral lines in the exceptional GRB 221009A[J]. *Science China Physics, Mechanics & Astronomy*, 2024, **67**(8): 289511

[7] LIU J Y, MAO J R, XIONG S L, *et al*. The production mechanism of the high-energy emission line in the brightest cosmic burst[OL]. arXiv preprint arXiv: 2509.14715, 2025

[8] YU Z H, WANG C W, XIONG S L, *et al*. Brightest gamma-ray-burst flare observed in GRB 221009A: bridging the last gap between the prompt emission and flare in gamma-ray bursts[J]. *The Astrophysical Journal Letters*, 2026, **998**(1): L21

[9] SUN H, WANG C W, YANG J, *et al*. Magnetar emergence in a peculiar gamma-ray burst from a compact star merger[J]. *National Science Review*, 2025, **12**(3): nwae401

[10] YI S X, WANG C W, SHAO X, *et al*. Evidence of minijet emission in a large emission zone from a magnetically dominated gamma-ray burst jet[J]. *The Astrophysical Journal*, 2025, **985**(2): 239

[11] MACCARY R, GUIDORZI C, MAISTRELLO M, *et al*. A set of distinctive properties ruling the prompt emission of GRB 230307A and other long γ-ray bursts from compact object mergers[J]. *Journal of High Energy Astrophysics*, 2026, **49**: 100456

[12] CHEN R C, ZHANG B B, WANG C W, *et al*. Evidence for a brief appearance of gamma-ray periodicity after a compact star merger[J]. *Nature Astronomy*, 2025, **9**(11): 1701-1713

[13] ZHANG Y Q, XUE W C, ZHANG J P, *et al*. Multi-instrument search for gamma-ray counterpart of X-ray transients detected by EP/WXT[J]. *The Astrophysical Journal Letters*, 2025, **987**(2): L38

[14] CAI C, XIONG S L, ZHANG Y Q, *et al*. Extending the short gamma-ray burst population from subthreshold triggers in Fermi/GBM and GECAM data and its implications[J]. *The Astrophysical Journal Letters*, 2025, **989**(2): L21

[15] ZHANG J P, WANG C W, YU Z H, *et al*. On the ultralong gamma-ray transient GRB 250702B/EP 250702a[J]. *The Astrophysical Journal Letters*, 2026, **997**(2): L45

[16] XIE S L, CAI C, YU Y W, *et al*. GECAM observations of the galactic magnetar SGR J1935+2154 during the 2021 and 2022 burst active episodes. I. burst catalog[J]. *The Astrophysical Journal Supplement Series*, 2025, **277**(1): 5

[17] XIAO S, TUO Y L, ZHANG S N, *et al*. Discovery of the linear energy dependence of the spectral lag of X-ray bursts from SGR J1935+2154[J]. *Monthly Notices of the Royal Astronomical Society*, 2023, **521**(4): 5308-5333

[18] XIAO S, YANG J J, LUO X H, *et al*. The minimum variation timescales of X-ray bursts from SGR J1935+2154[J]. *The Astrophysical Journal Supplement Series*, 2023, **268**(1): 5

[19] XIAO S, LI X B, XUE W C, *et al*. Individual and averaged power density spectra of X-ray bursts from SGR J1935+2154: quasi-periodic oscillation search and slopes[J]. *Monthly Notices of the Royal Astronomical Society*, 2024, **527**(4): 11915-11924

[20] XIAO S, ZHANG S N, XIONG S L, *et al*. The self-organized

criticality behaviours of two new parameters in SGR J1935+2154[J]. *Monthly Notices of the Royal Astronomical Society*, 2024, **528**(2): 1388-1392
[21] WANG C W, XIONG S L, WANG Y, *et al*. GECAM discovery of the second FRB-associated magnetar X-ray burst from SGR J1935+2154[J]. *Monthly Notices of the Royal Astronomical Society*, 2026, **546**(4): stag312
[22] TAN W J, WANG Y, WANG C W, *et al*. GECAM discovery of a peculiar magnetar X-ray burst (MXB 221120) from SGR J1935+2154 associated with a fast radio burst[J]. *Astronomy & Astrophysics*, 2026, **707**: A289
[23] WANG Y, WANG C W, XIONG S L, *et al*. Unveil a peculiar light-curve pattern of magnetar burst with GECAM observations of SGR J1935+2154[J]. *The Astrophysical Journal*, 2025, **993**(1): 24
[24] XIE S L, CHEN A M, YU Y W, *et al*. Eclipsed X-ray bursts from magnetar SGR J1935+2154 and the fireball measurements[J]. *The Astrophysical Journal*, 2026, **999**(2): 159
[25] ZHAO Y, LIU J C, XIONG S L, *et al*. The first GECAM observation results on terrestrial gamma-ray flashes and terrestrial electron beams[J]. *Geophysical Research Letters*, 2023, **50**(14): e2022GL102325
[26] WANG C W, XIONG S L, ZHAO Y, *et al*. GECAM discovery of peculiar oscillating particle precipitation events[J]. *Science China Physics, Mechanics & Astronomy*, 2026, **69**(2): 229513
[27] WANG C W, XIONG S L, XUE H B, *et al*. Pitch angle measurement method based on detector counts distribution. -I. Basic conception[J]. *Experimental Astronomy*, 2025, **60**(3): 25
[28] REN Y Z, ZHU F R, XIONG S L, *et al*. Systematic study of the simultaneous events detected by GECAM[J]. *Astronomy & Astrophysics*, 2026, **707**: A318

Author Biography

XIONG Shaolin XOING Shaolin Male, born in Feb. 1983 in Fengcheng city of Jiangxi Province, China. Currently working in the Institute of High Energy Physics, Chinese Academy of Sciences as researcher (professor). Proposed the GECAM mission as the Principal Investigator. Participated in other high-energy space telescopes including Insight-HXMT, POLAR, SVOM, POLAR2, eXTP, etc. Research interests include high energy astrophysics (e.g. GRB, GW, SGR, FRB) and high energy phenomena of from the Sun to the Earth (e.g. SFL, TGF, TEB), in terms of instrumentation, observation, data analysis and physical interpretation.
E-mail: xiongsl@ihep.ac.cn

0254-6124/2026/46(4)-0063-09 *Chin. J. Space Sci.* 空间科学学报

GUO Huadong, DOU Changyong, JIANG Nijun, TANG Yunwei. Recent Advances of the SDGSAT-1 for Supporting Global SDG Monitoring and Evaluation. *Chinese Journal of Space Science*, 2026, **46**(4): 63–71. CSTR:32142.14.cjss.2026–yg11. DOI:10.11728/cjss2026.04.2026–yg11

Recent Advances of the SDGSAT-1 for Supporting Global SDG Monitoring and Evaluation*

GUO Huadong[1,2,3] DOU Changyong[1,2,3] JIANG Nijun[1,2] TANG Yunwei[1,2]

1(*International Research Center for Big Data for Sustainable Development*, *Beijing* 100094)

2(*Aerospace Information Research Institute*, *Chinese Academy of Sciences*, *Beijing* 100094)

3(*University of Chinese Academy of Sciences*, *Beijing* 100049)

Abstract As a dedicated scientific satellite tailored to advance the implementation of the United Nations 2030 Agenda for Sustainable Development (2030 Agenda), the Sustainable Development Science Satellite 1 (SDGSAT-1) has entered its fifth year of in-orbit operation. This satellite has witnessed a rapid diversification in its research applications. The satellite's data have been used by more than 116 countries, and over 220 peer-reviewed papers have been published. Such remarkable research growth is attributable to the high-quality data products derived from SDGSAT-1's technological innovations, alongside its open data access policy and sustainably maintained operational status underpinned by the SDGSAT-1 Open Science Program. This paper presents a state-of-the-art review of the mission's research progress over the past two years and elaborates on the future development prospects for ongoing global SDG monitoring and assessment.

Key words SDGSAT-1, Earth observation, Sustainable Development Goals (SDGs), Remote sensing

Classified index V474

1 Introduction

Over the past decade, global communities have strived to achieve the 17 Sustainable Development Goals (SDGs) set forth in the United Nations (UN) 2030 Agenda for Sustainable Development (2030 Agenda). Collectively, these 17 SDGs, along with their 169 targets and 234 indicators, provide a comprehensive quantitative framework for measuring progress in peace and prosperity for people and the planet. However, the implementation of this optimistic vision faces challenges that were perhaps unforeseen, as the world has been drawn into more geopolitical conflicts, intensifying climate change, and a resurgence of unilateralism. These challenges have led to stagnation, uneven progress, and even regression in sustainable development in some regions and sectors, despite overall advancement[1]. Meanwhile, advances in science and technology, including artificial intelligence, space technology, and big data, continue to deliver new platforms and methodologies that are revolutionizing both the evaluation and realization of the SDGs by addressing limitations in data availability and resolution.

Earth Observation (EO) has emerged as a powerful and indispensable tool for advancing Sustainable Development Goal (SDG) evaluation[2], owing to its unique capacity to acquire objective datasets concerning environmental conditions and socioeconomic dynamics. The Sustainable Development Science Satellite 1 (SDGSAT-1) stands as a frontier of EO satellites dedicated to SDG-related applications. Developed by the International Re-

* Supported by the National Natural Science Foundation of China (W2412136)
Received May 20, 2026

search Center of Big Data for Sustainable Development Goals (CBAS), the satellite is specifically designed to characterize human-environment interactions. It is equipped with three advanced EO payloads, namely the Glimmer Imager (GLI), the Thermal Infrared Spectrometer (TIS), and the Multispectral Imager (MSI). All sensors feature a consistent swath width of 300 km while possessing distinct complementary advantages for diversified observation scenarios.

The GLI is dedicated to capturing spatiotemporal dynamics of terrestrial Artificial Light at Night (ALAN). It integrates RGB bands at 40 m spatial resolution and a 10 m panchromatic band, delivering unprecedented spectral and spatial resolution among all publicly available spaceborne EO datasets. The TIS enables accurate retrieval of land surface temperature at 30 m resolution, achieving the finest spatial resolution currently available for civilian satellite missions. Equipped with seven multispectral bands, the MSI includes two deep-blue bands and one red-edge band, which provide innovative insights into water quality monitoring and vegetation ecological research, respectively. Beyond independent operation of the three payloads, SDGSAT-1 supports synergistic observation modes: coordinated TIS-MSI imaging is performed in daytime, while joint TIS-GLI observation is conducted at night, supplying multi-dimensional complementary information for comprehensive target monitoring and analysis.

From late 2021 to mid-2024, SDGSAT-1 achieved initial remarkable progress in supporting SDG-related research, yielding more than 70 academic publications and attracting data users across 88 countries[3]. Over the past two years (2024–2026), the mission has gained further prominent momentum in international applications. Its research themes, scientific outputs and study regions have undergone extensive diversification. To date, the cumulative number of peer-reviewed publications has exceeded 220, and registered users of the SDGSAT-1 Open Science Program now span 116 countries worldwide.

More specifically, SDGSAT-1 relevant has covered 22 specific SDG targets across 11 SDGs[4,5], including SDG 1 (No Poverty), SDG 2 (Zero Hunger), SDG 3 (Good Health and Well-being), SDG 6 (Clean Water and Sanitation), SDG 7 (Affordable and Clean Energy), SDG 9 (Industry, Innovation and Infrastructure), SDG 11 (Sustainable Cities and Communities), SDG 12 (Responsible Consumption and Production), SDG 13 (Climate Action), SDG 14 (Life Below Water), and SDG 15 (Life on Land). Beyond the continued application of single-sensor datasets, recent studies have increasingly exploited multi-sensor synergistic observations. Furthermore, researchers have integrated SDGSAT-1 data with other widely adopted EO datasets to enhance temporal and spectral observation capabilities as well as socioeconomic data sources.

This paper reviews the latest advances of the SDGSAT-1 mission and its data application developments, with a particular emphasis on recent international studies, multi-sensor synergies, multi-satellite collaborative research, and advances in data processing methodologies. The remainder of this paper is organized as follows. Section 2 elaborates on the core technical strengths of SDGSAT-1 and recent progress in data quality improvement. Section 3 discusses the expanding application scope of SDGSAT-1 data products and their global influence. Section 4 outlines future prospects regarding sustainable development satellite constellations and potential international cooperation frameworks. Finally, Section 5 concludes the paper with summary remarks.

2 Evolution of SDGSAT-1 Operation

2.1 SDGSAT-1 Technical Specification

SDGSAT-1 has maintained stable operation for more than four years, and all three onboard sensors (technical parameters listed in Table 1) are expected to continue delivering high quality data sources for years to come. Figure 1 shows recent images of Beijing captured by SDGSAT-1, demonstrating the satellite's capability to monitor thermal environment, nighttime light distribution, and ground surface layout in the selected research area.

The design of SDGSAT-1 centered on the demands of monitoring human–nature interactions, which reflect the interconnected nature of the SDG global indicator framework. To provide global high-resolution imaging capability, SDGSAT-1 operates in a sun-synchronous orbit at an altitude of 505 km with an inclination angle of 97.5° (Table 2), achieving a revisit period of 11 days.

Table 1 Technical parameters of SDGSAT-1 sensors

Type	Parameter	Specification and unit
Multispectral imager	Swath width	300 km
	Spatial resolution	10 m
	Designed radiometric accuracy	Relative: ≤2% Absolute: ≤5%
	Bands and central wavelengths	Band 1 (deep blue): 400.63 nm
		Band 2 (deep blue): 438.47 nm Band 3 (blue): 495.10 nm Band 4 (green): 553.23 nm Band 5 (red): 656.75 nm Band 6 (red edge): 776.12 nm Band 7 (near-infrared): 854.02 nm
Thermal infrared spectrometer	Swath width	300 km
	Spatial resolution	30 m
	Designed radiometric accuracy	Relative: ≤5% Absolute: ≤1 K@300 K
	Bands and central wavelengths	Band 1: 9.35 μm Band 2: 10.73 μm Band 3: 11.72 μm
Glimmer imager	Swath width	300 km
	Spatial resolution	Panchromatic: 10 m, RGB: 40 m
	Designed radiometric accuracy	Relative: ≤2% Absolute: ≤5%
	Bands and central wavelengths	Blue band: 478.87 nm Green band: 561.20 nm Red band: 734.25 nm Panchromatic band: 680.72 nm

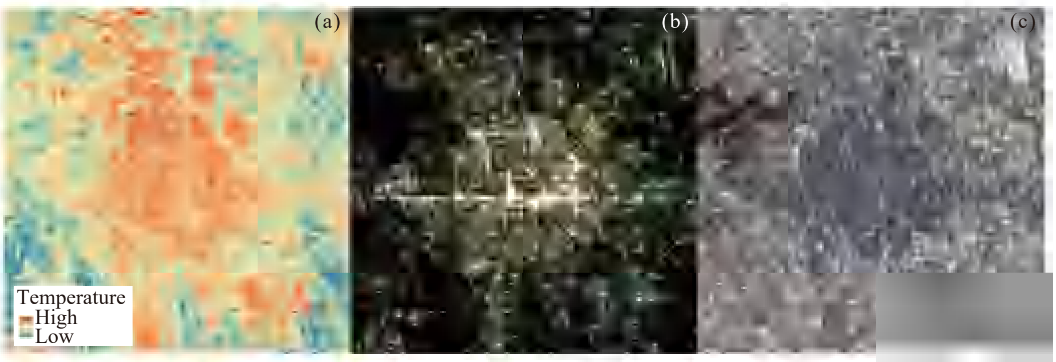

Fig. 1 Images of central Beijing captured by SDGSAT-1. (a) Nighttime band 2 TIS image, captured on 11 March 2026. (b) Nighttime RGB-composite GLI image, captured on 11 March 2026. (c) Daytime RGB-composite MSI image, captured on 2 February 2026

Its descending and ascending nodes occur at 09:30 AM and 09:30 PM local time, respectively, creating optimal conditions for monitoring daytime Earth surfaces and nighttime artificial light. The sun is at a moderate altitude when MSI data are collected, while GLI operates during the peak of nighttime human activity.

2.2 Data Quality Evaluation and Improvements

Post-launch calibrations of GLI[6], TIS[7] and MSI[8] have built the foundations for scientific applications of SDGSAT-1 data. From mid-2024 onwards, continuous

Table 2 Orbit parameters of SDGSAT-1

Parameter	Specification and unit
Type	Sun-synchronous orbit
Orbit period/min	90
Revisit period/d	11
Altitude/km	505
Inclination angle/(°)	97.5

efforts have been made to introduce data enhancement methods, data quality evaluations, and tailored spectral indices.

Regarding the GLI, researchers have established procedures to improve both radiometric and geometric accuracy. Tan *et al*.[9] and Yin *et al*.[10] have formulated a deep learning-based method and an automatic registration algorithm, respectively, to correct misalignment issues present in GLI images. Zhang *et al*.[11] have experimented with a radiative transfer model to perform atmospheric correction for GLI, while Wang *et al*.[12] have constructed a novel image reconstruction method to fill the GLI observation gap caused by the cloud cover. Furthermore, GLI-based spectral indices[13,14] have been developed and validated for the light source classification.

For the TIS, a series of recent works[15–18] have tested and proven its ability to accurately derive Land Surface Temperature (LST) and emissivity, while cross-calibrations between TIS and other EO thermal infrared data sources, including Landsat 9 TIRS-2[19] and FY-4 A AGRI[20], have yielded results that indicate reliable data quality.

Evaluation of the MSI's on-orbit radiometric performance[21,22] has demonstrated overall satisfactory long-term stability and signal-to-noise ratio. Additionally, the sensor-specific tasseled cap transformation of the MSI[23] has been developed, with initial applications in ecological monitoring[24].

2.3 Open Science Data Services

Open data sources are the cornerstone for addressing the data availability issues faced by SDG monitoring. Not only do they reduce the burden of data accessibility, but research methodologies and models developed using open data can also be better validated, applied, and disseminated. Data products from SDGSAT-1 are openly shared through the SDGSAT-1 Open Science Program*, initiated by CBAS. After operation for more than four years, this program has witnessed steady expansion and diversification of its user base. Since the last COSPAR report[3], the total number of data users has more than doubled, from 1500 in 2024 to over 3500 in early 2026. User backgrounds include researchers at universities and research institutes, as well as analysts and policy consultants in government and UN organizations. Furthermore, as a result of the reliable operation of the satellite, the total number of archived SDGSAT-1 images has reached 510000, offering global coverage. In addition to the access portal for archived data, the Open Science Program offers users the option to upload their research target locations and desired time windows, allowing them to obtain tailored data products.

Furthermore, CBAS has organized international SDGSAT-1 data processing and application training sessions. From 2024 to 2026, SDGSAT-1 specialists offered free in-person or online training to participants from Kenya, Small Island Developing States, and other developing countries. In the future, CBAS will continue to build capacity based on SDGSAT-1, its potential successor satellites and other infrastructure.

3 Advances in SDGSAT-1 Applications

In the past two years, advances in SDGSAT-1 applications have shown a tendency toward multi-sensor, multi-satellite, and international collaboration. From the launch of SDGSAT-1 in November 2021 to mid-2024, fewer than 3% of SDGSAT-1 publications utilized more than one SDGSAT-1 sensor, whereas from mid-2024 to early 2026, nearly 10% of papers published in this peri-

* https://www.sdgsat.ac.cn/

od have applied multi-sensor synergistic observations. The geographical scope of research has also expanded well beyond China in the past two years, most notably in Europe and in countries across South-Southeast Asia and Africa. Additionally, SDGSAT-1 is recognized as complementary to well-applied EO data sources, such as Sentinel-2, the Landsat series, and Visible Infrared Imaging Radiometer Suite (VIIRS) onboard the suomi National Polar-orbiting Partnership (NPP) satellite, achieving results with improved resolution and accuracy across various fields. The following subsections will introduce the progress of SDGSAT-1 applications in these three directions in detail.

3.1 Multi-sensor Applications

One of the most distinctive features of SDGSAT-1 is its ability to depict research targets in both the thermal and optical domains. For GLI-TIS synergistic observation, the application focuses on the detection of human activities. In a marine context, Qiu *et al*.[25] and Zhang *et al*.[26] have utilized this combination to study light and heat generated by offshore oil and gas platforms, while Zhang *et al*.[27] have fused the GLI and TIS data for ship detection. For the research on the urban thermal environment, Ye *et al*.[28] and Wang *et al*.[29] have applied TIS and GLI to investigate the correlation between urban heat distribution and human activity, as well as the spatial patterns of these phenomena.

For TIS-MSI collaboration, research advances have centered around environmental monitoring. Because MSI is sensitive to vegetation and land surface properties, it can be applied to study parameters correlated with LST variations derived from TIS[30,31]. The unique spectral ranges of TIS and MSI have also facilitated the derivation of critical vegetation health indicators[32], as well as land cover classification[33].

For the three-sensor joint application, Dou *et al*. [34] demonstrated the capability of this approach in monitoring ongoing disasters and conducting comprehensive post-disaster impact assessments. Following this example, SDGSAT-1's three sensors have been applied to monitor the 2025 Los Angeles wildfire[35].

3.2 Multi-satellite Observations

With the accumulation of SDGSAT-1 data, its compatibility with other satellite data has been increasingly exploited. Taking VIIRS Day/Night Band (DNB) data as an example, although GLI has an exceptional spatial resolution, its temporal resolution is significantly outmatched by VIIRS DNB. To combine their strengths, spatiotemporal fusion between VIIRS DNB and GLI has been attempted[36,37], yielding images applicable for global high-resolution nighttime light monitoring.

The combination of Sentinel-2 and SDGSAT-1 data has yielded results in the ecological domain. Gao *et al*.[38] mapped soil salinity patterns using TIS and Sentinel-2 multispectral data. Jiang *et al*.[39] showed that while multispectral data from both SDGSAT-1 and Sentinel-2 are sensitive to river features, delineation results based on SDGSAT-1 achieved better performance, likely due to its deep blue bands. For mangrove monitoring, SDGSAT-1 and Sentinel-2 data have been integrated for canopy height estimation[40] as well as for deriving leaf nitrogen and phosphorus content[41].

In a detailed comparison with Landsat-8/9 data, Xu *et al*.[24] found that SDGSAT-1 data can better depict the complex urban environments due to its higher spatial resolution, while both SDGSAT-1 and Landsat-8/9 data can effectively monitor regional ecological conditions. However, because SDGSAT-1 lacks a mid-infrared band, its data are relatively ineffective for ground wetness inversion.

3.3 Global Impact

The expansion of the SDGSAT-1 Open Science Program user base has led to significant diversification of study areas using SDGSAT-1 data. For Australia[42], Israel[43], Switzerland[44], the United States[45], Italy[46], and other European countries[47], the research focus includes the application of GLI for studying light pollution and the development of advanced data processing techniques.

On the other hand, studies in another group of countries are more concentrated on monitoring socioeconomic status and environmental conditions. In a Colombian study, GLI data were effectively integrated into air quality modelling[48], while the applications of GLI and TIS data of cities in Pakistan[49–51] have yielded insights into electricity consumption and heat-related health risk mapping. Similarly, Indonesian researchers have evaluated streetlight energy efficiency using GLI data[52]. In African countries, GLI[53] and TIS[54] data have been applied to study variations in nighttime light during Sahel conflicts and to support the Great Green Wall initiative, respectively. More broadly, road network illumination levels across much of Africa have been evaluated using GLI data[55].

4 Alliance of Sustainable Development Goals Satellites

To fully utilize existing EO platforms for the global implementation and monitoring of the SDGs, the Alliance of Sustainable Development Goals Satellites (ASSA)[*] was established in 2022. It currently encompasses seven major Chinese EO satellite series: SDGSAT, Haiyang (HY), Fengyun (FY), Huanjing (HJ), Ziyuan (ZY), Guotu (LT), and Gaofen (GF). Comprising over 60 satellites equipped with more than 150 sensors, ASSA delivers all-weather, 24/7 global coverage across multispectral, thermal infrared, and radar spectral domains.

As a public academic organization, ASSA focuses on defining EO service requirements for SDG applications, developing and integrating advanced EO methodologies and frameworks for SDG monitoring and implementation. It serves as an international hub for scientific collaboration and knowledge exchange, fostering dialogue among SDG stakeholders and facilitating the sharing of best practices and operational experience. Two core deliverables include a sustainable development satellite virtual constellation and dedicated SDG monitoring data products. Launched in September 2024, the first phase of the SDG satellite virtual constellation integrates SDGSAT-1, FY-3 E, HJ-2 A, HY-1 C, ZY3-03 and CBERS-04 A. ASSA is actively advancing multi-satellite data fusion and product delivery to strengthen global capacity in addressing challenges associated with SDG progress.

EO technology plays a pivotal role in advancing the 2030 Agenda, as exemplified by SDGSAT-1 and ASSA. They not only provide diverse, high-quality EO datasets for global SDG monitoring and assessment but also serve as an effective tool for investigating Earth system dynamics and human-environment interactions. In this context, during the 80 th United Nations General Assembly in September 2025, Chinese Premier Li Qiang announced at the High-Level Meeting on the Global Development Initiative that China will launch an International Alliance of Sustainable Development Satellites, aiming to provide robust space-based observation data in support of global development[**]. International partners and lite missions are warmly invited to join ASSA, to utilize and expand its collective resources, and to share perspectives on the potential of EO across scientific research and sustainable development sectors.

5 Conclusion

As highlighted in this study, SDGSAT-1 has accomplished fruitful achievements during its operational period from 2024 to 2026 and is poised to continuously generate influential research outcomes in the future. The design and operational framework of SDGSAT-1 represent a pioneering endeavor in Earth observation dedicated to SDG implementation, laying a solid foundation for subsequent follow-up satellite programs. Spearheaded by SDGSAT-1 and CBAS, the ongoing expansion of the sustainable development satellite network and supporting infrastructure will enable Earth observation to play an increasingly pivotal role in global sustainable development initiatives. Such contributions will extend throughout the remaining implementation period of the 2030 Agenda and well into the long-term future.

Acknowledgments The authors would extend their sincere gratitude to the researchers and colleagues within the CASEarth Satellite research teams from various institutes of Chinese Academy of Sciences, including the National Space Science Center, Aerospace Information Research Institute, Innovation Academy for Microsatellites, Changchun Institute of Optics, Fine Mechanics and Physics, Shanghai Institute of Technical Physics, all contributing under the Big Earth Data Science Engineering Program (CASEarth). We also wish to acknowledge the SDGSAT-1 engineering and operations teams, for their continuous support and contributions. The research findings are a component of the SDGSAT-1 Open Science Program, which is conducted by the International Research Center of Big Data for Sustainable Development Goals (CBAS). The data utilized in this study is sourced from SDGSAT-1 and provided by CBAS.

[*] www.assa4sdg.org.cn
[**] https://wwwsatel.globaltimes.cn/page/202509shtml./1344350

References

[1] United Nations. The Sustainable Development Goals Report 2025[R/OL]. (2025-7-14). https://unstats.un.org/sdgs/report/2025/

[2] ZHAO Q, YU L. Advancing sustainable development goals through earth observation satellite data: current insights and future directions[J]. *Journal of Remote Sensing*, 2025, **5**: 0403.

[3] GUO H D, DOU C Y, LIANG D, *et al*. SDGSAT-1: capabilities for monitoring and evaluating SDG indicators[J]. *Chinese Journal of Space Science*, 2024, **44**(4): 677-686

[4] GUO H D, DOU C Y, LIANG D, *et al*. SDGSAT-1: a professional scientific satellite for monitoring SDG indicators[J/OL]. *Proceedings of the IEEE*, (2026-01-12). https://ieeexplore.ieee.org/document/11334168

[5] GUO H D, DOU C Y, LIANG D, *et al*. The SDGSAT-1 mission and its role in monitoring SDG indicators[J]. *Remote Sensing of Environment*, 2025, **328**: 114885

[6] YAN L, HU Y H, DOU C Y, *et al*. Radiometric calibration of SDGSAT-1 nighttime light payload[J]. *IEEE Transactions on Geoscience and Remote Sensing*, 2024, **62**: 1000715

[7] HU Y H, LI X M, DOU C Y, *et al*. Absolute radiometric calibration evaluation of the thermal infrared spectrometer onboard SDGSAT-1[J]. *International Journal of Digital Earth*, 2023, **16**(2): 4492-4511

[8] CUI Z Z, MA C, ZHANG H, *et al*. Vicarious radiometric calibration of the multispectral imager onboard SDGSAT-1 over the Dunhuang calibration site, China[J]. *Remote Sensing*, 2023, **15**(10): 2578

[9] TAN P, LV M Y, GUO H D, *et al*. A misalignments correction method for SDGSAT-1 glimmer imagery based on object detection and cross correlation[J]. *IEEE Transactions on Geoscience and Remote Sensing*, 2025, **63**: 5630013

[10] YIN Z Q, WU M Q, NIU Z, *et al*. Geometric registration of SDGSAT-1 glimmer images guided by OpenStreetMap road network[J]. *IEEE Transactions on Geoscience and Remote Sensing*, 2025, **63**: 5650213

[11] ZHANG H Q, REN H Z, LI F G, *et al*. Atmospheric correction for nighttime light image using radiative transfer model[J]. *IEEE Transactions on Geoscience and Remote Sensing*, 2025, **63**: 4105016

[12] WANG C X, XU W, CHEN Z Q, *et al*. STARS: a novel gap-filling method for SDGSAT-1 nighttime light imagery using spatiotemporal and spectral synergy[J]. *Remote Sensing of Environment*, 2025, **322**: 114720

[13] JIA M M, ZENG H H, CHEN Z Q, *et al*. Nighttime light in China's coastal zone: the type classification approach using SDGSAT-1 Glimmer Imager[J]. *Remote Sensing of Environment*, 2024, **305**: 114104

[14] YAN Y Y, ZHANG R, WANG Z M, *et al*. Classification of nighttime light types in China's nature protected areas based on SDGSAT-1[J]. *International Journal of Digital Earth*, 2025, **18**(1): 2496791

[15] CAO L Q, ZHAO H, WANG D, *et al*. A novel land surface temperature retrieval method using channel correlation for atmospheric parameter modeling from SDGSAT-1 data[J]. *Remote Sensing of Environment*, 2026, **334**: 115190

[16] OUYANG X Y, SUN Z C, ZHOU S G, *et al*. Urban land surface temperature retrieval with high-spatial resolution SDGSAT-1 thermal infrared data[J]. *Remote Sensing of Environment*, 2024, **312**: 114320

[17] ZHONG X, ZHAO L H, REN P, *et al*. Land surface emissivity retrieval from SDGSAT-1: comparison of LSE products with different spatial resolutions[J]. *International Journal of Digital Earth*, 2024, **17**(1): 2297940

[18] ZHOU M, GUO H D, OUYANG X Y, *et al*. Land surface temperature retrieval from SDGSAT-1: assessment of different retrieval algorithms with different atmospheric reanalysis data[J]. *International Journal of Digital Earth*, 2025, **18**(1): 2492314

[19] ZHU M, WANG Q Y, YU J N, *et al*. First assessment of SDGSAT-1 TIS thermal infrared bands calibration using Landsat 9 TIRS-2[J]. *IEEE Journal of Selected Topics in Applied Earth Observations and Remote Sensing*, 2024, **17**: 6224-6232

[20] ZHU M, ZHAO X, ZOU L, *et al*. Cross calibration of SDGSAT-1/TIS thermal infrared bands with FY-4A/AGRI[J]. *IEEE Journal of Selected Topics in Applied Earth Observations and Remote Sensing*, 2024, **17**: 6233-6240

[21] YAN L, QIAO E C, DOU C Y, *et al*. Three-year On-orbit radiometric performance of the SDGSAT-1 multispectral imager (MSI)[J]. *IEEE Journal of Selected Topics in Applied Earth Observations and Remote Sensing*, 2025, **18**: 16707-16721

[22] LI W K, TANG S L, TIAN L Q, *et al*. Assessing on-orbit radiometric performance of SDGSAT-1 MII for turbid water remote sensing[J]. *Remote Sensing of Environment*, 2025, **321**: 114683

[23] JIANG N J, DOU C Y, TANG Y W, *et al*. Derivation of tasseled cap transformation coefficients for SDGSAT-1 Multispectral Imager at-sensor reflectance data[J]. *International Journal of Digital Earth*, 2024, **17**(1): 2413885

[24] XU H Q, SU G F, HE G J, *et al*. Exploring the ecological potential of SDGSAT-1 MII and TIS data: Methods, applications, and comparisons[J]. *Remote Sensing of Environment*, 2025, **330**: 114976

[25] QIU Y J, LI X M, YAN L, *et al*. Synergic sensing of light and heat emitted by offshore oil and gas platforms in the South China Sea[J]. *International Journal of Digital Earth*, 2024, **17**(1): 2441932

[26] ZHANG K L, FU D J, TANG J S, *et al*. Synergistic day-night multi-modal framework for offshore gas flare detection using SDGSAT-1 in the Southeast Asian Seas[J]. *Remote Sensing of Environment*, 2026, **337**: 115337

[27] ZHANG W C, WANG Q Y, LI L Y, *et al*. GTSD: glimmer and thermal infrared remote sensing dataset for night-time ship detection under thin clouds[J]. *International Journal of Digital Earth*, 2025, **18**(1): 2532781

[28] YE L, LONG T F, JIAO W L, *et al*. Fairly assessing nighttime urban cooling performance with a novel satellite-based index[J]. *Sustainable Cities and Society*, 2026, **141**: 107296

[29] WANG Q Y, BIAN J, HU Z Y, *et al*. High-resolution urban heat island analysis using SDGSAT-1 thermal infrared and glimmer data: the case of mainland Shanghai[J]. *International Journal of Digital Earth*, 2025, **18**(2): 2553792

[30] ZHONG X, ZHAO L H, REN P, *et al*. Downscaled high spatial resolution images from automated machine learning for assessment of urban structure effects on land surface temperatures[J]. *Building and Environment*, 2024, **264**: 111934

[31] LIU L S, LI Q Y, NIU Z G, *et al*. Comparative study on information extraction of urban wetlands and its thermal environment using the SDGSAT-1 data[J]. *International Journal of Digital Earth*, 2024, **17**(1): 2310728

[32] FU B L, WU Y, ZHANG S R, *et al*. Synergistic retrieval of mangrove vital functional traits using field hyperspectral and satellite data[J]. *International Journal of Applied Earth Observation and Geoinformation*, 2024, **131**: 103963

[33] FEROZ A, LIANG S, LI G Y, *et al*. Debris-covered glaciers mapping based on machine learning and multi-source satellite images over Eastern Pamir[J]. *Big Earth Data*, 2025, **9**(2): 265-297

[34] DOU C Y, TANG Y W, JIANG N J, *et al*. Analysis of Sichuan wildfire based on the first synergetic observation from three payloads of SDGSAT-1[J]. *The Innovation*, 2024, **5**(6): 100707

[35] UNDRR. Assessment of Los Angeles Wildfire Based on Multi-source Remote Sensing Data[R/OL]. (2025-01-22). https://www.preventionweb.net/publication/assessment-los-angeles-wildfire-based-multisource-remote-sensing-data

[36] ZHANG S Y, MA Y, CHEN H Y, *et al*. The spatiotemporal fusion for nighttime light based on SDGSAT-1 and VIIRS data[J]. *IEEE Transactions on Geoscience and Remote Sensing*, 2025, **63**: 4702919

[37] BIAN J H, AHMAD KHAN T, LI A N, *et al*. A new spatiotemporal fusion model for integrating VIIRS and SDGSAT-1 Night-time light data to generate daily SDGSAT-1 like observations[J]. *International Journal of Digital Earth*, 2025, **18**(1): 2472912

[38] GAO Z R, LI X J, ZUO L J, *et al*. Unveiling soil salinity patterns in soda saline-alkali regions using Sentinel-2 and SDGSAT-1 thermal infrared data[J]. *Remote Sensing of Environment*, 2025, **322**: 114708

[39] JIANG D M D, LI Y M, LIU Q H, *et al*. Evaluating the sustainable development science satellite 1 (SDGSAT-1) multi-spectral data for river water mapping: a comparative study with Sentinel-2[J]. *Remote Sensing*, 2024, **16**(15): 2716

[40] JIA M M, ZHANG R, ZHAO C P, *et al*. Synergistic estimation of mangrove canopy height across coastal China: Integrating SDGSAT-1 multispectral data with Sentinel-1/2 time-series imagery[J]. *Remote Sensing of Environment*, 2025, **323**: 114719

[41] FU B L, WU Y, ZHANG L, *et al*. Cross-scenario transfer learning for estimating mangrove nitrogen and phosphorus content from field hyperspectral data to SDGSAT-1 and Sentinel-2 images[J]. *Remote Sensing of Environment*, 2025, **329**: 114923

[42] LEVIN N, COOPER R M, KARK S. Quantifying night sky brightness as a stressor for coastal ecosystems in Moreton Bay, Queensland[J]. *Remote Sensing*, 2024, **16**(20): 3828

[43] LABROUSSE C, HASPEL C, LEVIN N. Quantifying the impact of the transition to LED lighting on night sky brightness and colour using ground-based measurements and satellite imagery[J]. *Journal of Quantitative Spectroscopy and Radiative Transfer*, 2025, **340**: 109450

[44] WEBER D, BOLLIGER J, ECKER K, *et al*. Night lights from space: potential of SDGSAT-1 for ecological applications[J]. *Remote Sensing in Ecology and Conservation*, 2025, **11**(5): 495-509.

[45] WANG L D, LV M Y, DOU C Y, *et al*. Evaluating the wilderness status of long-distance trails in the United States-Exploring the potential of SDGSAT-1 glimmer imager data[J]. *Remote Sensing of Environment*, 2025, **316**: 114499

[46] PESARESI M, UHL J H, LU L L, *et al*. Compositing high-resolution SDGSAT-1 nighttime light data by ranking of structural image features[J]. *Remote Sensing of Environment*, 2026, **337**: 115313

[47] SÁNCHEZ DE MIGUEL A. SDGSAT-1 EU+UK Plan-B[DS/OL]. (2025-12-18)[2026-04-24]. https://data.europa.eu/data/datasets/oai-zenodo-org-17970082?locale=mt

[48] ANTEZANA LOPEZ F P, CASALLAS A, ZHOU G H, *et al*. High-resolution anthropogenic emission inventories with deep learning in northern South America[J]. *Remote Sensing of Environment*, 2025, **324**: 114761

[49] FAHAD BAQA M, LU L L, WANG S Q, *et al*. How 2D/3D urban form shapes land surface temperature: a comparative analysis across four South Asian cities[J]. *GIScience & Remote Sensing*, 2026, **63**(1): 2640263

[50] KHAN T A, BIAN J H, LI A N, *et al*. Estimation of electric power consumption at 10 m for Punjab, Pakistan, using ensemble machine learning model and spatiotemporal fused SDG-

SAT-1-like nighttime light data[J]. *IEEE Transactions on Geoscience and Remote Sensing*, 2026, **64**: 4701717

[51] BAQA M F, LU L L, GUO H D, *et al*. Investigating heat-related health risks related to local climate zones using SDGSAT-1 high-resolution thermal infrared imagery in an arid megacity[J]. *International Journal of Applied Earth Observation and Geoinformation*, 2025, **136**: 104334

[52] AFRIANTO F, GRAHA D T R, PUSPORINI N, *et al*. Illuminating energy efficiency: satellite-guided insights for optimizing urban street lighting across Indonesian cities[J]. *Indonesian Journal of Energy*, 2025, **8**(1): 16-36

[53] ZHANG Y, LI X. Assessment of central Sahel crisis by nighttime light imagery[J]. *IEEE Journal of Selected Topics in Applied Earth Observations and Remote Sensing*, 2025, **18**: 13359-13371

[54] LI X S, SHEN T, KABO-BAH A T, *et al*. GGW-BDF: an online tool for using earth observation and Chinese ecosystem restoration experiences in support of the Great Green Wall initiative[J]. *International Journal of Digital Earth*, 2024, **17**(1): 2364683

[55] LI J H, WANG Y, HUANG H L, *et al*. Low and uneven rural road lighting coverage in Africa[J]. *Communications Earth & Environment*, 2025, **6**(1): 960

Author Biography

GUO Huadong (Corresponding author) Professor, Academician of the Chinese Academy of Sciences, the Chief Scientist of SDGSAT-1 science satellite, the Director General of the International Research Center of Big Data for Sustainable Development Goals (CBAS), Honorary President of the International Society for Digital Earth (ISDE), Chair of the Digital Belt and Road (DBAR) Program, and a member of the UN 10-Member Group to support the Technology Facilitation Mechanism for SDGs (2018–2021), President of ISDE (2015-2019), President of International Science Council Committee on Data (CODATA 2010-2014), and Chair of International Committee on Remote Sensing of Environment (2018-2019). He specializes in Big Earth Data in support of global sustainable development, radar for Earth observation, and Digital Earth science.
E-mail: hdguo@radi.ac.cn

0254-6124/2026/46(4)-0072-05 *Chin. J. Space Sci.* 空间科学学报

SU Yang, GAN Weiqun. Progress Report on ASO-S: 2024－2026. *Chinese Journal of Space Science*, 2026, **46**(4): 72–76. CSTR:32142.14.cjss.2026–yg08. DOI:10.11728/cjss2026.04.2026–yg08

Progress Report on ASO-S: 2024－2026*

SU Yang GAN Weiqun

(*Division for Dark Matter and Space Astronomy*, *Purple Mountain Observatory*, *Chinese Academy of Sciences*, *Nanjing* 210023)

Abstract This paper report on the progress of the Advanced Space-based Solar Observatory (ASO-S) mission and the related research. ASO-S was launched on 9 October 2022. Since the end of the commissioning phase at the end of July 2023, the three scientific payloads FMG, LST, and HXI have obtained unique datasets of solar activities, including X-ray flares, 360 nm white light flares, Coronal Mass Ejections (CMEs), filament eruptions, Lyα brightenings, *etc*. The data products and event lists have been released. The in-orbit tests and calibrations carried out during the commissioning phase, as well as the early results based on the ASO-S data, a total of 30 papers, were published in a topical collection of Solar Physics between 2023 and 2025. In total, more than 180 papers related to ASO-S have been published.

Key words Space astronomy, Solar physics, Spacecraft, Solar flares, CMEs, Solar X-ray bursts

Classified index P171

1 Introduction

ASO-S is China's first comprehensive solar observatory in space[1–4]. It has three scientific payloads FMG, HXI, and LST, designed to observe solar magnetic field, hard X-ray bursts of flares, 360 nm white light flares, Lyα activities, and CMEs.

This is the fourth report on ASO-S progress during 2024－2026, as a part of the CNCOSPAR national report series. The previous reports[5–7] provided an overview of the ASO-S project, including the history and background of the proposal, the Phase-B, the Phase-C, the Phase-D, the launch, the commissioning phase, and some early research based on ASO-S data.

2 ASO-S Observations and Event Lists

ASO-S has been observing the Sun since its launch in Oct. 2022 and obtained unique datasets of solar activities of the current 25 th solar cycle, including more than 80 X-class flares. A number of event lists have been established or released, such as LST/WST 360 nm white light flares (more than 500 events), LST/SDI Lyman-alpha Solar Flares (more than 5000 events. http://aso-s.pmo.ac.cn/event/sdiFlareListMonthly.jsp), HXI hard X-ray bursts (more than 2100 events. http://aso-s.pmo.ac.cn/hxi_flare/hxi_flare_list.html), and LST/SCI prominence events (http://aso-s.pmo.ac.cn/sodc/sciuvData.jsp). In particular, the list of HXI hard X-ray bursts developed by Fu Yu *et al*. is not only a list of HXI flares, but also an interactive tool (see Figure 1) for browsing the quicklook data of HXI, SDO/AIA, and EOVSA, and for selecting specific flares for statistical studies. In addition, a comprehensive database has been established for Extreme Solar Eruptions (http://aso-s.pmo.ac.cn/event/index.jsp). An example of erupting prominences and the Sun in Lyα is shown in Figure 2.

The payload science teams have been continuously improving data products, calibrations and scientific soft-

* Funded by XDB0560000, XDA15320000, 2022 YFF0503000, NSFC 12333010, NSFC 12233012, NSFC 11921003

Received May 20, 2026

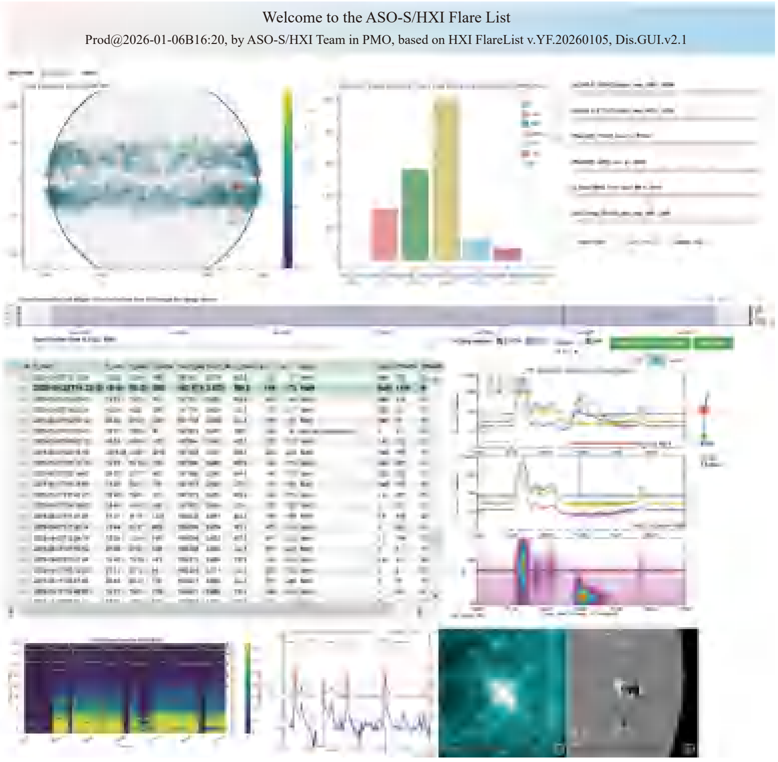

Fig. 1 This screenshot displays the interactive HXI flare list with comprehensive panels of flare parameters, HXI quicklook data, selection tools, EOVSA data, SDO/AIA images, *etc*.

Fig. 2 Composite image presents the simultaneous eruptions of two prominences observed in Lyα by ASO-S/LST payload on 21 Sept. 2025

ware. For example, the HXI team is testing the latest version, V1.50 beta, of the HXI interactive analysis software, which incorporates numerous functional improvements, including imaging speed, imaging quality, a new method of selecting background, a new version of the response matrix, a function for adjusting imaging parameters, *etc*. The calibration for the fine grids of HXI (Groups 1 and 2) is still under testing, at a stage comparable to that for STIX grid groups 1 and 2. LST released Level 1.2 data, which is improved from Level 1 based on a machine learning method [8]. LST also released SCI data of ten events.

Beyond monitoring solar activity, ASO-S has also observed other astronomical events, such as sun-grazing comets. On 4 April 2026, ASO-S/LST/SCI observed the Comet C/2026 A1 (MAPS) within a close distance of ~1.2 to 2.5 solar radii from the Sun's center. Therefore, unique dual-wavelength images of the comet in white light (700 ± 30 nm) and Lyα (121.6 nm) are obtained, providing a valuable opportunity for studying sun-grazing comets and corona.

3 In-orbit Testing and Calibration

Although the commissioning phase concluded at the end of July 2023, the associated papers on in-orbit tests were published intermittently from 2023 to 2025, as part of the topical collection in Solar Physics entitled "ASO-S Mission: Inflight Performance and First Results".

The overview of ASO-S and the first light images are presented in Gan *et al.*[4]. The details of the inflight testing and calibrations carried out during the commissioning phase for the FMG, HXI, and LST payload can be found in BAI *et al*.[9], Su *et al*.[10], and Chen *et al*.[11], respectively. The latest status for the Science Operation and Data Analysis Center (SODC) of ASO-S can be found in HUANG *et al*. [12]. SODC now provides data services to about 150 registered users from 13 countries.

4 Early Results

Here we present a few studies with ASO-S data. Based on the FMG synoptic magnetograms, Chen *et al*. [13] developed a comprehensive analysis tool FastQSL 2 for global magnetic connectivity, which has important applications in identifying magnetic reconnection sites and predicting solar wind speed. LI *et al*.[14] obtained the first Lyα Carrington map based on LST data, a key input for studies of Lyα corona. WANG *et al*.[15] revealed the origin of the October 2024 super geomagnetic storm with the key observations from the ASO-S/LST White-Light Coronagraph, which fills the observational gap between EUV Imaging and traditional coronagraphs from the Earth's perspective. Based on HXI data, CHEN *et al*.[16] did a statistical study of energetic C-class flares, *i.e*., C-class flares with significant X-ray flux above 30 keV, and found that only 5 of the 127 events are associated with CMEs, much lower than the expected rate from standard models and previous studies. This is an important result under the key scientific objectives (the nature of the solar magnetic field, flares, CMEs and their relationship) of ASO-S. More description of the early results of ASO-S can be found in Gan *et al*.[17].

4.1 White Light flares

Jing *et al*.[18] reported, for the first time, the occurrence rate of white-light flares at 360 nm (23.9%), revealing that such flares are not rare. This work was marked by the editor's choice. Jing *et al*.[19] further found that white-light flares in super active regions exhibit unique properties.

4.2 Quasi-Periodic Pulsations (QPP)

QPPs are a common feature of flares seen in different wavelengths. With HXI X-ray data, QPPs have been extensively investigated. For example, Li *et al*. [20] reported QPPs with a long period of about 200 s in HXR, microwave, and Lyα emissions of an X6.4 flare, and the associated sources were identified in HXR images. The long period is probably modulated by the slow magnetoacoustic wave originating from the neighboring sunspot. In another work, Li *et al*.[21] localized the flare QPP at a shorter period of about 1 s in the high-energy channels of HXRs and Gamma-ray continuum during an X9.0 flare, which may be interpreted by the interacting loop model. Ashfield *et al*.[22] investigated spectroscopic and X-ray observations of QPPs in a solar flare and found that the downwards velocities in the flare ribbon are periodically driven by a modulated deposition of accelerated electrons in the chromosphere as a result of repeated reconnection. This work was published in Nature Astronomy in 2026.

4.3 Stereoscopic Studies with ASO-S Data

The launch of ASO-S, in conjunction with Solar Orbiter, has enabled stereoscopic imaging observations of the Sun in both Lyα (LST and Metis) and hard X-rays (HXI and STIX), leading to studies of three-dimensional (3D) properties of flares and eruptions, *e.g.* Ryan *et al*. 2024 [23] and Mrozek *et al*. 2024 [24]. Moreover, Palumbo *et al*. [25] successfully reconstructed the first 3D image of the HXR source in a flare from the HXI and STIX data. Su *et al*. (under review) reported the first detection of strong anisotropy in the flare X-ray emissions received by HXI and STIX and obtained the pitch-angle distributions of the associated energetic electrons. Zhang *et al*.[26] tracked the 3D propagation of an erupted prominence using multi-viewpoint observations from SolO/EUI, ASO-S/LST/SCI, and GOES-16/SUVI. These studies highlight the value and significance of stereoscopic observations and offer scientific guidance for China's future deep-space solar missions, including SPO and LAVSO.

4.4 AI-Empowered Studies

AI has emerged as an increasingly powerful tool in both data processing and scientific research in Astronomy. Related AI methods and models, such as machine learning, have been extensively applied in the ASO-S mission, though so far primarily confined to data processing, feature recognition, and calibration. These works include the calibration of FMG magnetic field data[27,28], the improvement of LST images[8] leading to the production and release of LST level 1.2 data, the first HXR image reconstruction algorithm based on deep learning[29], and AI prediction of background profiles of 91 HXI imaging detectors (Liu *et al*. in prep.).

5 Research Organisation and International Collaborations

The second joint science assembly between ASO-S and CHASE was successfully held in Suzhou on 11-14 May 2025. Over 200 domestic participants attended the event, and 126 presentations were made. This conference has become one of the most important meetings of the solar physics community in China.

ASO-S mission has an open data policy and encourages international collaborations. In 2023, the ASO-S team launched its own program, *i. e.,* the ASO-S Guest Investigator Program (AGIP), to support international collaborations and enhance the scientific output of ASO-S data. By the end of April 2026, AGIP has supported 18 visits (including repeat visits) to the SDOC at Purple Mountain Observatory. These visitors come from seven countries to conduct independent or collaborative research based on or related to ASO-S data. A total of 41.5 man-months have been invested through AGIP, resulting in more than ten papers that are either published or in preparation.

Since the development phase of ASO-S instruments, stable collaborative relationships, regular online discussion mechanisms, and frequent reciprocal visits have been established between the HXI and STIX teams, and between the LST and Metis teams. We believe that international collaborations have been and will always be the best way and the right way for efficiently exploring the universe and conducting scientific research.

6 Conclusions

As the ASO-S continues collecting data of solar activities during the maximum of the 25 th solar cycle, we expect breakthroughs in the upcoming years in studies of flare energy release, energetic electrons, magnetic cause of solar eruptions, nature of white light flares, as well as Lyα enhancements.

Acknowledgement The work is supported by the Strategic Priority Research Program of the Chinese Academy of Sciences (XDB0560000, XDA15320000), the National Key R&D Program of China (2022YFF0503000), and the National Natural Science Foundation of China (12333010, 12233012, 11921003).

References

[1] GAN W Q, ZHU C, DENG Y Y, *et al*. Advanced space-based solar observatory (ASO-S): an overview[J]. *Research in Astronomy and Astrophysics*, 2019, **19**(11): 156

[2] GAN W Q, FENG L, SU Y. A Chinese solar observatory in space[J]. *Nature Astronomy*, 2022, **6**(1): 165

[3] GAN W Q, ZHU C, CHEN B, *et al*. China's first comprehensive space solar observatory[J]. *Chinese Astronomy and Astrophysics*, 2023, **47**(2): 441-445

[4] Gan W Q, Zhu C, Deng Y Y, *et al*. The advanced space−based solar observatory (ASO−S)[J]. *Solar Physics*, 2023, **298**(5): 68

[5] GAN W Q. Status of the advanced space-based solar observatory[J]. *Chinese Journal of Space Science*, 2020, **40**(5): 704-706

[6] GAN W Q. Progress report on ASO-S[J]. *Chinese Journal of Space Science*, 2022, **42**(4): 565-567

[7] GAN W Q. Progress report on ASO-S: 2022-2024[J]. *Chinese Journal of Space Science*, 2024, **44**(4): 687-689

[8] LIU H, LI H, ZOU S Z, *et al*. Improving image quality of the Solar Disk Imager (SDI) of the Lyα Solar Telescope (LST) onboard the ASO-S mission[J]. *Research in Astronomy and Astrophysics*, 2025, **25**(2): 025005

[9] BAI X Y, DENG Y Y, ZHANG H Y, *et al*. Calibration and performance of the Full−disk vector MagnetoGraph (FMG) on board the advanced space−based solar observatory (ASO−S)[J]. *Solar Physics*, 2024, **299**(11): 157

[10] SU Y, ZHANG Z, CHEN W, *et al*. The tests and calibrations of the hard X−ray imager aboard ASO−S[J]. *Solar Physics*, 2024, **299**(10): 153

[11] CHEN B, FENG L, ZHANG G, *et al*. Inflight performance and calibrations of the Lyman-alpha solar telescope on board the advanced space-based solar observatory[J]. *Solar Physics*, 2024, **299**(8): 118

[12] HUANG Y, LI Y P, LIU S, *et al*. Science operation and data analysis center of the advanced space−based solar observatory (ASO−S) mission[J]. *Solar Physics*, 2024, **299**(9): 135

[13] CHEN J, WIEGELMANN T, FENG L, *et al*. FastQSL 2: a comprehensive toolkit for magnetic connectivity analysis[J]. *SCIENCE CHINA Physics, Mechanics & Astronomy*, 2023, **66**(1): 15

[14] LI S T, FENG L, YING B L, *et al*. Carrington maps in H $_{\rm I}$ Lyα and their relationships with extreme-ultraviolet and magnetic-field maps[J]. *The Astrophysical Journal Letters*, 2024, **969**(1): L16

[15] WANG R, HU H D, ZHAO X W, *et al*. A major geomagnetic storm in 2024 October linked to sympathetic coronal mass ejection−prominence eruptions[J]. *The Astrophysical Journal Let-*

ters, 2026, **1002**(1): L23

[16] CHEN C X, SU Y, CHEN W, *et al*. Intense hard X-ray emissions in C-class flares: a statistical study with ASO-S/HXI data[J]. *The Astrophysical Journal Letters*, 2025, **987**(1): L4

[17] GAN Weiqun, SU Yang, FENG Li, *et al*. Brief review on early achievements of ASO-S in orbit[J]. *Science & Technology Review*, 2025, **43**(16): 43-61 (甘为群, 苏杨, 封莉, 等. “夸父一号” (ASO−S) 卫星早期成果概述 [J]. 科技导报, 2025, **43**(16): 43-61)

[18] JING Z C, LI Y, FENG L, *et al*. A statistical study of solar white-light flares observed by the white-light solar telescope of the Lyman-alpha solar telescope on the advanced space-based solar observatory (ASO-S/LST/WST) at 360 nm[J]. *Solar Physics*, 2024, **299**(2): 11

[19] JING Z C, LI Y, LI J W, *et al*. The M- and X-class white-light flares in super active region NOAA 13664/13697 observed by ASO-S/LST/WST[J]. *The Astrophysical Journal*, 2025, **992**(1): 72

[20] LI D, HONG Z X, HOU Z Y, *et al*. Localizing quasiperiodic pulsations in hard X-ray, microwave, and Lyα emissions of an X6.4 flare[J]. *The Astrophysical Journal*, 2024, **970**(1): 77

[21] LI D. Localizing short-period pulsations in hard X-rays and γ-rays during an X9.0 flare[J]. *Astronomy & Astrophysics*, 2025, **695**: L4

[22] ASHFIELD W, POLITO V, LÖRINČÍK J, *et al*. Spectroscopic observations of solar flare pulsations driven by oscillatory magnetic reconnection[J]. *Nature Astronomy*, 2026, **10**(1): 54-63

[23] RYAN D F, MASSA P, BATTAGLIA A F, *et al*. Triangulation of hard X-ray sources in an X-class solar flare with ASO-S/HXI and solar orbiter/STIX[J]. *Solar Physics*, 2024, **299**(8): 114

[24] MROZEK T, LI Z T, KARLICKÝ M, *et al*. Kink-and-disconnection failed eruption in 3D[J]. *Solar Physics*, 2024, **299**(6): 81

[25] Palumbo B, Massa P, Stiefel M Z, *et al*. 3D reconstruction of thermal hard X-ray sources in solar flares from combined STIX and HXI visibilities. *Astronomy & Astrophysics*, 2026, **710**: A105

[26] ZHANG Q M, PAN W W, YING B L, *et al*. Tracking an eruptive intermediate prominence originating from the farside of the sun[J]. *The Astrophysical Journal*, 2025, **985**(2): 237

[27] HU Z Y, JI K F, CHEN J, *et al*. Calibration scheme for spaceborne full-disk vector magnetograph under the influence of orbiter velocity[J]. *Astronomy & Astrophysics*, 2022, **666**: A93

[28] HU Z Y, JI K F, BAI X Y, *et al*. Nonlinear calibration method for FMG line-of-sight magnetic field[J]. *Universe*, 2025, **11**(4): 108

[29] XIA Y H, SU Y, LIU H, *et al*. A new solar hard X−ray image reconstruction algorithm for ASO−S/HXI based on deep learning[J]. *Solar Physics*, 2024, **299**(11): 158

Author Biography

SU Yang Male, born in Tai'an, Shandong on April 10, 1982, is currently a research fellow and lead scientist for ASO-S science at Purple Mountain Observatory, Chinese Academy of Sciences. He is also ASO-S/HXI payload scientist and data scientist. His research focuses on solar physics, hard X-ray imaging and related space astronomy.
E-mail: yang.su@pmo.ac.cn

0254-6124/2026/46(4)-0077-07 *Chin. J. Space Sci.* 空间科学学报

YUAN Weimin, BAO Congying. Einstein Probe: Unveiling the Transient X-ray Universe. *Chinese Journal of Space Science*, 2026, **46**(4): 77–83. CSTR:32142.14.cjss.2026–yg12. DOI:10.11728/cjss2026.04.2026–yg12

Einstein Probe: Unveiling the Transient X-ray Universe

YUAN Weimin BAO Congying

(*On behalf of the Einstein Probe team*)

(*National Astronomical Observatories*, *Chinese Academy of Sciences*, *Beijing* 100101)

Abstract The Einstein Probe (EP), a Chinese-led international X-ray astronomy mission with key contributions from ESA, MPE, and CNES, is advancing time-domain astrophysics through its unprecedented wide-field soft X-ray monitoring capability to discover and characterize cosmic X-ray transients. Launched in January 2024, EP carries two complementary instruments: the Wide-field X-ray Telescope (WXT), which employs lobster-eye micro-pore optics to monitor approximately 11% of the sky with exceptional sensitivity, and the co-aligned Follow-up X-ray Telescope (FXT), which provides high-resolution imaging, spectroscopy, and timing observations for rapid follow-up studies. During more than two years of in-orbit operations, EP has detected over 230 X-ray transients, including Tidal Disruption Events (TDEs), gamma-ray bursts (GRBs), rare compact binary systems, and previously unknown types of transients, thereby opening a new observational window for high-energy time-domain astrophysics. Major scientific achievements include the first demonstration of lobster-eye micro-pore focusing X-ray imaging over an extremely large field of view, the discovery of an intermediate-mass black hole through a tidal disruption event, the detection of a high-redshift gamma-ray burst with complex soft X-ray precursor emission, the identification of a weakly relativistic jet associated with a type Ic-BL supernova, and the discovery of unusual X-ray transients that highlight previously unrecognized manifestations of stellar collapse and compact-object interactions. These discoveries provide new insights into some of the most energetic and rapidly evolving astrophysical phenomena, ranging from stellar explosions and relativistic jets to tidal disruption events and black-hole accretion. Enabled by its unique instrumentation, autonomous rapid-response capability, and extensive international collaboration, EP is expected to continue delivering major discoveries and to remain a major facility for time-domain and multi-messenger astrophysics.

Key words Einstein Probe, Wide-field X-ray survey, Time-domain astronomy, X-ray transients, Lobster-eye optics, Multi-messenger astrophysics

Classified index P172.4, P145.8

1 Mission Overview

The Einstein Probe (EP), designated “Tianguan” in Chinese, represents an international collaboration in X-ray astronomy led by the Chinese Academy of Sciences (CAS) with key contributions from ESA, MPE, and CNES. Launched on 9 January 2024, *via* an LM-2C rocket from the Xichang Satellite Launch Centre, the 1.4-ton satellite occupies a 570 km low-Earth orbit with a 96-minute period, with a nominal 3-year operational lifetime and a goal extended to 5 years.

EP’s scientific payload features two synergistic instruments: the Wide-field X-ray Telescope (WXT) employs 12 lobster-eye modules to achieve an unprecedented 3850 square degrees field of view (approximately 11% of the sky) with 5-arcmin resolution at 0.5–4 keV,

Received May 20, 2026

delivering a 1–2 orders of magnitude sensitivity improvement over prior monitors. The co-aligned Follow-up X-ray Telescope (FXT) utilizes dual conventional Wolter-I mirrors providing >300 cm^2 effective area each at 1.5 keV and sub-30-arcsecond resolution, enabling precision localization and spectral and timing studies[1]. An artist's impression of the Einstein Probe in space is shown in Figure 1.

These capabilities directly support EP's core science objectives: (i) to discover and characterize cosmic X-ray transients, particularly faint, distant and rare types of X-ray transients, in large numbers; (ii) to discover and characterize X-ray outbursts from otherwise normally dormant black holes; (iii) to search for X-ray sources associated with gravitational-wave events and precisely locate them.

2 In-orbit Performance and Science Capabilities

Following its launch, EP demonstrated robust operational capabilities through efficient power management and precise attitude control. During the six-month commissioning phase, the WXT and FXT completed comprehensive in-orbit calibrations while validating the satellite's capacity for coordinated observations and autonomous rapid-response maneuvers. This phase ended with formal science verification on 22 July 2024, transitioning EP to routine operations while already delivering significant early results. Instrument verification confirms all specifications are exceeded. The specifications for the WXT and FXT models are shown in the Table 1.

On 27 April 2024, EP released its first-light images. The initial observations, which targeted the Galactic Centre, M87, Omega Centauri, and the Crab Nebula, successfully validated EP's dual instrumentation capabilities, demonstrating the capabilities of WXT's panoramic imaging and high sensitivity, as well as FXT's excellent light-collecting power, imaging quality and spectral resolution, large field-of-view for Wolter-I-type X-ray telescope, and millisecond timing resolution.

EP's commissioning and early observations have demonstrated its excellent science capabilities, including a large field of view and high sensitivity, a novel detecting window in soft X-rays, powerful follow-up capabilities, fast two-way spacecraft-ground telecommunications, and quick response and flexible observation scheduling. The unparalleled combination of such capabilities makes EP a promising game-changer in the field of high-energy time-domain astrophysics. This promise has been partly demonstrated by the exciting discoveries achieved already in the one and a half years of EP operations.

3 Science Operations

The EP Science Center (EPSC) is responsible for the sci-

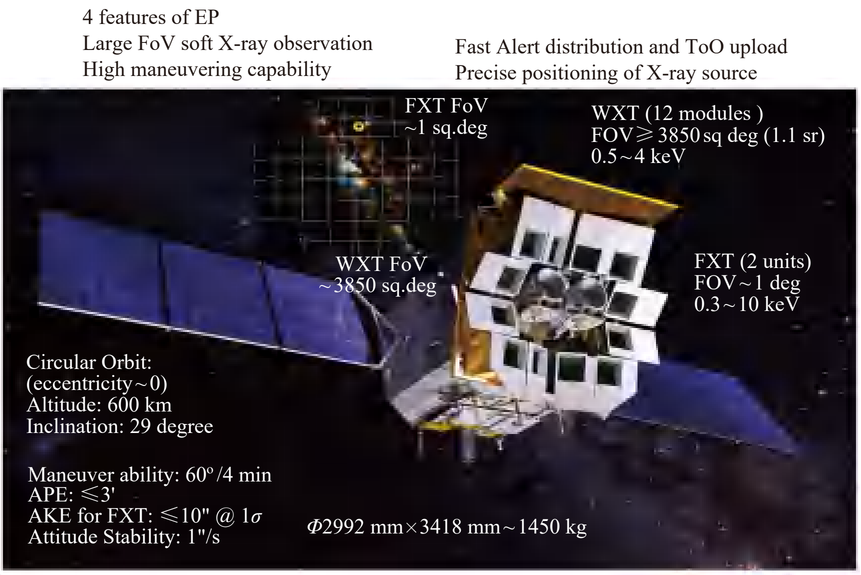

Fig. 1 Artist's impression of the Einstein Probe in space (Credit: IAMCAS)

Table 1 Specifications of the instruments

Parameters	Wide-field X-ray telescope	Follow-up X-ray telescope
Number of modules	12	2
Telescope optic	lobster-eye MPO	Wolter-I
Detector	CMOS	pn-CCD
Field of view	⩾3600 square degrees	⩾60′ (diameter)
Focal length /mm	375	1600
Effective area/ cm^2 (@1.25 keV)	2–3	~300 (one unit)
Spatial resolution (@1 keV)	5′ (FWHM)	20″–24″ (HPD, on-axis)
Bandpass /keV	0.5–4	0.3–10
Energy resolution /eV	122 @1.25 keV	100 @1.5 keV
Limiting flux /($erg \cdot s^{-1}\ cm^{-2}$)	~8.9×10^{-10} (27.65 mCrab) @10 s ~1.2×10^{-10} (3.9 mCrab)@100 s ~2.6×10^{-11} (0.8 mCrab)@1 ks	~1×10^{-14} @10 ks
Time resolution	50 ms (full-frame)	50 ms (full-frame) 2 ms (partial window) 42 μs (timing)

Note The typical limiting fuxes in 0.5-4 keV are derived for a point like source from simulations, assuming a power-law spectrum with a photon index of 2 and a Galactic absorption column 3×10^{20} cm^{-2}, MPO: micro-pore optics: FWHM: full width at half maximum, HPD half-power diameter mCrab: 1/1000 of the strength of the X-ray flux of the Crab nebular.

ence operations of the mission, including the planning and scheduling of EP observations, instrument calibration and health monitoring, data reduction and analysis of quick-look data, transient alerts handling and dissemination, ToO proposal handling, and user support. EPSC is operated predominantly at the National Astronomical Observatories, CAS (NAOC) and partly at Institute of High Energy Physics (IHEP), CAS for the operations of FXT.

EP employs dynamically prioritized observation modes. During survey operations, WXT executes 3 sequential 20-minute pointings per orbit, achieving full night-sky coverage every 3 orbits and completing all-sky mapping within six months. Simultaneously, FXT conducts Survey Target Observations (FSTOs) by observing an object close to the nominal pointing direction and selected from pre-approved targets in the annual call for proposals (currently, cycle-2 observations just started). Both modes remain interruptible by higher-priority events. When WXT detects transients exceeding onboard thresholds, the satellite immediately enters autonomous follow-up mode, terminating ongoing low-priority observations, slewing to the target coordinates, and initiating tiered FXT exposures lasting from one to several orbits. Meanwhile, the transient information, including the source coordinates, time and X-ray fluxes, is sent to EPSC in real-time *via* the Beidou satellite navigation system as well as the VHF system provided by CNES. Target-of-Opportunity (ToO) observations can be requested by EP users by submitting proposals to EPSC, which will be reviewed and, if approved, scheduled and executed. Time-critical ToO observations can be performed within 10 minutes of approval *via* BeiDou. Throughout all modes, WXT maintains persistent monitoring. The complete science and housekeeping datasets are downlinked *via* X-band, received by one of the ground stations at Sanya, Singapore, and Western Australia (the service of the latter stations is two provided by ESA).

EP starts to establish collaborations with other facilities to develop standardized response protocols, which will enable coordinated multi-wave studies aimed at maximizing the scientific yield from transient detections.

To date, EP has issued over 400 alerts through GCN and ATel circulars, which have prompted rapid multi-wavelength follow-up campaigns at by many space and ground-based telescopes, large and small, including Swift, XMM-Newton, NICER, NuSTARS, VLT, HST, JWST, ZTF, GMT, SALT, LCOGT, ALMA, VLA, ATCA, MeerKAT, demonstrating the broad interests of the astronomy community in transients discovered by EP.

4 Scientific Highlights

First realization of lobster-eye micro-pore focusing imaging with extremely large field of view (see Figure 2). EP-WXT achieved, for the first time, long-awaited lobster-eye micro-pore focusing imaging observations with a huge field of view of thousands of square degrees.

EP240222 a (22 Feb. 2024). An intermediate-mass black hole of several tens of thousands solar masses lurking in the halo of a nearby large galaxy, caught alive *via* tidally disrupting a star [2].

EP240315 a (15 Mar. 2024). A high-redshift (z=4.859) GRB exhibiting complex soft X-ray variability preceding and following the γ-ray emission, demonstrating WXT's capability to trace GRB evolution[3].

EP240408 a (8 Apr. 2024). Intermediate-timescale transient featuring a 12-second flare (300× flux increase) with anomalous spectral-temporal properties, suggesting a new transient class[4].

EP240414 a (14 Apr. 2024). Extragalactic transient (z=0.401) associated with type-Ic supernova SN 2024 gsa, revealing a weakly relativistic jet from massive stellar collapse—a new category distinct from the known GRB-supernova association[5]. Figure 3 shows the rest-frame peak energy–isotropic energy correlation (Amati relation).

J005245.1-722843 (27 May 2024). A rare binary consisting of a Be star and a white dwarf in the Small Magellanic Cloud caught through outburst, providing the first full thermonuclear flash light curve from a near-Chandrasekhar-mass O-Ne white dwarf accreting from a 12 M_S companion[6].

EP J182730.0-095633/EP240904 a(4 Sept. 2024). A new candidate black hole in a binary system in the Milky Way was unveiled *via* capturing a faint outburst[7].

EP241021 a (21 Oct. 2024). a new type of X-ray transient with month-duration evolution timescales with possible origin from a tidal disruption event with relativistic jet or unusually long-duration GRB[8].

LXT230307 a (7 Mar. 2023). The EP pathfinder LEIA (Lobster Eye Imager for Astronomy) detected the prompt X-ray emission likely originated from a temporary highly magnetized neutron star resulting from merger of two neutron stars, which was accompanied by a long GRB[9]. Figure 4 shows the multi-band light curve and spectral energy distribution obtained from the coordinated observations by LEIA and GECAM.

EP250702 a (2 Jul. 2025). X-ray precursor hours before gamma-ray emission, peak luminosity of 3×10^{49} erg·s^{-1}, and brightness decline by over five orders of magnitude within 20 days; one of the most plau-

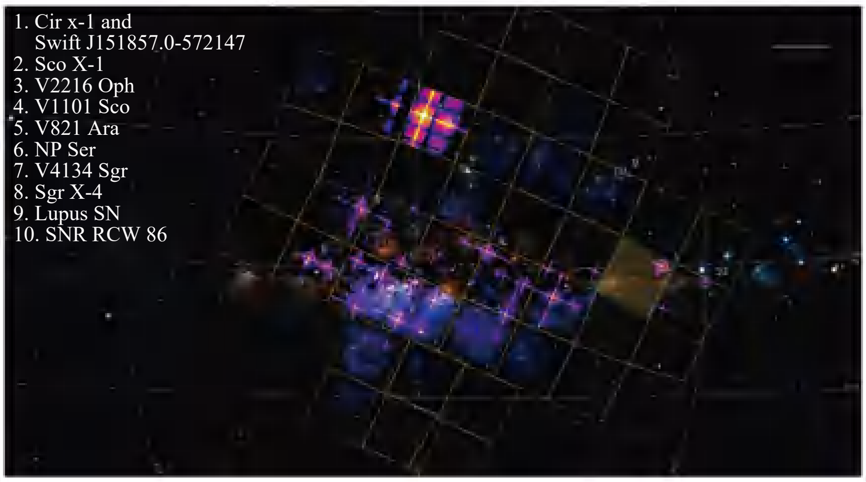

Fig. 2 Observation of WXT pointed to the center of the Milky Way Galaxy with an exposure time of about 4×10^4 s. The X-ray sources are drawn with color purple, which is stacked with Digitized Sky Surveys image provided by the Association of Universities for Research in Astronomy, Inc. The squares outline the field of view of WXT, mosaicked by 12 modules composed of 4 CMOS sensors each (Credit: EPSC/NAOC) (DSS image credit: AURA)

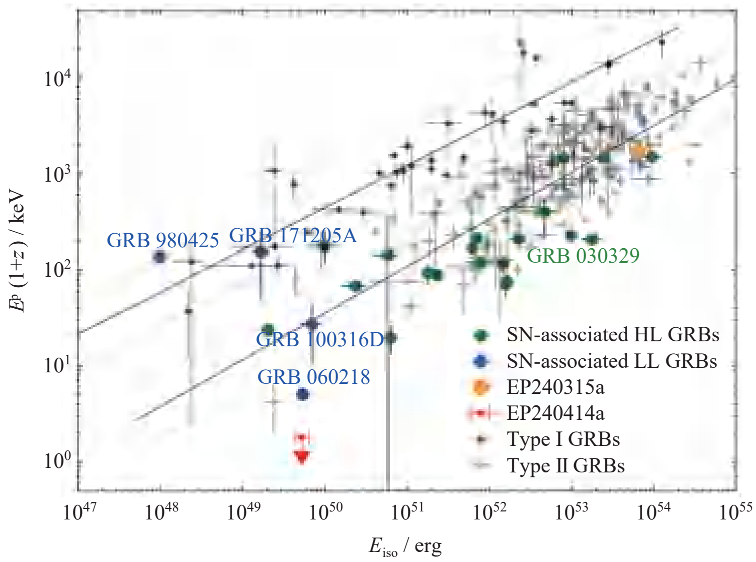

Fig. 3 Rest-frame peak energy and isotropic energy correlation (Amati relation). EP240414 a is a significant outlier compared with classical GRBs and some low-luminosity GRBs

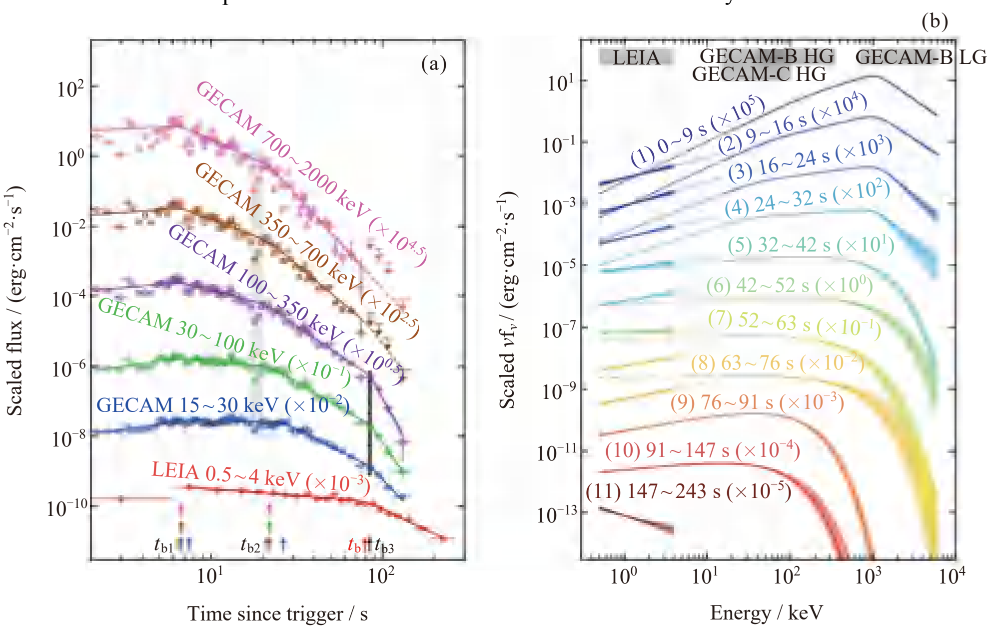

Fig. 4 Multi-band light curve and spectral energy distribution obtained by the coordinated observation by LEIA and GECAM

sible interpretations is a white dwarf disrupted by an intermediate-mass black hole (10^2–10^5 M_S), a scenario distinct from classical tidal disruption events and gamma-ray bursts[10]. Figure 5 shows EP250702 a's X-ray light curve (with comparisons) and spectral softening.

During the past more than two years of operations since launch, EP has detected more than 230 X-ray transients with high significance, including ~177 fast transients (Figure 6), and over 1800 stellar flares. Some of these transients can only be detected with EP, showcasing its unique ability to detect and characterize fleeting cosmic events. EP is expected to provide valuable insights into the fundamental physics that governs extreme astrophysical environments, ranging from violent stellar deaths to the formative periods of primordial stars and galaxies.

More information on the mission can be found at the EP website*.

* https://ep.bao.ac.cn

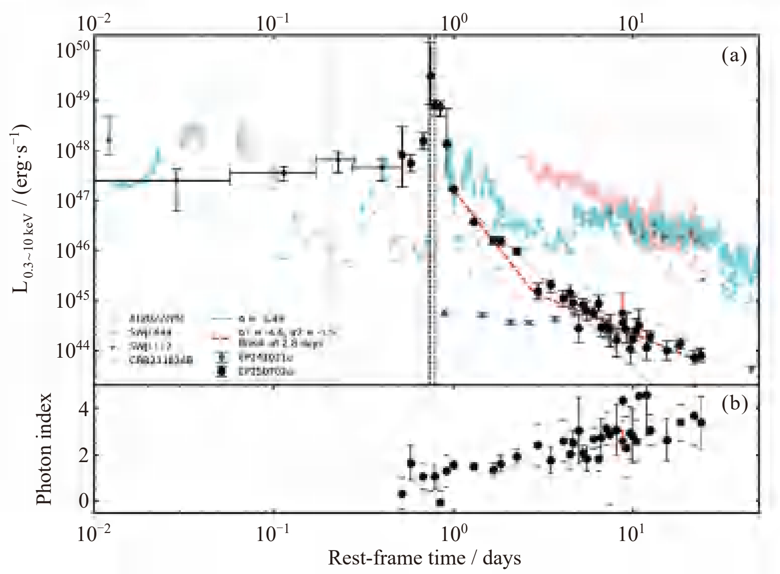

Fig. 5 (a) Long-term X-ray light curve of EP250702 a compared with other X-ray transients, including jetted TDEs, an ultra-long GRB, and a jetted TDE candidate EP241021. (b) Spectral softening of EP250702 a, as indicated by the temporal evolution of the photon index derived from absorbed power-law fits to the X-ray spectra[10]

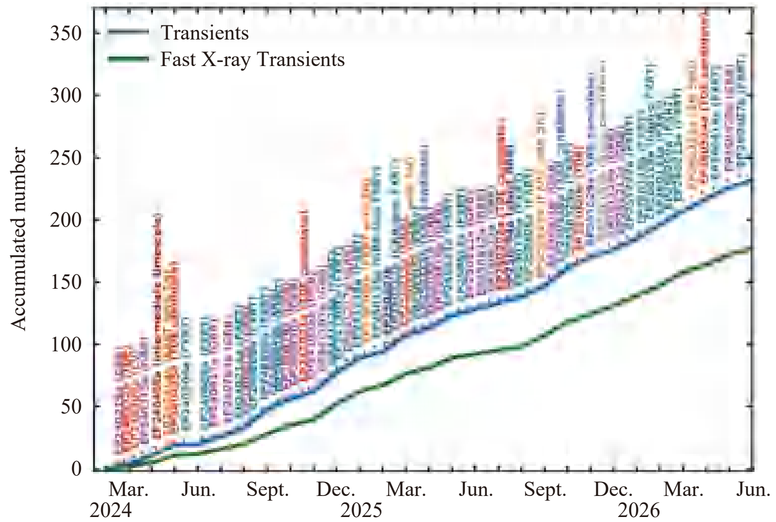

Fig. 6 Increasing number of X-ray transients detected by Einstein Probe since launch. So far, more than 230 X-ray transients have been detected, yielding a detection rate of about 100 transients per year. Selected sources that have been studied extensively are labeled

References

[1] YUAN W M, DAI L X, FENG H, *et al*. Science objectives of the Einstein Probe mission[J]. *Science China Physics, Mechanics & Astronomy*, 2025, **68**(3): 239501

[2] JIN C C, LI D Y, JIANG N, *et al*. An intermediate-mass black hole lurking in a galactic halo caught alive during outburst[OL]. arXiv preprint arXiv: 2501.09580, 2025

[3] LIU Y, SUN H, XU D, *et al*. Soft X-ray prompt emission from the high-redshift gamma-ray burst EP240315a[J]. *Nature Astronomy*, 2025, **9**(4): 564-576

[4] ZHANG W D, YUAN W M, LING Z X, *et al*. *Einstein Probe* discovery of EP240408a: A peculiar X-ray transient with an intermediate timescale[J]. *Science China Physics, Mechanics & Astronomy*, 2025, **68**(1): 219511

[5] SUN H, LI W X, LIU L D, *et al*. A fast X-ray transient from a weak relativistic jet associated with a type Ic-BL supernova[J]. *Nature Astronomy*, 2025, **9**: 1073-1085

[6] MARINO A, YANG H N, COTI ZELATI F, *et al*. Einstein probe discovery of EP J005245.1-722843: A rare be-white dwarf binary in the small magellanic cloud?[J]. *The Astrophysical Journal Letters*, 2025, **980**(2): L36

[7] CHENG H Q, ZHAO Q C, TAO L, *et al*. Einstein probe discovery of EP J182730.0-095633: A new black hole X-ray binary candidate in faint outburst?[J]. *The Astrophysical Journal Letters*, 2025, **991**(2): L41

[8] SHU X W, YANG L, YANG H N, *et al*. EP241021a: A months-duration X-ray transient with luminous optical and radio emission[J]. *The Astrophysical Journal Letters*, 2025, **990**(1): L29

[9] SUN H, WANG C W, YANG J, *et al*. Magnetar emergence in a peculiar gamma-ray burst from a compact star merger[J]. *National Science Review*, 2025, **12**(3): nwae401

[10] LI D Y, ZHANG W D, YANG J, *et al*. A fast powerful X-ray transient from possible tidal disruption of a white dwarf[J]. *Science Bulletin*, 2026, **71**(3): 538-546

Author Biography

YUAN Weimin Professor at the National Astronomical Observatories, Chinese Academy of Sciences (NAOC, CAS), and the Principal Investigator of the Einstein Probe mission. His research focuses on X-ray astronomy, high-energy astrophysics, and space instrumentation. He received his Ph.D. in Physics from the Technical University of Munich and the Max Planck Institute for Extraterrestrial Physics (MPE), Germany, in 1998. Dr. Yuan has led the Einstein Probe mission from its proposal and mission design to scientific operations, making significant contributions to the development of wide-field X-ray imaging based on lobster-eye optics and the exploration of the dynamic X-ray universe.
E-mail: wmy@nao.cas.cn

0254-6124/2026/46(4)-0084-18 *Chin. J. Space Sci.* 空间科学学报

WANG Chi, ESCOUBET Philippe, FORSYTH Colin, DAI Lei, REN Yong, LI Jing, LI Huawang, KONG Linggao, WANG Jindong, WANG Yongmei. Recent Scientific Progress and Mission Update for the Solar Wind Magnetosphere Ionosphere Link Explorer (SMILE). *Chinese Journal of Space Science*, 2026, **46**(4): 84-101. CSTR:32142.14.cjss.2026-yg10. DOI:10.11728/cjss2026.04.2026-yg10

Recent Scientific Progress and Mission Update for the Solar Wind Magnetosphere Ionosphere Link Explorer (SMILE)*

WANG Chi[1] ESCOUBET Philippe[2] FORSYTH Colin[3] DAI Lei[1]
REN Yong[1] LI Jing[1] LI Huawang[4] KONG Linggao[5,1]
WANG Jindong[1] WANG Yongmei[1]

1(*National Space Science Center*, *Chinese Academy of Sciences*, *Beijing* 100190)

2(*European Space Agency/European Space Research and Technology Centre*, *Noordwijk* 2201 *AZ*)

3(*Mullard Space Science Laboratory*, *University College London*, *London RH5 6 NT*)

4(*Innovation Academy for Microsatellites*, *Chinese Academy of Sciences*, *Shanghai* 201304)

5(*Institute of Science and Technology for Deep Space Exploration*, *Suzhou Campus*, *Nanjing University*, *Suzhou* 215163)

Abstract The Solar Wind Magnetosphere Ionosphere Link Explorer (SMILE) mission aims to study solar wind-magnetosphere-ionosphere coupling globally. This review summarizes recent scientific progress and mission status relevant to future SMILE observations. The focus is on dayside magnetopause and cusp dynamics, soft X-ray image interpretation, magnetic-reconnection-driven convection, and storm-substorm coupling. The recent progress of the SMILE platform, payloads, ground segment, and commissioning plan is also briefly reviewed. These studies and mission developments provide the physical and observational basis for interpreting SMILE observations during the early science phase and beyond.

Key words SMILE, Soft X-ray imager, Ultra-violet Imager, Light ion analyzer, Magnetometer, Storm-substorm coupling, Magnetospheric convection, Magnetosheath transients

Classified index P353

1 Introduction

Understanding and predicting the nonlinear, system-level behavior of Earth's magnetosphere remains a grand challenge in solar-terrestrial physics. *In situ* measurements have greatly advanced our knowledge of localized plasma processes. However, it remains difficult to assemble these local processes into a coherent global picture of magnetospheric dynamics. This difficulty is especially important for the solar wind-magnetosphere-ionosphere system, where the evolution depends on multiscale energy and mass transport and on coupling among different regions. Large-scale structures, including the bow shock, magnetopause, magnetosheath, cusps, and auroral oval, respond continuously to changes in solar wind dynamic pressure and interplanetary mag-

* Funded by the Strategic Priority Research Program on Space Science, the Chinese Academy of Sciences (XDA15350000)
Received May 20, 2026

netic field orientation. A key challenge, therefore, is to move from local descriptions of individual plasma processes toward a global and time-dependent view of the geospace system[1,2].

The Solar Wind Magnetosphere Ionosphere Link Explorer (SMILE) mission is designed to close this system-level observational gap. It combines global imaging with *in situ* measurements. SMILE carries four instruments: the Soft X-ray Imager, the Ultraviolet Imager, the Light Ion Analyzer, and the Magnetometer. These instruments will obtain soft X-ray images of the dayside magnetosheath and cusps, ultraviolet images of the northern auroral oval, and simultaneous *in situ* measurements of plasma and magnetic fields. The Soft X-ray Imager observes solar wind charge exchange emissions. Their main near-Earth sources are the magnetosheath and cusps. The magnetopause is not observed directly, but can be inferred from intensity structures in the soft X-ray images. In this way, SMILE directly addresses three mission-level questions: the fundamental modes of dayside solar wind-magnetosphere interaction, the substorm cycle, and the origin of coronal-mass-ejection-driven storms and their relationship to substorms[1,2].

Although routine SMILE science images are not yet available, recent simulation and observational studies have already provided important physical context for future SMILE observations. These studies are closely related to the mission's three science questions. They also address key processes in solar wind-magnetosphere-ionosphere coupling. The main topics include dayside boundary dynamics and structure, magnetosheath transients and magnetopause deformation, convection-driven current-system reorganization, and storm-substorm coupling with associated ionospheric and inner-magnetospheric responses. Accordingly, this review focuses on recent scientific progress from 2024 to 2026 in these areas and provides a brief update on the SMILE mission status, including platform and payload development, instrument testing, ground-segment preparation, launch activities, and in-orbit commissioning.

2 Recent Scientific Progress

2.1 Magnetosheath Transients, Soft X-ray Imaging, and Magnetopause Distortion

On the dayside, solar-wind plasma is first processed at the bow shock. It then flows through the magnetosheath and interacts with the magnetopause and cusp regions. This sequence forms a spatially structured and dynamically variable interaction region[3,4]. A key issue for SMILE observations is that SXI records line-of-sight-integrated soft X-ray emission produced by solar wind charge exchange. It does not image the magnetopause surface directly. The observed morphology therefore reflects both the three-dimensional boundary geometry and the soft-X-ray emissivity distribution along the line of sight. Localized brightening, reconstructed boundary displacement, and cusp-related signatures may have several causes. These include magnetosheath high-speed jets and jet-driven bow waves[5], shock-discontinuity-interaction structures and large-scale magnetopause distortion, storm-time density and speed enhancements with magnetospheric compression, and IMF-By-controlled cusp twisting.

Recent simulations of magnetosheath High-Speed Jets (HSJs) provide a physical basis for interpreting localized soft-X-ray enhancements in the magnetosheath. Ouyang *et al.*[5] used two-dimensional hybrid simulations to investigate HSJs and Bow Waves (BWs) downstream of quasi-parallel bow shocks, and compared the hybrid results with Particle-in-Cell (PIC) simulations under similar setups. Their results show that HSJs can compress the downstream magnetosheath/background plasma, produce local density increases and magnetic pileup, and eventually drive bow waves. Using the simulated H^+ flux and a geocoronal hydrogen distribution, they estimated the soft-X-ray intensity from the bow shock to the magnetopause and found that the soft-X-ray flux associated with HSJs and bow waves is more than one order of magnitude higher than that of the surrounding background magnetosheath plasma. This suggests that SMILE/SXI may distinguish signal differences between background magnetosheath plasma and HSJ-related structures, although realistic line-of-sight integration and exposure-time effects require further modeling.

Guo *et al.*[6] extended the discussion from local shock-scale simulations to a three-dimensional global hybrid simulation of SDI-driven magnetosheath jets, magnetopause response, and synthetic soft-X-ray signals. Their results show that Shock-Discontinuity Interactions (SDIs) deform the bow shock and redirect the solar-wind flow with little deceleration, producing ribbon-like jets flanking the core of a Hot Flow Anomaly (HFA) (Figure 1). These jets span the entire dayside magnetosheath and reach ～40 R_E (Earth radius) along the discontinuity. The SDI-driven structures produce large-scale magnetopause distortion, with amplitudes up to ～5 R_E and along-discontinuity extents of ～17 R_E. The study further derived soft-X-ray intensity from a line-of-sight integral of the emissivity and presented synthetic X-ray images. In these images, a pronounced intensity cavity appears at the HFA core, flanked by regions of enhanced X-ray intensity corresponding to the jets. This result links SDI-driven magnetosheath jets, magnetopause distortion, and synthetic soft-X-ray images.

Storm-time magnetopause compression introduces another important limitation for SXI image interpretation. Gong *et al*.[3] simulated dynamic soft-X-ray images generated by SWCX in the Earth's magnetosheath and cusps during the super storm of 10–11 May 2024, using the PPMLR-MHD model and photon-count images derived from SXI simulations. Their analysis evaluated the SXI simulation and the Tangent Fitting Approach (TFA) for reconstructing the 3 D structure of the magnetopause under dynamic and non-standard solar wind conditions. The results show that, when the magnetopause is within the FOV, the subsolar magnetopause can be reconstructed with errors within 0.5 R_E. However, under extreme solar wind conditions, the magnetopause location is compressed to 4.9 R_E (Figure 2), which exceeds the FOV of SXI. The limited FOV of SXI and the vignetting effect in SXI imaging therefore need to be considered carefully when interpreting storm-time SXI images and applying boundary tracing methods.

The dayside boundary also includes processes that are not purely magnetosheath transients. Zhang *et al*.[7] reported an O^+-rich ion diffusion region in dayside magnetopause reconnection during the May 2024 superstorm, showing that storm-enhanced ionospheric O^+ can reduce the reconnection rate. Gong *et al*. [6] further showed that the cusp boundary exhibits altitude-dependent three-dimensional twisting controlled by IMF B_y (the y-component of the interplanetary magnetic field), with the twisting angle increasing with both altitude and B_y.

These results support a time-dependent view of the dayside boundary. Because SXI measures line-of-sight-integrated solar wind charge exchange emission, the observed soft X-ray morphology is not a direct map of the magnetopause. It reflects the large-scale geometry of the magnetopause and cusps. It also reflects magnetosheath emissivity variations associated with plasma density and flow structures. Localized enhancements or boundary-

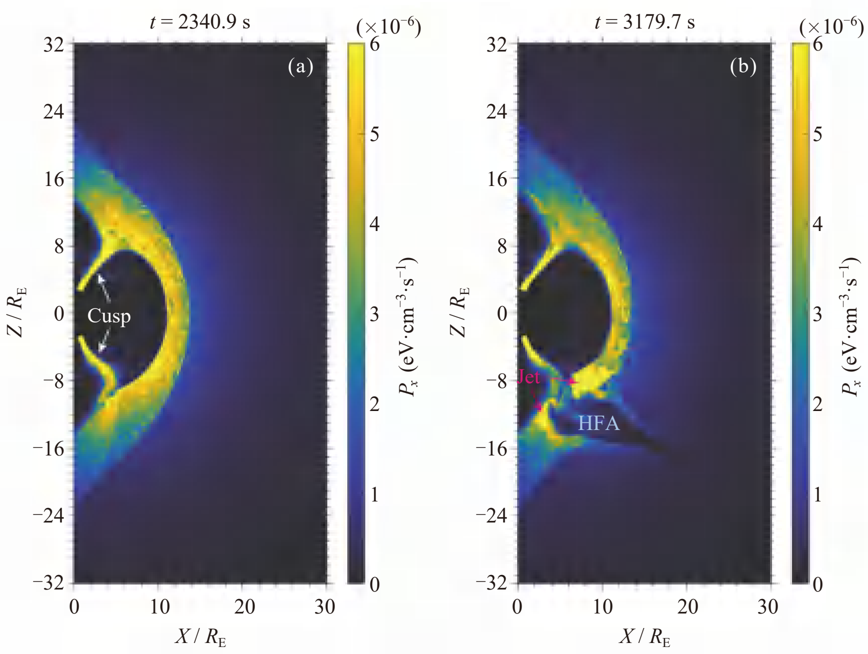

Fig. 1 X-ray image from a lunar-based soft X-ray imager based on a three-dimensional global hybrid simulation[4]

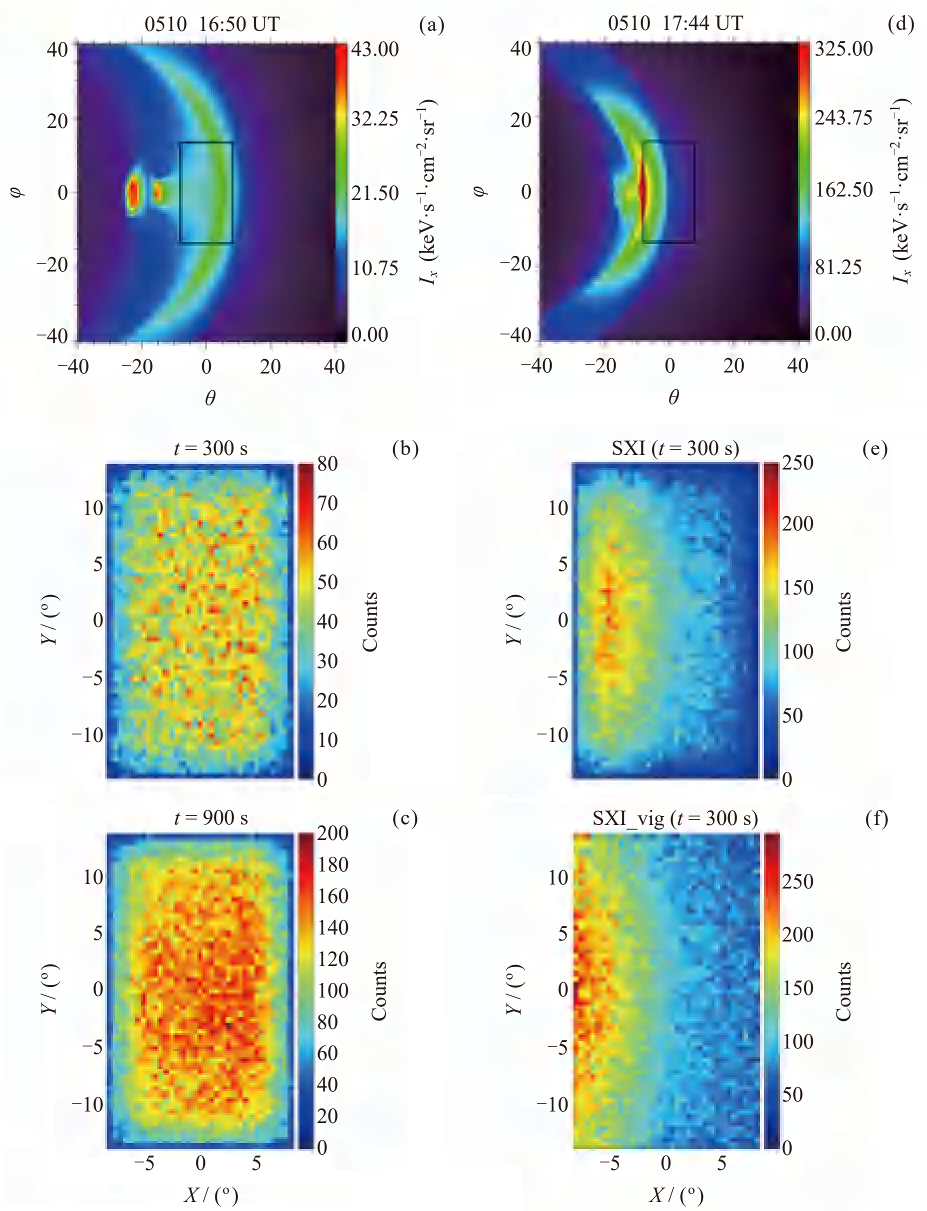

Fig. 2 Soft X-ray images and SXI photon-count images under a special viewing geometry (0510 denotes May 10). Panels (a)–(c) correspond to low solar wind number density: (a) shows the MHD-simulated X-ray image, and (b)–(c) show the SXI photon-count images with exposure times of 300 s and 900 s, respectively. Panels (d)–(f) correspond to high solar wind number density: (d) shows the MHD-simulated X-ray image, (e) shows the SXI photon-count image without the vignetting function, and (f) shows the SXI photon-count image with the vignetting function[3]

like features may therefore have multiple origins. They may trace magnetopause or cusp structures. They may also be influenced by high-speed jets and jet-driven bow waves, shock-discontinuity-interaction-driven jets around a hot flow anomaly core, cusp boundary twisting, storm-time compression, or reconnection-driven erosion of the dayside magnetosphere. The 2024–2026 studies reviewed here provide a physical basis for linking future SXI images to specific dayside boundary processes. They also show that soft X-ray intensity structures should not always be treated as direct boundary traces. UVI auroral imaging provides a complementary diagnostic by indicating whether a dayside disturbance is accompanied by an ionospheric response.

2.2 Reconnection-driven Magnetospheric Convection and Current-system Evolution

Dayside magnetopause reconnection allows solar wind energy and magnetic flux to enter the magnetosphere-ionosphere system[8,9]. Recent studies show that dayside reconnection can directly drive enhanced magnetospheric convection of closed field lines. The convection pattern and associated Region 1 and Region 2 field-aligned currents progress from the dayside to the nightside within about 10–20 min[8-10]. This subsection focuses on how dayside-driven magnetospheric convection is coupled to the evolution of Region 1 and Region 2 field-aligned currents[8,9]. It also discusses its connection to ionospheric two-cell convection and the associated DP-2 current[8,11]. Finally, it considers how large-scale convection electric fields penetrate into the inner magnetosphere[9,12].

Dai *et al.*[8] provide key simulation and observational evidence for this picture (Figure 3). Using global magnetohydrodynamic simulations and magnetosphere-ionosphere observations, they showed direct evidence for dayside-driven magnetospheric convection. An enhanced convection pattern appears within 10 min after the southward turning of the interplanetary magnetic field. The enhanced convection and associated Region 1 and Region 2 field-aligned currents then progress from the dayside toward the nightside within 10–20 min. During this interval, the simulated convection pattern is difficult to attribute to nightside reconnection. The simulations show neither sunward plasma flow nor the associated flow deflection expected from nightside tail reconnection. These results support the idea that dayside reconnection can act as an independent driver of magnetospheric convection. They also link magnetospheric convection to the ionospheric two-cell convection and its associated Hall current (DP-2 current).

The influence of ionospheric conductance on dayside-driven magnetospheric convection has also been quantified in the magnetosphere-ionosphere coupling system. Using global PPMLR-MHD simulations, Zhu *et al.*[9] showed that the temporal and spatial pattern of magnetospheric convection remains largely consistent among the different conductance. However, the convection strength and ionospheric currents change. In the nearly infinite conductance case, the magnetospheric electric field and convection velocity on the equatorial plane decrease by about 20%. In contrast, the ionospheric Region 1 field-aligned current and Pedersen current increase by about 30%. The response time of enhanced magnetospheric convection to the solar wind is not affected by ionospheric conductance. Instead, the 10–20 min timescale may correspond to the anti-sunward drag of reconnected magnetic field lines from the subsolar point to the flank magnetopause. Larger ionospheric conductance makes the ionospheric footprints of dragged field lines more stationary. This leads to stronger Region 1 field-aligned current, larger Pedersen current, and enhanced $\boldsymbol{J} \times \boldsymbol{B}$ force coupling between the ionosphere and magnetosphere, where $\boldsymbol{J}$ is the electric current density and $\boldsymbol{B}$ is the magnetic field.

Solar wind speed provides another important control on dayside-driven magnetospheric convection. Using controlled global MHD simulations with steady upstream parameters, Zhu *et al.*[10] compared fast and slow solar wind streams with speeds of 800 and 400 km·s^{-1}. In the fast-stream case, enhanced convection extends from the dayside magnetopause to 20 R_E downtail within 15 min. This is faster than the approximately 20 min response in the slow-stream case. Fast solar wind also drives stronger and deeper-penetrating convection electric fields in the closed magnetosphere (Figure 4a and 4b). It produces stronger Region 1 field-aligned currents and increased flow shear in the low-latitude boundary layer. The induced convection further shows discrete spatial and temporal channels. Their intervals are about 9 min in the slow-wind case and 2–4 min in the fast-wind case. These results show that solar wind speed controls the timing, penetration depth, and intensity of dayside-reconnection-driven convection.

The same physical chain can extend into the inner magnetosphere. Wang *et al.*[12] analyzed large-scale convection electric fields observed by the Van Allen Probes during 191 isolated high-speed solar-wind-stream events. They found that the convection electric field inside $L < 5.5$ strengthens with both solar wind speed and southward IMF B_z. Its penetration depth also increases with solar wind speed (Figure 4c). When the solar wind speed exceeds about 550 km·s^{-1}, significant convection electric fields can reach L～3. The study further showed that *AU*, *Kp*, and *Dst* respond systematically to convection electric field strength. This result links solar-wind-driven magnetospheric convection to ionospheric elec-

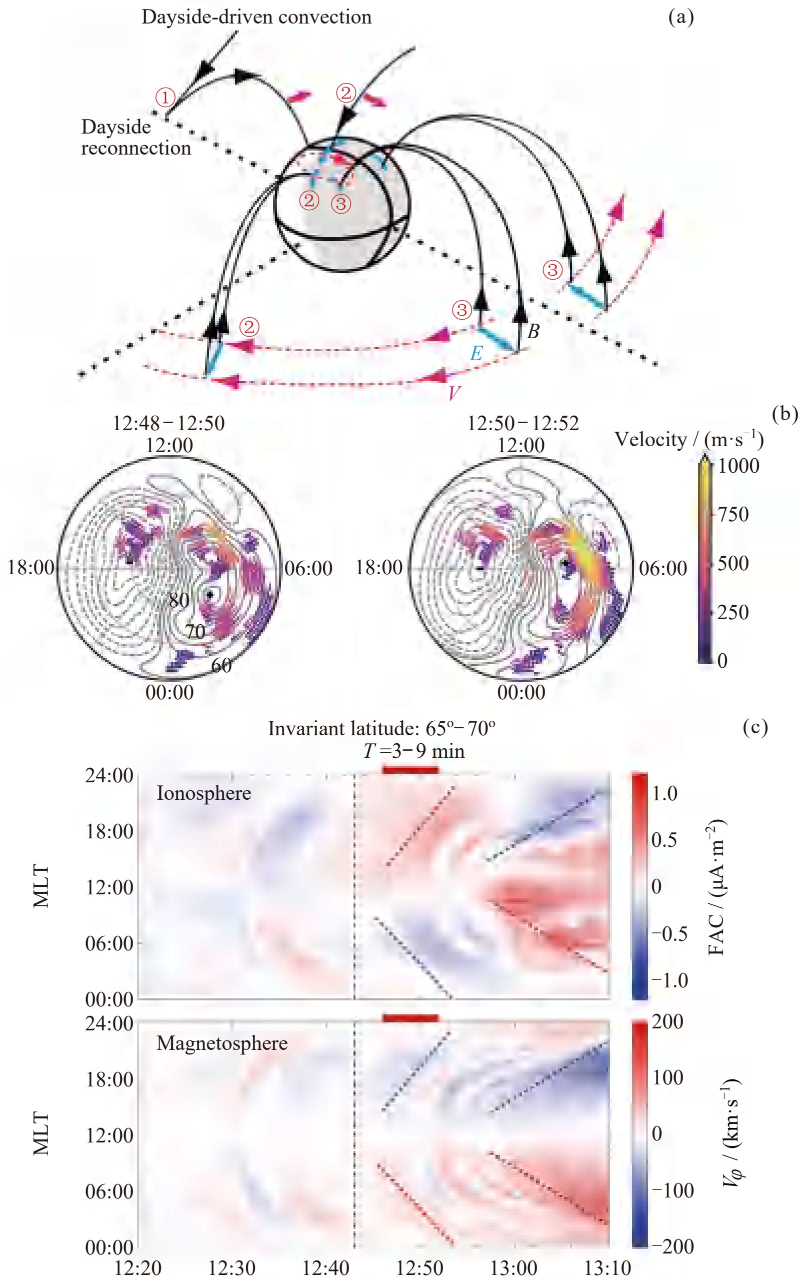

Fig. 3 Dayside-driven magnetospheric convection and its magnetosphere–ionosphere signatures. (a) Schematic of magnetospheric convection driven by dayside reconnection. (b) Ionospheric convection maps. (c) East-West keograms of the Field-Aligned Current (FAC) at the ionosphere and magnetosphere convection, with Local Time (LT) on the horizontal axis[8,14]

trojets, geomagnetic activity, and ring-current development.

Taken together, these studies support a coherent picture of dayside-reconnection-driven magnetosphere-ionosphere coupling. Southward turning of the interplanetary magnetic field initiates or strengthens dayside magnetopause reconnection. This reconnection then drives enhanced magnetospheric convection of closed field lines. The associated convection and Region 1 and Region 2 field-aligned currents progress from the dayside toward the nightside within approximately 10–20 min. Ionospheric conductance affects Region 1 field-aligned current, Pedersen current, current conservation, and the strength of magnetospheric convection. However, it does

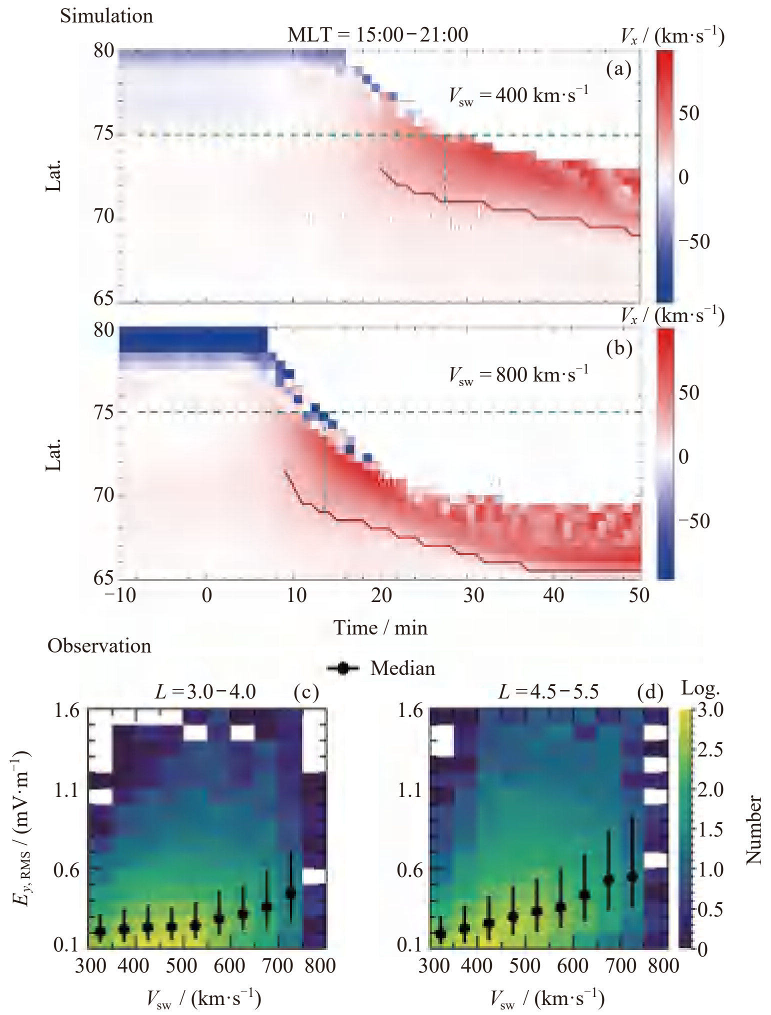

Fig. 4 Solar-wind-speed control of magnetospheric convection and inner-magnetospheric convection electric fields[10,12]

not change the response time of enhanced convection to the solar wind. Solar wind speed further controls the spatiotemporal evolution, penetration depth, intensity, and discrete channels of dayside-reconnection-driven convection. Under high-speed solar wind conditions, large-scale convection electric fields can penetrate deeply into the inner magnetosphere and reach lower L-shells. These studies therefore connect dayside reconnection with global convection and field-aligned-current evolution, DP-1 and DP-2 current-system development, storm–substorm coupling, and inner-magnetospheric convection electric fields.

This subsection suggests a timing and morphology test based on UVI auroral imaging. SXI observations can provide global context for the dayside configuration. UVI is especially relevant because the ionospheric response to magnetospheric convection and field-aligned-current reorganization is expressed through auroral morphology. Time sequences of UVI images can be used to examine auroral oval evolution. Key signatures include dayside auroral responses, magnetic-local-time-dependent auroral expansion, equatorward or poleward displacement, and nightside auroral intensification. These signatures can be compared with simulations, *in situ* measurements, and ground-based indices. Such comparisons can test whether the ionospheric response evolves on the 10–20 min timescale identified in recent convection studies. Thus, UVI provides an important diagnostic for dayside-driven convection and ionospheric current-system evolution. SXI supplies the corresponding dayside context.

2.3 Storm-substorm Coupling and Ionospheric/Inner-magnetospheric Responses

Storms and substorms involve a chain of linked processes, including changes in solar-wind driving, magnetospheric convection, magnetic reconnection, electric current systems, auroral activity, and energetic particles[12]. Recent studies increasingly emphasize that these processes should be examined through cross-regional coupling within the solar wind–magnetosphere–ionosphere system. The central issue addressed in this subsection is the role of enhanced dayside-driven convection and Region 1 FACs in triggering substorm onset[13]. A second issue is how dominant dayside and nightside reconnection organize the DP-2 and DP-1 components of auroral electrojets[11]. A further issue is how large-scale convection electric fields penetrate into the inner magnetosphere and influence geomagnetic indices, and how storms reshape the energy-dependent radial distribution of outer-belt electron fluxes.

The evolution of magnetospheric convection provides a useful framework for understanding storm-substorm coupling. Within this framework, the convection-driven motion of frozen-in magnetic field lines reorganizes large-scale current systems and governs the development of storms and substorms. This perspective is directly supported by recent work on solar-wind triggering of substorm onset during the May 2024 superstorm. Using coordinated global observations and simulations, REN *et al.*[14] showed that a shock-compressed southward interplanetary magnetic field enhanced dayside-driven convection, Region 1 field-aligned currents, and auroral currents (Figure 5). These disturbances extended rapidly from the dayside toward the nightside, and substorm expansion was initiated within ~6 min. Global simulations further showed that dayside-driven convection of closed field lines depleted nightside flux and thinned the near-Earth current sheet. This process lowered the onset threshold. After onset, nightside flux loading became significant. A reconnection X-line formed near 10 R_E and extended azimuthally. The westward electrojet then connected with Region 1 field-aligned currents to form the substorm current wedge. Together, these studies link magnetospheric convection evolution, current-system development, and the intrinsic relationship between storms and substorms within a single solar wind–magnetosphere–ionosphere coupling picture.

A complementary view comes from recent work on global current-system evolution. Using coordinated observations of storm-time intense substorms, WANG *et al.*[11] showed that substorm expansion is embedded within a global cycle of field-aligned currents and auroral electrojets. This cycle is coupled to large-scale plasma convection. It appears as coherent motion of current peaks across magnetic local time and magnetic latitude. The peaks first move antisunward and equatorward, and then return sunward and poleward. The cycle involves two auroral electrojet components (Figure 6): the convection-driven DP-2 current and the expansion-phase DP-1 substorm current. The antisunward-equatorward phase corresponds to intervals dominated by dayside reconnection. It begins with DP-2 and can transition stepwise into DP-1. The following sunward-poleward phase reflects intervals dominated by nightside reconnection. During this phase, DP-1 may either persist from the preceding interval or develop newly. These observations connect the expanding-contracting polar cap paradigm with the DP-1/DP-2 paradigm. They show that DP-1 onset can occur under either dayside- or nightside-dominated reconnection, whereas the full development of DP-1 commonly involves nightside-dominated reconnection.

Outer-radiation-belt morphology provides a further inner-magnetospheric consequence of storm-time coupling. WANG *et al.*[14] statistically analyzed the peak flux position L_{peak} and inner boundary position L_{min} of the outer radiation belt across storm phases using Van Allen Probes electron flux data from 226 keV to 2.6 MeV. They found an energy-dependent evolution of the outer radiation belt morphology. In the early recovery phase, L_{peak} converges to approximately L = 4.3–4.6 across the analyzed energy range, while L_{min} remains nearly unchanged for electrons above 1 MeV. These results indicate that storm-time convection activities, radial diffusion, local wave acceleration, and loss processes together shape the energy-dependent morphology of the outer radiation belt. Although the outer radiation belt is not a direct SXI or UVI imaging target, its storm-phase evolution represents an important inner-magnetospheric consequence of global solar-wind-magnetosphere driving.

For SMILE interpretation, the key issue is to distinguish convection-driven DP-2 responses from expansion-phase DP-1 and the development of the substorm

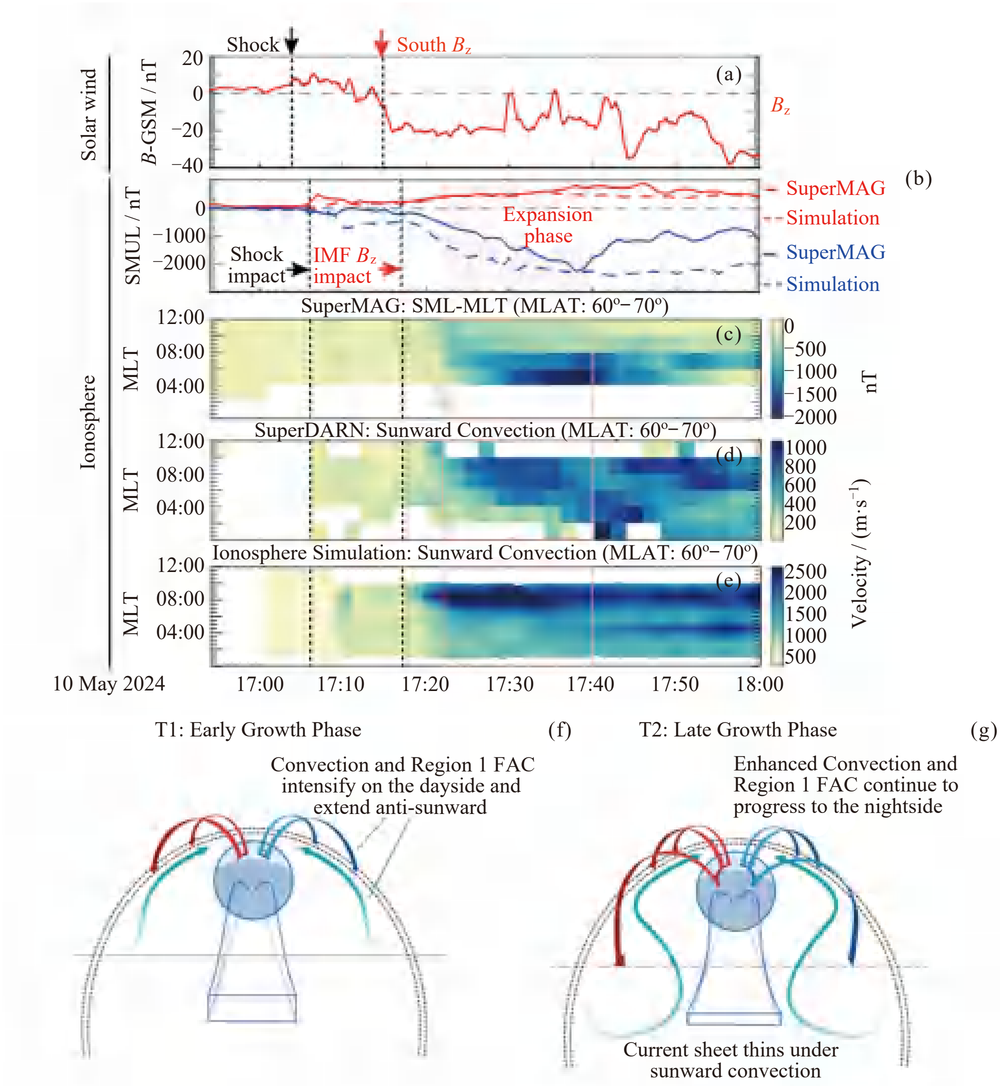

Fig. 5 Solar-wind triggering of substorm onset during the 10 May 2024 superstorm. (a) Magnetic field (the z-component of the interplanetary magnetic field, B_z). (b) Auroral electrojet indices. (c) Magnetic-local-time distribution of the SuperMAG auroral lower (SML) index. (d)–(e) Observed and simulated sunward ionospheric convection, with Local Time (LT) on the horizontal axis. (h)–(i) Schematic illustration of the early and late growth phases, showing the antisunward progression of enhanced convection and Region 1 field-aligned currents and the thinning of the near-Earth current sheet before substorm onset. The vertical axes show the magnetic field in Geocentric Solar Magnetospheric (GSM) coordinates, the SuperMAG auroral Upper and Lower (SMUL) indices, and magnetic local time (MLT), respectively[14]

current wedge. UVI observations, together with ground magnetic indices, SuperDARN convection maps, AMPERE FACs, and simulations, can help determine whether a storm-time substorm sequence is dominated by prompt dayside-driven convection, nightside loading–unloading evolution, or both. SXI provides the simultaneous dayside context through soft-X-ray imaging of the magnetopause, cusps, and magnetosheath structures.

3 Mission Update

3.1 Platform

The PF structure is a stacked structure, including the PM structure comprised of a large Carbon Fiber Reinforced Polymer (CFRP) primary structure and four propellant

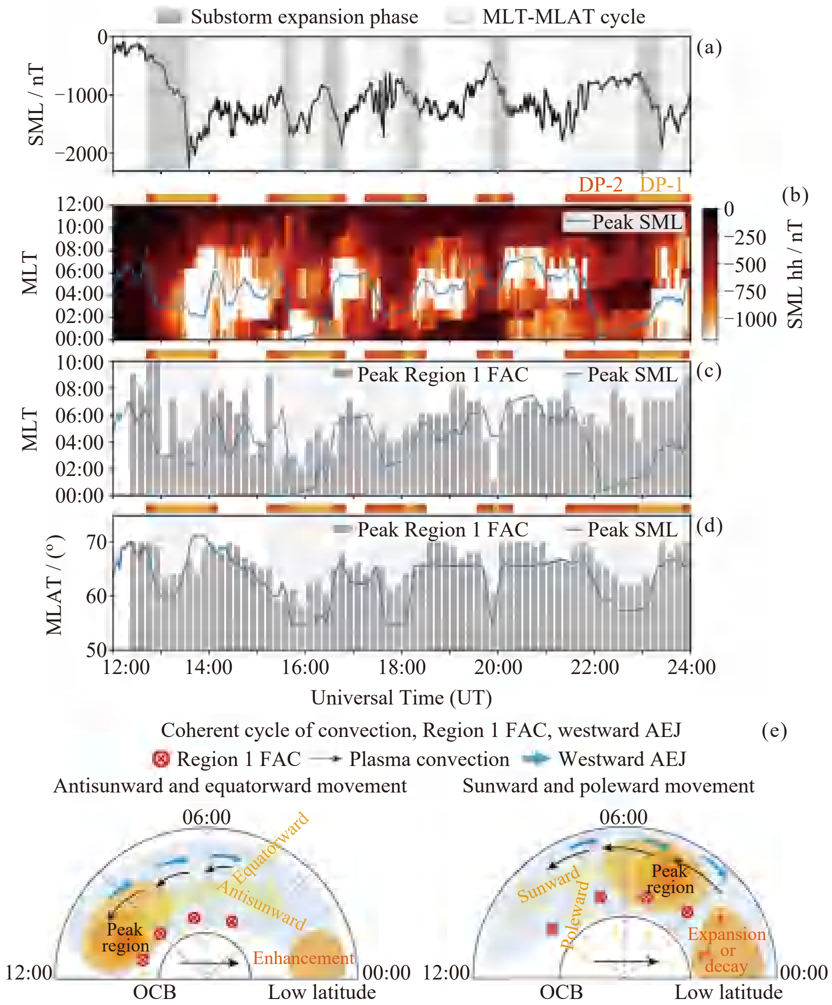

Fig. 6 Global cycle of field-aligned currents and auroral electrojets during storm-time substorms. (a) SML index. (b) Magnetic-local-time distribution of the westward auroral electrojet. (c)-(d) Temporal evolution of the magnetic local time and magnetic latitude of the peak Region 1 field-aligned current and peak SML. (e) Schematic illustration of the coherent cycle of plasma convection[11]

tanks, and the cubical-shaped SVM structure featuring several honeycomb panels and CFRP frames. There are two solar arrays mounted on the SVM +*Y* and -*Y* lateral panels, which are installed and deployed by two solar array mechanisms. The assembly of SVM and PM flight models has been completed in April 2024. And finished the environment tests during May to August 2024 (Figure 7–9).

3.2 Payload Module (PLM)

UVI FM is the latest instrument that delivered to PLM in December 2024. Then PLM FM finished the final integration and delivered to ESTEC. The UVI FM and PLM FM already completed the environment test separately and will join in the SC level environment test for the next step.

3.3 Instruments

3.3.1 SXI

SXI will use novel soft X-ray imaging technology to obtain global images of the large-scale structures of the magnetosheath for the first time. This is critical to understand the key features of magnetospheric global dynamics. SXI consists of a main telescope, an SXI electronics box and the front-end electronics. The telescope uses a Lobster-eye technique based on micropore optics to focus the X-rays onto the two very large CCD arrays located on the focal plane. The focal plane is protected from potential radiation damage by a shutter mechanism. Figure 10 shows the SXI Telescope Flight Model (FM) during integration in laboratory. SXI FM delivered to PLM in June 2024.

Fig. 7 Platform thermal vacuum test in May 2024

Fig. 8 Platform mechanical test in June 2024

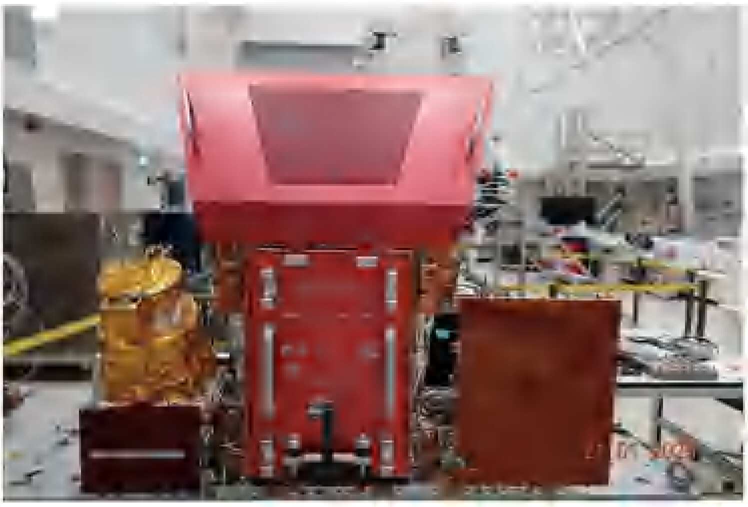

Fig. 9 PLM inspection before delivery in ESTEC in January 2025

3.3.2 UVI

UVI will capture global images of the aurora borealis with high spatial resolution. UVI consists of two key sub-assemblies: the optical module (UVI Camera, UVI-C), which is the heart of the instrument; and the electrical control unit (UVI-E). Due to the responsibilities for the development of UVI change to CAS with contributions from ESA. This caused a delay in the development of UVI. However, CAS and ESA are doing their utmost to minimize the schedule impact. The UVI-C Qualification Model (QM) has completed delivery to Airbus in May 2024, and completed the integrating test and environment test with PLM/FM. Following the development of QM, the UVI/FM completed the unit function test, qualification test and final calibration test. In October 2024, UVI FM passed the QAR and PSR organized by CAS and ESA. UVI FM delivered to ESTEC and integrated with PLM in November 2024. UVI FM takes part in all tests with the spacecraft and pre-launch activities in 2025, including deployment test. The FM of UVI is shown in Figure 11.

3.3.3 MAG

The MAG instrument will measure the in-situ magnetic field using a digital fluxgate magnetometer system consisting of two individual tri-axial fluxgate sensor heads mounted on a 3-meter-long deployable boom. In March 2024, MAG FM passed the QAR and PSR organized by CAS and ESA. It has now been delivered to Airbus, which is the first instrument of SMILE that has been delivered to ESA. The FM of MAG boom and electronic

Fig. 10 SXI Telescope FM in laboratory (credit to Leicester U., UK)

Fig. 11 UVI FM

box are shown in Figure 12.

After delivery, the MAG instrument was mounted to PLM and finished integration tests. In Nov 2024, after PLM level deployment test, the MAG was integrated to SMILE spacecraft in ESTEC together with the PLM. In 2025, the MAG instrument finished spacecraft level mechanical, thermal and EMC test. The spacecraft level MAG Boom deployment test was finished in July 2025, supported by 3 Helium blooms the boom was deployed successfully. The deployment test scene is shown in Figure 13.

3.3.4 LIA

Two identical LIA sensors are designed on the basis of a top-cap electrostatic analyzer for large dynamic flux range, wide Field of View (FOV) and high-resolution ion measurement. Since each LIA has 2π FOV, a large 4π FOV for the ion measurement can be achieved overall by the two LIAs. The FM of one LIA instrument is shown in Figure 14. The FMs of LIA have been calibrated at the National Space Science Center (NSSC) and cross calibration has been carried out in the Mullard Space Science Laboratory (MSSL) in September 2024. The calibration results at NSSC and MSSL are consistent very well. LIA has completed its QAR and delivered the FMs to ESTEC for spacecraft level tests in October 2024. LIA FMs were sent back to NSSC for performance check after all the tests done at ESTEC in September 2025. No performance degradation has been found after the performance check. The LIA FMs have been sent back to ESTEC in November, 2025 for the further integration and launch activities.

3.4 Ground Segment

The Ground Segment (GS) of the SMILE mission is jointly established by CAS and ESA. The GS architecture is illustrated in Figure 15 to demonstrate the respective responsibilities and ground-to-space links. The ground segment responsibilities and operation principles for CAS are science operations (joint responsibility), mission operations, telemetry, S-band Tracking and Command (TT&C) ground stations, X-band payload data communication station (Sanya as backup). The ground segment responsibilities and operation principles for ESA are Science Operations (joint responsibility), S-band TT&C ground stations (as support to Mission Op-

Fig. 12 FM of MAG boom (left) and electronic box (right)

Fig. 13 MAG Boom Deployment Test in July 2025 in ESTEC

erations), X-band payload data communication stations (DLR station as baseline).

The network link between ESOC and CCC is critical during launch and SC orbit transfer activities. So the backup link are established and tested before launch under CAS's responsibilities. The Ground segment operation rehearsal are completed in 2025 and the interface between units are compatible and verified.

3.5 Launch Vehicle

SMILE will be launched by a Vega-C VV-29 rocket provided by AVIO. The fit check with the satellite and the launch vehicle adapter has been conducted at the beginning of 2023 and did the fit check again for the FM in September 2025 in ESTEC as Figure 16.

Fig. 14 FM of LIA

Platform (PF) FM completed all environmental tests in IAMC before September 2024 and then prepare the shipment to ESTEC especially for the export control and also dangerous goods process. PF FM arrived ESTEC in December 2024 after the effort by CAS and ESA. After the successful interface test between PF and PLM, then start the SC integration and completed at the end of January 2025 as Figure 17.

SMILE SC completed EMC, AC magnetics, sine vibration, acoustics, solar panel deployment, thermal vacuum, DC magnetics tests and fit check with launcher from February to September 2025. After the final settlement of MLI and cleanliness of SC and then keep the SC in the container and waiting for the transportation from ESTEC to French Guyana Space Center.

SMILE SC and Ground Support Equipment (GSE) start the transportation in the beginning of February of 2026 from Amsterdam harbor to Kourou by boat through Atlantic Ocean (Figure 18). SMILE and GSE arrived Kourou two weeks later and transferred to S3 B cleanroom in CSG (Centre Spatial Guyanais). Then start SC inspection, alignment, functional and leakage test after the transportation. The SC was filled with propellant in March and delivered to AVIO to make installation

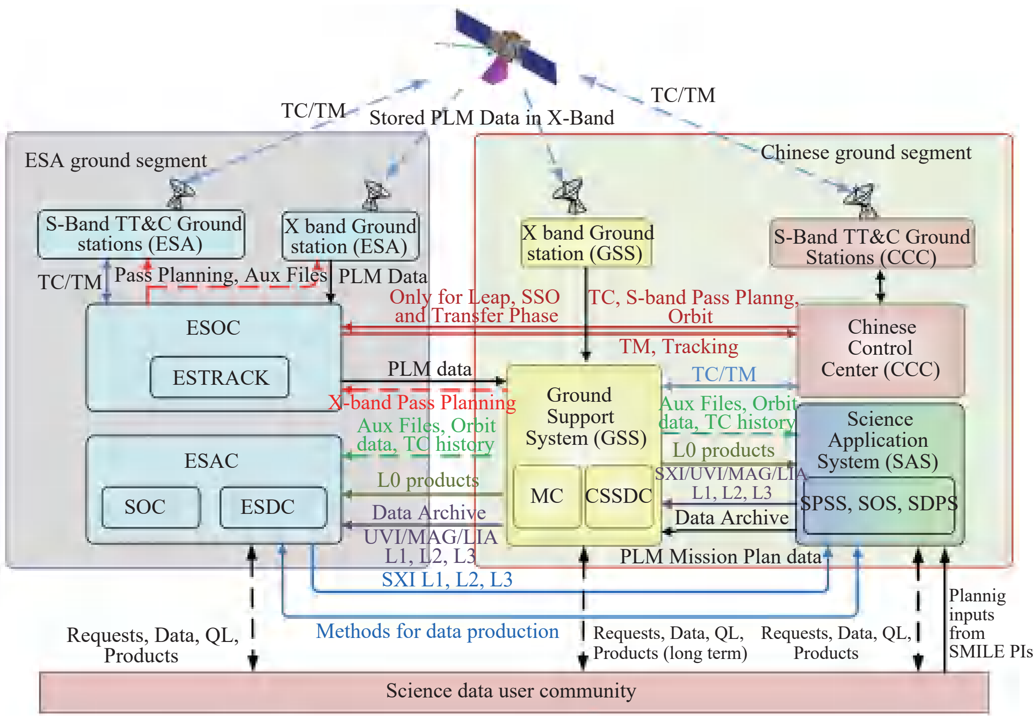

Fig. 15 SMILE ground segment architecture

Fig. 16 Vega-C fit Check with FM S/C in September 2025 in ESTEC (Credit to ESA/CAS)

Fig. 17 SC Integration in January 2025 in ESTEC (Credit to ESA/CAS)

with Vamper 1194 and capsuled in the Fairing (Figure 19). The SMILE satellite was launched on 19 May 2026 by Vega-C VV29 very smoothly as textbook. Now the satellite status is stable and already start the transfer obit for the second time. The SMILE satellite will reach the scientific orbit before end of June and then start the operation of instruments and in orbit commissioning. The IOCR (In Orbit Commission Review) will be held before end of September 2026 and then hand it over for GSS to operate and science team start to use the data for scientific analysis.

3.6 Post-launch Milestones

SMILE was successfully launched aboard a Vega-C rocket on flight VV29 on 19 May 2026. After launch, the spacecraft entered the orbit transfer phase. From 19 May to the end of June 2026, the satellite is planned to transfer from its initial 700 km circular orbit to the highly elliptical science orbit, with an altitude range of approximately 5000–121000 km. From early July to early September 2026, spacecraft and payload in-orbit commissioning tests will be carried out. The CAS–ESA joint In-Orbit Commissioning Review (IOCR) is expected to be completed in mid-September 2026, after which the mission will be handed over for science operations. According to the current mission plan, SMILE is designed for a nominal three-year in-orbit operation. A possible mission extension will be considered according to the spacecraft status and scientific operation needs.

Fig. 18 SC transportation in Amsterdam harbour

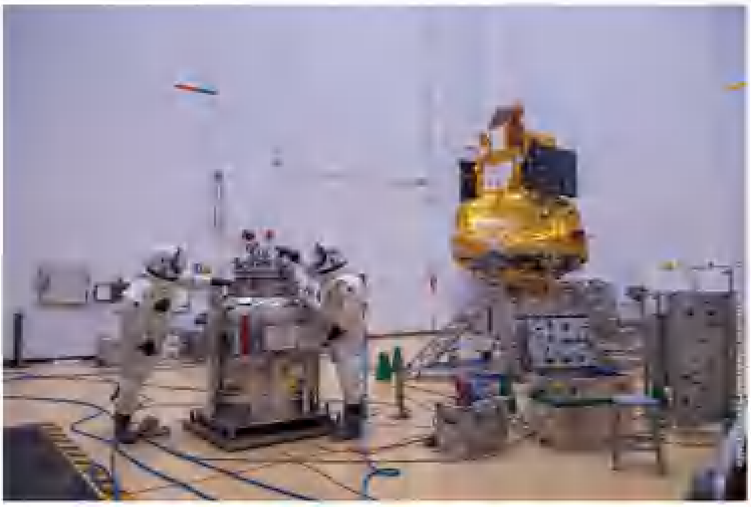

Fig. 19 SC was filled in propellant in S3 B

4 Summary and Outlook

The studies reviewed here support a system-level perspective on solar wind- magnetosphere-ionosphere coupling. The main processes should not be treated as isolated elements. Dayside boundary dynamics, reconnection-driven convection, current-system evolution, auroral activity, and inner-magnetospheric responses form a connected geospace chain. On the dayside, SXI-relevant soft-X-ray morphology is controlled by both boundary geometry and magnetosheath emissivity. The relevant geometry includes the magnetopause and cusps. The emissivity depends on plasma density and flow structures in the magnetosheath, and can be modified by high-speed jets, jet-driven bow waves, shock-discontinuity-interaction jets, HFA-related cavities, storm-time compression, and IMF By-dependent cusp twisting. In the magnetosphere-ionosphere system, dayside magnetic reconnection can rapidly drive closed-field-line convection within about 10–20 min after southward IMF turning. Region 1 and Region 2 field-aligned currents evolve with this convection. Ionospheric conductance affects current closure and convection strength, while solar wind speed controls the timing, intensity, penetration depth, and channelized structure of the response. During storms and substorms, this convection-centered picture links dayside triggering with nightside loading–unloading evolution. It also links DP-2 and DP-1 auroral-electrojet development, formation of the substorm current wedge, inner-magnetospheric convection electric fields, and radiation-belt responses.

This system-level picture also defines the observational role of SMILE. SXI provides global soft-X-ray context for the dayside magnetosheath, magnetopause, and cusps. UVI records the corresponding auroral and current-system responses in the ionosphere. These two image products therefore represent different parts of the same solar wind-magnetosphere-ionosphere coupling chain. Ground-based observations and numerical simulations are needed to connect dayside forcing, global boundary motion, ionospheric convection, and auroral current-system evolution. Within this framework, time sequences of UVI images can be used to assess how dayside solar-wind forcing is transmitted to auroral morphology changes, convection-driven FAC/electrojet reorganization, and expansion-phase substorm current-system development.

This connection becomes especially important as SMILE enters the stage of early observations and data interpretation. The scientific studies reviewed here are therefore not only preparatory studies for a future imaging mission. They also provide a practical basis for interpreting early SMILE observations once the mission begins science operations. In this sense, recent scientific progress and mission progress are closely linked. The mission update shows that SMILE is approaching the stage in which global SXI and UVI image sequences can be used to test the physical scenarios developed in recent simulations and coordinated observations.

Future SMILE-era studies will need to clarify how the 10–20 min directly driven dayside-convection response is related to the classical ~1 h loading-unloading response during storms and substorms. This issue is particularly important when convection-driven DP-2 signatures and expansion-phase DP-1 signatures coexist in auroral electrojets and field-aligned current systems. Synthetic SXI/UVI observations, multi-instrument timing analysis, ground-based observations, and model-data comparisons will be useful for connecting dayside forcing with ionospheric and inner-magnetospheric responses. With SMILE observations, these approaches may help convert global soft-X-ray and ultraviolet image sequences into a quantitative understanding of solar wind-magnetosphere-ionosphere coupling.

References

[1] WANG C, BRANDUARDI-RAYMONT G. Update on the ESA-CAS joint solar wind magnetosphere ionosphere link explorer (SMILE) mission[J]. *Chinese Journal of Space Science*, 2020, **40**(5): 700-703

[2] WANG C, ESCOUBET P, FORSYTH C, *et al*. Recent progress of the solar wind magnetosphere ionosphere link explorer (SMILE) mission[J]. *Chinese Journal of Space Science*, 2024, **44**(4): 692-698

[3] GONG Y Q, SUN T R, TANG B B, *et al*. Dynamic X-ray imaging of the magnetosheath expected during a super storm[J]. *Frontiers in Astronomy and Space Sciences*, 2025, **12**: 1563653

[4] GUO J, LU S, LU Q M, *et al*. Large-scale magnetosheath jets formed by shock-discontinuity interactions: A three-dimensional global hybrid simulation[J]. *Geophysical Research Letters*, 2026, **53**(9): e2025GL121533

[5] OUYANG W X, YANG Z W, GUO X C, *et al*. Magnetosheath jet-driven bow waves and their soft X-ray imaging: Hybrid and PIC simulations[J]. *Chinese Journal of Space Science*, 2024, **44**(6): 979-987

[6] GONG Y Q, SUN T R, ESCOUBET C P, *et al*. The effects of IMF B_y on the twisting of cusp[J]. *Journal of Geophysical Research*: *Space Physics*, 2026, **131**(5): e2025JA034856

[7] ZHANG A X, DUAN S P, DAI L, *et al*. Observations of the magnetopause reconnection ion diffusion region with high-density O^+ ions during the May 2024 superstorm[J]. *Geophysical Research Letters*, 2026, **53**(8): e2025GL121449

[8] DAI L, ZHU M H, REN Y, *et al*. Global-scale magnetosphere convection driven by dayside magnetic reconnection[J]. *Nature Communications*, 2024, **15**(1): 639.

[9] ZHU M H, DAI L, WANG C, *et al*. The influence of ionospheric conductance on magnetospheric convection during the southward IMF[J]. *Journal of Geophysical Research*: *Space Physics*, 2024, **129**(9): e2024JA032607

[10] ZHU M H, DAI L, REN Y, *et al*. Response of magnetospheric convection to the southward turning of the IMF in fast and slow solar wind streams[J]. *Journal of Geophysical Research*: *Space Physics*, 2025, **130**(11): e2025JA034529

[11] WANG T H, DAI L, ESCOUBET C P, *et al*. Substorm expansion embedded in a global cycle of field-aligned currents and auroral electrojets[J]. *Nature Communications*, 2026, **17**(1): 2970

[12] DAI Lei, WANG Chi, REN Yong, *et al*. Geomagnetic storms and substorms: progress and perspectives[J]. *Chinese Science Bulletin*, 2025, **70**(27): 4759-4774 (戴磊, 王赤, 任勇, 等. 磁暴和亚暴研究进展与展望 [J]. 科学通报, 2025, **70**(27): 4759-4774)

[13] REN Y, ZHU M H, DAI L, *et al*. Solar-wind triggering of substorm onset during the May 2024 superstorm: Coordinated global observations and simulations[J]. *Geophysical Research Letters*, 2026, **53**(4): e2025GL119629

[14] WANG X, DAI L, REN Y, *et al*. The evolution of Earth's outer radiation belt over geomagnetic storm phase in Van Allen Probe era[J]. *Journal of Geophysical Research*: *Space Physics*, 2024, **129**(11): e2024JA032674

Author Biography

WANG Chi The Director of the National Space Science Center, Chinese Academy of Sciences (CAS), and an Academician of CAS and the International Academy of Astronautics. He received his bachelor's degree from the University of Science and Technology of China in 1990 and his Ph.D. from the Massachusetts Institute of Technology in 1998. His research focuses on space physics and space weather. He currently serves as Chief Scientist of Phase IV of China's Lunar Exploration Program, the Chinese Principal Investigator of the Solar Wind Magnetosphere Ionosphere Link Explorer (SMILE) mission, and Commander-in-Chief of Phase II of the Chinese Meridian Project. His honors include the Special Prize of the National Science and Technology Progress Award, the Qian Xuesen Outstanding Contribution Award, and the First Prize of the Science and Technology Progress Award of the Chinese Geoscience Union

0254-6124/2026/46(4)-0102-03 *Chin. J. Space Sci.* 空间科学学报

WEI Jianyan, Bertrand CORDIER. Progress on SVOM Satellite Development. *Chinese Journal of Space Science*, 2026, **46**(4): 102–104. CSTR:32142.14.cjss.2024–yg29. DOI:10.11728/cjss2026.04.2024–yg29

Progress on SVOM Satellite Development

WEI Jianyan[1] Bertrand CORDIER[2]

1(*National Astronomical Observatories*, *Chinese Academy of Sciences*, *Beijing* 100101)

2(*CEA Paris-Saclay*, *Irfu/Département d'Astrophysique*, 91191 *Gif sur Yvette*)

Abstract SVOM (Space-based multi-band Variable Object Monitor) is a Chinese-French space mission mainly designed to study Gamma-Ray Bursts. The satellite has four instruments to detect and localize the prompt GRB emission and measure the evolution of the afterglow in the visible band and in soft X-rays, and a VHF communication system enabling the fast transmission of SVOM alerts to the ground. The ground segment includes an array of wide-angle cameras and two follow-up telescopes. It was launched into an orbit of ~635 km on 22 June 2024, with three years of nominal operations and two years extension. After the first two years in orbit, SVOM has detected 318 gamma-ray bursts, including 270 detected by GRM and 107 detected and localized by ECLAIRs, and is revealing a population of X-ray–rich bursts that had been only partially uncovered in the early 2000s by previous missions. GRB 250314A, detected by SVOM, is a burst from the early Universe with a redshift of approximately 7.3, which currently ranks as the third most distant gamma-ray burst ever spectroscopically confirmed.

Key words Space astronomy, Gamma-ray burst

Classified index V474

SVOM (Space-based multi-band Variable Object Monitor) is a mission dedicated to studying Gamma-Ray Bursts (GRBs)[1,2]. The mission was approved jointly by both Chinese and French space agencies. It was launched at Xichang Satellite Launch Center by Long March 2 C on 22 June 2024. The satellite (Figure1) has an orbit with an altitude of 635 km and an inclination of 29°. Following a commissioning and validation period, the scientific operation phase officially began in April 2025.

GRBs are extremely luminous transient sources appearing when a newborn stellar mass black hole or magnetar emits an ultra-relativistic jet towards the Earth. Consequently, the study of GRBs has the potential to revolutionize or expand our understanding of key astrophysical issues about the mechanisms driving stellar explosions and the radiation processes of relativistic jets. But in the next years, GRBs will also undoubtedly shed new light on the evolution of the young universe, particularly on the history of star formation, the metal enrichment of galaxies, and the reionization of the intergalactic medium[3]. GRB 170817 A, a normal short GRB detected by Fermi-GBM, was the first confirmed counterpart of gravitational-wave transients, which made GRBs an even hotter topic[4].

The scientific objectives of SVOM put a special emphasis on two categories of GRBs: very distant GRBs at $z > 5$, which constitute exceptional cosmological probes, and faint/soft nearby GRBs, which allow probing the nature of the progenitors and the physics at work in the explosion. These goals have a major impact on the design of the mission: The on-board hard X-ray imager is sensitive down to 4 keV and computes online image and rate triggers, and one of the follow-up telescopes on

Received May 24, 2026

Fig. 1 Artistic view of the SVOM satellite

the ground is sensitive in the NIR. In order to take advantage of the astrophysical potential of GRBs, SVOM is designed to (i) permit the detection of all known types of GRBs; (ii) provide fast, reliable GRB positions; (iii) measure the spectral shape of the GRB prompt emission from visible to MeV; (iv) measure the temporal properties of the GRB prompt emission from visible to MeV; (v) identify quickly the afterglows of detected GRBs at both X-ray and visible bands, including the ones that are highly redshifted ($z > 5$); (vi) measure the spectral shape of the early and late GRB afterglow from visible to X-rays; (vii) measure the temporal evolution of the early and late GRB afterglow from visible to X-rays.

SVOM mission design consists of a set of scientific instruments to implement the synergy between space and ground observations. The space-based instruments include: (i) ECLAIRs[5], a wide field-of-view hard X-ray imager and spectrometer; (ii) GRM[6], a wide field-of-view soft gamma-ray spectrometer; (iii) MXT[7], a narrow field-of-view low-energy X-ray telescope; (iv) VT[8], a narrow field-of-view visible/near infrared (NIR) telescope. An artist view of the SVOM satellite is shown in Figure 1. And the ground-based instruments include: (i) GFTs, two follow-up telescopes[9,10] (one of which featuring efficient NIR capabilities); (ii) GWAC[11], an array of wide field-of-view cameras in visible band. A network of ~50 VHF receiving stations[12], and a Beidou short-message system as supplement, are designed for real-time downlink communication. The Beidou short-message system also has the capability of real-time uplink communication.

SVOM is a unique multi-wavelength observatory with rapid slew capability and quick command up-link capability. Therefore, SVOM can also be a powerful target-of-opportunity observatory for the whole astronomy community beyond the specific objectives linked to GRBs. For example, the SVOM mission has been conceived to promptly point to the celestial fields where sources have been detected by wide field of view astronomical devices such as the upgraded generation of gravitational wave detectors (LIGO, VIRGO, GEO and KAGRA) and high-energy neutrino detectors (IceCube, KM3 NeT).

Highlights of early scientific results.

(1) Till 12 June 2026, SVOM has detected 318 gamma-ray bursts, including 270 detected by GRM and 107 detected and localized by ECLAIRs. Among the 107 bursts localized by ECLAIRs, 79 gamma-ray bursts were observed in soft X-rays, 66 were observed in the optical band, and redshift measurements were obtained for 40 events.

(2) After the first two years of operation, SVOM is revealing a population of X-ray–rich bursts that had been only partially uncovered in the early 2000 s by previous missions such as BeppoSAX and HETE-2. These bursts are primarily characterized by prompt emission dominated by X-rays, while releasing energy amounts comparable to those of long gamma-ray bursts associated with the collapse of massive stars. Figure 2 illustrates the contribution of SVOM.

(3) On 14 March 2025, the SVOM/ECLAIRs detected a gamma-ray burst, designated GRB 250314 A, and quick follow-up by SVOM/VT indicated it was a candidate of high redshift burst. An extensive follow-up campaign for this burst involving numerous ground-based and space telescopes finally revealed that it was a burst with a redshift of approximately 7.3[13], indicating that the explosion occurred when the Universe was only about 730 million years old. Observations by the James Webb Space Telescope (JWST) in July 2025 revealed the presence of an associated supernova. Therefore, GRB 250314 A offers an exceptional witness to the death of a massive star in the early Universe[14]. GRB 250314 A is currently the third most distant gamma-ray burst ever spectroscopically confirmed.

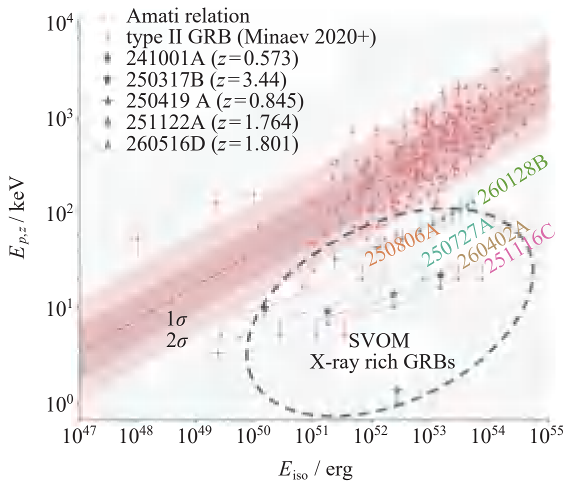

Fig. 2 Distribution of the characteristic photon energy emitted by more than 200 long gamma-ray bursts detected by previous missions (in red), as a function of their total radiated energy. The higher the total radiated energy, the more energetic the emitted photons (Amati relation). The X-ray–rich bursts detected by SVOM deviate from this correlation. Stars indicate events with known redshift; dashed tracks correspond to the $z = 0.5–5$ interval when the redshift is unknown (Credit: SVOM Collaboration)

References

[1] WEI J, CORDIER B, ANTIER S, *et al*. The deep and transient universe in the SVOM era: new challenges and opportunities–scientific prospects of the SVOM mission [J]. arXiv161006892W, 2016

[2] The mission : CORDIER B, WEI J, ZHANG S, *et al*. The SVOM mission, its profile and its system arXiv: 2604.24257, 2026

[3] GEHRELS N, RAMIREZ-RUIZ E, FOX D B. Gamma-ray bursts in the swift era[J]. *Ann. Re. Astron. Astrophys.*, 2009, **47**(1): 567-617

[4] GOLDSTEIN A, VERES P, BURNS E, *et al*. An ordinary short gamma-ray burst with extraordinary implications: fermi-GBM detection of GRB 170817A[J]. *Astrophys. J. Lett.*, 2017, **848**(2): 14

[5] ECLAIRs: GODET O, ATTEIA J-L, SCHANNE S, *et al*. ECLAIRs: the SVOM high-energy transient trigger camera, arXiv: 2604.24249, 2026

[6] GRM: SUN J, DONG W, HE J, *et al*. The Gamma-Ray Monitor onboard the SVOM satellite, arXiv: 2604.18985, 2026

[7] MXT: GOTZ D, CREPALDI S, DOUMAYROU E, *et al*. , The Microchannel X-ray Telescope on board the SVOM mission: in-flight scientific performance, arXiv: 2604.24246, 2026

[8] VT: QIU Y, XIN L, DENG J, *et al*. SVOM/VT: Instrument Overview, Science Objectives, and First-Year Performance, arXiv: 2604.24248, 2026

[9] C-GFT: WU C, KANG Z, LU X, *et al*. SVOM/C-GFT: Instrumentation and Performances on the SVOM Alerts, arXiv: 2604.24272, 2026

[10] F-GFT: BASA S, LEE W, WATSON A, *et al*. COLIBRI (SVOM/FM-GFT): Instrumentation and Performances on the SVOM Alerts, arXiv: 2604.24259, 2026

[11] GWAC: XIN L, HUANG L, CAI H, *et al*. Overview of Ground-based Wide-Angle Cameras array, arXiv: 2604.24260, 2026

[12] VHF network: CORDIER B, JANNIN L, LAFABRIE Ph, *et al*. The VHF alert network of the SVOM mission, arXiv: 2604.24263, 2026

[13] CORDIER B, WEI J, TANVIR N, *et al*. SVOM GRB 250314A at z ≃ 7.3: An exploding star in the era of re-ionization[J]. *Astronomy & Astrophysics*, 2025, **704**: L7

[14] LEVAN A, SCHNEIDER B, *et al*. JWST reveals a supernova following a gamma-ray burst at z ≃ 7.3[J]. *Astronomy & Astrophysics*, 2025, **704**: L8

Author Biography

WEI Jianyan Male, born at Lishui, Jiangsu province in August 1965. He is a research professror in astrophysics at National Astronomical Observarories, CAS. His major research fields cover active galactic nuclear, gamma-ray bursts, active stars, and instruments.
E-mail: wjy@nao.cas.cn

0254-6124/2026/46(4)-0105-04 *Chin. J. Space Sci.* 空间科学学报

WANG Chi, DONG Xiaolong, SONG Tingting, CAO Song, ZHANG Aibing, CHI Yixing. China's "Origins" Space Science Program. *Chinese Journal of Space Science*, 2026, **46**(4): 105–108. CSTR:32142.14.cjss.2026–yg18. DOI:10.11728/cjss2026.04.2026–yg18

China's "Origins" Space Science Program*

WANG Chi DONG Xiaolong SONG Tingting
CAO Song ZHANG Aibing CHI Yixing

(*National Space Science Center*, *Chinese Academy of Sciences*, *Beijing* 100190)

Abstract The "Origins" Program addresses the first-phase objectives to implement the *National Mid- and Long-term Plan for Space Science in China (2024–2050)*, which was released in October, 2024. Focusing on fundamental questions concerning the "Origins", this program encompasses four flagship space science satellite missions: Discovering the Sky at the Longest wavelength (DSL), the Solar Polar Orbit Observatory (SPO), the Earth 2.0 (ET) mission, and the Enhanced X-ray Timing and Polarimetry (eXTP) mission. These four missions are targeted for major discoveries and original scientific results on the grand questions about the early universe, space weather, earth-like exoplanets and physics of the extreme universe. By 2025, all four missions have completed the Preliminary Design Phase. These four missions have been scheduled to be launched before 2031.

Key words Space science, Science missions, Early universe, Space weather, Exoplanet

Classified index P353

1 Introduction

In October 2024, China released *National Mid- and Long-term Plan for Space Science in China (2024–2050)*[1], outlining a strategic roadmap for the nation's future space science endeavors. Against this backdrop, the "Origins" Program was proposed and started by the Chinese Academy of Sciences in 2025, which directly addresses the first-phase objectives of the *National Mid- and Long-term Plan for Space Science in China (2024–2050)*. The program is designed to carry out a coordinated set of four space science missions, with a target launch date by 2030. These missions aim to tackle fundamental questions about the early universe, exoplanets, solar activities and space weather, and the physics of extreme celestial objects. It is expected that major discoveries and original results will be achieved by the 2030 s in areas such as the dark age of the universe, the solar magnetic activity cycle and high-speed solar wind, Earth-like exoplanets, and the laws of physics under extreme cosmic conditions.

2 Discovering the Sky at the Longest Wavelength

The Discovering the Sky at the Longest Wavelength (DSL) mission represents a pioneering effort to open a new observational window in ultra-long-wave radio astronomy[2]. The mission adopts a unique constellation architecture consisting of one mother satellite and nine daughter satellites, all operating in a 300 km circular lunar orbit. By leveraging the highly clean electromagnetic environment on the far side of the Moon, DSL is uniquely positioned to conduct high-sensitivity observations at MHz frequencies, enabling breakthrough explorations of the cosmic dark age and dawn.

The scientific objectives of DSL are threefold. First, by performing high-precision measurements of the

* Supported by Program for Seizing the Commanding Heights of Science and Technology (GJ11050402)
Received May 20, 2026

all-sky radio spectrum, the mission aims to provide key observational evidence for revealing the evolutionary history of the cosmic dark ages and cosmic dawn. Second, it seeks to achieve the first high-resolution ultra-long-wave sky survey, thereby opening up a new window for low-frequency radio astronomical observations. Third, DSL will observe ultra-long-wave radio activities of the Sun and its planets, with the goal of uncovering the mechanisms governing their interactions with the interplanetary environment.

To accomplish these scientific objectives, DSL is equipped with two complementary types of payloads designed to operate across the ultra-long-wavelength band. The High Frequency Spectrometer (HFS), equipped on one high-frequency satellite, is configured to detect the power spectrum of cosmic radiation in the 30–120 MHz range with high sensitivity, enabling precise measurements of the radio spectrum. The Distributed Low-Frequency Interferometric Spectrometer (LFIS), equipped on eight low-frequency satellites, is designed to perform high-resolution imaging and spectral measurements across the full sky in the 0.1–30 MHz band, providing the first high-fidelity maps of the ultra-long-wavelength sky.

3 Solar Polar Orbit Observatory

The Solar Polar Orbit Observatory (SPO) is designed to address fundamental questions about the Sun's magnetic activity, solar wind generation, and heliospheric space weather processes[3]. The mission adopts a high-inclination solar polar orbit with an inclination exceeding 75° and an orbital period of less than 1.5 years, enabling unprecedented imaging observations of the solar polar regions. With a planned mission duration of 15 years, including 10 years dedicated to polar observations and over 800 days at latitudes above 55°, SPO will obtain the first frontal imaging of the solar polar regions, providing critical insights into the hidden engine that drives solar activity.

The scientific objectives of SPO are centered around three interconnected themes. First, to unveil the origin of the solar magnetic cycle. The mission aims to unveil the generation mechanism of the poloidal field through high-precision polar magnetic and velocity field observations, and to pinpoint the formation region of the toroidal field via polar helioseismology, thereby providing a complete picture of the solar dynamo process. Second, to understand the generation mechanism of the fast solar wind. SPO will combine polar remote-sensing observations with in-situ measurements to identify the source regions of the fast solar wind and its embedded fine structures, and quantify the relative contributions of magnetic reconnection and wave dissipation to the mass and energy supply of the solar wind. Third, to understand space weather processes in the solar system. The mission will utilize the global magnetic field distribution obtained from polar observations to provide complete initial and boundary conditions for whole-heliosphere MHD models, construct a self-consistent numerical model through iterative validation with multi-wavelength and in-situ data, and quantitatively characterize the three-dimensional structure and propagation of solar wind disturbances, thereby opening a new era of space weather and space climatology studies.

To achieve these ambitious goals, SPO carries a comprehensive suite of remote sensing and in-situ instruments. The remote sensing payloads include the Magnetic and Velocity Field Imager (MHI) for high-resolution, high-sensitivity observations of the photospheric vector magnetic field and Doppler velocity field across the full solar disk; the Extreme Ultraviolet Telescope (EUST) for high-resolution imaging and integrated spectral measurements in the extreme ultraviolet band; the White Light Coronagraph (VISCO) for visible-light imaging of the sub-Alfvénic solar wind from the low to high corona; the Heliospheric Imager (VLACOR) for tracking the propagation and evolution of solar wind structures, including coronal mass ejections, from the outer corona into the inner heliosphere; and the X-ray Imaging Telescope (XIT) for observations of solar high-energy X-ray spectra, light curves, and imaging. The in-situ payloads consist of the Solar Wind Ion Mass Spectrometer (SWIMS) for mass-resolved and angle-resolved measurements of solar wind ions, the Solar Wind Ion Retarding Potential Analyzer (SWIRPA) for fast and long-duration measurements of solar wind ions without degradation, and the Magnetometer (MAG) for precise measurements of the interplanetary magnetic field. This integrated payload suite enables SPO to simultaneously observe the Sun's polar magnetic field, the acceleration region of the solar wind, and the subsequent propagation of solar wind disturbances through the heliosphere, providing a holistic view of the Sun-heliosphere system.

4 The Earth 2.0

The Earth 2.0 (ET) mission is a space observatory at the Earth–Sun L2 point, designed to conduct a long-term, large-scale survey of exoplanets[4]. Its primary goal is to explore habitable Earth-like planets outside our solar system and to identify promising candidates for future extraterrestrial life searches. The spacecraft will be placed in a halo orbit around L2, providing a stable thermal and viewing environment essential for high-precision photometric observations over extended periods.

ET pursues three primary scientific objectives. First, the mission aims to discover Earth 2.0 s—Earth-sized planets orbiting Sun-like stars in the habitable zone—for the first time and to determine their occurrence rate. Second, by discovering a large population of terrestrial planets across a wide range of orbital distances and stellar environments, ET will reveal the statistical distribution and physical properties of the terrestrial-planet population. Third, the mission seeks to detect free-floating Earth-mass planets (rogue planets) for the first time and measure their occurrence rate, shedding light on the formation and ejection history of planetary systems.

To achieve these goals, ET carries two complementary instrument systems. The transit telescope array consists of six 28 cm aperture wide-field telescopes, achieving a photometric precision of 3.4×10^{-5}@6.5 h cumulative exposure. This array will continuously monitor approximately two million FGK stars in the Kepler field and its adjacent regions for four years, using the transit method to search for Earth-like exoplanets. The gravitational microlensing telescope is a 35 cm aperture telescope that will observe at least 30 million stars in the Galactic bulge region over a cumulative two-year period. By monitoring microlensing events and measuring microlens parallax in coordination with the ground-based telescopes, it will detect free-floating Earth-mass rogue planets and characterize their population. Together, the transit and microlensing surveys provide a powerful and complementary approach to discovering both bound terrestrial planets and unbound planetary-mass objects.

5 Enhanced X-ray Timing and Polarimetry

The Enhanced X-ray Timing and Polarimetry (eXTP) mission[5] is an X-ray space observatory designed to conduct research on the detection of dense celestial bodies such as black holes and neutron stars, with high time resolution, high energy resolution, and high-precision polarization. Operating from a circular orbit at 610 km altitude with an inclination of 20°, eXTP will explore the physical laws and principles under the extreme conditions in the universe, including extreme gravity, extreme magnetism, and extreme density. The mission will address fundamental questions such as: What happens near a black hole? What is the internal structure and composition of neutron stars? What are the properties of vacuum fluctuations in strong magnetic fields? By combining high-precision timing, spectroscopy, and polarimetry, eXTP will reveal how matter behaves in the most extreme environments ever observed.

The key scientific objectives of eXTP include: studying black hole and strong gravity physics via observing black hole accretion processes and exploring matter dynamics in strong gravity fields; studying magnetar and extreme magnetic field physics via observing magnetar vacuum polarization and measuring quantum electrodynamics effects in radiation from these stars; determining the dense matter equation of state (especially at supra-nuclear densities) and studying neutron star and extreme density physics via precise neutron star mass and radius measurements; and studying extreme condition physics via X-ray counterpart observations of gamma-ray bursts, gravitational wave bursts, high-energy gamma-ray and neutrino sources in the 2030 s.

To achieve these goals, eXTP carries two complementary focusing telescope arrays. The Spectroscopy Focusing Array (SFA) consists of six X-ray telescopes designed to perform high-sensitivity spectroscopy and timing measurements across the X-ray band. The Polarimetry Focusing Array (PFA) comprises three X-ray telescopes dedicated to high-precision X-ray polarimetry. Together, these instruments enable simultaneous measurements of spectral, timing, and polarimetric signatures from compact objects, providing a powerful and comprehensive probe of extreme physics in the universe.

6 Mission Progress

As of 2025, all four missions—DSL, SPO, ET, and eXTP—have successfully completed the Preliminary Design Phase (Phase B) and are advancing in parallel toward their respective launch readiness milestones.

In 2026, the Pathfinder-1 satellite will be launched to perform in-orbit validation of critical technologies for the main missions. All four satellites are scheduled for launch before 2031. After the launch, nominal observations will be conducted in succession and scientific data will be achieved, with the goal of delivering major discoveries and high-impact scientific results.

References

[1] Chinese Academy of Sciences; National Space Administration of China; China Manned Space Engineering Office. National Mid- and Long-term Plan for Space Science in China (2024-2050) [EB/OL]. (2024-10-16)[2026-04-01] https://www.gov.cn/lianbo/bumen/202410/content_6980618.htm

[2] CHEN Xuelei, YAN Jingye, DENG Li, *et al*. 2021 Discovering the sky at the longest wavelengths with a lunar orbit array[J]. *Philosophical Transactions of the Royal Society A*, 2021, **379**(2788): 20190566

[3] DENG Yuanyong, ZHOU Guiping, DAI Shuwu, *et al*. Solar polar-orbit observatory[J]. *Chinese Science Bulletin*, 2023, **38**(4): 298-308 (邓元勇, 周桂萍, 代树武, 等. 太阳极轨天文台 [J]. 科学通报, 2023, **38**(4): 298-308)

[4] GE Jian, ZHANG Hhui, DENG Hongping, *et al*. The ET mission to search for Earth 2.0 s[J]. *The Innovation*, 2022, **3**(4): 100271

[5] ZHANG Shuang-Nan, SANTANGELO Andrea, XU Yupeng, *et al*. The enhanced X-ray Timing and Polarimetry mission—eXTP for launch in 2030[J]. *Science China Physics, Mechanics & Astronomy*, 2025, **68**(11): 119502

Author Biography

WANG Chi The Director of the National Space Science Center, Chinese Academy of Sciences (CAS), and an Academician of CAS and the International Academy of Astronautics. He received his bachelor’s degree from the University of Science and Technology of China in 1990 and his Ph.D. from the Massachusetts Institute of Technology in 1998. His research focuses on space physics and space weather. He currently serves as Chief Scientist of Phase IV of China’s Lunar Exploration Program, the Chinese Principal Investigator of the Solar Wind Magnetosphere Ionosphere Link Explorer (SMILE) mission, and Commander-in-Chief of Phase II of the Chinese Meridian Project. His honors include the Special Prize of the National Science and Technology Progress Award, the Qian Xuesen Outstanding Contribution Award, and the First Prize of the Science and Technology Progress Award of the Chinese Geoscience Union.
E-mail: cw@spaceweather.ac.cn

0254-6124/2026/46(4)-0109-09 *Chin. J. Space Sci.* 空间科学学报

WANG Chi, XU Jiyao, ZHANG Qinghe, WANG Jiangyan, REN Liwen, YANG Fang. The Chinese Meridian Project (CMP) and the International Meridian Circle Program (IMCP): Overview, Progress, and Achievements. *Chinese Journal of Space Science*, 2026, **46**(4): 109–117. CSTR:32142.14.cjss.2026–yg07. DOI:10.11728/cjss2026.04.2026–yg07

The Chinese Meridian Project (CMP) and the International Meridian Circle Program (IMCP): Overview, Progress, and Achievements

WANG Chi XU Jiyao ZHANG Qinghe

WANG Jiangyan REN Liwen YANG Fang

(*National Space Science Center*, *Chinese Academy of Sciences*, *Beijing* 100190)

Abstract The National Major Scientific and Technological Infrastructure— the Chinese Meridian Project (CMP) — completed its Phase II acceptance and integration with Phases I in March 2025, and has since entered full operation. The project employs a detection architecture consisting of “one chain, three networks, and four focuses”, deploying 282 monitoring instruments across 31 stations within China’s territory and at both poles. This forms a grid-like comprehensive ground-based network monitoring the geospace environment along 100°E, 120°E, 30°N, and 40°N. Currently, this project has the world's most extensive, comprehensive, and capable such network. The data it acquires are openly shared globally, supporting worldwide cutting-edge scientific research on space weather and its warning/forecasting. This article highlights research advances achieved over the past two years using the CMP data, and briefly introduces the International Meridian Circle Program, which is currently being promoted and initiated based on the CMP.

Key words Chinese Meridian Project, International Meridian Circle Program, Sun, Interplanetary, Ionosphere, Middle and upper atmosphere

Classified index P35

1 Overview of the Chinese Meridian Project

The Solar-terrestrial space serves as a natural laboratory for contemporary scientific exploration and the primary arena for human space activities and space development. Monitoring and research on the Solar-terrestrial space environment to understand its characteristics, reveal cascading processes and patterns of space weather changes, and improve forecasting capabilities is essential for humanity to enter and utilize space.

Monitoring of the Solar-terrestrial space environment can be carried out through two approaches: ground-based and space-based. Compared with space-based monitoring, ground-based monitoring offers the 5 C advantages of being Continuous, Convenient, Controllable, Credible, and eConomical. Therefore, establishing ground-based space environment monitoring facilities in China, comprehensively conducting monitoring and research on complex and interlinked processes of the Solar-terrestrial space environment, and improving space weather forecasting capabilities are of great scientific significance and urgent demand. To meet this scientific and application demand, the Chinese Meridian

Received May 20, 2026

Project (CMP) came into being

The CMP is China's sole large research infrastructure dedicated to the observation and research of space weather. Through two phases of construction, it has deployed nearly 300 sets (or units) of monitoring equipment at 31 stations across China and the North and South Poles, forming a space environment monitoring network along two longitude lines (100°E and 120°E) and two latitude lines (40°N and 30°N)[1,2]. This monitoring network deploys advanced solar-interplanetary instruments along the Solar-terrestrial space chain, enabling end-to-end monitoring from solar eruptions to Earth's response (one chain). It employs geomagnetic, radio, and optical detection methods to construct a networked detection system covering the ionosphere, middle and upper atmosphere, and geomagnetic field over China (three networks). In the polar high-latitude region, northern mid-latitudes, low latitudes around Hainan, and the Qinghai–Tibet Plateau, it has built a number of internationally advanced or leading large-scale instruments for fine-scale "microscopic" detection (four focuses). The "one chain, three networks, four focuses" architecture achieves, for the first time in the world, a comprehensive, three-dimensional, multi-element detection of the entire Solar-terrestrial space environment, elevating China's ground-based space environment detection and research to a world-leading level and playing a key role in advancing our understanding and forecasting capabilities in the Solar-terrestrial domain.

The CMP-Phase II successfully passed its process acceptance in June 2024 and received national acceptance in March 2025. This marks the completion of the entire Chinese Meridian Project construction. After nearly two years of trial operation and formal operation, the data acquired have been made openly accessible to scientists worldwide*. Over the past two years, nearly 300 papers have been published based on CMP data, demonstrating its significant and emerging benefits for research and applications in the Solar-terrestrial space environment. This paper systematically reviews the main achievements from 2024 to 2025 in key research areas such as solar and interplanetary physics, the ionosphere, and the middle and upper atmosphere, all derived from CMP data. Additionally, it briefly introduces the International Meridian Circle Program, a major international initiative being advanced based on the CMP.

2 Major Research Achievements of CMP over the Past Two Years

2.1 Observation and Research of the Solar and Interplanetary Space

Based on Phase I, CMP-Phase II added a solar-interplanetary monitoring chain, deploying equipment such as solar radio and interplanetary scintillation monitors, thereby providing rich observational data support for the project's observation of solar activity eruptions and their geoeffectiveness.

The solar radio spectrum system (CBSm) built at Chashan, Rongcheng Station provides radio spectrum observations for studying the radiation mechanisms of solar eruptions. Using CBSm data, Li *et al*.[3] discovered a novel fine spectral structure in solar radio emission termed as "periodic beaded stripes". Based on the double plasma resonance instability and modulation by low-frequency MHD waves, they proposed a physical model that explains this new phenomenon and can be used to diagnose key parameters such as the source density and magnetic field. Yang *et al*.[4] automatically identified and statistically analyzed more than 105 Type I bursts. Lifetimes, bandwidths, polarization properties, and sub-second periodicities within burst chains were systematically characterized, yielding new constraints on the particle acceleration and radiation mechanisms underlying Type I bursts. In addition, Cui *et al*. [5] investigated a Type II burst without an accompanying CME. They found that the jet-induced disturbance evolved into a shock wave in a coronal loop with low Alfvén speed, which further drove the Type II burst and the associated Type III/N bursts, revealing a new mechanism for high-frequency Type II bursts under weak-activity conditions.

The IPS telescope is a pivotal interplanetary monitoring device within the Solar-terrestrial monitoring chain of the CMP. It is China's first IPS observation-dedicated facility and currently the world's largest in aperture. Recently, researchers have made significant progress in hardware-software integration and first-light detection using this instrument. Fan *et al*.[6] employed

* https://www.meridianproject.ac.cn/en/

PANDA, a diffusion model-based generative AI calibration method, to control the digital-analog hybrid beamforming architecture, enabling phased array feed calibration under variable radio frequency interference. Xiong *et al*. [7] used the telescope to detect dual-polarization IPS signals from the radio source 3 C446 and derive the solar wind speed, enabling remote sensing of the solar wind speed at 24 solar radii.

2.2 Observation and Research of the Ionosphere

2.2.1 Study of Ionospheric Response to Extreme Geomagnetic Storms

The years 2024 and 2025 are right at the peak of the 25 th solar activity cycle. The continuous, multi-instrument, and large-scale monitoring of the CMP provides favorable means for studying the response mechanisms of the ionosphere to intense eruptive solar activities.

Flares are among the most violent activity phenomena on the Sun, accompanied by suddenly enhanced X-ray and Extreme Ultraviolet (EUV) radiation. Recent studies have shown that in some flares, the EUV radiation increases again during the late phase, a phenomenon referred to as the EUV late phase of solar flares. Based on multi-source ionospheric and geomagnetic observation data from the CMP and other facilities, as well as results from the TIEGCM driven by realistic solar radiation spectra, Liu *et al*. [8] provided the first direct evidence that the flare late phase significantly affects ionospheric electron density. Liu *et al*.[9] further utilized data from more than 200 geomagnetic observatories worldwide, combined with simulation results, and found that the EUV late phase of flares can influence the ionospheric current system.

Geomagnetic storms are dramatic disturbances in the Earth's space environment triggered by solar eruptions. The Super Geomagnetic Storm of May 2024 was the most intense geomagnetic storm in nearly two decades, injecting a large amount of solar wind and magnetospheric energy into the Earth's atmosphere and causing severe disturbances in the ionospheric environment. For this event, Chen *et al*.[10] reported unprecedented observational evidence of extreme ionospheric electron density depletion and its hemispheric asymmetry, and confirmed that the negative ionospheric storm led to HF signal interruption. Their analysis showed that changes in neutral composition and disturbance electric fields jointly caused the sharp electron density depletion, while neutral winds from the summer hemisphere to the winter hemisphere, together with the asymmetry in the neutral composition ratio (O/N_2), were the main reasons for the north-south asymmetry. In addition, researchers have investigated various ionospheric changes and irregularities of different scales during multiple geomagnetic storms, including: mid-latitude density enhancement structures [11], storm-time east-west asymmetric responses[12], super plasma bubbles[13,14], nighttime ionospheric enhancements [15,16], and storm-time thermospheric temperature changes[17,18]. These studies reveal the diversity and complexity of the ionospheric response to solar activity, and provide support for a deeper understanding of how solar activity drives different types of ionospheric variations.

2.2.2 Study of Ionospheric Irregularities in Mid- and High-Latitude Regions

The polar region is the main area where solar wind mass and energy are injected into Earth's space. Studying the solar wind-magnetosphere-ionosphere coupling processes in the polar region under different interplanetary conditions is of great significance for both fundamental research and forecasting applications in space weather. Traditional understanding holds that under northward IMF conditions, the energy coupling efficiency is very low. Zhang *et al*.[19] discovered a typhoon-like phenomenon above the ionosphere around the Earth's north geomagnetic pole under extremely quiet geomagnetic conditions, and named it as "space hurricane". They found that the space hurricane is a huge funnel-shaped magnetic spiral structure generated by a stable high-latitude lobe reconnection and current continuity. By accelerating polar ionospheric plasma upwelling and electron precipitation into the ionosphere, it opens a huge and rapid energy transfer channel between the solar wind and the magnetosphere. Lu *et al*.[20] and Xiu *et al*. [21] revealed for the first time that the space hurricane is accompanied by enhanced convection electric fields and Joule heating, which heats the local ionosphere/thermosphere, drives ion upwelling, and disturbs the polar thermosphere to excite gravity waves. Lu *et al*.[22] further confirmed the lobe reconnection mechanism of the space hurricane by statistically analyzing its occurrence frequency, temporal and spatial distribution characteristics, and plasma properties in the Southern Hemisphere.

The mid-latitude ionosphere connects the polar and low-latitude ionospheres and serves as an important region for coupling and disturbance propagation between high, middle, and low latitudes, where the ionospheric dynamic processes are particularly complex. The Chinese Dual Auroral Radar Network (CN-DARN) of the CMP enables continuous monitoring of the ionospheric environment over Asian middle and high latitudes, covering 40°N–80°N, extending more than 4000 km northward and spanning over 10000 km east-west, providing new opportunities for studying ionospheric disturbances in this region. Based on continuous observations from CN-DARN, Zhang *et al*.[23] found that CN-DARN completely captured the rare spatiotemporal evolution process of dawnside Subauroral Polarization Streams (SAPS), and revealed a direct physical connection between the dawnside SAPS acceleration and auroral intensification. They also determined that, during intense geomagnetic storms, high-speed ionospheric irregularities induced by the dawnside SAPS can intrude into Chinese airspace and disturb the stability of the regional ionospheric environment. In addition, they quantified the impact of auroral activity on high-frequency communication in the Asian region. Using a total of 12 high-frequency radars, including the CN-DARN radars and six international SuperDARN radars, Zhao *et al*.[24] successfully achieved simultaneous, large-scale, high-spatiotemporal-resolution observations of two types of SAPS on both the dusk side and the dawn side during an intense geomagnetic storm. They clarified the key differences between the two types of SAPS in terms of spatial distribution, temporal evolution, and formation conditions.

2.2.3 Study of Ionosphere in Low-latitude Regions

Due to the complex structures such as ionospheric irregularities and the equatorial anomaly, as well as rich dynamic and electrodynamic processes, the low-latitude region is one of the areas where severe space weather phenomena occur most frequently on Earth, and it is also a region of strong thermosphere-ionosphere coupling. The low-latitude ionospheric environment can significantly affect various high-technology systems, including satellite communication and navigation, making it a key area of focus for international space environment observation and research in recent years. The CMP has deployed a series of observational instruments in the low-latitude region of Hainan, China, including radio radars, lidars, and magnetometers, providing strong data support for ionospheric research in this region.

The CMP has built an incoherent scatter radar in Hainan, which is the only phased-array ISR currently operational at low latitudes. Researchers have used this facility to conduct research on the dynamics of the low-latitude ionosphere over Hainan. Zhang *et al*.[25] developed a sophisticated algorithm to derive neutral wind and electric field from multiple beams SYISR measurements, providing a new data source for studies of ionospheric dynamics and low-latitude atmosphere-ionosphere-magnetosphere coupling. Yue *et al*.[26] observed the 150-km echo anomaly in the UHF band for the first time; Xu *et al*. [27] and Zhao *et al*. [28] obtained the vertical characteristics of Large-Scale Traveling Ionospheric Disturbances (LSTIDs) and ionospheric holes triggered by rocket launches, respectively. These efforts will provide an important observational basis for studying the regional characteristics of the ionosphere over East Asia.

Equatorial Plasma Bubbles (EPBs) are common irregular structures in low-latitude regions, containing various small- and medium-scale field-aligned irregularities. These irregular structures interfere with radio wave propagation applications, adversely affecting communications, navigation, and other systems. Using observations from the CMP, researchers have conducted studies on the large-scale characteristics of plasma bubbles in low-latitude regions, the evolution of bubble structural features, and the fine structures within bubbles, achieving a series of breakthroughs. Hu *et al*. [29], using Low lAtitude long Range Ionospheric raDar (LARID), for the first time depicted a complete picture of EPB originating over the Indian Ocean and then drifting and evolving over a large east-west extent to influence the South China Sea. Sun *et al*. [30], through comprehensive observational studies of plasma bubble events during several magnetic storms, presented the large-scale spatial distribution characteristics of super plasma bubbles extending to mid-latitudes, discussed their controlling factors, and revealed the promoting effect of rapid penetration electric fields accompanying the southward turning of the IMF B_z component during storms on super plasma bubble events. Jia *et al*.[31] revealed the distribution and maintenance mechanisms of small- and medium-scale irregularities within plasma bubbles in the different dissipation phases; Jia *et al*.[32] explored the mechanism by which irregularities extend outside the bubbles and confirmed the existence of inter-bubble electrostatic reconnection. By comprehensively utilizing observations from the CMP's calcium ion lidar and radio radar, Sun *et al*.[33] captured for the first time the depletion and bifurcation structures of EPBs, surpassing the detection limits of conventional radars and demonstrating that metal ions can serve as a "developer" for EPBs, providing a new means to study the mapping process of EPBs along magnetic field lines.

2.3 Observation and Research of the Middle and Upper Atmosphere

The middle and upper atmosphere is a key transition region from Earth's atmosphere to space. Solar activity has a significant impact on the middle and upper atmosphere. Meanwhile, through complex coupling processes among different atmospheric layers, activities in the lower atmosphere or the lithosphere can also drive environmental changes in the middle and upper atmosphere and the ionosphere. Key scientific issues such as the effects of space weather events on the middle and upper atmosphere, the coupling between the upper and lower atmospheres, and the latitudinal and longitudinal transmission of energy and momentum represent frontier directions in current basic space physics research.

Leveraging the observational network of the CMP, researchers have conducted in-depth studies on anomalous changes in the neutral atmosphere of the Mesosphere and Lower Thermosphere (MLT) region, the middle and upper atmosphere, and the ionospheric structure during typical space weather events. Using MST radar observations from the CMP's Wuhan and Beijing stations, Li *et al*. [34] found for the first-time direct evidence that substorm events affect the atmospheric wind field in the mid-latitude MLT region through Joule heating, extending the influence of geomagnetic activity on geospace to the mid-latitude lower thermosphere. Additionally, Chen *et al*. [35] discovered for the first time that the solar eclipse can trigger an intermediate descending layer, revealing the complex dynamic processes and their coupling effects in the geospace environment during an eclipse. Hu *et al*. [36] observed rare large-scale stripe-shaped irregularities and found that MSTIDs (Medium-Scale Traveling Ionospheric Disturbances) lead to the generation of field-aligned irregularities in the low-latitude F region, indicating that equatorial plasma bubbles are not the only source of field-aligned irregularities in the low-latitude F region.

In the middle and upper atmosphere, tides and gravity waves are important atmospheric wave phenomena, serving as key mediators for cross-layer coupling between the lower atmosphere and the middle/upper atmosphere. Using the CMP's meteor radar chain, Wang *et al*.[37] investigated the Quasi-Biennial Oscillation (QBO) disruption. Their results suggest that the QBO wind affects mid-latitude mesospheric diurnal tides by modulating both the solar radiative absorption by subtropical stratospheric ozone and the tidal-gravity wave interaction in the mesosphere. Wang *et al*.[38] analyzed the effects of topography differences (plateau *vs*. coastal terrain) at similar latitudes on gravity wave activity, finding that the seasonal variations in gravity wave activity over Kunming and Sanya/Fuke may be related to the unique surface wind patterns over Kunming and the convective systems over the Tibetan Plateau. Based on observations from the CMP's airglow imager network, Li *et al*.[39] for the first time observed a large-scale, long-distance propagating mode of atmospheric gravity waves, which were generated by the interaction between tsunamis (triggered by the Tonga volcanic eruption) and the atmosphere. Combining meteor radar data from the CMP's Mohe station and Germany's Collm station, He *et al*. [40,41] analyzed nine years of atmospheric wind observations in the meteor layer. They identified for the first time higher-order solar-synchronous tides with periods of 4.8 hours and 4 hours, clarified that multi-day disturbances are primarily driven by atmospheric normal modes with their dynamic mechanisms significantly influenced by seasonal factors, and revealed nonlinear interactions among more than ten normal modes as well as between normal modes and tides. These interactions promote the transfer and dissipation of energy from planetary to smaller scales. Collectively, these findings demonstrate that variations in the mesosphere can be linked to changes in the troposphere/stratosphere lower atmosphere via atmospheric waves such as tides and gravity waves, providing new insights into the coupling between the lower and middle/upper atmospheres.

2.4 Research Progress in Space Weather Forecasting

The completion of the CMP has, on the one hand, facilitated major breakthroughs in original scientific research, and on the other hand, provided valuable observational data for the development of space environment forecasting technology.

The spatiotemporal variation of ionospheric Total Electron Content (TEC) is extremely complex, and its prediction is of great significance for the accuracy and stability of radio communication, navigation, positioning, and related applications. Using ionospheric GNSS observation data from the CMP, Yang *et al.* [42] developed a Convolution Long Short-term Memory (ConvLSTM) network model for TEC forecasting (with a spatial resolution of 5°×2.5° (longitude×latitude) and a time resolution of 1 h). Performance evaluation results show that the model achieves average Root Mean Square Errors (RMSE) of 2.81, 3.16, and 3.41 TECU for 1-day, 2-day, and 3-day TEC forecasts, respectively, demonstrating a significant improvement in performance compared to the 1-day forecast product of the IRI-Plas model.

Ionospheric scintillation, a phenomenon of radio signal fluctuation caused by ionospheric irregularities, can significantly reduce the accuracy and stability of navigation systems. Therefore, establishing accurate and effective ionospheric scintillation prediction models is of great importance for improving the reliability of navigation and communication systems. Gao *et al*.[43] proposed an ionospheric scintillation prediction method based on a dynamic spatiotemporal decomposition framework. This method can predict the distribution of the ionospheric scintillation index in low-latitude regions reasonably accurately one hour in advance. Its flexible dynamic modeling framework and extensibility for external variables can serve as a reference for modeling complex dynamic systems in other space weather events.

When a solar storm strikes Earth, the violently disturbed geomagnetic field induces geoelectric potentials on the Earth's surface, which in turn generate Geomagnetically Induced Currents (GIC) in ground-based power grids, threatening the safe operation of power systems. It is generally believed that high-latitude regions face a higher risk of GIC damage to power grids due to intense geomagnetic disturbances. In recent years, as the geomagnetic latitude of China has increased, assessing the impact of GIC on China's regional power grids has become increasingly important. Wang *et al*.[44] studied the characteristics of geomagnetic field responses over China during the strong "Mother's Day" geomagnetic storm in 2024 and used a GIC model to evaluate the potential impact of this storm on the power grid in eastern Inner Mongolia. The results show that the intensity of this geomagnetic storm exceeded that of the November 2004 geomagnetic storm and was comparable to the March 1989 event. This work clearly reveals the disturbance characteristics of strong geomagnetic storm events on the geomagnetic field over China and their impact mechanism on the eastern Inner Mongolia power grid, fully demonstrating the large-area monitoring capability of the CMP and providing important scientific support for future geomagnetic storm risk assessment and extreme space weather protection.

2.5 Joint Observation and Research with Other Large-scale Scientific Facilities

Water ice, one of the most important resources on the Moon, exists in the polar regions, and detecting water ice in the lunar polar regions is a current hot topic in lunar research. Previous studies have indicated the presence of water ice in permanently shadowed regions of the lunar south pole using various methods; however, questions regarding the content, distribution, and form of water ice remain unresolved. Li *et al*.[45] innovatively utilized the CMP's SYISR (Sanya Incoherent Scatter Radar) and the Five-hundred-meter Aperture Spherical radio Telescope (FAST) to form a ground-based bistatic radar system, obtaining circular polarization ratio radar images of the lunar south pole. By combining multi-source data, they estimated the upper limit of water ice content and its potential distribution in the lunar south polar region. The upper limit and distribution obtained in this study provide important information for research on the evolution of lunar water ice and can serve as a reference for selecting landing sites for future missions aimed at collecting water ice from the lunar south pole.

3 International Meridian Circle Program

Building upon the solid foundation of the Chinese

Meridian Project, China, in partnership with global collaborators, has initiated the International Meridian Circle Program (IMCP)[46,47]. The IMCP aims to establish a globally distributed network of ground-based instruments—primarily along the 120°E and 60°W meridians—spanning multiple countries and continents, which will operate for at least a full solar cycle (11 years). By combining space-based observations, the IMCP will unravel the top-down and bottom-up mechanisms through which solar energy and terrestrial activity transfer into and disperse within geospace. Furthermore, the program will develop data-driven space weather models and high-precision forecasting products, providing a critical scientific basis for mitigating space weather disasters and promoting the peaceful utilization of space[48].

Looking ahead to the next solar cycle and beyond, the IMCP will establish an international scientific organization headquartered in Beijing to guide and coordinate global activities across four core pillars[49]. First, it will enhance global space weather monitoring by expanding the ground-based network through the establishment of key observatories and extending coverage to the 30°E and 150°W meridian chains, thereby enabling 24/7 solar eruption tracking, geospace-atmosphere coupling monitoring, and interdisciplinary solid Earth observations. Second, the organization will advance interdisciplinary research to investigate the solar drivers of space weather, energy coupling mechanisms, global and regional geospace characteristics, and the impacts of lithosphere-atmosphere processes, while pioneering next-generation space weather models and AI-driven forecasting. Third, it will establish a globally distributed data platform to integrate and standardize data streams from thousands of heterogeneous instruments worldwide, fostering open-data sharing. Finally, the program aims to cultivate a multi-layered global collaboration network by launching the open-access journal *Space Plus*, initiating joint research initiatives, and organizing international academic workshops and schools.

Ultimately, the IMCP represents a paradigm shift in heliophysics, leveraging unprecedented international cooperation to address global space weather challenges and answer the fundamental questions governing the solar-terrestrial coupling system.

References

[1] WANG C. New chains of space weather monitoring stations in China[J]. *Space Weather*, 2010, **8**(8). DOI: 10.1029/2010SW000603

[2] WANG C, XU J Y, CHEN Z Q, *et al*. China's ground-based space environment monitoring network-Chinese meridian project (CMP)[J]. *Space Weather*, 2024, **22**(7): e2024SW003972

[3] LI C Y, CHEN Y, WANG B, *et al*. A novel fine spectral structure of solar radio bursts with periodic beaded stripes observed by CBSm of CMP-II[J]. *Science China Physics, Mechanics & Astronomy*, 2025, **68**(10): 109611

[4] YANG Y Z, NING Z J, SONG Y X, *et al*. High-resolution observational features of type I solar radio bursts[J]. *The Astrophysical Journal*, 2025, **985**(2): 257

[5] CUI Y L, KONG X L, LI Z T, *et al*. A solar jet-induced perturbation propagating through coronal loops and in-loop electron beam transport as indicated by type II and type N radio bursts[J]. *Astronomy & Astrophysics*, 2026, **706**: A197

[6] FAN J, WANG W, PENG J H, *et al*. Design and performance of phased array feed system for the meridian project phase II interplanetary scintillation telescope[J]. *Journal of Geophysical Research*: *Space Physics*, 2025, **130**(12): e2025JA034585

[7] XIONG M, WANG W, SU C, *et al*. First light for the new 30 m parabolic radio telescope at ArQi: Implications for space weather monitoring[J]. *The Astronomical Journal*, 2026, **171**(3): 125

[8] LIU J, QIAN L Y, WANG W B, *et al*. Energy deposition into the ionosphere during a solar flare with extreme-ultraviolet late phase[J]. *The Astrophysical Journal Letters*, 2024, **963**(1): L8

[9] LIU X Q, FAN X Y, LIU J, *et al*. Response of global ionospheric currents to solar flares with extreme ultraviolet late phases[J]. *The Astrophysical Journal*, 2024, **963**(1): 27.

[10] CHEN Y H, AA E, YUAN T J, *et al*. The extreme depletion of ionospheric electron density and its hemispheric asymmetry during the May 2024 storm[J]. *National Science Review*, 2025, **12**(10): nwaf307.

[11] YANG Y Y, LIU L B, LI W B, *et al*. Localized plasma density peak at middle latitudes during the April 2023 geomagnetic storm[J]. *Journal of Geophysical Research*: *Space Physics*, 2024, **129**(2): e2023JA032165.

[12] GUO X, ZHAO B Q, YU T T, *et al*. East–west difference in the ionospheric response during the recovery phase of May 2024 super geomagnetic storm over the East Asian[J]. *Journal of Geophysical Research*: *Space Physics*, 2024, **129**(9): e2024JA033170

[13] SUN W J, LI G Z, ZHAO B Q, *et al*. Midlatitude plasma blob-like structures along with super equatorial plasma bubbles during the May 2024 great geomagnetic storm[J]. *Geophysical Research Letters*, 2024, **51**(21): e2024GL111638.

[14] HAN C Y, LI G Z, SUN W J, *et al*. Generation and evolution of post-sunset equatorial plasma bubbles in East and Southeast Asia during the July 2022 geomagnetic storm[J]. *Advances in Space Research*, 2024, **73**(3): 1843-1853.

[15] HAO H L, ZHAO B Q, JIN Y Y, *et al*. Latitude variation of the

post-sunset plasma density enhancement during the minor geomagnetic storm on 27 May 2021[J]. *Journal of Geophysical Research: Space Physics*, 2024, **129**(3): e2023JA032156.
[16] HAO H L, ZHAO B Q, YUE X N, *et al*. Latitudinal characteristics of the post-sunset enhancements in ionospheric electron density during the geomagnetic quiet period in May 2021 over East-Asian region[J]. *Journal of Geophysical Research: Space Physics*, 2024, **129**(10): e2024JA033047.
[17] LI S Y, REN Z P, YU T T, *et al*. The daytime variations of thermospheric temperature and neutral density over Beijing during minor geomagnetic storm on 3-4 February 2022[J]. *Space Weather*, 2024, **22**(2): e2023SW003677
[18] LI S Y, REN Z P, YU T T, *et al*. A case study of thermospheric exospheric temperature responses during the G- condition at Mohe and Beijing stations[J]. *Journal of Geophysical Research: Space Physics*, 2024, **129**(10): e2024JA032653
[19] ZHANG Q H, ZHANG Y L, WANG C, *et al*. A space hurricane over the Earth's polar ionosphere[J]. *Nature Communications*, 2021, **12**(1): 1207.
[20] LU S, XING Z Y, ZHANG Q H, *et al*. Observations of three-dimensional ionospheric plasma properties in a space hurricane[J]. *Frontiers in Astronomy and Space Sciences*, 2024, **11**: 1507824.
[21] XIU Z F, MA Y Z, ZHANG Q H, *et al*. Direct observation of the space hurricane disturbed polar thermosphere[J]. *Geophysical Research Letters*, 2024, **51**(1): e2023GL106735.
[22] LU S, XING Z Y, ZHANG Q H, *et al*. A statistical study of space hurricanes in the Southern Hemisphere[J]. *Journal of Geophysical Research: Space Physics*, 2024, **129**(6): e2024JA032753.
[23] ZHANG J J, DENG X, XU J Y, *et al*. Auroral activity observed from unusual latitudes in China and its underlying significance[J]. *The Innovation Geoscience*, 2026, **4**(1): 100197
[24] ZHAO B L, ZHANG J J, ZHANG Q H, *et al*. Simultaneous observation of duskside and dawnside subauroral polarization streams during an intense magnetic storm[J]. *Geophysical Research Letters*, 2025, **52**(17): e2024GL114160.
[25] ZHANG N, YUE X N, CAI Y H, *et al*. F region neutral wind and electric field measured by SYISR and evaluation[J]. *Journal of Geophysical Research: Space Physics*, 2024, **129**(5): e2024JA032514.
[26] YUE X N, WANG J Y, WANG Y H, *et al*. First detection of the enigmatic low latitude 150-km echoes in the UHF band[J]. *Geophysical Research Letters*, 2024, **51**(19): e2024GL110344.
[27] XU S, DING F, YUE X N, *et al*. The observation of traveling ionospheric disturbances using the Sanya incoherent scatter radar[J]. *Remote Sensing*, 2024, **16**(17): 3126
[28] ZHAO L X, DING F, YUE X N, *et al*. Vertical structural evolution of ionospheric holes triggered by rocket launches observed by the Sanya incoherent scatter radar[J]. *Journal of Geophysical Research: Space Physics*, 2024, **129**(12): e2024JA033171.
[29] HU L H, LI G Z, NING B Q, *et al*. Extremely long-range observations of ionospheric irregularities in a large longitude zone from Pacific to Africa using a low latitude over-the-horizon radar in China[J]. *Geophysical Research Letters*, 2024, **51**(16): e2024GL109579
[30] SUN W J, LI G Z, ZHANG S R, *et al*. Regional ionospheric super bubble induced by significant upward plasma drift during the 1 December 2023 geomagnetic storm[J]. *Journal of Geophysical Research: Space Physics*, 2024, **129**(6): e2024JA032430.
[31] JIA W, LI Y X, CHEN G, *et al*. Concurrent observations of plasma bubbles and field-aligned irregularities in low-latitudes of China[J]. *Journal of Geophysical Research: Space Physics*, 2025, **130**(7): e2025JA033788.
[32] JIA Y L, CHEN G, XU J Y, *et al*. Why do small-scale irregularities migrate beyond the equatorial plasma bubble?[J]. *Geophysical Research Letters*, 2025, **52**(13): e2024GL114399
[33] SUN W J, JIAO J, YANG G T, *et al*. First observation of ionospheric plasma bubble signatures by Ca^+ lidar at low latitude[J]. *Geophysical Research Letters*, 2025, **52**(6): e2025GL114696.
[34] LI Y X, CHEN G, ZHANG S D, *et al*. Observational evidence for the neutral wind responses in the mid-latitude lower thermosphere to the strong geomagnetic activity[J]. *Space Weather*, 2024, **22**(9): e2023SW003830.
[35] CHEN G, CAI X S, ZHANG S D, *et al*. Intermediate descending layers emerged simultaneously in five different locations during the solar eclipse on 21 June 2020[J]. *Journal of Geophysical Research: Space Physics*, 2024, **129**(7): e2023JA032340.
[36] HU P F, CHEN G, YAN C X, *et al*. Study of the long-lasting daytime field-aligned irregularities in the low-latitude F-region on 13 June 2022[J]. *Remote Sensing*, 2024, **16**(15): 2738.
[37] WANG J Y, LI N, YI W, *et al*. The impact of quasi-biennial oscillation (QBO) disruptions on diurnal tides over the low- and mid-latitude mesosphere and lower thermosphere (MLT) region observed by a meteor radar chain[J]. *Atmospheric Chemistry and Physics*, 2024, **24**(23): 13299-13315.
[38] WANG J Y, YI W, LI N, *et al*. The climatology of gravity waves over the low-latitude region estimated by multiple meteor radars[J]. *Remote Sensing*, 2024, **16**(16): 2870.
[39] LI Q Z, XU J Y, GUSMAN A R, *et al*. Upper-atmosphere responses to the 2022 Hunga Tonga–Hunga Ha′apai volcanic eruption via acoustic gravity waves and air–sea interaction[J]. *Atmospheric Chemistry and Physics*, 2024, **24**(14): 8343-8361.
[40] HE M S, FORBES J M, JACOBI C, *et al*. Observational verification of high-order solar tidal harmonics in the Earth's atmosphere[J]. *Geophysical Research Letters*, 2024, **51**(8): e2024GL108439.
[41] HE M S, FORBES J M, STOBER G, *et al*. Nonlinear interactions of planetary-scale waves in mesospheric winds observed at 52°N latitude and two longitudes[J]. *Geophysical Research Letters*, 2024, **51**(24): e2024GL110629.
[42] YANG J Y, HUANG W G, XIA G Z, *et al*. Operational forecasting of global ionospheric TEC maps 1-, 2-, and 3-day in advance by ConvLSTM model[J]. *Remote Sensing*, 2024, **16**(10): 1700.
[43] GAO Z X, CHEN Y H, AO X Z, *et al*. ISNet: Decomposed dynamic spatio-temporal neural network for ionospheric scintillation forecasts[J]. *Space Weather*, 2025, **23**(6): e2024SW004239

[44] WANG J, YAN Y, LUO B X, *et al*. The new geomagnetic monitoring network in China: Insights from the 2024 Mother's Day superstorm[J]. *Space Weather*, 2026, **24**(2): e2025SW004610

[45] LI M Y, SUN J H, YUE X A, *et al*. Upper limit of ice content at the lunar south pole as revealed by the Earth-based SYISR-FAST bistatic radar system[J]. *Science Bulletin*, 2025, **70**(10): 1691-1698

[46] LIU W, BLANC M, DONOVAN E, *et al*. Science Objectives and Observation System for the International Meridian Circle[R]. Beijing: ISSI-BJ, 2019

[47] LIU W, WANG C, SHEN X H, *et al*. International meridian circle program[J]. *Chinese Journal of Space Science*, 2020, **40**(5): 723-725

[48] LIU W, BLANC M, WANG C, *et al*. Scientific challenges and instrumentation for the International Meridian Circle Program[J]. *Science China Earth Sciences*, 2021, **64**(12): 2090-2097

[49] LIU W, MICHEL B, WANG C, *et al*. Progress of international meridian circle program[J]. *Chinese Journal of Space Science*, 2022, **42**(4): 584-587

Author Biography

WANG Chi Male, born in February 1967 in Shaoyang City, Hunan Province, China, is currently a professor at the National Space Science Center, Chinese Academy of Sciences (CAS), and an academician of the CAS. His research foc-uses on the large-scale structures of the solar wind, the interaction between the solar wind and Earth's magnetosphere, and related fields. He has published more than 300 articles in a batch of academic journals like Nature.
E-mail: cw@spaceweather.ac.cn

0254-6124/2026/46(4)-0118-17 *Chin. J. Space Sci.* 空间科学学报

WANG Jinsong, GUAN Min, XU Na, JIA Shuze, FANG Meng, ZONG Weiguo, YAO Yixin, ZHANG Yu, LIU Chang, XIAN Di, FAN Cunqun. Progress of Fengyun Meteorological Satellite Integrated Observation System (2024–2026). *Chinese Journal of Space Science*, 2026, **46**(4): 118–134. CSTR:32142.14.cjss.2026–yg17. DOI:10.11728/cjss2026.04.2026–yg17

Progress of Fengyun Meteorological Satellite Integrated Observation System (2024–2026)*

WANG Jinsong GUAN Min XU Na JIA Shuze
FANG Meng ZONG Weiguo YAO Yixin
ZHANG Yu LIU Chang XIAN Di FAN Cunqun

1(*National Satellite Meteorological Center* (*National Centre for Space Weather*), *Beijing* 100081)

2(*Key Laboratory of Radiometric Calibration and Validation for Environmental Satellites*)

3(*Key Laboratory of Space Weather*, *Beijing* 100081)

4(*Innovation Center for Fengyun Meteorological Satellite* (*FYSIC*), *Beijing* 100081)

Abstract This paper systematically presents the comprehensive progress of the Fengyun (FY) meteorological satellite integrated observation system during 2024–2026. With the successful launched of FY-3H polar-orbiting satellite and FY-4C geostationary satellite, the FY constellation has improved the polar four-orbit networking and geostationary two-satellite coordinated configuration, realizing optimized GEO-LEO satellites collaborative observation. Major breakthroughs have been made in hyperspectral detection, active microwave remote sensing, high-precision geolocation and radiometric calibration, as well as intelligent ground operation. The product system has been expanded to 85 geophysical parameters in six categories, with significant innovations in multi-source data fusion, physical-constrained retrieval and AI-driven algorithms. FY satellite data have been widely applied in weather forecasting, severe disaster monitoring, climate change assessment, ecological environment protection, space weather services and key industrial fields. Up to now, FY satellites have provided data and application services to 139 countries and regions, conducted international emergency support for disaster prevention and mitigation, and deeply participated in global meteorological governance. This paper summarizes the technological advances, application benefits and global contributions of the FY system, and prospects its future development in higher precision, intelligence and global services.

Key words Fengyun meteorological satellite, Observation system, Ground segment, Remote sensing application, Global meteorological service

Classified index P715.6

1 Introduction

The Fengyun (FY) meteorological satellite integrated observation system constitutes a critical national space infrastructure of China, serving as the core space-based observation platform for meteorological disaster prevention and mitigation, climate change adaptation, ecological civilization construction, and space environment se-

* Supported by NSFC under grant 42274217 and China Meteorological Administration "Space Weather Monitoring and Alerting" Key Innovation Team (CMA2024 ZD01)

Received May 20, 2026

curity. It also acts as a major vehicle for China's engagement in global meteorological governance and provision of global public meteorological services. Over more than 50 years of development, the FY satellite program has established a complete operational architecture featuring coordinated polar-orbiting and geostationary satellite series, which have been formally integrated into the core constellation of the World Meteorological Organization (WMO) Global Operational Meteorological Satellites, emerging as a major player in the international meteorological satellite community[1–5].

The period 2024–2026 marked comprehensive breakthroughs for the FY Satellite System toward the core goals of constellation improvement, technological innovation, application deepening, and global service. The layout of the FY constellation has been optimized and upgraded: the polar-orbiting series added the FY-3H satellite, updating a four-satellite, four-orbit coordinated observation pattern; the geostationary series successfully launched the FY-4C satellite, establishing an observation mode of dual-satellite networking, east-west deployment, and mutual backup. Core technologies are independently controllable. Key technologies such as hyperspectral detection and active microwave remote sensing have achieved breakthroughs, and observation accuracy and data quality have been further improved.

The ground segment has completed intelligent upgrading. The Fengyun Smart Brain integrated operation and control system has entered operational service, significantly enhancing end-to-end, full-factor monitoring and command decision-making capabilities. High-precision geolocation and calibration technologies have been increasingly sophisticated. The product portfolio has expanded to cover 85 geophysical parameters across six categories: clouds and radiation, atmosphere, land, ocean, cryosphere, and space weather, fully satisfying the fundamental Earth observation requirements of the WMO Integrated Global Observing System (WIGOS). Multiple product algorithms and key technologies have seen innovative breakthroughs. Data services have expanded to 139 countries and regions worldwide.

Satellite data have achieved remarkable results in numerical weather prediction data assimilation, disaster monitoring and early warning, climate assessment, space weather forecasting, and key industry services. International services and cooperation have been deepened steadily. The capability of FY satellites to serve the Belt and Road Initiative has improved, and China's participation in the governance of FY satellite affairs has enhanced its international service and influence.

2 FY Constellation

From 2024 to 2026, the FY constellation added FY-3H and FY-4C, realizing an optimized high-low orbit constellation layout, upgrades to satellite platforms and core payloads, and innovation in coordinated observation architecture [6].

2.1 Newly Launched Satellites

2.1.1 FY-3H

FY-3H is the eighth satellite in the FY-3 series. Launched successfully on 27 September 2025, it is currently under commissioning and will take over from FY-3D to become China's new-generation afternoon-orbit operational meteorological satellite upon completion. FY-3H carries nine sets of advanced remote sensing instruments (Table 1).

Building on the core operational capabilities of global imaging and atmospheric vertical sounding inherited from the FY-3 series, FY-3H has expanded two major capabilities.

(1) The new-generation GAS-II has been carried. Adopting advanced spectral splitting and area-array detection technologies, it achieves, for the first time, high-precision global detection of column concentrations of CO_2 and CH_4 with a 100 km swath, 3 km spatial resolution, and up to 0.04 nm spectral resolution. This provides independent space-based data support for global climate monitoring, greenhouse gas accounting, and China's dual carbon strategy. The key technologies including refined spectral calibration, high-precision radiometric calibration, and precise geolocation of the instrument have successfully broken through. The obtained spectral lines clearly reveal rich atmospheric absorption spectral information reflected by bright targets in cloudy areas, dark ocean targets, and medium-brightness land targets, as shown in Figure 1.

(2) The space weather monitoring instruments have been upgraded**.** The improved WAI-II achieves 130° field-of-view lamp calibration and 10 km high-resolution aurora imaging for the first time, accurately captur-

Table 1 FY-3H remote sensing instruments

	Instruments full name	Acronym	Status
1.	Medium Resolution Spectral Imager-III	MERSI-III	Inherited
2.	Hyperspectral Infrared Atmospheric Sounder-II	HIRAS-II	
3.	Micro-Wave Temperature Sounder-III	MWTS-III	
4.	Micro-Wave Humidity Sounder-II	MWHS-II	
5.	Micro-Wave Radiation Imager-II	MWRI-II	
6.	GNSS Radio Occultation Sounder-II	GNOS-II	
7.	Ionospheric PhotoMeter-II	IPM-II	
8.	Greenhouse-gases Absorption Spectrometer-II	GAS-II	New
9.	Wide-field Auroral Imager-II	WAI-II	Improved

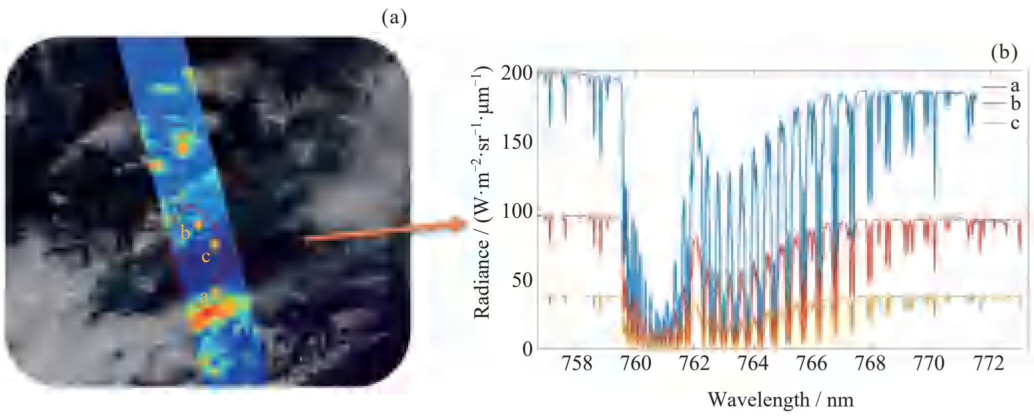

Fig. 1 Refined spectra of different detection targets for GAS-II (a-Cloud area, b-Land, c-Ocean). (a) Regional monitoring data acquired by GAS-II on global orbits. (b) High-resolution spectra (758–772 nm) for cloud, land, and ocean targets

ing auroral boundaries and particle precipitation information, and greatly improving support for space weather early warning and research.

In addition, FY-3H has simultaneously optimized functions such as atmospheric temperature and humidity profile detection, and land-surface and ocean observation, serving the three core fields of numerical weather prediction, climate assessment, and space environment monitoring in an all-round way.

2.1.2 FY-4C

FY-4C is the second operational satellite in China's new generation geostationary meteorological satellite series. It was successfully launched on 27 December 2025, and is under commissioning. After that, it will replace FY-4 A and become an important part of the geostationary orbit layout of FY satellites. Together with FY-4B, it establishes an operational pattern of dual-satellite operation and in-orbit backup for geostationary meteorological satellites.

The satellite platform inherits the three-axis stabilized attitude control technology of the FY-4 series and adds electric propulsion, sun tracking, and dual-channel Ka-band data transmission, achieving high-precision control and positioning as well as long-life stable operational service capability. FY-4C is equipped with six remote sensing instruments (Table 2).

Compared with previous satellites, its capabilities of remote sensing instruments have been comprehensively improved.

(1) Enhanced imaging and sounding capabilities. For the first time internationally, AGRI has realized full-disk imaging capability of 500 m true color and 250 m panchromatic, with imaging time reduced from 15 min to 10 min, and 1 min high-frequency continuous observation over key areas. The spatial resolution of GIIRS is improved from 12 km to 8 km, temporal resolution from

2 h to 1 h, spectral accuracy from 7 ppm to 5 ppm (1 ppm=10^{-6}), and radiometric accuracy from 0.7 K to 0.5 K. LMI has a high-speed imaging capability of 500 frames per second and can intelligently identify lightning events from 30 Gbit·s^{-1} massive data streams.

(2) Expanded space weather observation capabilities. Three newly developed space weather instruments are deployed: MUSI realizes hyperspectral ionospheric detection in the extreme ultraviolet band from geostationary orbit for the first time; SUVI and SXUS fill the gaps in China's geostationary orbit solar activity monitoring and forecasting technologies. Figure 2 shows the four-channel images of solar flare observed by SUVI on FY-4C.

It can be seen that FY-4C has achieved comprehensive upgrades in imaging accuracy, detection dimensions, and instrument functions, making it the geostationary meteorological satellite with the strongest comprehensive detection capability in the world.

2.2 Coordinated Observation of the FY Constellation

2.2.1 Joint Observation System of GEO-LEO Satellite

As of May 2026, 10 FY satellites are in-orbit operation illustrated in Figure 3, building a globally unique integrated observation network based on GEO and LEO satellites. For LEO satellites, FY-3E/F/G/H form a full network in four near-earth orbits: sun-synchronous early-morning, morning, afternoon orbit, and drift orbit. China has become the only country in the world to operate four civil LEO meteorological satellites simultaneously. For GEO satellites, FY-4B and FY-4C work together to achieve full regional coverage. FY-4C is equipped with an inter-satellite communication subsystem, and will carry out intelligent inter-satellite linkage with FY-3 in the future, further improving observation efficiency by leveraging the respective advantages of satellites in different orbits.

2.2.2 Overall Performance Improvement of FY Constellation

The overall observation performance of FY constellation has been improved. The global observation timeliness of FY-3 satellites has been shortened from 12 h to 4 h, and the observation timeliness of FY-4 reaches up to 1 min. FY-3 satellites realize full-spectrum three-dimensional quantitative observation, and FY-4 satellites focus on regional high-timeliness dynamic monitoring.

Table 2 Remote Sensing Instruments on FY-4C

	Instrument	Acronym	Status
1.	Advanced Geostationary Radiation Imager	AGRI	Improved
2.	Geostationary Interferometric Infrared Sounder	GIIRS	
3.	Lightning Mapping Imager	LMI	
4.	Solar extreme-UltraViolet Imager	SUVI	New
5.	Multi-band ionosphere Ultraviolet Spectral Imager	MUSI	
6.	Solar X-ray and extreme-Ultraviolet Spectral fluxmeter	SXUS	

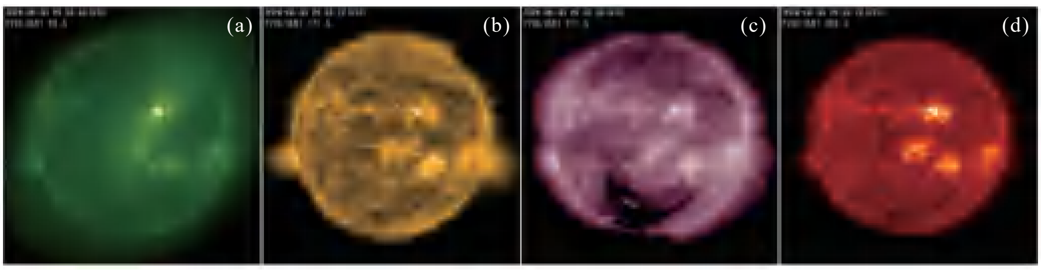

Fig. 2 X1.1 class solar flare observed by FY4 C/SUVI at wavelengths of 94 Å (a), 171 Å (b), 211 Å (c) and 304 Å (d) at 20:50 UTC on 30 June 2026

Fig. 3 FY Constellation

A breakthrough has been made in multi-band cooperative detection technology for instruments, achieving full-spectrum coverage from soft X-ray, ultraviolet, visible, infrared to microwave. Among them, the visible channel of FY-4 satellites reaches 250 m spatial resolution, and the infrared hyperspectral detection spectral resolution reaches 0.625 cm^{-1}. The number of channels of HIRAS-II on FY-3 has increased from 1370 to 3053, and the spectral coverage has been expanded to three bands (650–1136 cm^{-1}, 1210–1750 cm^{-1}, 2155–2555 cm^{-1}). MWTS and MWHS realize synchronous high-precision detection of atmospheric temperature and humidity. Precipitation Measurement Radar can detect weak precipitation changes of 0.2 $mm\cdot h^{-1}$. The space weather monitoring system has formed a multi-instrument coordinated architecture of GNOS-II, IPM-II, and WAI-II, realizing all-round space weather monitoring and early warning from the atmosphere to the ionosphere and from electron density to particle precipitation, while greatly enhancing solar activity monitoring capability.

3 Ground Segment

3.1 Operation and Control

An intelligent integrated operation and control system centered on the Fengyun Smart Brain has been constructed for the ground segment, realizing centralized monitoring and intelligent scheduling of the entire operational process and all factors of FY satellites (see Figure 4). It covers the full chain of “satellites – ground stations – control – research – production – service – application”. It is an innovation in AI-integrated systems for FY satellite operation and control.

The Fengyun Smart Brain integrates core information such as in-orbit satellite status, ground station network operation, data processing progress, product distribution, and application service effectiveness, enabling one-screen control of macro situations and layer-by-layer penetration of micro details. Through hierarchically progressive thematic interfaces, it completes refined monitoring in multiple scenarios including instrument operation, IT resource scheduling, data preprocessing, product quality inspection, disaster monitoring, and international services.

3.2 Data Processing

3.2.1 Geolocation

During 2024–2026, key breakthroughs were made in technologies including orbit motion compensation (OMC), attitude-orbit error correction, resident and navigation accuracy analysis, and limb sounding tangent height correction. A high-precision geolocation technology system adapted to GEO-LEO satellites and imaging/sounding instruments has been further improved.

An OMC algorithm model adapted to FY-4 instru-


Fig. 4 Fengyun Smart Brain: an intelligent command and decision platform for multi-satellite integrated operation control, satellite-ground monitoring, data quality evaluation, and application services

ments has been developed, and a multi-attitude reference conversion system has been established, effectively compensating for scanning registration errors of large-field-of-view long-linear-array instrument and significantly improving the navigation accuracy and geolocation calculation efficiency [7]. On-orbit measured data from FY-4 GIIRS are used to verify and analyze the resident and navigation accuracy. The results show that the detector achieves a resident accuracy of 1/10 pixel and a navigation accuracy of 1 pixel [8]. The attitude-orbit error source tracing and correction model of FY-3D have been completed, and the on-orbit attitude solution algorithm has been optimized, effectively suppressing orbit and attitude system errors. The along-track and cross-track positioning accuracy of 1-km resolution images of the MERSI-II has been improved by 20% [9]. For the Ultraviolet Limb Sounder (OMS) on FY-3F, an ellipsoidal virtual tangent height solution model has been constructed to quantify the impacts of the Earth ellipsoid, attitude-orbit parameters, and installation deviations on limb tangent point positioning. High-precision tangent height correction is realized through pitch installation parameter correction, with tangent height correction accuracy better than 0.4 km, cross-track pointing deviation better than 0.1°, and annual vertical pointing seasonal variation less than 0.01°, meeting the geometric correction accuracy requirements for atmospheric trace gas profile retrieval[10].

3.2.2 Calibration

A full-link high-precision radiometric calibration system integrating laboratory calibration, on-board calibration, active external calibration, and inter-calibration for FY satellites has been fully established, realizing full-spectrum and full-factor calibration for visible, infrared, microwave, and active radar, with data consistency and long-term stability reaching international advanced levels.

Meanwhile, new calibration methods have been developed for different instruments, and pre-launch calibration verification and in-orbit calibration evaluation have been carried out[11,12]. For active radars, a satellite-ground integrated external calibration technology using ground Active Radar Calibrators (ARC) has been developed, realizing in-orbit measurement of radar antenna patterns and absolute calibration of the entire system, ensuring the accuracy of quantitative products such as three-dimensional precipitation and sea surface wind fields[13]. The in-orbit radiometric performance of MERS-III has been systematically evaluated using the global Pseudo Invariant Pixel (PIP) cross-platform comparison method. Results show that the radiometric bias standard deviation of most channels is less than 2%, temporal radiometric stability is better than 3.5%, and overall evaluation uncertainty is lower than 3.38% [14].

Artificial intelligence technology has been introduced, and an AI Infrared Radiometric Calibration (AIRC) method for FY-4 satellites has been proposed. A Radiometric Calibration Neural Network (RCNN) has been constructed to learn the mapping relationship based on historical high-precision calibration data, realizing the transformation from Reference Traceability (RT) to State Traceability (ST). The calibration accuracy is comparable to that of the blackbody calibration system, promoting the construction of a unified observation system for infrared hyperspectral instruments [15].

3.2.3 Product System and Algorithm Innovation

From 2024 to 2026, FY satellite product system has been continuously enriched and improved, forming six categories and 85 geophysical parameter products covering cloud and radiation, atmosphere, land, ocean, cryosphere, and space weather, fully meeting the core observation requirements of the WIGOS for the six Earth spheres. Products are divided into a five-level system according to standardized processing flows, covering raw observation data, Level-0 unpacked and spliced data, Level-1 radiometric corrected data, Level-2 geophysical quantitative parameters, and Level-3 spatiotemporally fused gridded products. Each level is supported by self-developed algorithms and quality control models.

FY satellites products have broken through the limitations of traditional single physical algorithms, forming product algorithm innovations including multi-source data fusion, physical model optimization, spatio-temporal refined reconstruction, and machine learning technologies, covering atmosphere, land, ocean, space weather, and other fields.

(1) Atmospheric product algorithm optimization. In cloud remote sensing, for FY-4 satellites, a Cloud Amount Neural Network (CLANN) for AGRI 3 D cloud amount has been developed, with high consistency

CALIPSO data (correlation coefficient up to 0.92)[16]. A deep learning-based cloud mask model, Convolutional Attention Cloud Mask Network Plus Plus (CACM-Net++) has been developed, producing more consistent cloud distributions, particularly over nighttime land regions[17]. An algorithm for Cloud-Cleared Radiances (CCR), from collocated observations of hyperspectral IR sounders and advanced imagers onboard the same geostationary platform has been developed, effectively solving the problem of high uncertainty in GIIRS CCRs, increasing GIIRS effective observation data volume by three times, and recovering 37% of partially cloudy fields of view. The CCRs can be assimilated as CLRs in numerical weather prediction (NWP) models without worrying about the cloud impact [18]. For FY-3 MERSI nighttime cloud detection, a Transformer-based Nighttime Cloud Detection (TNCD) framework, which integrates spatial features and utilizes an advanced Transformer architecture with relative position encoding, layer scaling, and channel attention mechanisms, has been proposed, with overall accuracy exceeding 90% when applied to MERSI cloud detection[19]. In aerosol remote sensing, an improved aerosol retrieval algorithm based on a nonlinear surface model from FY-3D/MERSI-II data[20], FY-4B land aerosol retrieval algorithms coupling hourly land surface models with spatio-temporal variability characteristics [21], and an adaptive dark-target algorithm for retrieving land aerosol optical depth have been established [22]. Fengyun satellite aerosol optical depth products are equipped with the capability to monitor episodic events such as winter haze over India and summer wildfires across North America, as illustrated in Figure 5.

(2) Land and ocean product algorithm iteration. For land surface elements, the FY-3E WindRAD water cloud model has been optimized, and pixel-by-pixel parameter fitting combined with SMAP data has realized high-precision surface soil moisture in low-to-moderate vegetation conditions, with ubRMSD controlled at 0.02–0.06 $cm^3 \cdot cm^{-3}$[23]. A regional-scale all-sky gridded diurnal near-surface air temperature (T_{air}) estimation method based on FY-4B measurements has been constructed, realizing all-sky hourly gridded retrieval of T_{air} with a correlation coefficient greater than 0.95[24]. For ocean surface elements, aiming at complex sea conditions such as rainy days and typhoons, a Lightweight Deep Neural Network (LWDNN) for FY-3D MWRI sea surface wind speed has been developed, with RMSE less than 2.0 $m \cdot s^{-1}$ under all weather conditions and less than 1.5 $m \cdot s^{-1}$ in the clear-sky region, in the wind speed range of 20–70 $m \cdot s^{-1}$, the results are shown in Figure 6[25]. The backscatter characteristics of Open Water (OW), First-Year Ice (FYI), and Multi-Year Ice (MYI) under different seasonal, wavelength, and polarization conditions based on the unique capabilities of FY-3E WindRAD scatterometer has been investigated. It pro-

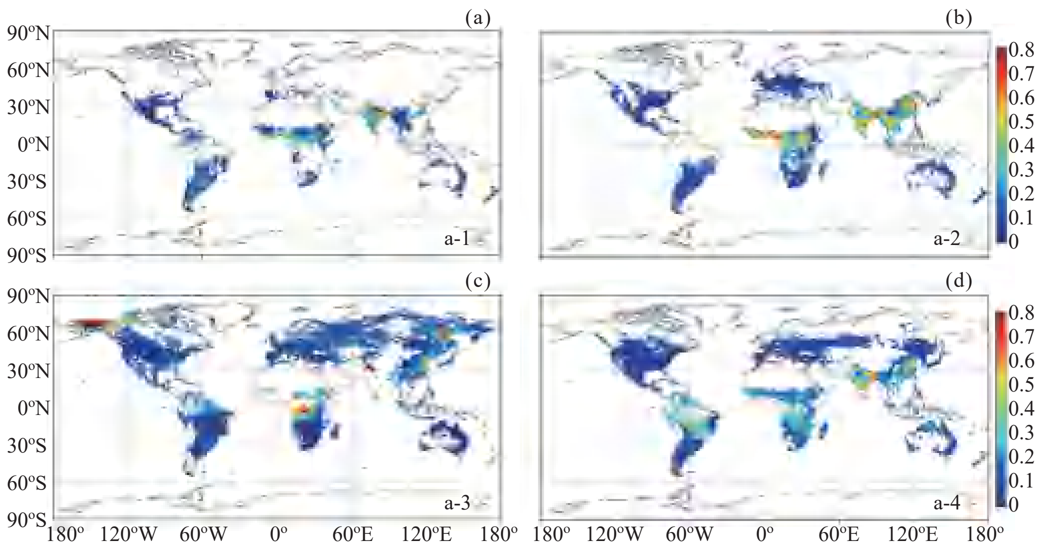

Fig. 5 Spatial distribution of monthly average AOD retrievals obtained from MERSI-II during Jan. 2022 (a), Mar. 2022 (b), Jul. 2022 (c), and Nov. 2021 (d)

vides vital support for the development and refinement of algorithms for FY-3E WindRAD operational sea ice products [26].

(3) Space weather product algorithm innovation. A TIEGCM-based inversion model for Ionosphere-Thermosphere (I-T) parameters is constructed by integrating sparse observational data with physics-based numerical simulations. Driven by three-dimensional electron density fields, the model combines high-resolution data-constrained electron density reconstructions with the Thermosphere-Ionosphere-Electrodynamics General Circulation Model (TIEGCM) to achieve end-to-end inversion of implicit I-T physical parameters. The Architecture of the TIEGCM-based inversion model is shown in Figure 7. Supervised neural networks pre-trained on massive TIEGCM simulation datasets are embedded into the framework to automatically capture the intrinsic coupling relationships among diverse I-T state variables, supporting rapid, stable, and physically consistent parameter retrieval[27]. A deep learning-based vertical decomposition model for ionospheric Total Electron Content (TEC) has been developed, which maps global ionospheric TEC data to vertically layered electron density profiles (60–800 km) using a Multilayer Perceptron (MLP) model, achieving significantly higher accuracy than the IRI-2020 model and enabling cost-effective, high-resolution global ionosphere reconstruction for space weather applications[28].

(4) Artificial intelligence technology application. in addition to the various machine learning methods men-

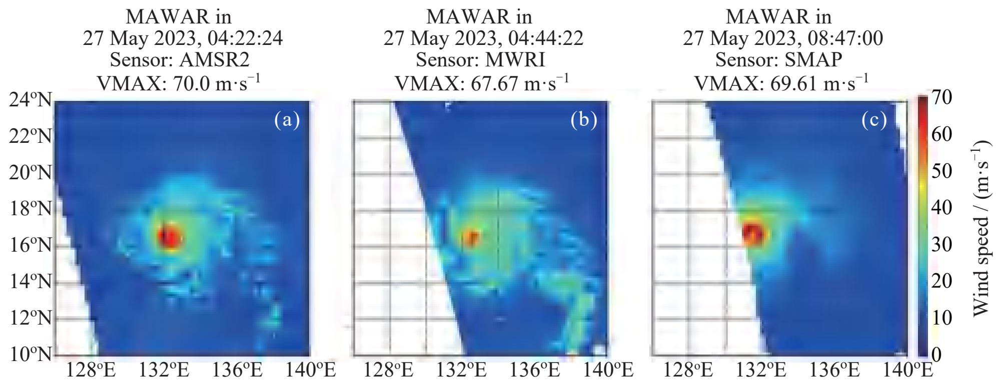

Fig. 6 Spatial distributions of the AMSR2 all-weather SSWS (left column), MWRI SSWS retrieved by the LWDNN (middle column), and SMAP SSWS (right column) for typhoon MAWAR

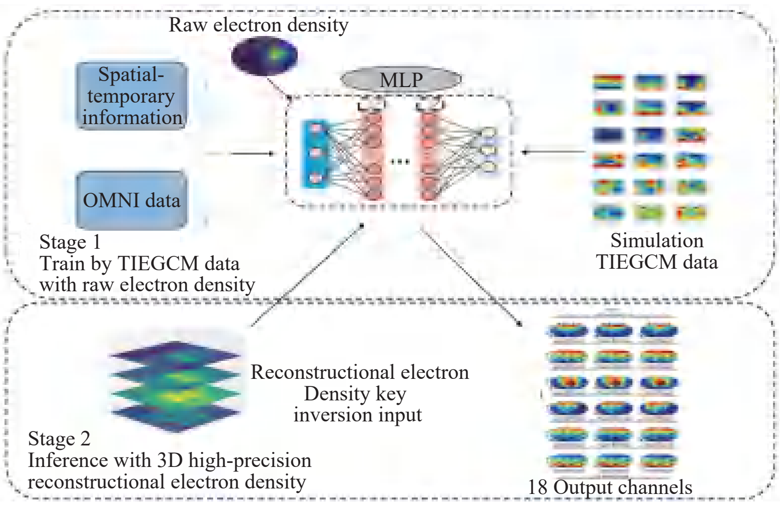

Fig. 7 Architecture of the TIEGCM-based inversion model for end-to-end mapping from observable data to latent ionosphere-thermosphere state variables

tioned above, a Deep Diffusion Model for Satellites (DDMS) has been pioneered, constructing an AI convective nowcasting system that realizes large-scale thunderstorm nowcasting with 15-min resolution and up to 4 h in advance. As shown in Figure 8, for the 29 July 2023 extreme torrential rainfall over Beijing-Tianjin-Hebei induced by typhoon Doksuri, NowcastNet and PredRNN-v2 fail in 4 h forecasts, and PySTEPS cannot capture convective cell evolution; DDMS outperforms all contrasting methods obviously[29]. Based on the Light Gradient Boosting Machine (LGBM) machine learning framework, an FY-4B AI precipitation estimation model has been constructed, with multi-dimensional accuracy indicators superior to international precipitation products such as GPM/IMERG[30]. The U-Net deep learning model is used to intelligently identify Trapped Lee Waves (TLWs) propagating in the lower troposphere, explaining the causes of environmental disasters related to strong turbulence in mountainous areas in the afternoon[31].

These new AI technologies make up for the lack of observation data, effectively characterize the multi-scale spatio-temporal evolution of the atmosphere and ionosphere, significantly improve the refinement and intelligence level of geophysical and space physical parameter retrieval, and provide new technical support for meteorological satellite products and applications.

3.3 Data Services

3.3.1 Data Archiving

A large-capacity, high-reliability, intelligent data archiving and management system has been built. As of April 2026, the archived satellite data volume has exceeded 59 PByte, covering 57 satellites in 12 series at home and abroad, with more than 1500 data products. Figure 9 shows the statistics of satellite data archiving from 1988 to 2025. Data management adopts standardized classification, intelligent retrieval, and efficient access technologies to realize rapid archiving, precise retrieval, and secure backup of data, ensuring long-term preservation and efficient access.

3.3.2 Data Services

In terms of data sharing services, a space-ground integrated comprehensive meteorological satellite data service system has been constructed, providing data sharing services through satellite direct reception stations, the China Meteorological Administration Data Broadcasting System (CMACast), the WMO Information System (WIS), the FY Satellite Data Service Network, and satellite data resource pools, enabling the acquisition, exchange, management, and service of domestic and foreign satellite data. As of the end of April 2026, the number of registered users on the FENGYUN Satellite Data Service website has exceeded 207000, with 1.859 million orders completed and data ordered exceeding 8 PByte.

4 Remote Sensing Application

4.1 Fengyun Earth Platform

After three years of construction, the Fengyun Earth Platform has for the first time realized synchronous direct access to FY satellite products at the national,

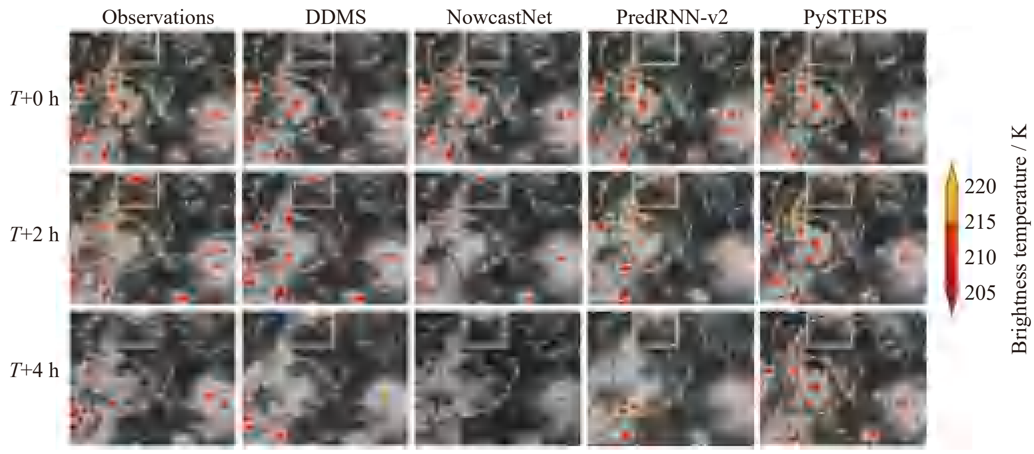

Fig. 8 4 h lead time nowcasting comparison of multiple models for the severe convective extreme rainstorm event in the Beijing-Tianjin-Hebei region on 29 July 2023 associated with Typhoon Doksuri

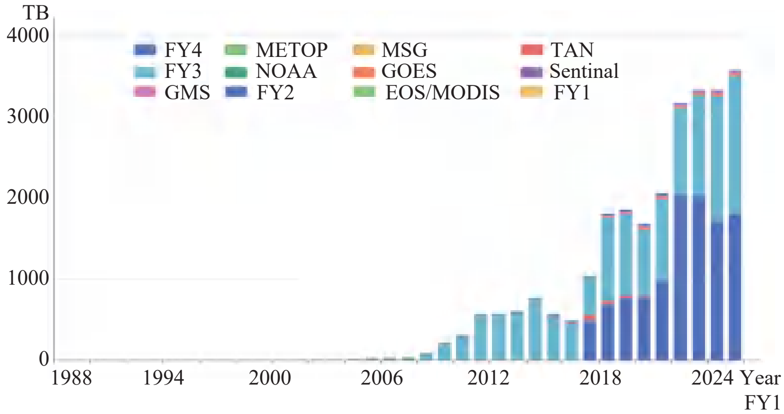

Fig. 9 Statistics of satellite data archiving from 1988 to 2025

provincial, municipal, and county levels. It has built a nationally unified and full-domain covered satellite remote sensing application service foundation.

Guided by the core philosophy of IT-based, Interactive, and Instant (I^3), Fengyun Earth Platform has achieved a series of key technological innovations. It pioneered the deep integration of traditional database and big data management technologies, enabling full-process quality monitoring and online real-time computing of 148 categories and 934 types of massive multi-source heterogeneous satellite data. A light-weight, highly available cloud-client service architecture has been constructed, breaking through technologies including 10000-level concurrent user access, minute-level cloud image push, and high-rate data compression. It overcame the core technologies of space-ground integrated intelligent observation and cooperative control, reducing the FY-4B rapid scan observation region switching time from 2 hours to 15 min and delivering satellite product services to users within 5 min. The platform systematically addresses three major bottlenecks in satellite application: service timeliness, algorithm scientificity, and product fusion. It has innovatively developed a multi-source satellite fusion algorithm and quantitative remote sensing product system, comprehensively enhancing the intelligent, intensive, and real-time application level of FY satellites, and providing original technical support for the operational application of China's meteorological satellites.

4.2 Meteorological Forecasting and Disaster Monitoring Applications

4.2.1 Support for NWP and Data Assimilation

FY satellite observation data have been fully integrated into China's global NWP model (CMA-GFS) and regional NWP systems. Satellite data assimilation accounts for 88%, and FY satellite data assimilation accounts for more than 25%. Focusing on FY-3 series MWTS, MWHS, HIRAS, and FY-4 series GIIRS, key technologies such as fast radiative transfer, near-surface microwave assimilation, adaptive water vapor assimilation, and thinned quality control have been broken through, significantly improving data assimilability and assimilation efficiency. The daily assimilable data volume, such as FY-3F MWTS and FY-3E HIRAS has exceeded 450000 profiles, with an assimilability rate of over 50% [32]. After assimilation of 15 min intensive observation data from FY-4B GIIRS, the analysis of typhoon thermal structure and environmental fields has been significantly improved, and the track forecast errors for super typhoons such as Gaemi and Yagi in 2024 have been significantly reduced by up to 22.5%, providing core support for the precision development of meteorological forecasting[33].

4.2.2 Severe Weather Monitoring and Early Warning

An all-weather, full-coverage, high-timeliness severe weather monitoring and early warning system based on FY satellites has been constructed, realizing accurate monitoring and early warning of multiple types of disasters such as typhoons, rainstorms and severe convection, cold waves, dust storms, and heavy fog.

(1) Typhoon monitoring: Geostationary satellites capture the whole process of genesis, movement, and intensity change with high-frequency imaging. Combined with infrared and microwave detection of FY-3 satel-

lites, the bottom circulation structure and eyewall position of typhoons is observed, and the temperature anomaly structure is identified. Precipitation measurement radar obtains the three-dimensional structure of precipitation cloud systems and cloud physical characteristics, supporting typhoon positioning, intensity determination, and wind-rain impact forecasting (Figure 10)[34].

Rainstorms and severe convection: FY-4B High-speed imager realizes minute-scale, 250 m resolution regional intensive observation, capable of capturing convective initiation signals 30–40 min in advance and accurately tracking the development and evolution of convective systems.

(3) Cold waves: Polar-orbiting and geostationary satellites collaboratively monitor cold air advancement, rain-snow phase transition, snow cover, and strong winds at sea[35,36].

(4) Sandstorms: Multi-channel spectral data enable rapid identification, quantitative intensity analysis, and path tracking; products such as dust aerosol optical depth, dust index, dust visibility, and PM10 concentration are retrieved to quantitatively assess dust storm intensity.

(5) Heavy fog: Multi-channel brightness temperature threshold technology distinguishes fog from low clouds and surface targets, and quantitatively retrieves micro-physical parameters such as fog optical depth, liquid water particle size, and liquid water content[37].

From 2024 to 2026, FY satellites have supported the response to many major severe weather events, providing key data support for disaster prevention and mitigation decision-making.

4.3 Climate Monitoring and Assessment Applications

Based on long-sequence observation data of FY satellites, a global climate comprehensive monitoring system covering key elements such as outgoing longwave radiation, sea surface temperature, snow cover, sea ice, land surface temperature, and vegetation has been built, integrated into the FY Satellite Remote Sensing Climate Operational Platform, realizing real-time dynamic monitoring of key climate parameters globally. In particular, land surface temperature reconstruction technologies have been developed: the RMSE after reconstruction using a two-point machine learning method is about 2.6 K[38]; the temporal dimension reconstruction technology based on diurnal variation models reduces the RMSE of summer land surface temperature in the Heihe River Basin to less than 4 K[39].

Based on multi-source fused long-sequence datasets, large-scale climate system monitoring such as global convective activity, polar vortices, monsoons, and ENSO has been carried out. For the western Pacific subtropical high, the index system has been optimized, spatial morphology determination methods improved, and ridge line descriptions perfected, significantly improving the indicative ability for abnormal summer precipitation and high temperatures in China[40]. Coupling FY satellite cloud and water vapor products has formed a complete technical chain of satellite observation – circulation diagnosis – anomaly attribution.

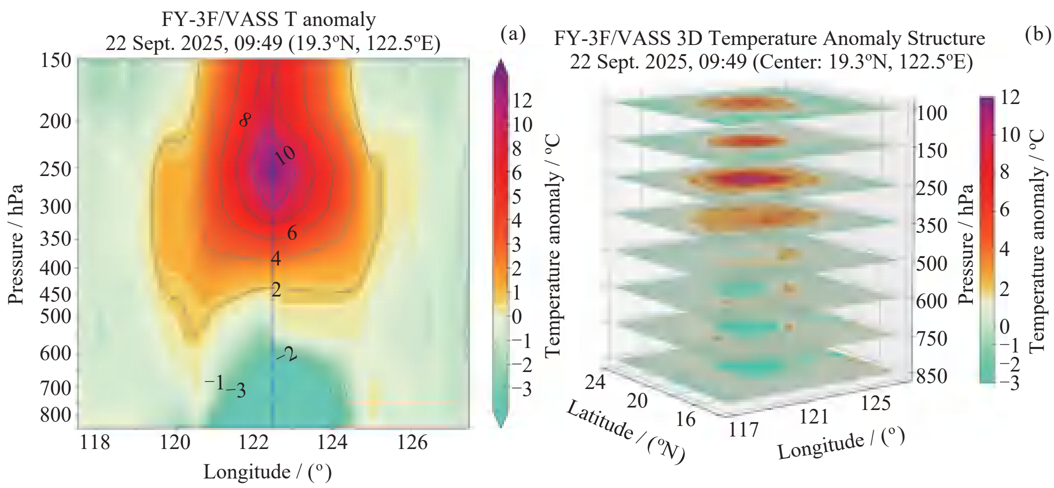

Fig. 10 3 D temperature structure of Typhoon Bolaven

Integrating FY satellite data with ground observations and reanalysis data, an extreme climate event index system for China and Eurasia has been established, realizing refined monitoring and comprehensive assessment of the intensity, duration, and impact range of extreme climate events in key global regions. With the application of new products from FY-3H and FY-4C, the quantification and refinement of climate monitoring and climate change response will be further improved.

4.4 Ecological and Environmental Remote Sensing Applications

In the terrestrial ecology field, dynamic monitoring of vegetation growth, droughts, flood and key ecological regions has been realized. Relying on satellite vegetation index products, continuous monitoring of ecological quality and vegetation coverage in key regions such as the Yangtze River Basin, the Yellow River Basin, the Qinling Mountains, the Qinghai-Tibet Plateau, and Northeast Ecological Function Zone has been carried out. In aquatic ecology and flood monitoring, FY satellites efficiently identify water bodies using multi-spectral features, realizing continuous tracking of dynamic changes in water area of key lakes and reservoirs, forming a more than 30-year long-sequence dataset (Figure 11) [41].

In the atmospheric environment remote sensing monitoring, FY-3 series has enabled China to carry out global atmospheric environment remote sensing monitoring with independent satellites for the first time, realizing all-weather, quantitative monitoring of aerosols, ozone, polluting gases, greenhouse gases *etc.*[42]. The FY-3F Ultraviolet Hyperspectral Ozone Sounder, through nadir + limb combined detection mode, improves the monitoring accuracy of stratospheric and tropospheric ozone, polluting gases, and aerosols, supporting regional atmospheric environmental quality evaluation and pollution source tracing [43]. The GAS-II on FY-3H realizes global greenhouse gas column concentration detection with 100 km swath and high spectral resolution for the first time. A Global Emission Inventory of Biomass Burning (GEIOBB) has been developed, providing important data support for improving air quality simulation[44].

4.5 Space Weather Applications

4.5.1 Space Weather Forecasting Models

China's first-generation full-chain operational numerical forecasting system for space weather has been established. Key technologies including cross-scale, cross-material-state, cross-model and cascaded coupling have been broken through in the system development. Numerical space weather forecasting with full-chain coverage and partial regional coupling is realized, and full-process management of numerical models is supported to enable routine operational execution at minute-level intervals. Panoramic characterization of the Sun-Earth space environment under data-sparse conditions has also been achieved, and comprehensive promotion of forecasting service capacity has been accomplished accord-

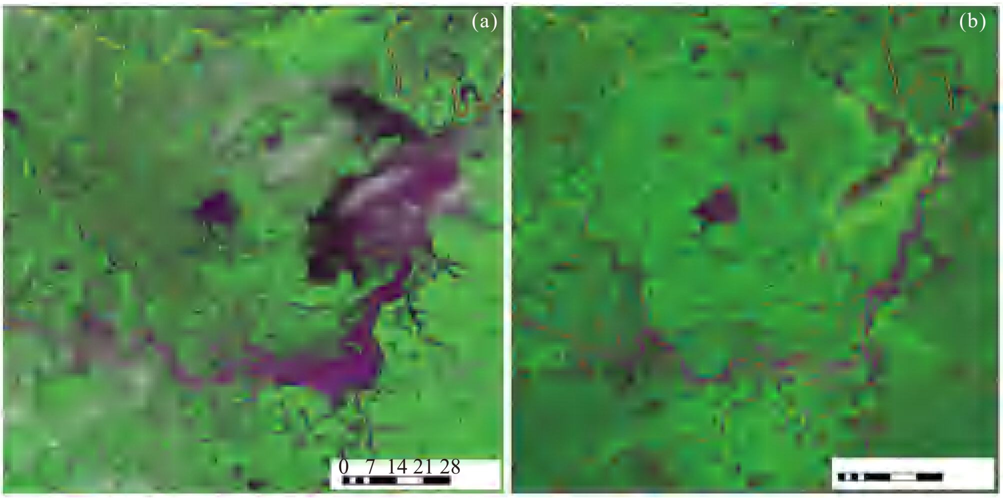

Fig. 11 Water reduction of the Dongting Lake induced by high temperature and drought monitored by FY-3D on 14 June (a) and 5 September (b) in 2022

ingly.

The world's first chained intelligent forecasting model for space weather – the Fengyu AI Large Model – has been independently developed, and its schematic diagram is shown in Figure 12. Cross-domain operator optimization technologies based on domestically controllable AI frameworks are adopted, and an original chained training architecture together with an intelligent coupling optimization mechanism has been pioneered. By means of full-chain coupled training, the complete physical processes of solar wind disturbing the Earth's space environment are faithfully reproduced, and full-chain AI modeling covering the solar wind, magnetosphere and ionosphere is implemented for the first time globally. Prediction errors of global Total Electron Content (TEC) for multiple extreme intense geomagnetic storm events in the past two years have been controlled within 10%, and world-leading technical performance has been attained.

4.5.2 Space Weather Monitoring Operations

Routine monitoring of the solar-terrestrial space environment with FY-3 and FY-4 satellites has been carried out, monitoring solar EUV radiation, solar flares, geomagnetic indices, auroral morphology and particle precipitation, ionospheric total electron content, airglow changes, space particles and magnetic field disturbances, *etc*., realizing real-time data acquisition, operational processing, and product generation. Monitoring data have been fully integrated into the national space weather monitoring and early warning operational system.

On this basis, the Fengyun Space integrated space weather operational platform has been built independently, forming a closed-loop technical architecture of observation – retrieval – forecasting – service. The platform integrates multi-source observation and physical forecasting models, with capabilities including space weather diagnosis, short-term forecasting, medium-to-long-term trend early warning, extreme event analysis, and emergency response. It provides customized services for highly sensitive industries such as aerospace, aviation, communications, and electric power, and fully supports the operation of the ICAO Global Space Weather Center, carrying out regular international joint monitoring, rotating early warnings, and global space weather briefings, providing important scientific and technological support for global aviation safety and space facility protection.

4.6 Key Industry Applications

FY satellite agricultural remote sensing services cover planting area extraction, growth monitoring, yield estimation, and agro-meteorological disaster assessment. High spatio-temporal resolution vegetation indices are reconstructed using satellite data fusion technology, and a winter wheat yield estimation model is constructed by coupling BP neural networks, realizing refined crop yield retrieval and spatial distribution mapping at farmland and county scales, forming a large-scale, dynamic food production assessment capability to serve precision agricultural production and national food security[45]. For road and air transportation, monitoring and early warning services for road icing and extreme weather from FY satellites are provided to ensure traffic safety and trans-

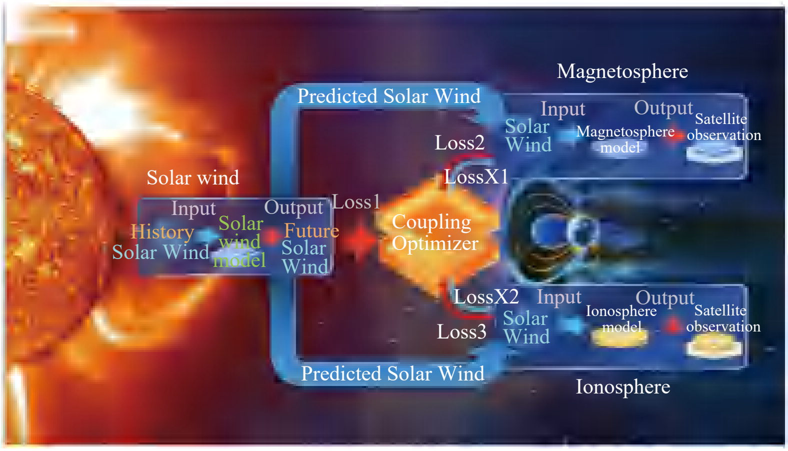

Fig. 12 Schematic diagram of Fengyun AI large model

portation efficiency. Monitoring and early warning of power grid mountain fires, and assessment of wind and solar energy resources are carried out to improve the safe operation of energy facilities and resource development efficiency[46].

5 Global Services and International Cooperation

5.1 Global Data Sharing and Distribution

Adhering to the concept of global openness and sharing, a comprehensive, multi-level, and efficient FY global data sharing and distribution system has been built. As of May 2026, FY satellite data services cover 139 countries and regions worldwide, with a cumulative data distribution volume of more than 8 PByte to international users and over 1.85 million international data service orders completed. Data distribution is fully connected to the WIS, compatible with international common data formats and standards. Overseas service nodes such as South Africa, Ethiopia, and the United Arab Emirates have been opened to optimize global data access speed, reducing cloud platform product loading time from seconds to milliseconds, greatly lowering the threshold for international users to use data. Meanwhile, a regular international data training mechanism has been established to provide FY satellite data application training for developing countries, enhance local users' data application capabilities, and promote the wide application of FY satellite data in global meteorology, disaster prevention, and ecology.

5.2 Global Services

Relying on the FY satellite system, precise and practical remote sensing application services are provided for countries along the Belt and Road Initiative and other developing countries, helping local disaster prevention and mitigation and sustainable development. The FY Satellite Emergency Support Mechanism (FY-ESM) has registered 38 international emergency users. From 2024 to 2026, it has provided more than 190 international disaster emergency remote sensing services for many countries around the world. The Mazu Early Warning Program has been implemented and applied in many developing countries, improving their extreme weather early warning capabilities. Meanwhile, exclusive meteorological support services are provided for the Pacific Games and other events, helping regional connectivity and people's livelihood improvement, demonstrating China's commitment to global public services.

As a core part of ICAO-designated China-Russia Consortium (CRC), the center upgrades the integrated ICAO space weather service platform, unifies advisory formats and product grids, and opens mobile-based global service access. It collaborates with other three global space weather centers to align warning thresholds and optimize aviation service. Supported by FY satellite observations and self-developed AI model as well as numerical prediction system, it improves ionosphere and geomagnetic disturbance prediction, provides forecast products and regular aviation meteorology training for airlines and air traffic control system. As China's first civil aviation-based global space weather center, it completed seven international duty rotations from 2024 to 2026 to serve 193 ICAO member states.

5.3 Cooperation with International Organizations

The FY satellite system is deeply integrated into the global meteorological governance system, comprehensively strengthening cooperation with international organizations such as the WMO and the Coordination Group for Meteorological Satellites (CGMS), realizing standard alignment, data interoperability, and capacity building. It fully participates in the construction of WIGOS, and FY satellite data have been officially included in the WMO Global Shared Core Dataset. As a core member of the CGMS space-based observation benchmark, it participates in the formulation of international meteorological satellite observation standards, calibration standards, and product standards, promoting the internationalization of China's meteorological satellite technical standards.

In-depth cooperation has been carried out with the European Organization for the Exploitation of Meteorological Satellites (EUMETSAT), Russia, and many meteorological satellite agencies in the Asia-Pacific region, conducting cross-data verification, joint retrieval, technical exchanges, and personnel training. The 15 th Asian-Pacific Meteorological Satellite User Conference has been successfully held, building a platform for regional meteorological satellite cooperation and exchanges. Through all-round international cooperation, the international influence of FY satellites has been continuously enhanced, making it an important core force for the coordinated development of global meteorological satellites.

6 Future Development

In the future, the FY satellite system will continue to optimize the constellation layout, promote two-way upgrading of satellite observation and application capabilities, and drive the FY satellite system toward higher precision, greater intelligence, and a more complete pedigree.

In terms of observation capabilities, key technologies such as hyper-spectral full-spectrum detection, real-time on-board calibration, intelligent on-orbit processing, and high-speed large-capacity data transmission will be broken through to further improve spatial, temporal, and spectral resolution and observation reliability. In terms of application capabilities, artificial intelligence, big data, and cloud computing technologies will be deeply integrated to optimize quantitative remote sensing retrieval algorithms, enhance capabilities in numerical prediction assimilation, intelligent disaster early warning, accurate climate assessment, and chained space weather forecasting. The global service system will be improved, the scope of data services expanded, and the international service model optimized to build a more inclusive and efficient global satellite meteorological service platform.

Meanwhile, the collaborative development of operational FY satellites and commercial meteorological small satellites will be promoted to build a new meteorological satellite observation system with complementary advantages, resource sharing, and coordinated observation. The integration and joint retrieval of FY satellite data and commercial satellite data will be promoted to enrich the product system and improve application service accuracy. A cooperation model of technological collaborative innovation, unified standard specification, and win-win result sharing will be explored to promote the industrialization development of China's meteorological satellites.

7 Conclusion

From 2024 to 2026, FY meteorological satellite integrated observation system has achieved all-round breakthroughs in constellation construction, observation capability, ground operation, data processing, application services, and international cooperation. The polar four-orbit networking and geostationary two-satellite coordinated constellation have been fully established, with FY-3H and FY-4C successfully launched. The intelligent operation and control system, high-precision calibration, and innovative product algorithms have been achieved, supporting remarkable applications in weather forecasting, disaster monitoring, climate assessment, ecological environment, space weather, and key industries. Adhering to openness and sharing, FY satellites have provided services to 139 countries and regions, deeply participating in global meteorological governance. In the future, the FY system will further enhance observation and application capabilities, deepen global services and international cooperation, and make greater contributions to global meteorological development and space technology progress.

References

[1] WANG Jinsong, GUO Qiang, XU Na. Theory and Practice of the Effectiveness-Evaluation System for Fengyun Meteorological Satellites[M]. Beijing: China Meteorological Press, 2025 (王劲松, 郭强, 徐娜. 风云气象卫星效能体系概论与实践 [M]. 北京: 气象出版社, 2025)

[2] CHEN Lin, XU Na, WANG Jinsong, *et al*. FengYun satellites: from observations to quantitative applications[J]. *National Remote Sensing Bulletin*, 2025, **29**(6): 1462-1479 (陈林, 徐娜, 王劲松, 等. 风云卫星: 从观测到定量应用 [J]. 遥感学报, 2025, **29**(6): 1462-1479)

[3] WANG Jinsong, GUAN Min, YUAN Muye, *et al*. Innovation and application of Fengyun meteorological satellite observation system[J]. *Satellite Application*, 2025(9): 6-14 (王劲松, 关敏, 袁牧野, 等. 风云气象卫星观测体系创新与应用 [J]. 卫星应用, 2025(9): 6-14)

[4] ZHANG Peng, LI Rui, ZHAO Kun, *et al*. Development of an integrated meteorological observation system in China[J]. *Acta Meteorologica Sinica*, 2025, **83**(3): 729-760 (张鹏, 李锐, 赵坤, 等. 中国综合气象观测系统的业务发展 [J]. 气象学报, 2025, **83**(3): 729-760)

[5] GUAN Min, ZHANG Yong, LI Yun, *et al*. Current development and future trends of Fengyun meteorological satellites[J]. *Advances in Earth Science*, 2025, **40**(2): 138-154 (关敏, 张勇, 李云, 等. 我国风云气象卫星发展现状与未来展望 [J]. 地球科学进展, 2025, **40**(2): 138-154)

[6] National Satellite Meteorological Center. FengYun Series Satellites[EB/OL]. [2026-05-08]. http://www.nsmc.org.cn/nsmc/en/

satellite/index.html

[7] WANG Jiachen, WANG Jing, LIU Chengbao, *et al*. Orbit motion compensation modeling and simulation analysis for FY-4 geostationary meteorological satellite[J]. *Geomatics and Information Science of Wuhan University*, 2024, **49**(10): 1879-1890 (王嘉琛, 王静, 刘成保, 等. 风云四号卫星轨道运动补偿算法建模与仿真分析 [J]. 武汉大学学报 (信息科学版), 2024, **49**(10): 1879-1890)

[8] SHANG Jian, LIU Chengbao, YANG Lei, *et al*. Resident and navigation accuracy analysis of interferometric infrared sounder onboard FY-4 satellite[J]. *Journal of Telemetry, Tracking and Command*, 2024, **45**(6): 1-10 (商建, 刘成保, 杨磊, 等. FY-4 卫星高光谱大气探测驻留控制与定位精度分析 [J]. 遥测遥控, 2024, **45**(6): 1-10)

[9] LU Wenqiang, HU Xiuqing, HUANG Yong, *et al*. Analysis of FY-3D satellite attitude and orbit accuracy and its influence on geolocation[J]. *Geomatics and Information Science of Wuhan University*, 2024, **49**(2): 256-263 (鲁文强, 胡秀清, 黄勇, 等. FY-3D 卫星姿轨误差标校及对定位影响研究 [J]. 武汉大学学报 (信息科学版), 2024, **49**(2): 256-263)

[10] WANG Jiachen, SHANG Jian, YANG Lei, *et al*. Geolocation of the tangent point and tangent height correction for spaceborne ultraviolet limb sounder[J]. *Optics and Precision Engineering*, 2026, **34**(2): 179-190 (王嘉琛, 商建, 杨磊, 等. 星载紫外临边探测仪切点几何定位与切高订正 [J]. 光学 精密工程, 2026, **34**(2): 179-190)

[11] XIE X X, GUO Y, HE J Y, *et al*. Calibration of microwave humidity sounder-II onboard FengYun-3F in pre/postlaunch phases[J]. *IEEE Transactions on Geoscience and Remote Sensing*, 2024, **62**: 5302009.

[12] WANG Q, WANG Y M, XU N, *et al*. Preflight spectral calibration of the ozone monitoring suite-nadir on FengYun 3F Satellite[J]. *Remote Sensing*, 2024, **16**(9): 1538.

[13] SHANG J, SHI H Q, YUAN M, *et al*. Satellite-ground integrated external calibration of the WindRAD scatterometer onboard FY-3E satellite[J]. *IEEE Transactions on Geoscience and Remote Sensing*, 2025, **63**: 5100910.

[14] MIAO S X, SUN K M, HU X Q, *et al*. On-orbit radiometric performance assessment of FY-3F MERSI-III: a cross-platform intercomparison approach based on global pseudo-invariant pixels[J]. *IEEE Journal of Selected Topics in Applied Earth Observations and Remote Sensing*, 2025, **18**: 21514-21531.

[15] CHEN B Y, WU A Q, HUI W, *et al*. Radiometric calibration using artificial intelligence: constituting uniform observing systems for infrared satellites[J]. *IEEE Transactions on Geoscience and Remote Sensing*, 2025, **63**: 5001616.

[16] LIN H, LI J, MIN M, *et al*. CLANN: cloud amount neural network for estimating 3D cloud from geostationary satellite imager[J]. *Remote Sensing of Environment*, 2025, **318**: 114600.

[17] YANG J Y, QIU Z F, ZHAO D Z, *et al*. CACM-Net++: FY-4B AGRI day and night cloud mask algorithm modeling[J]. *IEEE Transactions on Geoscience and Remote Sensing*, 2026, **64**: 4104612.

[18] GONG X Y, LI Z L, LI J, *et al*. Cloud-cleared radiances from collocated observations of hyperspectral IR sounder and advanced imager onboard the same geostationary platform[J]. *IEEE Transactions on Geoscience and Remote Sensing*, 2024, **62**: 5531418.

[19] WU Y H, LI B, LI J, *et al*. Enhancing nighttime cloud detection for moderate resolution imagers using a transformer based deep learning network[J]. *Remote Sensing of Environment*, 2026, **332**: 115067.

[20] SI Y D, CHEN L, WANG Y Y, *et al*. An improved aerosol retrieval algorithm based on nonlinear surface model from FY-3D/MERSI-II remote sensing data[J]. *IEEE Transactions on Geoscience and Remote Sensing*, 2024, **62**: 4103017.

[21] SI Y D, WANG L, CHEN L, *et al*. Coupling hourly land surface models with spatiotemporal variability characteristics: a study on FY-4B/AGRI land aerosol retrieval algorithm[J]. *IEEE Transactions on Geoscience and Remote Sensing*, 2025, **63**: 4107820.

[22] SI Y D, GAO L, CHEN L, *et al*. An adaptive dark-target algorithm for retrieving land AOD applied to FY-4B/AGRI data[J]. *IEEE Journal of Selected Topics in Applied Earth Observations and Remote Sensing*, 2024, **17**: 14035-14049.

[23] SONG P L, LIU X Z, SUN L, *et al*. Soil moisture estimation based on FY-3E backscattering data for enhanced daily coverage to SMAP observations in the dawn-dusk orbit[J]. *Remote Sensing of Environment*, 2024, **309**: 114209.

[24] XU R H, WANG X, HU Y H, *et al*. Estimation of all-sky gridded diurnal near-surface air temperatures at regional scale from FY-4B measurements[J]. *IEEE Journal of Selected Topics in Applied Earth Observations and Remote Sensing*, 2025, **18**: 1288-1301.

[25] ZHANG Y K, XU N, ZHAI X C, *et al*. A lightweight deep neural network for sea surface wind speed retrievals from the FY-3D/MWRI[J]. *IEEE Transactions on Geoscience and Remote Sensing*, 2025, **63**: 4102515.

[26] ZHAI X C, TIAN S R, SHANG J, *et al*. Intercomparison of Ku- and C-band backscatter feature parameters for arctic sea ice using spaceborne FengYun-3E WindRAD scatterometer[J]. *IEEE Transactions on Geoscience and Remote Sensing*, 2025, **63**: 4214824.

[27] CHEN Z, ZHANG J L, WANG J S, *et al*. A TIEGCM-based inversion model for ionosphere-thermosphere parameters driven by three-dimensional electron density[J]. *Science Advances*, 2026, **12**(16): eaea2406.

[28] ZHANG J L, ZHANG J X, CHEN Z, *et al*. Deep learning-based vertical decomposition of ionospheric TEC into layered electron density profiles[J]. *Atmosphere*, 2025, **16**(5): 598.

[29] DAI K, LI X T, FANG J Y, *et al*. Four-hour thunderstorm nowcasting using a deep diffusion model for satellite data[J]. *Proceedings of the National Academy of Sciences of the United States of America*, 2025, **122**(51): e2517520122.

[30] LIU N Q, JIANG J Y, MAO D Y, *et al*. Artificial intelligence-based precipitation estimation method using Fengyun-4B satellite data[J]. *Remote Sensing*, 2024, **16**(21): 4076.

[31] XU A, XUE H L, WU R H, *et al*. An observation of the trapped lee waves using Fengyun-4 satellite images and a U-Net network[J]. *Geophysical Research Letters*, 2025, **52**(7): e2024GL113858

[32] LEI Lili, WENG Fuzhong, DUAN Wansuo, *et al*. Overview and prospect of data assimilation in numerical weather prediction[J]. *Acta Meteorologica Sinica*, 2025, **83**(3): 503-535 (雷荔傈, 翁富忠, 段晚锁, 等. 数值天气预报资料同化的发展与展望 [J]. 气象学报, 2025, **83**(3): 503-535)

[33] YIN R Y, HAN W. Impact of targeted sounding observations from FY-4B GIIRS on two super typhoon forecasts in 2024[J]. *IEEE Geoscience and Remote Sensing Letters*, 2025, **22**: 5500805

[34] XIANG Chunyi, DONG Lin, LIU Da, *et al*. Thermodynamic and dynamic mechanism of maintenance of typhoon Doksuri remnant vortex after its landfall in 2023[J]. *Meteorological Monthly*, 2024, **50**(11): 1289-1305 (向纯怡, 董林, 刘达, 等. 2023 年台风杜苏芮登陆后残涡维持的热力和动力机制研究 [J]. 气象, 2024, **50**(11): 1289-1305)

[35] NIU Ning, REN Suling, QIN Danyu. Application of FY-4A satellite data in monitoring of the cold wave from 6 to 8 January 2021[J]. *Meteorological Monthly*, 2024, **50**(6): 661-674 (牛宁, 任素玲, 覃丹宇. FY-4A 数据在 2021 年 1 月 6-8 日寒潮监测中应用 [J]. 气象, 2024, **50**(6): 661-674)

[36] NIU N, REN S L, MAO D Y, *et al*. The application of meteorological satellite products in the extreme sea-effect snowstorm monitoring in East Asia[J]. *Journal of the Meteorological Society of Japan. Ser. Ⅱ*, 2024, **102**(6): 633-653

[37] TAN Juan, QIAN Chuanhai, HUANG Bin, *et al*. The current status and future perspectives of sea fog monitoring and forecasting in China[J]. *Advances in Meteorological Science and Technology*, 2024, **14**(2): 17-23,32 (谭娟, 钱传海, 黄彬, 等. 我国海雾监测预报业务现状及未来展望 [J]. 气象科技进展, 2024, **14**(2): 17-23,32)

[38] LI Y X, ZHU S Y, ZHANG G X, *et al*. Reconstruction of hourly FY-4A AGRI land surface temperature under cloud-covered conditions using a hybrid method combining spatial and temporal information[J]. *Remote Sensing*, 2024, **16**(10): 1777

[39] LUO Yumei, ZHU Shanyou, LI Yueli, *et al*. Analyzing the influence of missing periods on the time dimensional reconstruction of summer land surface temperature in the Heihe River Basin using FY-4A AGRI data[J]. *Journal of Geo-Information Science*, 2024, **26**(3): 709-724 (罗雨梅, 祝善友, 李悦丽, 等. 缺失时段对黑河流域夏季 FY-4A AGRI 地表温度时间维重建的影响分析 [J]. 地球信息科学学报, 2024, **26**(3): 709-724)

[40] LIU Yunyun, ZHANG Daquan, SONG Lianchun, *et al*. Revision and application of the western Pacific subtropical high indices[J]. *Acta Meteorologica Sinica*, 2024, **82**(6): 801-815 (刘芸芸, 章大全, 宋连春, 等. 西太平洋副热带高压指数的修订与应用 [J]. 气象学报, 2024, **82**(6): 801-815)

[41] WANG Jinsong, REN Suling, YANG Bingyun, *et al*. Current status and future prospects of FengYun meteorological satellite remote sensing operational application[J]. *Advances in Meteorological Science and Technology*, 2026, **16**(1): 11-25 (王劲松, 任素玲, 杨冰韵, 等. 风云气象卫星遥感业务应用现状及展望 [J]. 气象科技进展, 2026, **16**(1): 11-25)

[42] GAO L, ZHANG Q Q, WANG Y P, *et al*. A review on the Chinese Fengyun series meteorological satellites for atmospheric composition monitoring[J]. *Bulletin of the American Meteorological Society*, 2026, **107**(5): E1092-E1108.

[43] XU J, WANG Y P, CHEN L *et al*. First total ozone column observations from the Ozone Monitoring Suite-Nadir (OMS-N) onboard China's FengYun-3F satellite[J]. *Science China Earth Sciences*, 2025, **68**(11): 3665-3683.

[44] LIU Y, CHEN J, SHI Y S, *et al*. Global Emissions Inventory from Open Biomass Burning (GEIOBB): utilizing Fengyun-3D global fire spot monitoring data[J]. *Earth System Science Data*, 2024, **16**(8): 3495-3515.

[45] ZHOU X J, WANG T, ZHENG W, *et al*. Reconstruction of fine-spatial-resolution FY-3D-Based vegetation indices to achieve farmland-scale winter wheat yield estimation via fusion with sentinel-2 data[J]. *Remote Sensing*, 2024, **16**(22): 4143.

[46] GUAN Min, ZHANG Yong, XIE Lizi, *et al*. Research on the contribution of Fenyun meteorological satellite remote sensing applications to national economic development[J]. *Meteorological Soft Sciences*, 2025, **150**(4): 61-66 (关敏, 张勇, 谢利子, 等. 气象卫星遥感应用服务对国民经济发展的贡献研究 [J]. 气象软科学, 2025, **150**(4): 61-66)

Author Biography

WANG Jinsong Professor, Director-General of the National Satellite Meteorological Center (National Center for Space Weather) and Chief Designer of China's Fengyun meteorological satellite program. His research interests include satellite meteorology and space physics. He serves as Chair of the Satellite Meteorology Committee of the Chinese Meteorological Society and a member of the Scientific Advisory Panel of the World Meteorological Organization (WMO). He has been recognized through major national talent programs and has received several honors, including the China Youth Science and Technology Award, the Jeoujang Jaw Outstanding Science Award, and the Special Government Allowance from the State Council of China.
E-mail: wangjs@cma.gov.cn

0254-6124/2026/46(4)-0135-12 *Chin. J. Space Sci.* 空间科学学报

LIU Yuxin, ZOU Bin, MA Chaofei, FENG Qian, LU Yunfei, YANG Dian. Advances in China's Ocean Satellite Observation System Since 2024. *Chinese Journal of Space Science*, 2026, **46**(4): 135–146. CSTR:32142.14.cjss.2026–yg06. DOI:10.11728/cjss2026.04.2026–yg06

Advances in China's Ocean Satellite Observation System Since 2024*

LIU Yuxin ZOU Bin MA Chaofei
FENG Qian LU Yunfei YANG Dian

(*State Key Laboratory of Satellite Ocean Environment Dynamics*, *National Satellite Ocean Application Service*, *Beijing* 100081)

Abstract Since 2024, China's ocean satellite program has made systematic progress in the construction of observation systems, expansion of mission portfolios, enhancement of ground-support capabilities, product development, and intelligent applications. An ocean satellite observation system composed of ocean color satellites, ocean dynamic satellites, and ocean surveillance and monitoring satellites has been initially established, providing multi-satellite coordinated observation capabilities over China's coastal seas, the global ocean, and polar regions. The successful launch of HY-4A has filled a gap in China's spaceborne ocean salinity observation capability and provided a foundational capacity for operational global ocean salinity monitoring and related scientific research. The stable operation of ground receiving systems, calibration and validation sites, and data-sharing infrastructure has provided reliable support for networked ocean satellite observations and operational applications. The upgrading of the ocean color satellite data processing system, the development of application-ready products for the Yellow Sea and East China Sea, and the generation of multi-parameter polar sea-ice products indicate that China's ocean satellite product system is evolving from basic data provision toward thematic, refined, and operational applications. The development of artificial intelligence foundation models represented by "SkyOcean" further suggests that ocean satellite applications are extending from two-dimensional sea-surface observations toward three-dimensional environmental reconstruction and prediction services.

Key words China's ocean satellites, Ocean salinity observation, Application products, Intelligent applications, Networked observation

Classified index P715.6

1 Introduction

Ocean satellites are an important technical means for achieving large-scale, continuous, and dynamic monitoring of the marine environment. They play an increasingly important role in marine ecological and environmental protection, marine disaster early warning, marine resource development, polar monitoring, and global ocean governance. After more than two decades of development, China has established an observation system covering ocean color satellites, ocean dynamic satellites, and ocean surveillance and monitoring satellites, and has developed systematic operational capabilities for monitoring sea surface wind fields, sea surface height, sea surface temperature, ocean color, sea ice, maritime targets, and coastal resources and environments.

* Supported by National Key R&D Program of China (2022RDC2013302)
Received May 20, 2026

In recent years, China's ocean satellite program has exhibited several major characteristics. First, the range of observed variables has continued to expand. New missions such as ocean salinity observation have been advanced, and ocean remote sensing is extending from traditional monitoring of sea-surface parameters toward more comprehensive marine environmental sensing. Second, the product system has been continuously upgraded. Driven by demands related to marine ecological and environmental protection and restoration, as well as polar monitoring, a more refined, thematic, and operational product chain is gradually taking shape. Third, intelligent applications are developing rapidly. Artificial intelligence, foundation models, and multi-source data fusion methods are promoting a transformation of ocean remote sensing services from "data provision" to "intelligent services". Fourth, ground operations, calibration and validation, and data services have been continuously improved, indicating that China's ocean satellite development is moving from the stage of capability establishment toward capability enhancement and system maturity.

Against this background, this paper reviews and summarizes the major advances in China's ocean satellite program since 2024 from the perspectives of observation system evolution, ground support and data services, typical applications and product development, international cooperation, and future mission planning. The objective is to provide a reference for subsequent ocean satellite development planning, application deployment, remote sensing operational system construction, and related scientific research.

2 Evolution of China's Ocean Satellite Observation System

2.1 Current Operational Status of the In-orbit Ocean Satellite System

At present, China operates 11 ocean satellites in orbit, carrying 18 types of payloads in five major categories, including visible-light, hyperspectral, radar, microwave, and infrared sensors. These satellites have initially established high-precision, quantitative, and high-revisit spaceborne observation capabilities covering the global ocean, polar regions, and sea areas under China's jurisdiction. An independent ocean satellite observation system has essentially been formed (Table 1).

In terms of functional positioning, ocean color satellites mainly undertake long-term monitoring of sea surface temperature, ocean chlorophyll concentration, suspended sediment concentration, water transparency, and typical marine ecological and environmental variables. Ocean dynamic satellites primarily serve the retrieval of dynamic environmental parameters such as sea surface wind fields, sea surface height, ocean waves, sea surface salinity, and large-scale sea surface temperature. Ocean surveillance and monitoring satellites, supported by Synthetic Aperture Radar (SAR) and other payloads, provide high-resolution observational support for maritime target detection, ecological disaster monitoring, refined coastal dynamic environment retrieval, sea-ice identification, and monitoring of intertidal zones and coastal wetlands.

Currently, HY-1C and HY-1D have formed a dual-satellite network for operational ocean color observations. HY-1E, as a second-generation ocean color observation research and experimental satellite, marks the upgrading of China's ocean color satellite series and significantly enhances the capability for observing global ocean color environmental information. For ocean dynamics monitoring, China has established a five-satellite network composed of HY-2B, HY-2C, HY-2D, the China–France Oceanography Satellite (CFOSAT), and the Ocean Salinity Detection Satellite. This system provides all-weather, day-and-night capabilities for acquiring global ocean dynamic environmental information multiple times per day. For ocean surveillance and monitoring, GF-3 and two 1-m-resolution C-band SAR operational satellites together form an ocean surveillance and monitoring satellite constellation, providing operational and quantitative radar satellite data for multiple sectors, including ocean management, land resources, and emergency response.

Overall, ocean color satellites, ocean dynamic satellites, and ocean surveillance and monitoring satellites have gradually formed a coordinated and complementary configuration in terms of observed variables, spatial and temporal resolution, and spectral resolution. The multi-source satellite coordination model is shifting from "coexistence of platforms" toward "operational link-

Table 1 Overview of China's in-orbit ocean satellites

Category	Representative satellites	Main observation variables/applications
Ocean color satellites	HY-1C, HY-1D, HY-1E	Sea surface temperature, ocean color, water optical parameters, marine ecological environment, and disaster monitoring
Ocean dynamic satellites	HY-2B, HY-2C, HY-2D, CFOSAT, HY-4A	Sea surface wind field, sea surface height, ocean waves, sea surface salinity, sea surface temperature, *etc*.
Ocean surveillance and monitoring satellites	GF-3, 1 m C-SAR 01/02	Maritime target detection, refined coastal observations, sea-ice identification, wetland monitoring, *etc*.

Note: Products related to the CFOSAT scatterometer and the HY-2D microwave scatterometer have been discontinued because of payload antenna anomalies.

age". Compared with the HY-2 series satellites, which have advantages in high revisit frequency and wide coverage, SAR has stronger data acquisition capability and refined observation advantages in coastal waters, promoting the evolution of ocean dynamic environment observations from an "HY-2 wide-coverage-dominated" mode to a coordinated mode of "wide coverage plus refined supplementation". Meanwhile, in monitoring marine ecological disasters under cloudy and rainy conditions, SAR can work synergistically with optical remote sensing owing to its all-time, all-weather, and cloud-penetrating technical advantages, substantially improving the continuity and reliability of monitoring operations. In addition, the combined application of AIS and surveillance and monitoring satellites provides effective technical support for identifying and monitoring anomalous vessels.

2.2 Ocean Salinity Observation Mission

The construction of China's ocean satellite system has continued to improve, and the mission portfolio is expanding from the stable acquisition of traditional marine environmental parameters, such as ocean color, sea surface temperature, sea surface wind field, and sea surface height, toward integrated sensing of marine environmental variables. Ocean salinity is an important parameter for understanding ocean water-mass structure, the global water cycle, air–sea freshwater exchange, and climate-change processes. It is also a key observational variable linking ocean dynamic processes and air–sea interaction. Therefore, the Ocean Salinity Detection Satellite mission is of representative significance.

Successfully launched on 14 November 2024, the Ocean Salinity Detection Satellite (HY-4A) is China's first remote sensing satellite with ocean salinity information acquisition as its core objective. It fills the gap in China's spaceborne ocean salinity observation capability and further improves the national ocean satellite observation system[1]. The satellite primarily targets sea surface salinity observations while also supporting soil moisture detection. Sea surface salinity products can be applied to marine environmental monitoring and forecasting, polar monitoring, and research on air–sea interaction and climate change. Soil moisture products can support drought monitoring and agricultural environmental monitoring. In terms of accuracy indicators, the single-pass accuracy of HY-4A sea surface salinity products in low- and mid-latitude regions can reach 1 psu@50 km, while the 30-day averaged accuracy in open-ocean areas can reach 0.1 psu@200 km. The accuracy of soil moisture observations is better than 4%. These indicators show that the related observation products have the basic capability to support operational global-scale ocean salinity observations and related scientific research.

In terms of observational performance, HY-4A has global continuous observation capability, with a coverage rate of no less than 98% over global sea areas within three days. It can therefore effectively meet the needs for monitoring the global distribution of ocean salinity and its spatiotemporal variability. The satellite operates in a sun-synchronous, repeating frozen dawn–dusk orbit at a mean altitude of approximately 654.7 km with an orbital inclination of 98.0004°. This orbit is conducive to improving global coverage efficiency, maintaining consistency in observation conditions, and satisfying requirements for long-term stable operation.

Regarding payload configuration, HY-4A carries two main payloads: an L-band Aperture Synthesis Microwave Radiometer (LASMR) and a Microwave Imager Combined Active and Passive (MICAP) (Figure 1). The LASMR focuses on L-band brightness temperature observations and provides high-sensitivity, multi-inci-

Fig. 1 Schematic diagram of the Ocean Salinity Detection Satellite

dence-angle observation data for sea surface salinity retrieval. The MICAP obtains environmental correction information, such as sea surface roughness and sea surface temperature, through synergistic observations by a microwave radiometer and a microwave scatterometer. It also provides a long-term stability reference for L-band radiometric brightness temperature detection and enables RFI detection and mitigation (Table 2). In-orbit test results show that the multi-parameter joint retrieval method constructed using dual-payload observations and a radiative transfer model performs well in sea surface salinity retrieval and environmental parameter correction, and that the functions and performance of the relevant payloads meet the design specifications.

2.3 Coordinated Development of Public-service and Commercial Satellites

As marine environmental monitoring requirements increasingly shift toward greater refinement, timeliness, and scenario-specific applications, a single class of public-service operational satellites can no longer fully meet multi-level observation needs. In recent years, commercial remote sensing satellites have developed rapidly in high-resolution imaging, rapid revisit, flexible constellation deployment, and thematic applications. They have demonstrated certain advantages in refined coastal observations, maritime target identification, polar supplementary monitoring, and disaster emergency response, and are becoming an important complementary force in the national ocean observation system. Commercial satellites are entering the field of marine environmental observation at an accelerated pace, initially forming a development trend characterized by coordination with public-service operational satellites. New observation capabilities represented by “Blue Carbon-1”, “Tianmu-1”, and multiple types of small SAR satellites effectively supplement public-service operational satellites in high-resolution, high-frequency, and region-specific observations. The ocean satellite observation system is thus showing a development trend in which national operational backbone satellites play the leading role while commercial supplementary satellites provide coordinated support.

Among these new capabilities, the “Blue Carbon-1” ocean remote sensing satellite, successfully launched in January 2025, carries a high-resolution imaging spectrometer with eight visible spectral channels and two shortwave-infrared spectral channels, enabling remote sensing observations at 10 m resolution. The “Tianmu-1” constellation currently has 23 satellites operating stably in orbit. Based on BDS/GNSS remote sensing technology, it is compatible with signals from the four major navigation systems, namely BeiDou, GPS, Galileo, and GLONASS. It provides high-frequency global three-dimensional detection capability and can acquire environmental variables such as global sea surface wind fields and sea ice on an all-time and all-weather basis[2]. In addition, small SAR satellites such as Haisi-1, Chaohu-1, Hongtu-1, and Luojia-2 have been launched and put into operation in succession, and their data products have become important supplementary sources for ocean satellite observations.

From the perspective of system functions, public-service operational satellites have advantages in long-term continuous operation, observational stability, and

Table 2 Payloads and technical specifications of the Ocean Salinity Detection Satellite

Payload component	Main function	Technical specifications
LASMR	Acquires L-band sea-surface radiometric brightness temperature	1.400–1.427 GHz; 20 MHz; V/H/T3; sensitivity better than 1.5 K; stability better than 0.12 K; calibration accuracy 1.0 K; resolution better than 38 km; swath width better than 950 km
MICAP: microwave radiometer, L band	Provides brightness temperature detection and a stability reference	1.400–1.427 GHz; 25 MHz; V/H/T3; sensitivity better than 0.15 K; stability better than 0.12 K; resolution better than 75 × 50 km; swath width better than 950 km
MICAP: microwave radiometer, C band	Provides environmental correction information	6.9 GHz; 200 MHz; V/H; sensitivity better than 0.5 K; stability better than 0.3 K; resolution better than 15 × 25 km; swath width better than 950 km
MICAP: microwave radiometer, K band	Provides environmental correction information	18.7 GHz; 200 MHz; V/H; sensitivity better than 0.5 K; stability better than 0.3 K; resolution better than 15 × 25 km; swath width better than 950 km
MICAP: microwave scatterometer	Acquires sea surface roughness and supports RFI detection and mitigation	1.25 GHz; HH/VV/HV/VH; bandwidth ⩽5 MHz; peak power ⩾200 W; calibration stability better than 0.1 dB; resolution 50–100 km; swath width better than 950 km

strong operational assurance capabilities, and therefore constitute the main body of national-level marine environmental monitoring and operational services. Commercial satellites have greater advantages in flexible deployment, rapid response, application innovation, and differentiated supply, making them suitable for high-frequency supplementary observations, refined monitoring of specific regions, and emergency response tasks. The coordinated development of these two types of satellites can improve the spatiotemporal coverage, observation accuracy, and service efficiency of the ocean observation system.

3 Development of Ground Support and Data Service Capabilities

3.1 Data Reception and Ground Operation System

China's ocean satellite ground operation system has established a complete operational chain covering data reception, mission scheduling, calibration and validation, and transmission and distribution. The ground receiving system, composed of three fixed stations in Beijing, Mudanjiang, and Hainan, together with the mobile station on the research vessel Xuelong, is equipped with 24 sets of multiple types of antennas. It has integrated reception capability for polar-orbiting and geostationary satellites and can simultaneously support the real-time acquisition and transmission of data from 15 satellites.

According to the 2025 operational statistics of the National Satellite Ocean Application Service, approximately 25900 data-reception orbits were completed in 2025, with a total data volume exceeding 385 TB. This indicates that China's ocean satellite data reception capability has entered a stage of stable and efficient operation. The continuous enhancement of ground-system operational capabilities provides fundamental support for networked ocean satellite observations and operational applications.

For data calibration and validation, China has established a network of calibration and validation sites covering key sea areas nationwide. This network includes nine calibration sites and 23 observation stations, such as the Yellow Sea and East China Sea optical validation site, the Xi'an scatterometer calibration station, the Zhuhai Wanshan altimeter calibration site, and the Xisha offshore calibration site. It has formed coordinated support capabilities for multiple payload types and established integrated capabilities for radiometric calibration, product validation, and in-orbit performance evaluation. These capabilities provide a reliable data-reference basis for quantitative retrieval and long-term time-series applications of ocean satellites.

3.2 Data Processing, Sharing, Distribution, and Operational Services

In terms of data processing and sharing services, China has established data processing and distribution systems covering multiple satellite series, including ocean color and dynamic environment satellites. The system has approximately 2 Pflops of computing capability and 50 PB of storage capacity, supports the processing of data from various ocean payloads, and can meet the needs of large-scale operational production and long-term historical archiving. Through the ocean satellite internet service system of the National Satellite Ocean Application Service (Figure 2), users worldwide can perform data retrieval, ordering, and customized distribution. The service user base covers government departments, research institutions, universities, and international users, with more than 6800 registered users.

Meanwhile, in response to operational application needs, throughout 2025, the National Satellite Ocean Application Service pushed approximately 6516 TB of data to more than 600 users through its operational sharing platform. HY-1 ocean color satellites and HY-2 series dynamic environment satellites were the main data sources, while multi-source data such as CFOSAT and SAR were also included.

Overall, China's ocean satellite data services are transforming from "data provision" toward "high-quality services and application support", thereby providing a solid foundation for marine scientific research and operational applications.

4 Progress in Typical Applications and Product Development

With the continuous improvement of China's networked ocean satellite observation capability, ground processing capability, and operational service capability, ocean satellite applications have expanded from single-image interpretation and basic parameter retrieval to an integrated operational support system for national marine ecological early-warning monitoring, marine disaster prevention and mitigation, global marine environmental monitoring, polar observations, maritime safety supervision, and marine resource development (Table 3).

Ocean color satellites, ocean dynamic satellites, and ocean surveillance and monitoring satellites are complementary in terms of observed variables, spatial and temporal resolution, and application scenarios, providing stable data sources and product support for different application requirements. On this basis, product forms and application modes are also evolving from the provision of basic imagery toward application-ready products, operational thematic products, and intelligent products.

4.1 Development of Application-ready Products for the Yellow Sea and East China Sea

To meet the needs of marine ecological monitoring and marine disaster emergency response in the Yellow Sea and East China Sea, the "China Ocean Color Satellite Yellow Sea and East China Sea Imagery and Remote Sensing Index Dataset" has been developed based on HY-1C, HY-1D, and HY-1E satellite data. Designed for satellite remote sensing monitoring of the Yellow Sea and East China Sea, this dataset provides application-ready remote sensing imagery, remote sensing indices, cloud-cover information, and other thematic products.

Fig. 2 Schematic diagram of the ocean satellite internet service system

With medium spatial resolutions of 50 m/100 m and daily product updates, it provides stable data support for monitoring marine ecological disasters, including green tides caused by *Ulva prolifera*, *Sargassum*, red tides, and offshore oil spills.

In terms of product design, this dataset does not simply provide single-scene raw imagery. Instead, based on reflectance calculations from L1B data acquired by optical payloads such as CZI, cloud identification processing is performed by considering the characteristics of different satellite sensors. Remote sensing index products, including NDVI, RVI, and BRVI, are further generated (Figure 3). Taking floating algae monitoring as an example, this product chain extracts floating algal pixels over the sea by applying multi-index threshold constraints and filtering non-cloud and non-land pixels. It then generates thematic products for operational floating algae monitoring through multi-orbit data mosaicking, observation-domain masking, human–computer interactive correction, and statistical analysis of coverage area and distribution range.

Overall, although medium-resolution products are weaker than high-resolution imagery in representing fine spatial details, they can still effectively reflect overall

Table 3 Operational support system of ocean satellites

Application field	Main observation requirements	Main satellites/payloads	Typical products	Operational applications
Marine ecological early-warning monitoring	Ocean color, chlorophyll, floating algae, red tides, oil spills	HY-1C/D/E, GF-3, 1 m C-SAR	Chlorophyll, suspended sediment, floating algae index, oil spill identification products	Monitoring of green tides caused by *Ulva prolifera*, red tides, *Sargassum*, and oil spills
Marine disaster prevention and mitigation	Sea surface wind field, ocean waves, sea ice, sea surface height	HY-2B/C/D, CFOSAT, GF-3, 1 m C-SAR	Wind field, ocean waves, sea level anomaly, sea-ice products	Monitoring of typhoons, storm surges, and sea-ice disasters
Global marine environmental monitoring	Sea surface temperature, ocean color, sea surface height, sea surface salinity	HY-1C/D/E, HY-2B/C/D, GF-3, 1 m C-SAR, CFOSAT, HY-4A	Global marine environmental parameter products	Research on climate change and air–sea interaction
Polar monitoring	Sea-ice extent, concentration, edge, and polar environment	HY-1C/D/E, HY-2B, GF-3, 1 m C-SAR	Multi-parameter polar sea-ice products	Polar navigation and climate-change assessment
Maritime safety and resource management	Vessels, maritime targets, wetlands, shorelines	GF-3, 1 m C-SAR, AIS	Vessel identification, wetland classification, refined coastal observation products	Marine regulation, emergency response, and resource management

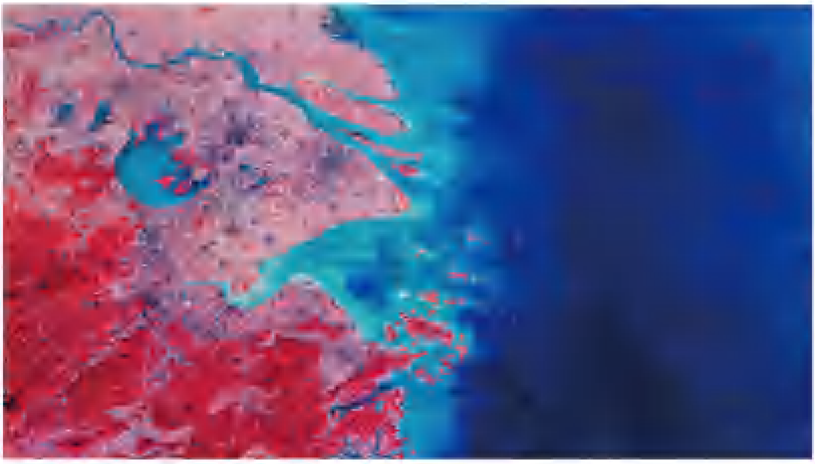

Fig. 3 Local image example from the "China Ocean Color Satellite Yellow Sea and East China Sea Imagery and Remote Sensing Index Dataset"

distribution patterns and area scales, making them suitable for large-scale and continuous operational monitoring. This dataset represents the development of China's ocean color remote sensing products from basic imagery provision toward thematic and application-ready products for regional operational applications.

4.2 Upgrade of the Ocean Color Satellite Data Processing System

As the operational applications of China's ocean color satellites continue to deepen, the related data processing system has gradually moved beyond the initial stage of satisfying basic product production and entered an upgrade stage oriented toward multi-scenario applications, improved product quality, and thematic expansion. Although HY-1C and HY-1D have both exceeded their five-year design lifetimes, they remain in stable operation in orbit. Through upgrades to the operational processing programs for COCTS L2 and L3 data, a Version 2.0 product system has been established and has replaced the previous version for archiving and distribution.

This upgrade is reflected in three aspects: product form, product type, and product quality. First, the quick-look display has been improved from a single display mode to the overlay of RGB imagery and chlorophyll-a information, enhancing product retrieval and rapid interpretation capabilities. Second, new NDVI L2/L3 products and L3 products of remote sensing reflectance, Rrs, in visible bands have been added, expanding thematic application capabilities for coastal ecological environment and marine disaster monitoring. Third, based on cross-comparison with similar MODIS products, the upgraded chlorophyll-a concentration and sea surface temperature products show clear improvements in both spatial structure representation and quantitative accuracy (Figure 4).

From the perspective of system evolution, the upgrade of the COCTS data processing system has not only enhanced the application value of in-orbit operational satellites but also indicates that China's ocean color satellite ground processing system is continuously evolving from a "product-production-oriented" system toward a "quality-driven and application-oriented" system. This provides a foundation for improving data processing, product calibration, and operational service capabilities for subsequent ocean color satellites.

4.3 Progress in Multi-parameter Polar Sea-ice Products

Polar regions are among the most sensitive key regions to global climate change and are also important frontiers for research on air–sea interaction, cryosphere evolution, and the global water cycle. In recent years, relying on China's ocean satellites, operational monitoring capabilities for polar marine environments have continued to improve. An operational multi-parameter polar sea-ice product system has been developed, focusing on sea-ice concentration, sea-ice extent, sea-ice type, and sea-ice drift velocity. This development promotes the extension of polar remote sensing monitoring from single-parameter retrieval to multi-parameter coordinated observation and integrated application (Figure 5). The retrieval and productization of multiple sea-ice parameters based on the active and passive microwave payloads of HY-2B constitute important progress at this stage[3,4] .

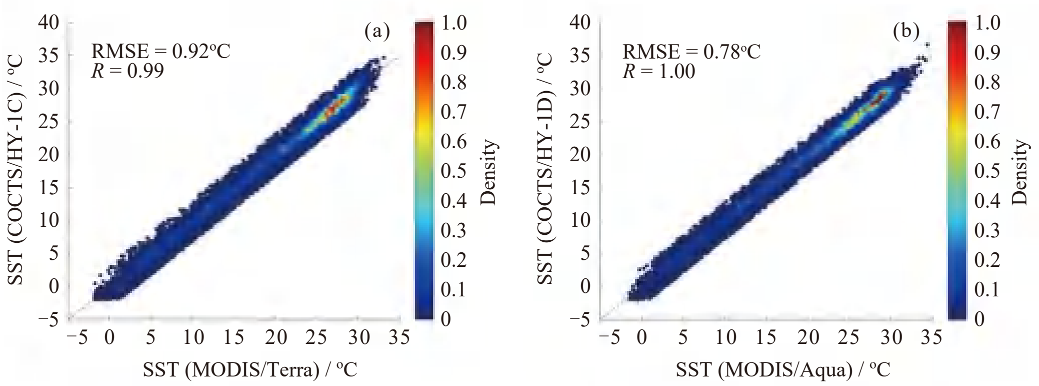

Fig. 4 Consistency comparison between upgraded sea surface temperature daytime products from COCTS on HY-1C/D and corresponding MODIS products, using data from 20 June 2025 as an example. (a) HY-1C *vs.* Terra; (b) HY-1D *vs.* Aqua

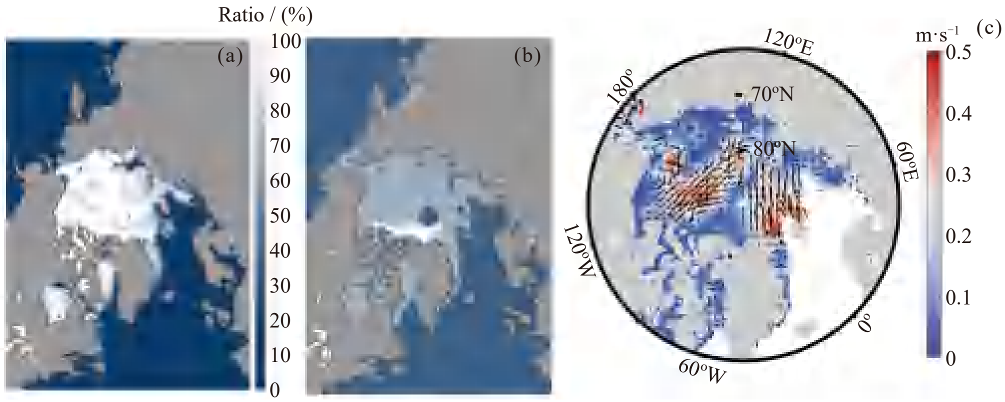

Fig. 5 Schematic diagram of operational multi-parameter polar sea-ice products based on the active and passive microwave payloads of HY-2B. (a) Sea-ice concentration; (b) sea-ice extent and type, (c) sea-ice drift velocity

For sea-ice concentration, in response to sensor differences among brightness temperature data from different microwave radiometers, related studies have developed a Bootstrap retrieval method based on dynamic brightness temperature tie points. Through steps such as dynamic feature selection, weather filtering, climatological constraints, and land-contamination correction, the consistency and stability of sea-ice concentration retrieval have been improved. In situ observation-based evaluation results indicate that sea-ice concentration products retrieved from Chinese satellite data achieve accuracy comparable to that of international counterpart products, as measured by correlation coefficient, bias, and root-mean-square error.

For sea-ice extent and sea-ice type, the synergistic observation advantages of the HY-2B microwave scatterometer and scanning microwave radiometer have been used to develop dynamic support vector machine models for ice–water discrimination and sea-ice type classification. These models enable effective identification of first-year ice and multi-year ice during the Arctic freezing season. Comparisons with mainstream international products, such as NSIDC and OSISAF, as well as independent observations from MODIS and SAR, indicate that the results for sea-ice extent and type have high consistency and can meet operational application requirements.

For sea-ice drift, to address the insufficient texture information in low-resolution passive microwave data, an Arctic freezing-season sea-ice drift retrieval method has been developed based on HY-2B/SMR 37 GHz brightness temperature data. Retrieval accuracy is improved through techniques including brightness temperature resampling, texture enhancement, sub-pixel displacement estimation, and multi-polarization result fusion. Validation using Arctic buoy data shows that the retrieved sea-ice drift velocities are in good agreement with observations.

4.4 Regional Ocean Artificial Intelligence Foundation Model

Artificial intelligence is becoming an important direction in the development of ocean satellite remote sensing operations. Compared with traditional ocean remote sensing, which mainly provides sea-surface state information, operational marine environmental services increasingly require reconstruction of subsurface three-dimensional thermohaline and dynamic structures and prediction of future states. In this context, regional ocean artificial intelligence foundation models represented by "SkyOcean" have begun to enter operational application scenarios.

"SkyOcean" is designed for the northwestern Pacific region. Based on multi-source satellite fusion products, it establishes a regional ocean AI application framework covering the chain of "remote sensing–reconstruction–prediction". The model extends observational applications from two-dimensional sea surface information to the prediction of three-dimensional spatial structures and their temporal evolution. It is capable of generating prediction products for the next 10 days, spanning from the sea surface to a depth of 650 m, with a spatial resolution of 1/8° (Figure 6).

Validation based on Argo observations shows that the prediction errors of temperature, salinity, and cur-

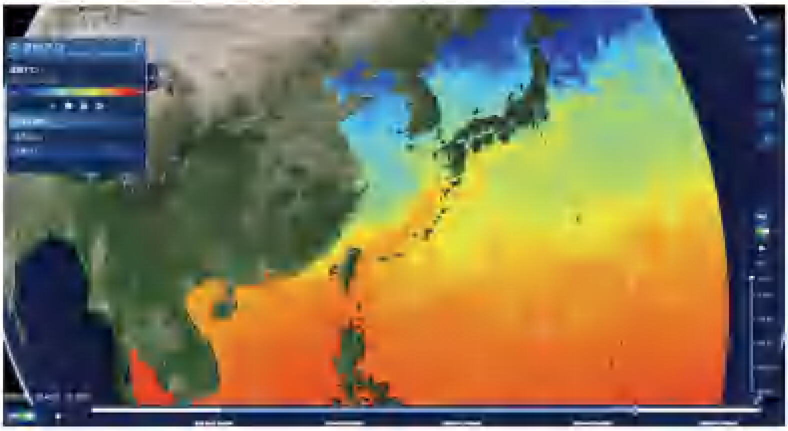

Fig. 6 Schematic diagram of the "SkyOcean" foundation model

rent fields are smaller than those of operational numerical forecasts. It also has application capability for the three-dimensional characterization, identification, and tracking of typical ocean dynamic processes such as mesoscale eddies, and has already been put into operational use.

Overall, the exploration of foundation models represented by "SkyOcean" indicates that China's intelligent applications of ocean satellites have begun to move beyond local tasks such as image recognition and single-parameter estimation toward higher-level applications, including multi-source fusion sensing, three-dimensional environmental reconstruction, and prediction services.

5 Progress in International Cooperation

In recent years, China's international cooperation in ocean satellites has formed a multi-level cooperation pattern centered on data exchange, joint development, application demonstrations, and capacity building. Cooperation regions include Europe, Africa, ASEAN countries, and Latin America.

In cooperation with Europe, the National Satellite Ocean Application Service has established an operational data exchange mechanism with the European Organisation for the Exploitation of Meteorological Satellites, promoting the integration of Chinese ocean satellite data into operational systems such as the European Centre for Medium-Range Weather Forecasts. It has also continued to advance cooperation with the Centre National d'Études Spatiales of France on CFOSAT, achieving significant results in sensor performance validation, algorithm development, calibration and validation, scientific product generation, and global data sharing. This cooperation has further promoted the extension of next-generation China–France ocean satellite collaboration toward subsequent coordinated missions. Meanwhile, China has also carried out altimeter calibration cooperation with relevant institutions in Greece, continuously improving the quantitative application level of ocean satellites.

In cooperation with developing countries, relying on the China–Africa Satellite Remote Sensing Application Cooperation Center and the China–ASEAN Satellite Remote Sensing Application Center, China has actively provided products and technical services to African and ASEAN countries, including sea surface wind fields, sea surface temperature, ocean color anomalies, mangrove monitoring, and fishery environmental support (Figure 7). China has also promoted bilateral cooperation and demonstration applications with multiple countries. Overall, China's international cooperation in ocean satellites is gradually expanding from "data sharing" toward "joint research and development, joint application, and joint services", providing strong support for global marine environmental monitoring, disaster prevention and mitigation, and sustainable ocean development.

6 Conclusions and Outlook

Since 2024, China's ocean satellite observation system has made systematic progress in networked operation,

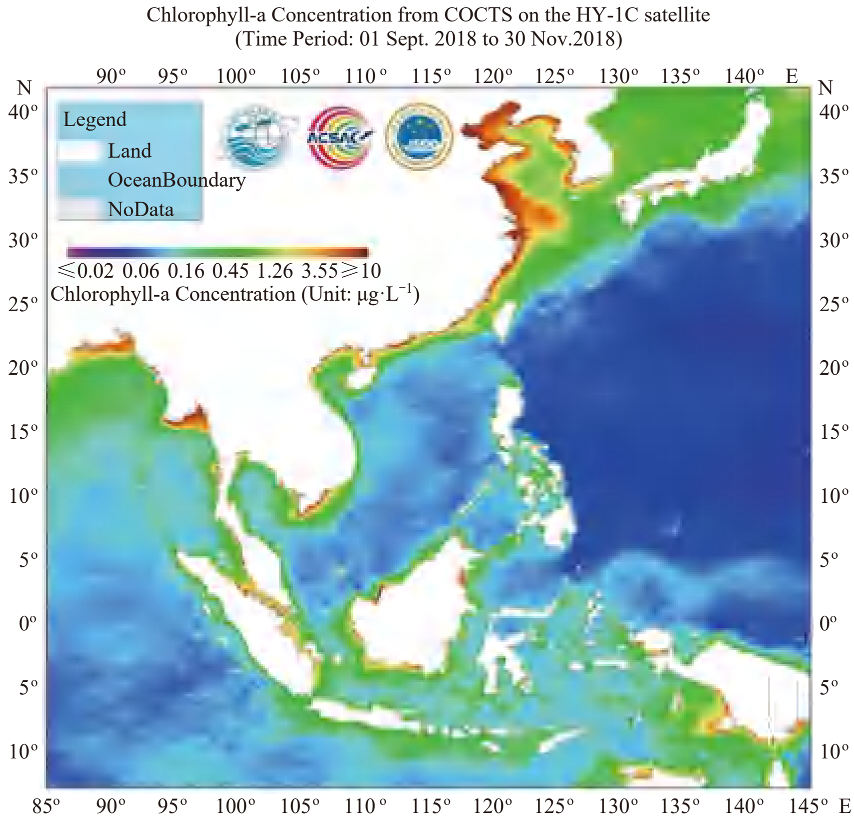

Fig. 7 Example of chlorophyll concentration monitoring products for China–ASEAN sea areas

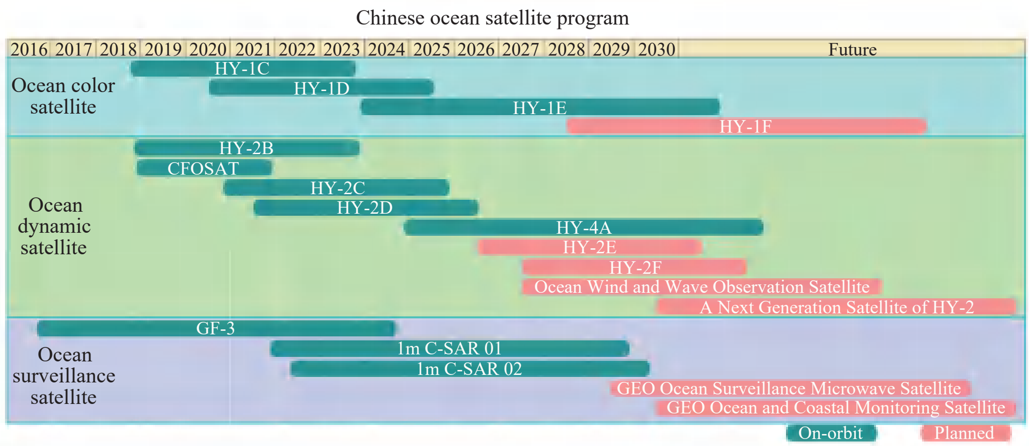

Fig. 8 Development plan of China's ocean satellites

expansion of observed variables, application product upgrading, ground-support capability development, and intelligent applications. The observation system has continued to improve, and the successful launch of HY-4A has filled the gap in China's spaceborne ocean salinity observation capability. The development of ocean color application-ready products, the upgrade of the COCTS processing system, and the generation of multi-parameter polar sea-ice products indicate that the product system is extending from basic product provision toward quality optimization, thematic deepening, and operational services. Intelligent applications represented by "SkyOcean" show that ocean satellite applications are expanding from sea-surface observations toward three-dimensional environmental representation and prediction services. At the same time, capabilities in ground operations, calibration and validation, and data distribution services have continued to improve, providing solid support for the operational use of ocean satellites.

According to existing plans (Figure 8), China will focus on advancing missions such as next-generation operational ocean color satellites, HY-2E/F, next-generation polar-orbiting ocean dynamic satellites, sea wind and wave detection satellites, and geostationary ocean observation satellites. These missions will gradually build an integrated observation system characterized by coordinated development of "polar-orbiting + geostationary" and "operational satellites + research satellites".

Looking ahead, while maintaining existing observation capabilities, it is necessary to continuously improve spatial and temporal resolution and observation accuracy, further address shortcomings in polar observations, and develop capabilities for sea surface current fields and subsurface profile detection. At the same time, China's ocean satellite development should continue to focus on multi-satellite and multi-payload consistency and long-term stable calibration, construction of high-timeliness and high-quality product chains, improvement of coastal complex-environment observation capability, physical consistency and reliability of multi-source fusion products, and the interpretability of artificial intelligence. Only by continuously promoting the coordinated evolution of the observation system, ground-support system, and intelligent application system can ocean satellites better support marine ecological early warning, disaster prevention and control, resource development, and global ocean governance.

References

[1] NSOAS. Successful launch of China's first ocean salinity detection satellite[EB/OL]. 2024-12-14(2026-06-12). http://www.nsoas.org.cn/eng/item/268.html

[2] Peng L. Tianmu-1 constellation[J]. *Satellite Applications*, 2024(6): 70. (in Chinese)

[3] WU S H, SHI L J, ZOU B, *et al*. Daily sea ice concentration product over polar regions based on brightness temperature data from the HY-2B SMR sensor[J]. *Remote Sensing*, 2023, **15**(6): 1692

[4] ZENG T, SHI L J, SHI Y N, *et al*. Polar Sea Ice Monitoring using HY-2B satellite scatterometer and scanning microwave radiometer measurements[J]. *Remote Sensing*, 2024, **16**(13): 2486

Author Biography

LIU Yuxin (First author) Male, born in 1987 in Shangqiu City, Henan Province, currently an Associate Researcher at the National Satellite Ocean Application Service. His main research direction is ocean remote sensing and its applications.
E-mail: liuyuxin@mail.nsoas.org.cn

ZOU Bin (Corresponding author) (Corresponding author) Male, born in 1969 in Guangshan County, Henan Province, currently a Senior Engineer at the National Satellite Ocean Application Service and a master's supervisor. His main research direction is ocean remote sensing and its applications.
E-mail: zoubin@mail.nsoas.org.cn

0254-6124/2026/46(4)-0147-07 *Chin. J. Space Sci.* 空间科学学报

HUANG Shusong, XIA Tian, ZHANG Wenhui, ZHAO Yingfen, CHEN Weirong. Recent Progress of Earth Observation Satellites in China Since 2024. *Chinese Journal of Space Science*, 2026, **46**(4): 147–153. CSTR:32142.14.cjss.2026–yg13. DOI:10.11728/cjss2026.04.2026–yg13

Recent Progress of Earth Observation Satellites in China Since 2024

HUANG Shusong XIA Tian ZHANG Wenhui
ZHAO Yingfen CHEN Weirong

(*China Centre for Resources Satellite Data and Application*, *Beijing* 100094)

Abstract Since 2024, China has continuously launched new Earth observation satellites, and now 33 satellites are operating stably in orbit. These satellites are equipped with optical, multispectral, infrared and radar payloads to produce rich remote sensing data. Their spatial resolution covers low, medium and high levels, enabling multi-spectral, all-time and all-weather observation across the globe. The remote sensing data are widely used in natural resource detection, environmental governance, disaster prevention and mitigation, urban mapping, agricultural and forestry investigation, geological exploration and ocean forecasting, bringing substantial social and economic benefits. This article summarizes the overall status of China's Earth observation satellites since 2024, focusing on satellite launch progress, data coverage and data distribution performance.

Key words Earth observation satellites, Remote sensing data, Data archiving, Data distribution, Data coverage

Classified index V474.1

1 Introduction

Earth observation satellites serve as an indispensable technical support for multiple fields including natural resource investigation, environmental monitoring and protection, disaster prevention and mitigation, urban planning and mapping, agricultural and forestry surveys, land surveying, geological exploration and ocean forecasting. The remote sensing data acquired by these satellites are of great significance to national economic development, social stability and national security.

At present, a total of 33 Earth observation satellites are operating in orbit. China has launched 3 new Earth observation satellites from 2024 up to now. Table 1 presents the catalogue of in-orbit satellites.

1.1 CSES 02

On 14 June 2025, at 15:56 UTC+8, the China Seismo-Electromagnetic Satellite-02 (CSES 02) was successfully deployed into a sun-synchronous orbit *via* a Long March 2D launch vehicle from the Jiuquan Satellite Launch Center. The flawless launch and orbital insertion represent a significant advance in China's space-borne geophysical observation infrastructure, strengthening the integrated space-air-ground monitoring network for natural hazard mitigation[1].

As a flagship Sino-Italian collaborative project formalized by a Memorandum of Understanding witnessed by the heads of state of both nations in 2019, CSES 02 is the first operational satellite dedicated to geophysical field measurements under China's National Civil Space Infrastructure Development Plan (2021–2035). Equipped with nine state-of-the-art scientific instruments, including a co-developed electric field detector and an Italian-built high-energy particle detector, the satellite has a de-

Received May 24, 2026

Table 1 List of in-orbit satellites in China (as of 31 May 2026)

Number	Satellite	Launch date	Design life/a
1	GF-1	26 Apr. 2013	5–8
2	CBERS-04	7 Dec. 2014	3
3	GF-4	29 Dec. 2015	8
4	ZY-3 02	30 May 2016	5
5	GF-3	10 Aug. 2016	8
6	CSES	2 Feb. 2018	5
7	GF-1B	31 Mar. 2018	6
8	GF-1C	31 Mar. 2018	6
9	GF-1D	31 Mar. 2018	6
10	GF-6	2 Jun, 2018	8
11	ZY-1E	12 Sept. 2019	5
12	GF-7	3 Nov. 2019	8
13	CBERS-04A	20 Dec. 2019	5
14	GFDM	3 Jul. 2020	8
15	ZY-3 03	25 Jul. 2020	8
16	HJ-2A	27 Sept. 2020	5
17	HJ-2B	27 Sept. 2020	5
18	GF-5B	7 Sept. 2021	8
19	SCSY-1	14 Oct. 2021	3
20	GF-3B	23 Nov. 2021	8
21	ZY-1F	26 Dec. 2021	8
22	LT-1A	26 Jan. 2022	8
23	LT-1B	27 Feb. 2022	8
24	GF-3C	7 Apr. 2022	8
25	DQ-1	16 Apr. 2022	8
26	CM-1	4 Aug. 2022	8
27	HJ-2E	13 Oct. 2022	8
28	GF-5 01A	9 Dec. 2022	8
29	HJ-2F	9 Aug. 2023	8
30	JZ-1	13 Aug. 2023	8
31	CSES 02	14 Jun, 2025	6
32	ZY-3 04	16 Dec. 2025	8
33	DQ-2	17 Apr. 2026	8

signed operational lifetime of 6 years. Its primary mission is to perform continuous, quasi-real-time measurements of global electromagnetic fields, plasma parameters in the ionosphere, and neutral atmospheric properties. By detecting electromagnetic perturbations associated with crustal activities, anthropogenic sources, and atmospheric electrical phenomena, CSES 02 will enhance early warning capabilities for earthquakes, tsunamis, volcanic eruptions, and extreme weather events. Furthermore, it will provide valuable data products for emergency response, geodetic surveying, space weather forecasting, and international scientific cooperation under the Belt and Road framework.

The CSES constellation now has two satellites in a 180°phased configuration sharing the same orbit. Building upon the proven technology of CSES-01 (launched in 2018), CSES-02 features enhanced payload performance and expanded measurement capabilities. The dual-satellite configuration will substantially increase the temporal and spatial coverage of observations, enabling more comprehensive and timely monitoring of geophysical phenomena globally.

1.2 ZY-3 04

On 16 December 2025, at 11:17 UTC+8, the Ziyuan-3 04 (ZY-3 04) satellite, a high-precision stereoscopic mapping platform, was successfully deployed into a sun-synchronous orbit *via* a Long March 4B launch vehicle from the Taiyuan Satellite Launch Center. The flawless orbital insertion represents another milestone in China's space-based geodetic and remote sensing infrastructure[2].

As part of China's National Civil Space Infrastructure Development Plan, ZY-3 04 carries three-line array stereoscopic cameras, a multispectral imager, and a high-precision laser altimeter, enabling simultaneous high-resolution stereoscopic and multispectral imaging. Operationally, it joins ZY-3 02 and 03 in orbit to form a stereoscopic Earth observation constellation. This capability significantly enhances large-scale topographic mapping and geographic information renewal, delivering high-accuracy data to support natural resource management activities including infrastructure development, resource inventory and monitoring, spatial planning, land use regulation, and compliance enforcement.

1.3 DQ-2

On 17 April 2026, at 12:10 UTC+8, the High-Precision Greenhouse Gas Comprehensive Exploration Satellite (DQ-2) was successfully deployed into a prescribed sun-synchronous orbit via a Long March 4C launch vehicle from the Jiuquan Satellite Launch Center. The flawless mission execution represents a critical milestone in China's space-based atmospheric environment monitoring infrastructure[3].

As an operational satellite specified in China's National Civil Space Infrastructure Development Plan, DQ-2 is equipped with five state-of-the-art scientific instruments, enabling multi-modal high-precision measurements of greenhouse gases and atmospheric trace pollutants. Its observational data will serve the operational needs of multiple national authorities, including the Ministry of Natural Resources, Ministry of Agriculture and Rural Affairs, National Forestry and Grassland Administration, and China Meteorological Administration, providing essential support for the implementation of the dual carbon strategy and the Beautiful China Initiative.

Upon commissioning, DQ-2 will operate in constellation with existing atmospheric monitoring satellites to establish a space-based environmental platform integrating laser, ultraviolet, visible, and infrared observation technologies. This constellation delivers integrated active-passive remote sensing with unprecedented hyperspectral and high temporal resolution for greenhouse gases, anthropogenic pollutants, and atmospheric aerosols. It provides a robust foundation for China's integrated space-ground environmental monitoring system, enabling synergistic observations of regional air pollution and greenhouse gas emissions. Furthermore, it will deliver sustained, high-quality spatial data to support ecological conservation, climate change governance, treaty compliance, energy efficiency improvement, and air pollution mitigation.

2 Data Coverage

This section describes the data coverage of Earth observation satellites acquired since 2024. Given that data products from atmospheric environmental monitoring missions and geophysical field monitoring missions cannot be effectively visualized in terms of spatial and temporal coverage, such data are excluded from the present analysis. Accordingly, the discussion covers only data coverage performance of optical and SAR remote sensing satellites.

2.1 Optical Satellites

Chinese optical satellites fall into three types: visible/multispectral, hyperspectral, and thermal infrared. Since 2024, 10 domestic optical satellites have operated with 2-meter-class payloads; valid data (cloud cover ⩽ 20%) provided cumulative global coverage of 3.34×10^8 km^2 (Figure 1). Two sub-meter-class satellites covered 7.6×10^7 km^2 globally with valid data (cloud ⩽ 20%) (Figure 2). Six hyperspectral satellites achieved

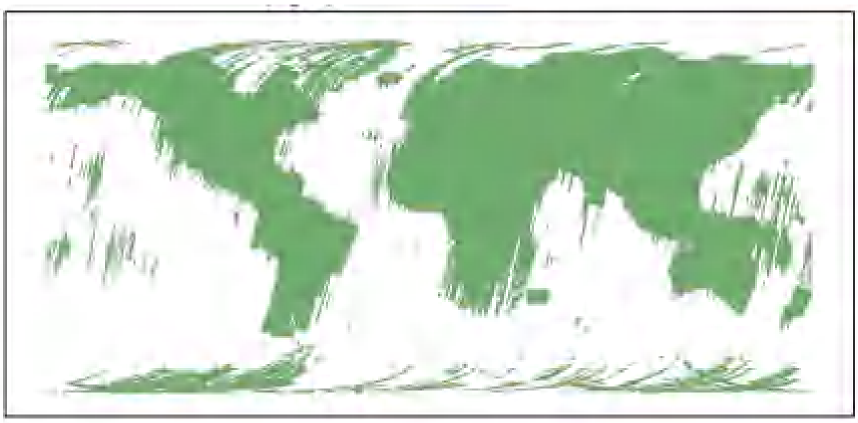

Fig. 1 Global valid data coverage of 2-meter class resolution optical satellites (cloud cover ⩽ 20%)

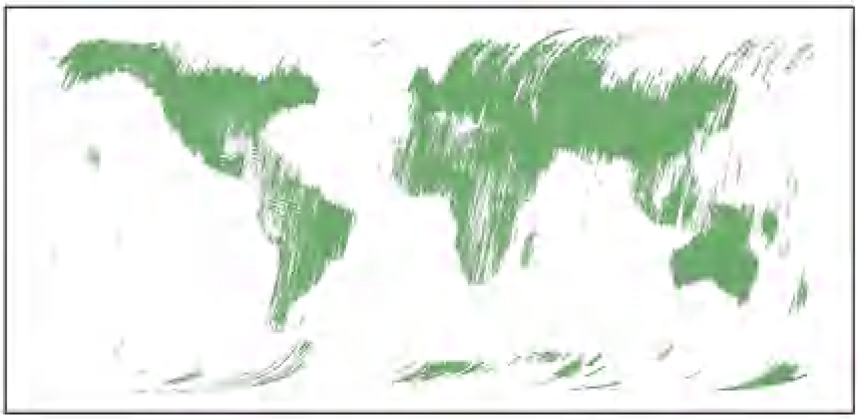

Fig. 2 Global valid data coverage of sub-meter class resolution optical satellites (cloud cover ⩽ 20%)

8.6×10^7 km^2 coverage (Figure 3), and six thermal infrared satellites reached 1.05×10^8 km^2 (Figure 4).

2.2 SAR Satellites

Eight SAR satellites operate in C, S, and L bands. They have accumulated 4.68×10^8 km^2 of global coverage since 2024 (Figure 5).

3 Data Distribution

China Earth Observation satellite data are distributed to research institutions, governments, commercial firms, and individuals. As of 31 May 2026, cumulative distributed imagery reached 121707293 scenes; 69416044 are high-resolution (⩽2.5 m) products (Table 2).

4 Conclusion

Over the past three decades, China's Earth observation satellite program has evolved into a comprehensive operational system with multi-spectral, all-time and all-weather global observation capabilities, and has made remarkable progress in constellation-based collaborative observation and on-orbit intelligent information processing[4–8]. As of mid-2026, a substantial fleet of civilian Earth observation satellites are operating stably in orbit with increasingly diverse payload configurations, which have greatly expanded the breadth and depth of remote sensing applications.

Commercial aerospace growth transformed industry development through mass production, frequent launches, and vertical integration. Mission costs decreased substantially, development cycles shortened, and applications expanded to agricultural insurance, commodity trading, infrastructure monitoring, and cultural heritage protection. Demand for quality remote sensing services drove improvements in payload specifications,

Fig. 3 Global valid data coverage of hyperspectral optical satellites (cloud cover ⩽ 20%)

Fig. 4 Global valid data coverage of thermal infrared optical satellites (cloud cover ⩽ 20%)

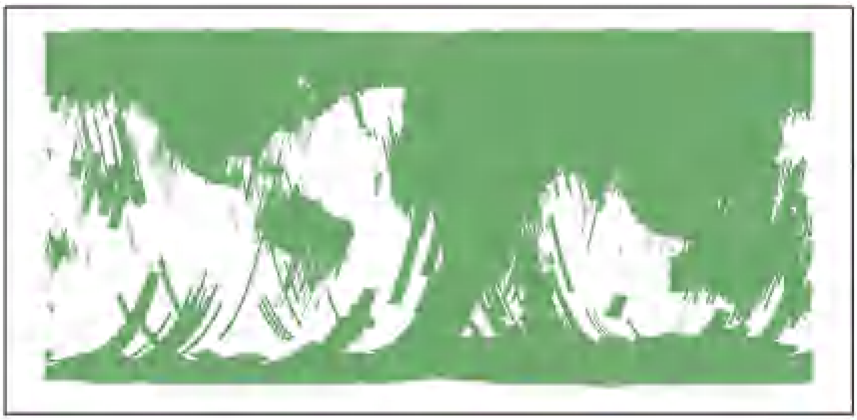

Fig. 5 Global coverage of SAR satellites

radiometric accuracy, and data delivery efficiency, accelerating coordinated space and ground segment development.

By 2030, China will establish a globally leading Earth observation constellation across multiple orbital types and modalities. The system will feature sub-meter spatial resolution, 1-day global revisit for key regions, and full-spectrum hyperspectral detection. Integrated capabilities include autonomous mission planning, on-orbit real-time interpretation, automatic target recognition,

Table 2 Statistics of imagery data distribution (as of 31 May 2026)

Satellite (Payload)	Distribution / scenes
CBERS-01/02	331001
CBERS-02B	806966
HJ-1A	4016256
HJ-1B	1662455
SJ-9A	997632
HJ-1C	382011
GF-5	1009098
ZY-1 02C	1811628
ZY3-01	3202018
GF-1	26284427
GF-2	26592631
CB-04	1914055
GF-4	4203039
ZY3-02	3502655
GF-3	4630961
GF-1B	2691566
GF-1C	2470165
GF-1D	2507470
GF-6	3723628
ZY-1E	1111389
GF-7	2790774
CB04A	231850
ZY3-03	1293772
HJ-2A	3020296
HJ-2B	3005590
GF-5B	5141788
GF-3B	1678766
ZY-1F	1434835
LT-1A	589715
LT-1B	576664
GF-3C	1669067
DQ-1(WSI)	1023839
CM-1(DMC)	2465881
HJ-2E	873163
GF-5 01A	1315333
HJ-2F	609021
JZ-1	68580
ZY3-04	67308
total	121707293

and intelligent information delivery, reducing data-to-service cycle times. These advances will provide high-precision Earth observation data and services to support ecological civilization construction, dual carbon strategy implementation, disaster risk reduction, and global sustainable development goals, deepening integration between remote sensing technology and the digital economy.

References

[1] China's First operational geophysical field exploration satellite Zhangheng 1-02 (CSES-02) Successfully Launched[EB/OL]. (2025-06-14)[2026-06-09]. https://www.cnsa.gov.cn/n6759533/c10680560/content.html (我国首颗地球物理场探测业务卫星—张衡一号 02 星成功发射 [EB/OL]. (2025-06-14)[2026-06-09]. https://www.cnsa.gov.cn/n6759533/c10680560/content.html)

[2] China Successfully launches stereoscopic mapping satellite Ziyuan-3 04[EB/OL]. (2025-12-16)[2026-06-09]. https://www.cnsa.gov.cn/n6758823/n6758838/c10722622/content.html (我国成功发射立体测绘卫星资源三号 04 星 [EB/OL]. (2025-12-16)[2026-06-09]. https://www.cnsa.gov.cn/n6758823/n6758838/c10722622/content.html)

[3] China successfully launches high-precision greenhouse gas comprehensive exploration satellite[EB/OL]. (2026-04-17)[2026-06-09]. https://www.cnsa.gov.cn/n6758823/n6758838/c10739812/content.html (高精度温室气体综合探测卫星成功发射 [EB/OL]. (2026-04-17)[2026-06-09]. https://www.cnsa.gov.cn/n6758823/n6758838/c10739812/content.html)

[4] YAN Wei, CHEN Weirong, LI Liutong, *et al*. Development of China's civil land observation synthetic aperture radar satellites and their application in natural disaster monitoring[J]. *Satellite Application*, 2026(2): 13-21 (严薇, 陈卫荣, 李六彤, 等. 我国民用陆地观测合成孔径雷达卫星的发展以及在自然灾害监测中的应用 [J]. 卫星应用, 2026(2): 13-21)

[5] LI Zhaozhou, ZHU Xiaobo, LI Zhengqiang, *et al*. Development of polarization payloads for China's civil land observation satellites and their typical demonstration applications[J]. *Satellite Application*, 2025(12): 6-11 (李照洲, 朱晓波, 李正强, 等. 我国民用陆地观测卫星偏振类载荷发展及其典型示范应用 [J]. 卫星应用, 2025(12): 6-11)

[6] ZHU Xiaobo, GUO Zhaohui, LIU Sihan, *et al*. Atmospheric environment monitoring satellite and its typical applications[J]. *Satellite Application*, 2025(5): 37-41 (朱晓波, 郭朝辉, 刘思含, 等. 大气环境监测卫星及其典型应用 [J]. 卫星应用, 2025(5): 37-41)

[7] LI Liutong, SUN Xuejiao, LI Junjie, *et al*. Development, products, services and applications of China's civil synthetic aperture radar land observation satellites[J]. *Satellite Application*, 2024(6): 6-13 (李六彤, 孙学娇, 李俊杰, 等. 我国民用合成孔径雷达陆地观测卫星发展与卫星产品、服务及应用 [J]. 卫星应用, 2024(6): 6-13)

[8] WANG Xiaoyan, LYU Zheng, LI Junjie, *et al*. Goumang terrestrial ecosystem carbon monitoring satellite and its applications[J]. *Satellite Application*, 2023(7): 18-22 (王小燕, 吕争, 李俊杰, 等. 陆地生态系统碳监测卫星句芒号及其应用 [J]. 卫星应用, 2023(7): 18-22)

Author Biography

HUANG Shusong (First author) Male, born in September 1989 in Yangxin County, Shandong Province, is currently a senior engineer at China Centre for Resources Satellite Data and Application. He is engaged in the research of remote sensing satellite operation management, data process and direct economic benefit evaluation of Remote Sensing Satellite.
E-mail: huangshusong@cresda.cn

CHEN Weirong（Corresponding author） (Corresponding author) Female, born in April 1980, is a research professor. She has successively led the research on Synthetic Aperture Radar (SAR) data processing algorithms, the R&D and operation of China's terrestrial satellite ground processing systems, as well as data management, distribution and satellite data services.
E-mail: weirong49@163.com

Secretariat Contact:

LI Xiaoyu, XU Yongjian

CNCOSPAR Secretariat

Tel: 86-10-6258 6404

Fax: 86-10-6263 2257

E-mail: xuyongjian@nssc.ac.cn